Functional Supramolecular Metallo-Assemblies

Stuart T. Onions

A thesis submitted in partial fulfilment of the requirements of The Nottingham Trent University for the degree of Doctor of Philosophy

January 2005

The Nottingham Trent University
Clifton Lane
Nottingham
NG11 8NS
UK

Abstract

The formation and characterisation of a novel range of homonuclear [2 x 2] grids are reported. These are formed by metal ion directed self-assembly of selected first row transition metal ions displaying an octahedral coordination preference with a single ligand strand. These assemblies display electronic communication between metal centres, indicated by both electrochemical and magnetic studies. Further manipulation of the ligand strand along with the inert character of the Cr(III) ion allowed the formation of a series heteronuclear [2 x 2] grids displaying magnetic interactions.

The attempted preparation of a series of mixed oxidation [2 x 2] grids *via* controlled potential electrolysis (CPE) is presented along with the successful preparation of a mixed oxidation Mn_9 [3 x 3] molecular grid, which displays antiferromagnetic exchange. This is first time the CPE has been manipulated within a grid-like structure to produce mixed oxidation species in a controlled manner.

A series of ligand strands with the potential to from [4 x 4] molecular grids are reported. Grid-like structures are structurally characterised with Mn(II) and Pb(II) metal ions some of which suffer from incomplete metal ion coordination. Other structural motifs are observed and rationalised in terms of the encoding within the ligand framework. The magnetic properties are consistent with the structures observed. These assemblies are some of the largest reported with the chosen metal ions and the largest in all cases to formed in a controlled predictable manner.

The first ever series of tetrametallic triple stranded helicates are reported which have been characterised in the solid-state and in solution. These display weak magnetic communication between metal centres with mixtures of both ferro- and anti-ferromagnetic behaviour, which is rationalised by the geometry of bridging ligands. Systematic alteration of the ligand framework produced a Cu_8 circular helicate displaying weak ferromagnetic behaviour, an Mn_6 assembly suffering from incomplete metal ion coordination and a Cu_{20} assembly displaying strong antiferromagnetic exchange.

Acknowledgements

I would like to principally thank my supervisor over the last three years, Dr. C. J. Matthews, for his enthusiasm and his ability to come up with interesting and sophisticated ideas, as well as all the people that went in and out of Lab S114 for the past three years, including numerous Erasmus and undergraduate project students.

Equally important are those people that helped characterise the compounds that I prepared. This extensive list includes Dr. A. Franklin (ESI-MS), Dr. D. J. Price (magnetic measurements), Prof. A. Harrison (magnetic measurements), Prof. L. K. Thompson (magnetic measurements), Dr. M. T. Lemaire (magnetic measurements), Dr. S. L. Heath (X-ray), Dr. R. Warrington (X-ray), Prof. W. Clegg (X-ray), Dr. P. N. Horton (X-ray), Dr. S. J. Coles (X-ray), Prof. M. B. Hursthouse (X-ray), Dr. M. E. Light (X-ray), Dr. M. R. J. Elsegood (X-ray), Dr. P. Meadows (^{207}Pb N.M.R. at JEOL LTD) and most of the technical staff at the Nottingham Trent University.

Finally, I would like to thank all my friends over the past few years for constructively distracting me from my work whenever necessary and most importantly to my family, especially my mother, for supporting me all these years.

Abbreviations

Bipy = 2,2'-Bipyridine
CFSE = Crystal Field Stabilisation Energy
COSY = Correlated Spectroscopy
m-CPBA = *meta*-Chloroperoxybenzoic acid
CPE = Controlled Potential Electrolysis
CV = Cyclic Voltammetry
DCM = Dichloromethane
DMF = *N,N*-Dimethylformamide
DMSO = Dimethyl sulfoxide
DPV = Differential Pulse Voltammetry
EPR = Electron Paramagnetic Resonance
ESI-MS = Electrospray Ionisation Mass Spectrometry
EtOAc = Ethyl acetate
FTIR = Fourier Transformer Infra Red
L = Ligand
M = Metal
MeCN = Acetonitrile
MeOH = Methanol
MLCT = Metal to Ligand Charge Transfer
NMR = Nuclear Magnetic Resonance
OAc = Acetate
OTf = Trifluoromethanesulfonate
Pdz = Pyridazine
PrOH = n-Propanol
Py = Pyridine
Pym = Pyrimidine
Pyz = Pyrazine
SQUID = Superconducting Quantum Interference Device
SMM = Single Molecule Magnet
TEA = Triethylamine
TEAP = Tetraethylammonium perchlorate
TFA = Trifluoroacetic acid

TIP = Temperature Independent Paramagnetism

TLC = Thin Layer Chromatography

TMSCN = Trimethylsilyl cyanide

UV = Ultra Violet

Contents

Chapter One

Introduction

1.0 Aim

This study aims to produce a variety of high nuclearity supramolecular assemblies that will be formed by the self-assembly of suitably designed organic ligands with first row transition metal ions that have a preferred coordination geometry. Assemblies that incorporate paramagnetic metal ions are the primary targets, particularly if the adjacent metal ions are in close proximity, since this will favour the formation of assemblies possessing magnetic and electrochemical properties. The formation of these functional assemblies will progress current synthetic strategies within the field of molecular magnetism by developing a "designed approach". Molecular based materials of this type are relevant towards the discovery of new nanotechnologies, particularly for producing high-density data storage materials.

1.1 Background

There is currently a massive demand from industrialised nations for ever-smaller technologies. Consequently, there is intense research into materials and techniques that allow the fabrication of these. Current magnetic nanotechnologies are fabricated in two distinct ways; firstly the "top down" approach which mechanically manipulates a certain material that exhibits the desired property on a macroscopic scale into smaller particles (~ 150 nm).[1] Problems occur as these materials, based on ceramics and metal oxides, approach the nanometre domain because of difficulties in producing particles of uniform size. At this domain the superparamagnetic limit is being reached, which is a phenomenon that occurs as the ambient thermal energy overcomes the energy barrier to reorientation of the magnetisation of the macroscopic particles.[2] The second technique is the "bottom up" approach that utilises supramolecular chemistry[3] to build large molecular assemblies with nanometre dimensions from small molecules. These assemblies do not have the problems associated with macroscopic particles because the magnetic behaviour is derived from within each individual assembly and is intramolecular in origin rather than relying on intermolecular interactions between individual molecules.[2]

The use of supramolecular chemistry to produce assemblies through molecular interactions based on hydrogen bonding, π-π stacking, van der Waals forces and the formation of coordinate bonds is well documented.[3] The latter interaction is often referred to as metal ion directed assembly and is achieved by the addition of a transition metal ion with a preferred coordination geometry to a suitable ligand.[4] This produces a discrete molecular assembly, and those containing multiples of transition metal ions often possess novel physiochemical properties that are different to those exhibited by individual metal ions.[5]

Assemblies displaying magnetic properties have caused much excitement in the past ten years because such compounds have the ability to act as bulk magnets at low temperatures.[6a] Consequently, these materials have been termed single molecule magnets (SMM) and it has been suggested that they could be manipulated as high density data storage materials and act as Q-bits in a quantum computer.[6b] Current research within this field is primarily concerned with the synthesis of new types of SMM and further developing those already discovered to achieve higher operating (blocking) temperatures.[6c] To understand the magnetic interactions occurring within such assemblies certain theories can be applied that are underpinned by the theory of magnetic susceptibility.

1.2 Magnetic Susceptibility

All compounds when placed within a homogeneous magnetic field will either move to a region of high magnetic field or to a region of low magnetic field. Compounds that move to a low region are termed diamagnetic; a consequence of paired electrons and thus all compounds are diamagnetic to some extent. Those that move to a higher region are termed paramagnetic and this is a consequence of unpaired electrons present within the compound. Furthermore, paramagnetism can give rise to various other effects, the most common of these are ferromagnetism and antiferromagnetism.

The paired electrons that occupy the closed shell of a paramagnetic compound interact with the applied field as diamagnets. In accurate work the influence of these must be taken into account to exclusively examine the paramagnetic behaviour of the species being studied. This can be achieved by either measuring the assembly with a suitable diamagnetic metal ion or more commonly by estimating the value using pre-determined values, *i.e.*, Pascal's constants.[7]

Assemblies that contain either only one metal ion or those that contain multiple metal ions separated by long bridging groups usually show magnetic properties associated with a single ion.[6] However, those which contain multiple metal ions that are in close proximity and separated by a suitable diamagnetic bridge/s have the potential for intramolecular exchange. The route provided by the bridge is termed a *superexchange pathway* and Anderson originally proposed the origins of the exchange by using the valence bond approach.[8]

For simplicity, Anderson assumed a dinuclear model where the two paramagnetic centres are separated by a single diamagnetic bridge. The single unpaired electron is located in an orbital that is non-orthogonal to the full *p* orbital of the bridge to give a linear array of M-L-M. The overlap between the partially filled *d* orbital and the filled *p* orbital leads to partial donation of electron density to the *d* orbital (Fig. 1, partial donation represented by smaller arrows). Such donation leads to pairing of the electrons in accord with Pauli's exclusion principle, yielding a net antiferromagnetic interaction.

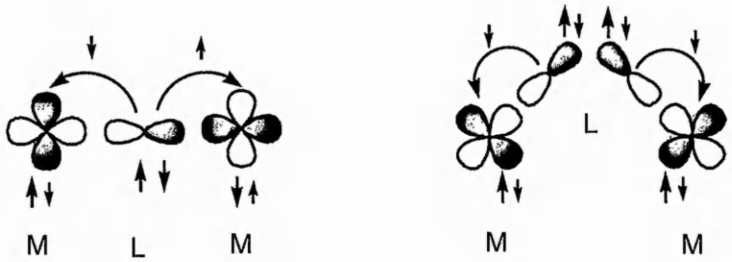

Figure 1 Left: orbital representation of superexchange leading to antiferromagnetic behaviour. Right: orbital representation of superexchange leading to ferromagnetic behaviour. Note: small arrows represent partial donation of electron density.

Anderson's description of ferromagnetic behaviour was limited to the two electron effect associated with the individual metal ions. Improving this theory, Goodenough proposed a mechanism that takes into account the partial bond formation of the ligand orbitals with non-orthogonal metal ion orbitals.[9] In this case (Fig. 1) the M-L-M has an angle of 90° so that the metal *d* orbitals interact with separate orbitals on the ligand. Partial donation of electron density from one orbital associated with the ligand to a half filled *d* orbital on the metal results in a level of pairing according to Pauli's exclusion principle. Spin correlation within the ligand always favours the parallel alignment of the spins in different orbitals, which encourages an equivalent spin configuration in the second orthogonal *p* orbital. Consequently, the spins all obey the Pauli exclusion principle, thus an overall unpaired electronic effect is observed termed ferromagnetic behaviour.

Further work by Kanamori has shown that the sign of the superexchange interaction is closely connected to the symmetry relationship between the metal ion and the ligand orbitals.[10] From the combination of theories, the Goodenough-Kanamori rules may be formulated:

(1) When the two metal ions have their magnetic orbitals that contain the unpaired electrons pointing towards each other in a way that allows for reasonable orbital overlap, then the exchange is antiferromagnetic.

(2) When the orbitals are arranged such that they have reasonable contact but no overlap then the exchange is ferromagnetic.

(3) If a magnetic orbital of one metal ion overlaps with an empty orbital of the other metal ion then the interaction is again ferromagnetic.

These rules can only be applied to systems of high symmetry with only monoatomic diamagnetic bridges. However, this approach is adequate for the systems produced during this study if a reasonable level of symmetry is assumed.

Several more sophisticated approaches have been developed, particularly by Kahn, who approached the problem from a molecular orbital point of view. It is claimed that such an approach allows the user to pre-design the desired magnetic properties by application of such a theory, but is limited to low nuclearity systems.[11]

The following section will discuss the determination of the relative exchange between metal centres rather than the mechanism. Determination of such parameters is important for higher nuclearity work because more precise theories become difficult to apply and consequently magneto-structural correlations are important.

Determination of Exchange Parameters

The molar magnetic susceptibility, χ_m, is defined as the partial derivative of the molar magnetisation, M, with respect to the applied field, H. In a relatively weak magnetic field it is appropriate to relate χ_m to the field, H, such that (1):

$$\chi_m = \frac{M}{H} \qquad (1)$$

For mononuclear species that are magnetically dilute, with only one unpaired electron the variation of χ_m with temperature follows the Curie law (2):

$$\chi_m = \frac{N\beta^2 g^2}{3kT} S(S+1) \qquad (2)$$

Where N = Avogadro's number, β = the Bohr magneton, k = Boltzmann constant, T = absolute temperature and g is the spin g-factor. This equation is rarely applicable because most systems are not magnetically dilute, thus the introduction of a constant can accommodate intermolecular interactions between individual molecules and is known as the Weiss constant, θ.

To calculate the molar magnetic susceptibility of a species that contains more than one paramagnetic centre, the way in which they interact must be determined. For example, in a dinuclear species with $S = 1/2$ represented as S_A and S_B the interactions between the metal centres leads to a molecular spin singlet ($S = 0$) and a molecular spin triplet ($S = 1$), with the energy gap noted as $-2J$ (Fig. 2). The $S = 1$ spin state can be split further by axial zero field splitting, D, which is a consequence of second order spin-orbit coupling and is termed an anisotropic interaction.

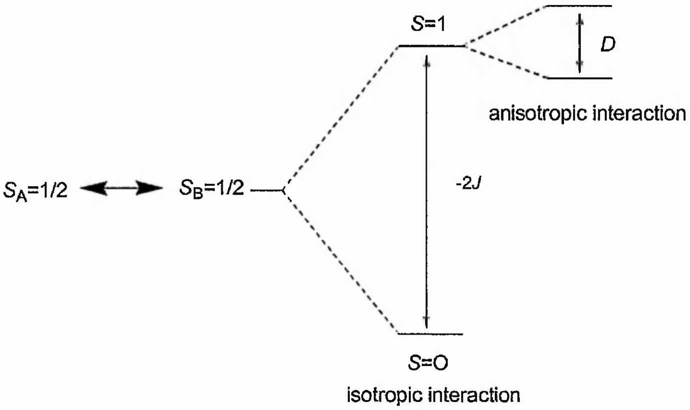

Figure 2 Schematic representation of energy levels in an interacting dinuclear species with $S = 1/2$.

The difference in energy, $2J$, is often referred to as the isotropic exchange integral and from its sign simple conclusions can be made. If $2J$ is negative then $S = 0$ and therefore the single electrons must have paired up to give antiferromagnetic behaviour. When $2J$ is positive then $S = 1$ with the electrons unpaired and is therefore termed ferromagnetic behaviour.

Calculation of χ_m must also consider that within a species that contains unpaired electrons there are a variety of spin configurations that can be adopted due to the availability of alternative orbitals lying close in energy. The occupation of the different spin configurations is caused by thermal energy and can be modelled according to the Boltzmann distribution law. Thus, calculation of a microscopic molar magnetisation is made for each of these individual spin configurations and weighted according to the Boltzmann distribution law which, followed by summation, yields the macroscopic molar magnetisation. Such an equation was originally developed by Van Vleck[12] and later manipulated by Bleaney and Bowers for a dinuclear Cu(II) system (3).[13]

$$\chi_m = (1-\rho)\ \frac{2N\beta^2 g^2}{kT}\ \frac{1}{3+\exp(-2J/kT)}\ + \chi_p \rho \quad (3)$$

χ_p and ρ account for paramagnetic impurities that often occur in Cu(II) and other paramagnetic assemblies which become more significant at low temperatures.

These ideas can be extended further to explain the magnetic interactions in larger assemblies with larger numbers of paramagnetic species, however the mathematics become very complicated. Spin-vector coupling, which was originally developed by Kambe[14] can significantly simplify the situation by assuming certain levels of symmetry within large assemblies and is the method most often used by chemists.[15] Also, it is possible to include other phenomena that affect the molar susceptibility such as temperature independent paramagnetism (TIP).

Temperature Independent Paramagnetism (TIP)

This is a correction factor that can be accounted for in terms of magnetic susceptibility, χ_m, to account for second order Zeeman splitting. This splitting can lower the energy of the thermally populated levels by a constant amount and thus the calculated χ_m is increased by a constant amount. Therefore TIP should be subtracted from experimental values of χ_m, unlike diamagnetic contributions that should be added.

Units in Magnetism

Unfortunately there is a mixture of units used to define different magnetic quantities, however the most common system employed is the unrationalised cgs emu system. In this system the permeability of free space, μ_0, is defined as unity and therefore in a vacuum the intensity of the magnetic field, B, is related to magnetic induction, H, (4):

$$B = \mu_0 H \qquad (4)$$

The volume magnetic susceptibility is a dimensionless quantity; traditionally expressed in the units emu cm^{-3} that derive from the dimension of emu being the cm^3. Logically the molar magnetic susceptibility has units cm^3 mol^{-1} and the effective magnetic moment is expressed in the Bohr magneton. This is defined as:

$$\mu = \left(\frac{3k}{N\beta^2} \right)^{1/2} (\chi_m T)^{1/2} \qquad (5)$$

Magnetic interactions can cause interesting phenomena such as spin crossover and SMM behaviour with the latter being a goal of this project in terms of new strategies for high nuclearity assemblies.

1.3 Single-Molecule Magnets

The most studied example of a SMM is $[Mn_{12}O_{12}(O_2CMe)_{16}(H_2O)_4]$ more often referred to as "Mn_{12}", which was originally reported in 1980 by Lis,[16] however the magnetic studies were not carried out until 1993 by the groups of Gatteschi and Hendrickson.[17] They discovered that the assembly showed hysteresis in a magnetisation against field plot and also proved that this hysteresis was of molecular origin because no evidence of three-dimensional magnetic order was observed in magnetisation, susceptibility or specific heat measurements.[2]

In this particular case there are eight Mn(III) ions and four Mn(IV) with respective ground state spins of $S = 2$ and $S = 3/2$ (Fig. 3). This gives rise to an overall $S = 10$ ground state spin for the Mn_{12} assembly, which derives from antiferromagnetic coupling between the four Mn(IV) and the eight Mn(III) implying a total of 21 microstates (+10 to -10). Thus, once the assembly is cooled in an external field it will occupy one of the two maximum ground states (+10 or –10) and the assembly is now magnetised (Fig. 3).

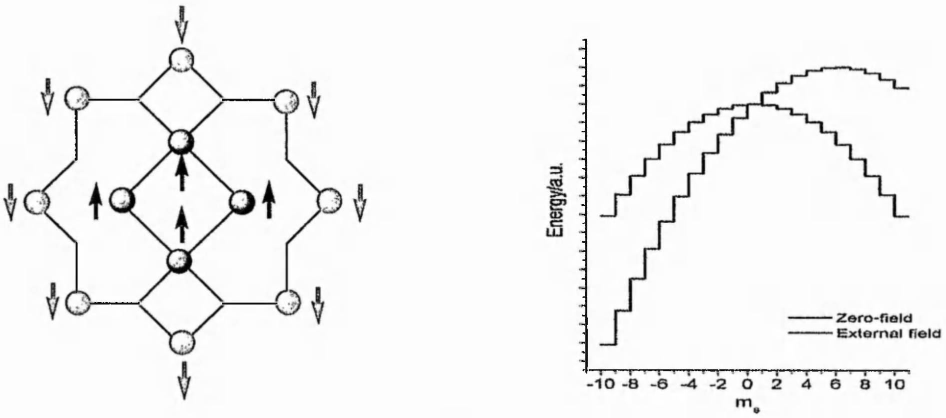

Figure 3 Left: The Mn_{12} core with the Mn(III) ions on the outside (red), *i.e.*, spins down and the Mn(IV) (blue) ions on the inside, *i.e.*, spins up and right: The distribution of spin-states in an applied field for Mn_{12}.

The reason for this overwhelming occupation of one particular state is because there is a splitting of the energy levels once it is placed inside an external field due to some spins aligning with the field (higher in energy) and some opposing the field (lower in energy). When the assembly is removed from a magnetic field it stays magnetised (at low temperatures) due to the energy barriers between each microstate. This particular assembly has a half-life of three months at 1.8 K and therefore this temperature must be increased before such materials can be exploited commercially.

It has been deduced from current SMM's that there are three parameters that are essential for a compound to act as a SMM.[18a] Firstly, the compound should have a high ground spin state (S_{gs}) and secondly a negative value of the axial zero-field splitting parameter (D). Both of these are related to the energy barrier for reorientation of magnetisation that is equal to DS^2. A larger value of S_{gs} can only be achieved by the addition of more magnetically coupled centres and D relates to the anisotropy of the spin and thus can be given a larger negative value by the use of highly anisotropic metal ions. The third parameter is the isotropic exchange integral that should have the largest value possible to allow SMM's to operate nearer room temperature.

Using the above parameters it is possible to establish synthetic strategies towards SMM's.[18] Two distinct strategies are common in the literature; design and serendipity, with the latter being considerably more utilised and producing novel SMM's. However, there has been no increase in the energy barrier to reorientation *via* the serendipitous approach from the original Mn_{12}, consequently the designed approach will be manipulated during this study.

1.4 Synthetic Approach: Serendipity and Design

Serendipitous Approach

This utilises ligands that exhibit more than one coordination preference along with metal ions that demonstrate fixed coordination geometries. Many of the approaches also rely upon deficiency of a chosen ligand and thus a lack of binding sites available for the selected metal ion, this consequently leads to the formation of bridges between metal centres which often leads to high nuclearity assemblies.[18b] The following section will discuss SMM's prepared by the serendipitous approach in terms of specific metal ions.

Vanadium

There are a series of vanadium SMM's in the literature reported by Christou and Hendrickson which all have the same central $[V_4O_2]^{8+}$ core with the vanadium in the +3 oxidation state.[19] The most interesting example, in terms of magnetic properties, is $[V_4O_2(O_2CEt)_7(bipy)_2](ClO_4)$ which has a butterfly structure made up from two V_3O triangles sharing a V-V edge. The assembly has a $S = 3$ spin ground state and a large value of zero field splitting, $D = -1.5$ cm^{-1} and consequently $[V_4O_2(O_2CEt)_7(bipy)_2](ClO_4)$ is a SMM.

Manganese

Christou and Hendrickson have manipulated Mn_{12} in a hope to increase its blocking temperature by varying the type of carboxylate ligand used and have been able to draw conclusions from these structural analogues. Firstly, changes in the carboxylate group can alter the relative orientation of Jahn-Teller distorted Mn(III) ions, which in turn alters the anisotropy of the spin and consequently the energy barrier to reorientation. They also noted that even the degree to which the system is solvated can also alter the orientation of the Mn(III) ions. However, these structural diversities have been unsuccessful in increasing the energy barrier to reorientation.[2]

Recently Christou has reported $[Mn_{25}O_{18}(OH_2)(N_3)_{12}(pdm)_6(pdmH)_6]Cl_2$ which has the highest spin ground state reported with a value of $S = 51/2$ at 2 K.[20] The assembly is a mixed valent $Mn(II)_6Mn(III)_{18}Mn(IV)$ which is prepared from a concoction of $MnCl_2{\cdot}4H_2O$, pyridine-2,6-dimethanol ($pdmH_2$), NaN_3 and tetramethylammonium hydroxide in a methanol/ acetonitrile mix. The central cation has a mixture of alkoxide bridged cores that hold the cage together with external azide and pyridine-2,6-dimethoxide anions completing the coordination to encapsulate the core. Variable field studies at temperatures ranging from 1.8 to 4.0 K provide evidence for the large ground spin state along with a small negative axial zero field splitting ($D = -0.022\ cm^{-1}$) and therefore the assembly may be a SMM. This is confirmed through single crystal studies on a micro SQUID at very low temperatures (0.04 - 1.0 K), yet the energy barrier to reorientation is relatively low, ~ 12 K (cf. Mn_{12} 66 K) due to the small value of axial zero field splitting.

Iron

Gatteschi and co-workers have utilised Fe(III) due to its large spin value ($S = 5/2$) and its tendency to promote ferromagnetic exchange. The most studied is that commonly referred to as "Fe8", which was originally prepared by Wieghardt (Fig. 4).[21] The formula is $[Fe_8O_2(OH)_{12}(tacn)_6]Br_8$ (tacn = 1,4,7-triazacyclononane) and comprises an octanuclear core. Analysis of the temperature dependence of the magnetic susceptibility provides evidence for a $S = 10$ spin ground state, which can readily occur assuming six Fe(III) ions with their spins up and two with their spins down.[22] More detailed investigation by high-field EPR and inelastic neutron scattering provide information that the ground state is largely split under the influence of zero field.[23]

The work of Powell and Heath reports a series of high nuclearity Fe(III) assemblies, in which the degree of bridging is controlled by pH.[24] This work has produced a series of Fe_{19} assemblies that display both high ground spin state ($S > 33/2$) and hysteresis.[25] Fig. 4 shows the ligand which is fully deprotonated when coordinating Fe(III) ions and this captures a portion of the $Fe(OH)_2^+$ lattice to yield a high nuclearity assembly. Of interest are that subtle changes in the ligand, *i.e.*, R = Me or Et (rather than H) that introduce ordering between the individual layers of clusters to form tilted stacks and thus are a significant development in the ordering of magnetic particles. Also the stacking is independent of the counter anion used in the cases of NO_3^- and Cl^-.[24]

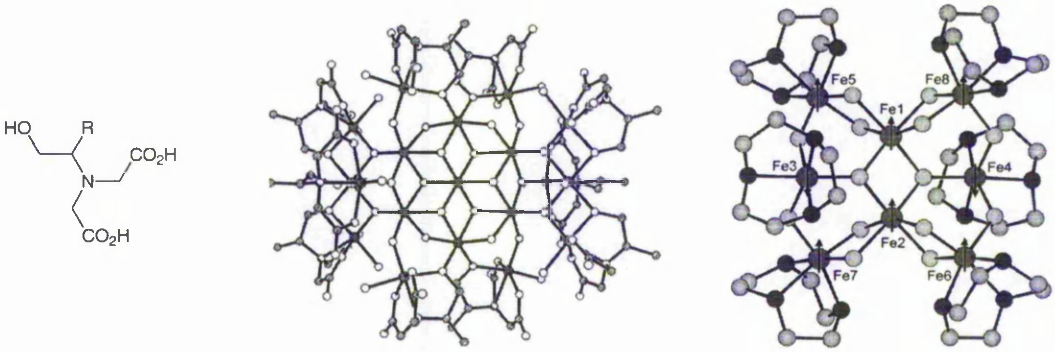

Figure 4 Left: The ligand (H_3heidi) where R=H, Me (H_3metheidi) or Et (H_3etheidi), middle: crystal structure of $[Fe_{19}(metheidi)_{10}(\mu_3\text{-}OH)_6(\mu\text{-}OH)_8\text{-}(\mu_3\text{-}O)_6(H_2O)_{12}]^+$ and right: $[Fe_8O_2(OH)_{12}(tacn)_6]^{8+}$ core with arrows representing direction of spin. Blue = N, Yellow = O.

Cobalt

The most recent example of a cobalt SMM was reported by Murray and Gudel; $[(NMe_4)_3Na\{Co_4(cit)_4[Co(H_2O)_5]_2\}]$ is a hexanuclear Co(II) assembly with a central $[Co_4O_4]$ core where each oxygen atom is derived from a tridentate citrate alkoxide group (cit = $[C(O^-)(CO_2^-)(CH_2CO_2^-)_2]$).[26] The magnetic studies of this compound in its solvated and partially solvated forms indicate that it is indeed a SMM with an energy barrier to reorientation of approximately 32 K, which is the highest reported for a non-manganese assembly.

Nickel

Winpenny has produced a cyclic dodecanuclear nickel complex which is the first SMM based on Ni(II) centres.[27] The cyclic structure of twelve Ni(II) ions is held together by bridging pyridonate and acetate ligands (Fig. 5). It has crystallographic S_6 symmetry and all rings within the structure pack parallel to each other and perpendicular to the crystallographic c-axis. Isothermal magnetisation studies at 150 mK and 25.5 μ_b confirm an overall $S = 12$ ground spin state, indicating ferromagnetic exchange between the twelve, $S = 1$, Ni(II) ions. A more recent detailed study indicates that it has an energy barrier of approximately 10 K to reorientation of magnetisation. Resonant quantum tunnelling has been observed and an accurate value of D, which is -0.067 K, has also been determined. Inelastic neutron scattering indicates a more complex exchange between the Ni(II) centres, with a total of three interactions, two ferromagnetic (11 and 2 cm^{-1}) and one antiferromagnetic (-0.9 cm^{-1}).[28]

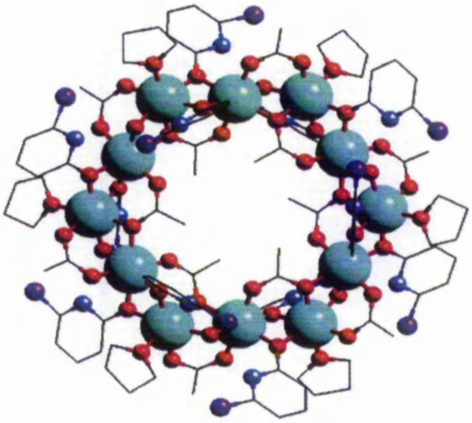

Figure 5 Crystal structure of $[Ni_{12}(chp)_{12}(O_2CMe)_{12}(H_2O)_6(THF)_6]$ (chp = 6-chloro-2-pyridonate). Ni = Green, O = Red and N = Blue.

Further Manipulation of SMM's

Other authors have been developing SMM's in different ways. Larionova has used thermal derivatives of the previously prepared Mn_{12} in the hope of fine-tuning its properties.[29] Upon heating to 403 K, water and acetic acid are lost from the assembly allowing the incorporation of ammonia. This forms a new SMM that is described as having peculiar magnetic behaviour. In terms of future applications, Cornia has organised the Mn_{12} SMM on a gold surface by the introduction of a long alkyl chain with terminal thiol and acetyl protected thiol groups.[30] Also, Coradin and Larionova have introduced Mn_{12} into a mesoporous silica host that causes ordering between Mn_{12} clusters due to host-guest interactions.[31]

Designed Approach

This approach has a variety of applications in other fields rather than just the preparation of magnetic materials, for example chirality, energy transfer and metal-metal bonding.[32] Most work is based upon diamagnetic metal ions or paramagnetic metal ions that are separated by long bridging groups that hinder magnetic exchange. The following section will very briefly mention helicates, along with simple definitions, together with some that display magnetic interactions. Following this, a more comprehensive section on grids some of which display magnetic exchange along with other physical properties.

Helicates

Helicates are undoubtedly the most prevalent architecture that fall into the designed category.[33] Lehn originally defined the term helicate in 1987, which is not to say helicity was not observed before then, it was just not commented on.[34] In a helicate the ligands wrap around the two or more metal centres defining the helical axis with the distance between one turn of the helical axis and the next known as the pitch (Fig. 6).[35]

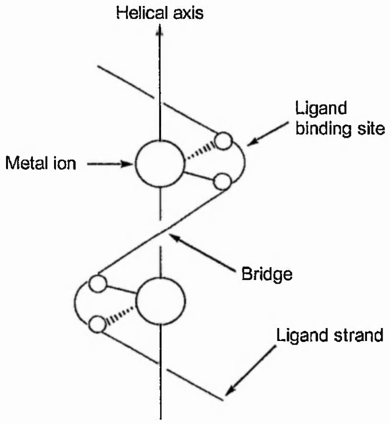

Figure 6 Schematic representation of a helical structure.

The majority of helicates found in the literature only contain two metal centres and are usually diamagnetic. However, when paramagnetic ions are included they are usually spaced by long bridging groups that impede magnetic exchange. For example, it was observed that the reaction of L(A) with Cu(I) forms a double helix due to the tetrahedral nature of the ion while L(B) forms a trinuclear double helix when reacted with Cu(I).[34]

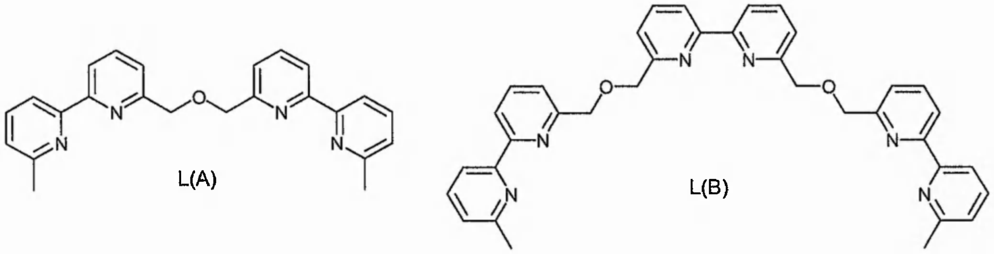

Figure 7 Ligands L(A) and L(B) form double and triple stranded helicates respectively with tetrahedral metal ions.

Hannon has produced a variety of relatively simple dinuclear double stranded helicates with tetrahedral metal ions. The ligand design, originally developed by Busch and Stratton[36], is based around the condensation of a simple amine with an aldehyde.[37a] The resulting imine ligands are usually susceptible to hydrolysis, but by the incorporation of an aromatic ring joined to the imine moiety the stability is enhanced (Fig. 8). L(C) unsurprisingly forms triple helicates with metal ions that exhibit an octahedral coordination preference and has been reported for Fe(II) and Ni(II).[37b]

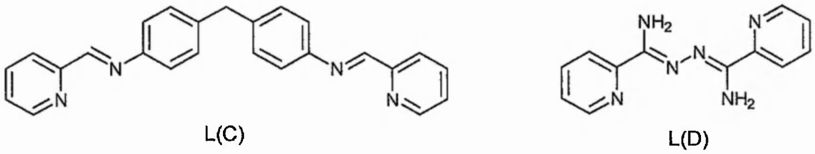

Figure 8 L(C) forms both double and triple helicates with tetrahedral and octahedral metal ions respectively while L(D) forms triple helicates with octahedral metal ions with close metal ion proximity.

Thompson has subsequently shown with similar imine based ligands that the diazine group present within the ligand framework can act as a donor and a bridge allowing magnetic exchange between adjacent metal centres to be observed (Fig. 9, L(D)).[38] When L(D) was reacted with Mn(II) and Ni(II) dinuclear triple stranded helicates formed. For the Mn(II) motif there is an acute twist of the metal magnetic orbitals around the diazine N-N bonds which causes the expected ferromagnetic exchange ($2J = 2.1\ \text{cm}^{-1}$), whereas the Ni(II) structure shows no intramolecular exchange.

From the vast amount of literature available three key features controlling helicate formation have been summised[35]:

1) Metal ion coordination preference,
2) Coordination environment provided by the ligand pocket,
3) The nature of the bridging group.

Building on these design strategies it was soon realised that even more complex assemblies could be made. The most logical is an extension from the one-dimensional helicate into a two-dimensional grid.

[2 x 2] Grids

The first [2 x 2] square grid-like arrangement was prepared *via* the self-assembly of rigid a ligand that contained linear arrays of bidentate coordination sites designed to accommodate metal ions with a preferred tetrahedral coordination environment.[39] Following this lead it was demonstrated that the [2 x 2] motif could be used to incorporate paramagnetic octahedral metal ions by using ligands that contained tridentate pockets and consequently introducing functionality into the grid.

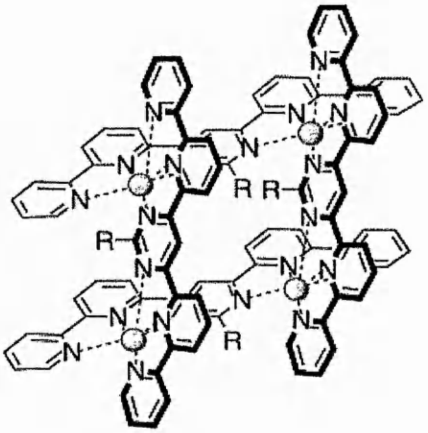

Figure 9 Schematic representation of [2 x 2] grid. R = H, Me, Ph.

For example Lehn *et al.* have been studying [2 x 2] grids that are based upon pyrimidine and pyridine ring systems (Fig. 9). Initial work with the diamagnetic Pb(II) ion proved that the ligand design was suitable, demonstrating the power of a designed approach.

This grid was characterised by conventional techniques (X-ray, ^{1}H NMR) and non-conventional techniques, which included ESI-MS and ^{207}Pb NMR.[40]

Following this result, the incorporation of paramagnetic metal ions into the motif was pursued. First reported was a series of homometallic systems which have incorporated most of the first row of transition metal ions along with Cd(II) and Hg(II) from the second and third row, respectively.[41] The Co(II) and Ni(II) complexes have been made subject of detailed magnetic studies. These demonstrated that there is weak antiferromagnetic exchange between the neighbouring ions *via* the superexchange pathway provided by the central pyrimidine ring. Of particular interest is the Fe(II) assembly; communication of this showed that spin crossover could be induced under the influence of heat, light and pressure.[41c] Unfortunately, the spin transition is not sharp due to the number of Fe(II) ions present. A further study demonstrated the effects that substituents on the ligand could have on the spin transition by means of steric and electronic effects, in a hope to fine-tune this property. It was inferred from this study that steric effects were having more effect over the spin transition induced by heat rather than electronic ones.[41d]

Heterometallic [2 x 2] grids have also been synthesised by Lehn; whereby one tridentate site situated on a single ligand strand is blocked and in turn this protected strand reacted with a relatively inert metal ion (Os (II) or Ru (II)) to yield a corner piece. Subsequent deprotection and reaction with a suitable labile metal ion (Co (II), Fe (II) or Ni (II)) gives a heterometallic [2 x 2] grid with the metals in the desired *syn* arrangement with respect to each other (Fig 10).[42a]

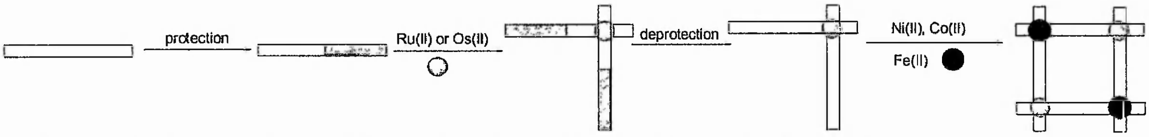

Figure 10 Schematic representation of controlled formation of heterometallic grid.

A more recent investigation of the mixed $Ru(II)_2Fe(II)_2$ and $Os(II)_2Fe(II)_2$ grids demonstrated that both compounds had very intense absorption bands in the UV region (attributed to spin-allowed ligand centred transitions), as well as intense metal-to-ligand charge transitions. Unfortunately, neither grid exhibits luminescence at room temperature or at 77 K, which is in contrast to both mononuclear species that display luminescence at room temperature in acetonitrile and at 77 K in butyronitrile. Detailed assignment of the electrochemical behaviour has also been made and it is apparent that these systems can be viewed as multi-level molecular electronic species capable of reversibly exchanging a number of electrons.[42b]

Further work of Lehn has attempted to incorporate some order between individual grids. Firstly, incorporation of hydrogen bond donor/ acceptors at the terminal aromatic rings leads to an infinite one-dimensional chain rather than the expected two-dimensional, grid of grids (Fig. 11). Anions and solvent molecules are situated between the layers, stopping any interaction between them.[43]

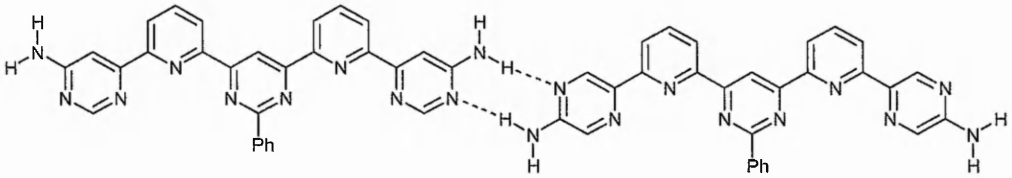

Figure 11 Formation of intermolecular hydrogen bonds to cause organisation between [2 x 2] grids.

Lehn has bound the [2 x 2] motif to a surface to demonstrate the possible applications of such compounds towards high data storage. Such grids have a distinct advantage over those assemblies formed *via* the serendipitous approach because they are essentially flat therefore can be ordered on a surface in a uniform manner.[44a]

The most interesting example of Lehn's work in terms of magnetic properties is a homometallic [2 x 2] grid which is limited to a single communication.[44b] L(E) provides two symmetrical tridentate pockets that share an alkoxy bridge causing close metal ion proximity (Fig. 12). The only assembly reported is with Cu(II) that forms a [2 x 2] grid structure with metal-metal separations less than 4.1 Å and bridging angles between metal centres around 141°. Unfortunately, the assembly shows very weak coupling between adjacent metal centres due to the arrangement of the magnetic orbitals on the Cu(II) ion. No other assemblies are reported with L(E) that maybe a consequence of the hydrolytically sensitive imine bonds.

Thompson and Matthews have produced a number of [2 x 2] grids with first row transition metals ions, in an attempt to discover novel magnetic properties within the motif. To achieve this, the metal ions are brought into close proximity with respect to each other. Ligand L(F) has also been shown to form pentanuclear structures[45], but under the correct conditions the [2 x 2] grid motif can be formed with Mn(II), Cu(II), Co(II), Ni(II) and Zn(II). A mixed Cu(II)$_3$Fe(III) system has also been prepared.[4c]

Unfortunately, the ligand does not satisfy the coordination requirements of these transition metal ions, except Cu(II) that adopts a five coordinate square-based pyramidal type geometry, causing both solvent molecules and anions to make up the vacant sites. Variable temperature and variable field studies have been reported for these assemblies to determine the nature of the intramolecular exchange and the spin ground state. The Mn(II), Co(II) and Ni(II) display expected antiferromagnetic exchange which can be rationalised in terms of the large M-O-M bridging angle (> 120°) (Fig. 12).[4c]

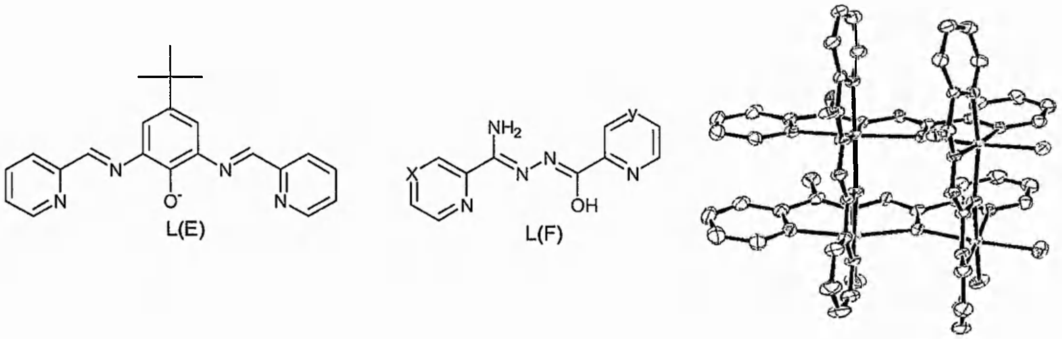

Figure 13 Left: L(E) only forms a [2 x 2] grid with Cu(II) and may be susceptible to hydrolysis, middle: L(F) forms heteroleptic and homoleptic [2 x 2] grids with first row transition metal ions, X = CH, N, Y = CH, N and right: $[Ni_4(L(F)\text{-}H)_4(H_2O)_4]^{4+}$ cation including water molecules making up vacant coordination sites.

Interestingly, the Cu(II) complex displays a magnetic profile which is indicative of an intramolecular ferromagnet. The close spacing of the metal centres and the very large Cu-O-Cu bridge angle would normally imply antiferromagnetic behaviour. The data obtained were fitted to equation 6. ($S = 1/2$).

$$\chi_m = \chi_m(1-\rho) + \frac{(2N\beta^2 g^2 \rho)}{3kT} + TIP \qquad (6)$$

To give $g = 2.119$, $2J = 8.4\ \mathrm{cm}^{-1}$, $\rho = 0.00002$, $\theta = -0.5\ \mathrm{K}$ and TIP = $0.000234\ \mathrm{cm}^3\ \mathrm{mol}^{-1}$. Further study at 2 K, using magnetisation data as a function of field can also be fitted to give $g = 2.119$ and confirms the expected $S = 2$ ground state. This outcome can be explained because the Cu(II) complex has an orthogonal arrangement of $d_{x^2-y^2}$ magnetic orbitals.[4c]

Recently both Brooker and Stoeckli-Evans have been working with the ligand L(G), this has a pyrazine ring as the central bridging group, along with alkoxide and imine groups to make up the rest of the donors (Fig. 13).

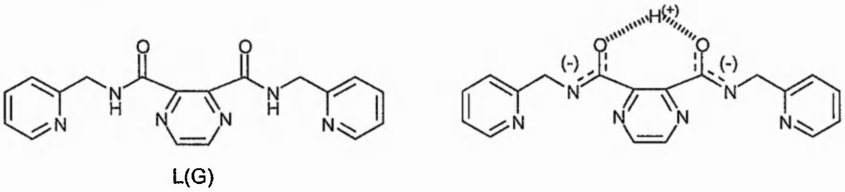

Figure 13 L(G) in its non-coordinating and deprotonated coordination modes.

Brooker has reported that reaction of this ligand with one equivalent of $Cu(BF_4)_2 \cdot 6H_2O$ in acetonitrile yields a dimeric copper assembly in which neither of the protons have been lost from the ligand but one has been transferred to the terminal pyridine ring and preventing the ring from being involved in coordination.[46] Interestingly, it was noted that upon addition of one equivalent of triethylamine to a solution of the dimeric species in acetonitrile a change in colour from deep-navy blue to grass green is observed. This green complex has been identified as a [2 x 2] grid with one proton lost per ligand and the remaining proton bound between the formally negatively charged alkoxide oxygens (Fig. 13).[46] Stoeckli-Evans has not reported the dimeric Cu(II) intermediate, but has formed the [2 x 2] grid motif with both $Cu(ClO_4)_2 \cdot 6H_2O$ and $NiCl_2 \cdot 6H_2O$. Variable temperature magnetic studies have been performed on these latter two complexes and display weak antiferromagnetic exchange, with $2J = -5.87\ \mathrm{cm}^{-1}$ and $2J = -2.64\ \mathrm{cm}^{-1}$, respectively.[47]

There have been numerous single reports of [2 x 2] grids from other authors and these will be discussed briefly in the following section. Pecararo *et al.* reported a tetranuclear Mn(II) grid-like complex that contained a formally negatively charged ligand, L(H) (Fig. 14), reducing the assembly's charge to +4. Catalytic studies on the disproportionation of H_2O_2 to O_2 show that the assembly is highly efficient but suffers from a poor binding constant and at low concentration the assembly appears to be completely inactive, which suggests the formation of lower nuclearity species.[48]

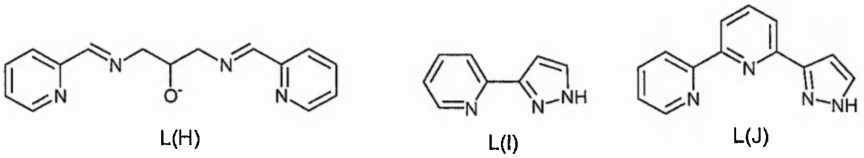

Figure 14 L(H), L(I) and L(J) respectively with L(H) in its deprotonated form.

Ward and McCleverty reported mononuclear complexes of Ni(II) and Zn(II) when reacted with L(I),[49] however in the case of Cu(II) a tetranuclear [2 x 2] grid complex is formed because of its stereoelectronic preference.[50] Two of the coppers have their coordination geometry made up with four N donors and one DMF molecule giving a square-pyramidal environment, while the other two Cu(II) ions have five N donors and again with a square-pyramidal environment. A simple extension of ligand L(I) gives ligand L(J) that also forms mononuclear complexes with transition metal ions, however this again gives a grid-like structure with each Cu(II) environment made up from four N donors and one DMF molecule. Both assemblies exhibit strong intramolecular antiferromagnetic exchange with $2J \sim -63.5$ and $-170\ \text{cm}^{-1}$ for L(I) and L(J) respectively.[51]

von Zelewsky has demonstrated a rational designed approach that provides rigid ligands made up of aromatic rings with a central pyrazine ring that is substituted in the 2,5 positions allowing the formation of an interwoven [2 x 2] grid. Furthermore, the incorporation of a chiral element into the ligand *via* a pinene moiety, L(K), (Fig. 15) allows the formation of predominantly the *R,R* diastereomer and is the only example in the literature of a chirally resolved grid.[52]

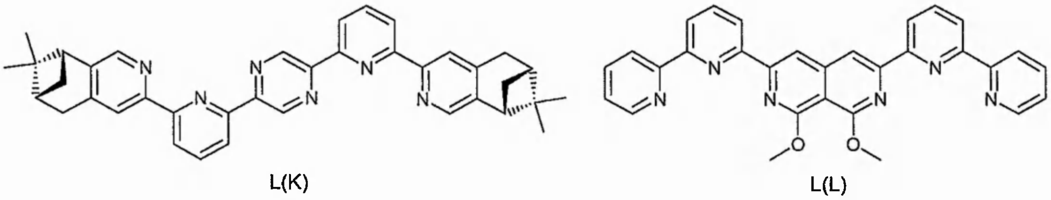

Figure 15 L(K) incorporating the pinene unit as a chiral element and L(L) with its naphthalene spacer.

A mixed oxidation $Fe(II)_3Fe(III)$ system has been reported by Chun-Ying which is constructed *via* self-assembly of bis(2-acetylpyridine)thiocarbazone that acts as both linker and reducing agent. Magnetic measurements suggest that there is only one Fe(III) present within the [2 x 2] motif, but cannot be identified from the crystal structure due to similar iron coordination environments. Also the Ni(II) and Zn(II) analogues are reported with the former assembly showing antiferromagnetic behaviour that is typical of Ni(II) in a square arrangement.[53]

The last example of a [2 x 2] grid is that provided by Glass. L(L) forms a [2 x 2] grid when added to $Co(OAc)_2$, which is a mixture of Co(II) and Co(III) due to reduction of the ligand. Addition of HBr yields the Co(III) grid with a formal charge of +6 because two of the ligands are protonated. This grid has a large internal cavity because of the naphthalene spacer that could be used to allow binding of other motifs. Also the methoxy substituents that are reduced to alkoxy groups could allow the introduction of other functionalities.[54]

[3 x 3] Grids

The first [3 x 3] grid was formed utilising a ligand that provided a linear array of bidentate pockets that could suitably bind to a tetrahedral metal ion. This was reported by Lehn and co-workers using Ag(I) as the metal ion and an extended pyridazine/ pyridine based ligand.[55a] They demonstrated that the grid was stable in solution by ^1H and ^{109}Ag NMR, the latter spectrum showed a single entity with three resonance intensities of 4:4:1 representing the four corners, the four inner sides and the central Ag(I) ion. Solid-state characterisation was achieved by X-ray crystallography showing the expected [3 x 3] grid with a slight slant to the whole structure, which is probably a consequence of the relatively large size of the Ag(I) ion. A recent mechanistic solution study has shown the existence of a variety of exclusive intermediates which form at specific concentrations as the ratio of Ag(I) to ligand is increased from 1:1 to the ideal 3:2. On the addition of more Ag(I) there is no evidence to suggest that other species are present in solution, demonstrating the robustness of the grid.[55b]

Lehn has also extended the pyrimidine/ pyridine system based upon that used to form the [2 x 2] grids (Fig. 16). Initial work with this ligand, L(M), with Pb(II) demonstrated that the [3 x 3] motif could be formed, but could only be characterised in solution (^{1}H NMR, ESI-MS).[46] A more recent comprehensive study with various transition metal ions has utilised ESI-MS as a probe. This article demonstrates that unfortunately, the most stable motif is that of a so called [2 x 3] grid (Fig. 16), which is predominately formed because of a combination of the sterically restrained ligand, low donor power of the pyrimidine ring and the relatively small size of these ions (c.f. Pb(II)).[56]

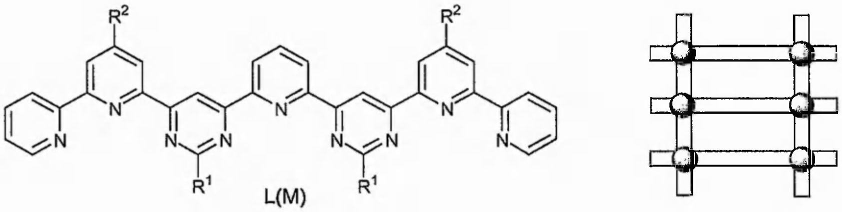

Figure 16 L(M) with the ability to form a [3 x 3] grid and a schematic representation of a [2 x 3] grid.

Remarkably, a complete [3 x 3] grid is formed by the reaction of $Zn(BF_4)_2 \cdot 6H_2O$ with the ligand ($R_1 = R_2 = H$) when the reaction is maintained at reflux for nineteen days in acetonitrile, however this is not the case for $Zn(OTf)_2 \cdot H_2O$ or $Zn(OAc)_2 \cdot 2H_2O$ where the [2 x 3] grid forms. The reasons for this are unclear, it is suggested that the more strongly bonded triflate and acetate anions compete for the metal and that these anions could be bound up in some of the coordination pockets.[56]

A simple extension of the L(F) gives L(N) with the capability of forming a [3 x 3] grid that has the metal ions in close proximity due to the alkoxide bridge (Fig. 17). The complex $[Mn_9((L(N))\text{-}2H)_6](ClO_4)_6 \cdot 18H_2O$ involves a homoleptic structure with six parallel ligands, arranged in two groups of three, above and below the grid plane of nine alkoxide bridged Mn(II) centres (Fig. 18).[4a] The close proximity (3.9 - 4.0 Å) of the Mn(II) centres and large Mn-O-Mn (126 - 130°) leads to antiferromagnetic exchange and an overall $S = 5/2$ spin ground state. More detailed magnetic studies of this assembly have been undertaken and demonstrate significant magnetic anisotropy due to zero field splitting.[57]

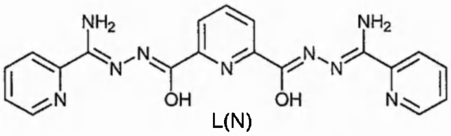

L(N)

Figure 17 L(N) provides a linear array of three tridentate pockets that share alkoxide bridges giving close metal-metal proximity.

Of particular interest is the electrochemistry; this displays five reversible waves between +0.72 and +1.58 V (Fig. 18). From coulometry studies it was discovered that the first wave represents a four-electron oxidation, while the following four waves each represent a one-electron oxidation. The most oxidised grid is in the form Mn(II)Mn(III)$_8$ and it is proposed that the individual Mn(II) lies at the centre of the grid. These results show that mixed valent assemblies could possibly be synthesised in a controlled manner.

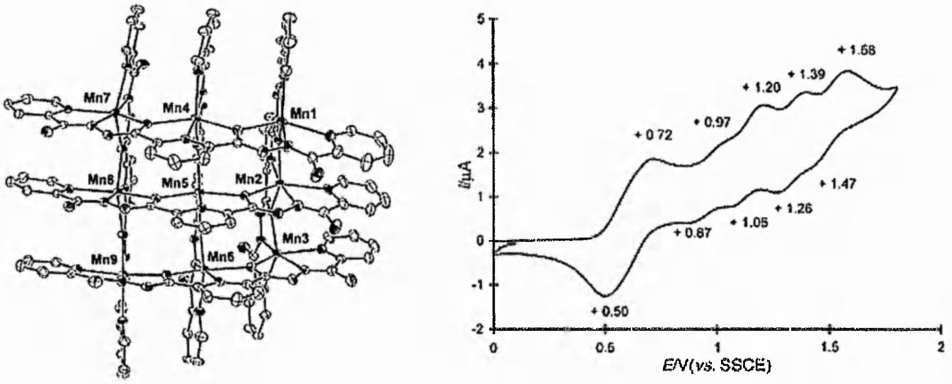

Figure 18 Left: structural representation of $[Mn_9((L(N))\text{-}2H)_6]^{6+}$ cation and right: Cyclic voltammetry for Mn(II)$_9$ grid in acetonitrile (0.5mM, 0.1M Net_4ClO_4; Pt working electrode, Pt counter electrode, SSCE reference electrode; BAS CC27 voltammograph; 100mVs^{-1}).

The analogous Cu(II) grid has also been reported, this has essentially the same inner core as the Mn(II) structure, with a similar disposition of the Cu(II) orbitals to that found in the case of the Cu$_4$ square grid.[1b] The magnetic moment of the grid shows a steady decrease from 6.4 μ_B at room temperature to 5.5 μ_B at 25 K, followed by a sharp rise to 6.9 μ_B at 2 K. This indicates a fairly strong antiferromagnetic exchange along with a ferromagnetic contribution. Magnetisation studies at varying field strength at 2 K are best fitted to an S = 7/2 spin ground state which confirms the presence of competing exchange mechanisms at this temperature.

Higher Order Grids

Work with higher order grids is extremely rare and has been quoted as a synthetic challenge by one author[58] and has been restricted to diamagnetic metal ions, except in one case.[61] Lehn has produced a [4 x 5] grid along with a quadruple helicate that contain 20 and 10 Ag(I) ions, respectively, with the ligand L(O) (Fig. 19).[59] Room temperature ^1H NMR studies display a mixture of peaks that were difficult to assign, however at high and low temperatures two separate species were predominant, again no assignment was made. Upon crystallisation a mixture of the [4 x 5] grid along with the quadruple helicate co-crystallise. The reason for this vacant coordination in the grid is unclear. It is suggested that the overall structure is more stable because there is one less ligand present. This ligand absence allows the opposing set of ligands to adopt a *cis* conformation, which is lower in energy.

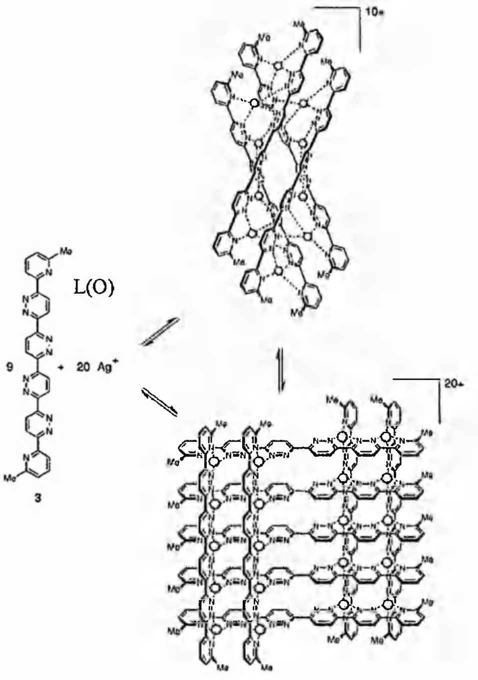

Figure 19 L(O) forms an equilibrated mixture of both a Ag_{20} grid and a Ag_{10} quadruple helicate when reacted with Ag(I).

Recently Lehn has reported a fully characterised Pb_{16} [4 x 4] grid based upon the extended ligand, L(P).[60] The crystal structure shows the fully metalated grid with the Pb(II) ions having varying coordination modes (7 - 9) due to the binding of the triflate anion/ s and/ or water. The eight ligands are arranged into two perpendicular disposed sets of four outer and four inner ligands, resulting in an irregular [4 x 4] grid. Also, there is detailed analysis of the effects of excess metal salt and determination of the structures formed, which include a $Pb_{12}L(P)_4$ hash type structure that appears to be stable even on the addition of more metal salt.

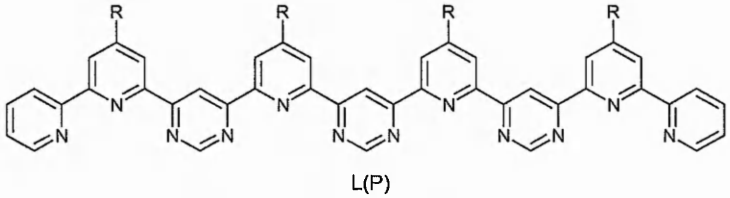

Figure 20 L(P) has the ability to form [4 x 4] grids. R = $S^{n}pr$.

Matthews and co-workers have produced a Cu_{12} picture frame type grid that suffers from incomplete metal ion coordination due to restraints of the ligand and is best described as a "picture frame" type structure (Fig. 21).[61] It also incorporates a single Na^+ ion in one of the central tetrahedral cavities that has been shown not to be involved in the self-assembly process. Magnetisation studies have been undertaken, but are very complex due to a complete lack of symmetry within the structure and only a reasonable fit of the Curie-Weiss law is seen above 200 K.

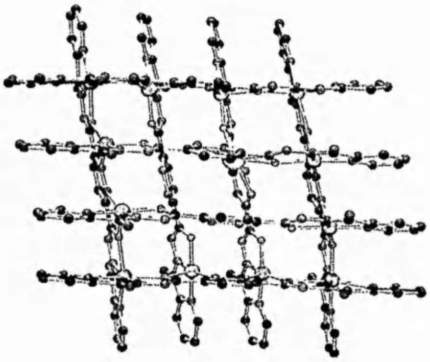

Figure 21 Cu_{12} "picture frame". Green = Cu(II), Blue = N, Yellow = Na(I) and Red = O.

Design vs. Serendipity

Currently within the field of functional assemblies there is varying opinion as to the best strategy and thus a discussion of their advantages and disadvantages is apt.[18] The serendipitous approach relies initially on luck to produce a preliminary result and then the ability to use rational and experience to further develop this initial result. Advantages include the ability to produce compounds of high nuclearity in a few synthetic steps; also these compounds often exhibit high levels of molecular anisotropy, which is an advantage in terms of SMM properties. One point that is often put forward is that the assemblies formed are not restricted by the imagination of the chemist and therefore highly unsymmetrical assemblies can be formed which could not be predetermined by the designed approach. The main disadvantages include low yields and mixtures of products.

Rational design allows the chemist to design a particular system with the desired properties incorporated. Advantages include the production of a single predetermined assembly usually in high yields. However, disadvantages include difficulties with the synthesis of the larger ligand systems required, low nuclearities and low levels of molecular anisotropy.

1.5 Characterisation Techniques

Characterisation of large assemblies that contain paramagnetic ions provides an interesting challenge because traditional techniques that are used with organic compounds are not all accessible. Over recent years the development of new techniques and more refined traditional ones has allowed the chemist to "fully characterise" such assemblies. These include EPR, ESI-MS, cyclic voltammetry, variable temperature and field magnetic studies and X-ray crystallography. Some of these techniques are less common than others and will therefore be discussed below.

Variable Temperature and Field Magnetic Studies

Recent developments within the field of superconductivity have allowed for the production of more routine superconducting magnets that can produce large magnetic fields. These were mainly developed for use in such fields as metal separation technology, medical magnetic resonance imaging (MRI) and magnetic energy storage.

At a similar time Anderson and Powell developed the Josepheson junction that had originally been proposed in theory by Josepheson in 1962. The Josepheson junction has been thoroughly studied in superconducting computer circuits and can act as a digital switching element capable of changing states in a few picoseconds. This device has the ability to observe quantum electrodynamic phenomena. A common use of the Josepheson junction is in a superconducting quantum interference device (SQUID). The use of the Josepheson junction allows the SQUID to resolve changes in an external magnetic field of 10^{-15} T, whilst operating in fields up to 7 T. The extreme sensitivity is achieved by a combination of the non-linear behaviour of the Josepheson junction and the quantised state of the superconducting coil.

The SQUID allows measurement of small intra- and inter-molecular exchange processes. Manipulation of the raw data from the SQUID allows the user to initially look at what types of exchange mechanisms are present within the assembly. Further manipulation and application of the correct theories allow for the determination of parameters such as the *g*-factor and the magnitude of the exchange integrals.

Electrochemistry

The most common type of electrochemistry utilised by the coordination chemist is cyclic voltammetry (CV) because it is one of the most versatile electrochemical techniques. It has the capability for rapidly observing redox behaviour over a wide potential range and involves the cycling of the potential of an electrode, which is immersed in a stationary solution, and subsequently measures the resulting current. The equipment necessary to carry out a CV measurement is shown in Fig. 22. The most common type of electrochemical cell is based upon a three-electrode system, where the working electrode (WE) is monitored and controlled accurately with respect to the reference electrode (RE) *via* a potentiostat. The cyclic waveform is then imposed on the potential at the WE *via* a waveform generator. A cyclic voltammogram is therefore obtained by measuring the current at the working electrode during the potential scan thus the voltammogram is simply a display of current versus potential.

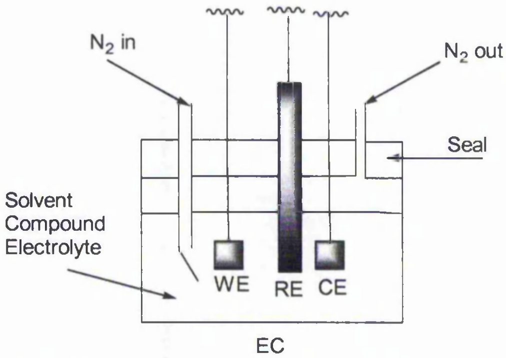

Figure 22 Schematic representation of typical three electrode set-up, WE = working electrode, RE = reference electrode, CE = counter electrode and EC = electrochemical cell.

A typical voltammogram for a high nuclearity assembly can display sets of peaks that can be attributed to certain metal centres. For a reversible system, pairs of peaks are generated because of the nature of the cyclic waveform, with the separation between the pairs of peaks of one particular oxidation/ reduction step determining whether the system is chemically reversible (~ 57 mV). It appears that the nature of the bridging ligand is essential to allow communication between metal centres and that conjugation is important between metal centres. Moreover, if an assembly displays a series of peaks corresponding to transformation from one oxidation state to another then it may be possible, if the state is stable, to prepare mixed oxidation/ reduction systems by bulk electrolysis.

Electrospray Ionisation Mass Spectrometry (ESI-MS)

ESI-MS is a particularly "soft" variation of mass spectrometry that generates ions directly from solution by creating a fine spray of highly charged droplets in the presence of a strong electric field (typically 3.5 kV) but at reasonably low temperatures (50-100 °C). As the droplet size decreases, the electric charge density on its surface increases. Eventually the mutual repulsion between like charges on this surface becomes so great it exceeds the forces of surface tension, and consequently the ions begin to leave the droplet through what is known as a "Taylor cone". The ions are then electrostatically directed into the mass analyser. Vaporisation of these droplets leads to the production of both singly and multiply charged gaseous ions (Fig. 23).

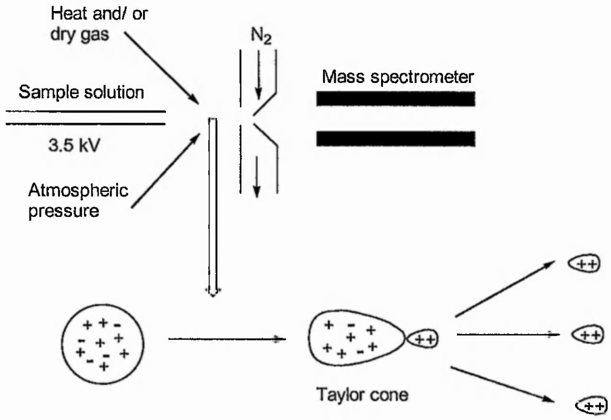

Figure 23 Schematic representation of ESI-MS and the formation of a Taylor cone.

For assemblies that contain a large number of cations and consequently a large number of anions, it is the loss of these anions, which allow the formation of charged particles. Because mass spectrometers measure the ratio of mass to charge (*m/z*) they can detect very high molecular weights of multiply charged species that would otherwise be beyond the mass range of a conventional mass spectrometer.

1.6 Prelude

A review of current literature shows that there are very few examples using the rational design approach to produce functional molecular assemblies. However, this thesis has developed metal directed self-assembly strategies to produce metallosupramolecular assemblies that show both magnetic and electrochemical properties. The key to this strategy is the design of the organic ligand, as previous designs of organic ligands have provided poor superexchange pathways. This design contains various nitrogen heterocycles linked by diazine and alkoxide bridges that allow the unpaired electrons on the chosen transition metal ions to communicate. Manipulation of this approach has produced a number of novel assemblies that will be discussed in terms of nuclearity and ligand design.

Initial work, based upon the preparation of a series of novel homometallic [2 x 2] grids, produced the expected structural motifs, which exhibit both electrochemical and magnetic behaviour (chapter 3). Further investigation manipulating the inert Cr(III) ion allowed the formation of a series of heterometallic [2 x 2] grids, which exhibit intramolecular magnetic exchange (chapter 4).

Attempts at the preparation of mixed oxidation [2 x 2] grids will be mentioned along with the preparation of a mixed oxidation $Mn(II)_5Mn(III)_4$ [3 x 3] grid, which is the only example of a designed mixed oxidation system in the literature (chapter 5). Those which contain Mn(III) are particularly attractive due to their potential SMM behaviour.

Further investigation produced [4 x 4] grid motifs based upon various types of ligand systems including two novel Pb_{16} grids and the first ever [4 x 4] grids to contain paramagnetic ions in the form of two Mn_{16} structures (chapter 6). The latter of these display magnetic exchange consistent with their structures, with suitable modelling of the data also reported. Evidence for other structural motifs is also provided and suggestions provided for their formation along with their magnetic properties.

The formation of a series of tetrametallic triple helicates that exhibit intramolecular interactions *via* a diazine bridge, along with a pentametallic copper chain all of which formed around a central pyridazine ring will be discussed (chapter 7). Examination of the tetrametallic helical chains indicates weak magnetic interactions between adjacent metal centres and no electrochemical communication. Systematic examination of the ligand framework yielded a variety of pyrimidine bridged structural motifs including an octanuclear Cu(II) circular helicate that exhibits weak intramolecular ferromagnetic exchange and another structure containing twenty Cu(II) ions that are held together by a mixture of helical and grid-like binding modes (chapter 8).

Finally, a section that contains miscellaneous structures along with a number of ligands that have the potential to form high nuclearity assembles will be discussed (chapter 9). The assemblies formed with the latter ligands do not provide any real evidence to support formation of grid-like assemblies and consequently the reasons for this are discussed.

Chapter Two

Experimental

2.0 Organic Synthesis

NMR spectra were measured on a JEOL EX 270 instrument at 270 MHz for ^1H and at 67.8 MHz for ^{13}C, using the residual solvent as internal standard. Coupling constants (*J*) are given in Hz. Infrared spectra were recorded on a Perkin-Elmer 1600 Series FTIR machine by the preparation of a KBr disc. Melting points were obtained from a Gallenkamp apparatus and are uncorrected. Mass spectra were obtained on a platform Micromass LC. Chemical analyses were performed externally by The University of Nottingham. Solvents and chemicals were purchased from Lancaster synthesis and Avocado, and used as received. Dry diethyl ether was obtained by distillation over sodium/benzophenone. DMF (700 ml) was dried over CaH_2 (35 g) followed by distillation under reduced pressure (14 mm of Hg) and stored over molecular sieves (4 Å) under a nitrogen atmosphere. Dry methanol and ethanol (700 ml) were obtained by heating under reflux a mixture of magnesium (5.0 g) and iodine (0.7 g) for four h followed by distillation and storage over molecular sieves (4 Å) under a nitrogen atmosphere. Flash column chromatography was performed on silica gel (40-60 mesh). TLC was performed on glass-backed plates and the detection of compounds was achieved by either long or short length UV light. Compounds (**7**), (**15**), (**18**) and (**38**) are all imidate esters that decompose on contact with moisture and hence no chemical analysis was attempted whilst compounds (**14**) and (**27**) have been prepared by alternative routes than those reported in the literature[68,115] and hence no chemical analysis was attempted on these either.

[2 x 2] Ligand

Preparation of 6-hydrazido-2,2'-bipyridine (**1**)

To a stirred solution of methyl 2,2'-bipyridino-6-carboxylate[62] (17.2 g, 80.4 mmol) in EtOH (350 ml) was added, dropwise, hydrazine monohydrate (16.1 g, 320 mol) and the solution allowed to stir overnight. The resultant precipitated crude product was collected *via* filtration, washed with a small quantity of cold diethylether and dried under vacuum at 50 °C for 6 h. Recrystallisation from methanol yielded the desired 6-hydrazide-2,2'-bipyridino (**1**) (15.2 g, 88.4 %) as an almost colourless crystalline solid (m.p. 175-176 °C (MeOH)); (Found: C, 61.7; H, 4.7; N, 26.3.

requires C, 61.7; H, 4.7; N, 26.2 %); ν_{max} (KBr)/cm^{-1} 3557-3301 (NH, NH_2), 1677 (C=O (hydrazide)), 1621 (C=C (arom.)), 1583 (C=N (arom.)), 1512, 1429, 994 (py. ring), 968, 747 and 699; δ_H (270 MHz; DMSO-d_6) 10.2 (1 H, s (br.), N-*H*), 8.9 (1 H, d, *J* 8.2, *H*-3), 8.7 (1 H, d, *J* 4.2, *H*-6), 8.5 (1 H, d, *J* 7.4, *H*-3'), (3 H, m, *H*-4, 5, 4'), 7.5 (1 H, t, *J* 7.2, *H*-5') and 4.6 (2 H, s (br.), RN*H*$_2$); δ_C (68.7 MHz; DMSO-d_6) 162.5 (*C*ONHNH$_2$), 154.3 (*C*-2', 2), 149.4 (*C*-6), 149.1 (*C*-6'), 138.7 (*C*-4), 137.2 (*C*-4'), 124.6 (*C*-5'), 122.5 (*C*-3'), 121.9 (*C*-5) and 121.7 (*C*-3); *m/z* (ESI) 215 ((M+H), 100 %).

Preparation of *N*-(2,2'-bipyridine-6'-carboxyamido)pyridine-2''-amidine (**L1**)

To an ice-cold solution of sodium methoxide (0.08 g, 1.4 mmol) in dry MeOH (50 ml) was added 2-cyanopyridine (1.46 g, 14.0 mmol). The reaction mixture was allowed to warm to room temperature overnight. Glacial acetic acid (0.08 ml, 1.4 mmol) was then added and the solution allowed to stir for 10 min, followed by the addition of 6-hydrazido-2,2'-bipyridine (**1**) (3.00 g, 14.0 mmol). The resulting solution was heated under reflux for 4 h, cooled in ice and the ensuing precipitate of (**L1**) collected *via* filtration and dried under vacuum at 60 °C for 6 h (4.2 g, 94.5 %) m.p.199-200 °C; (Found: C, 62.8; H, 4.5; N, 25.9. $C_{17}H_{14}N_6O$ +1/3 H_2O requires C, 62.9; H, 4.5; N, 26.1 %); ν_{max} (KBr)/cm^{-1} 3399-3149 (NH, NH_2), 1656 (C=O (hydrazide)), 1618 (C=C (arom.)), 1581 (C=N (arom.)), 1524, 1468, 1171, 994 (py. ring) and 757; δ_H (270 MHz; DMSO-d_6) 10.7 (2 H, s, N*H*$_2$), 8.8 (1 H, d, *J* 7.9, *H*-3'), 8.7 (1 H, d, *J* 4.0, *H*-6''), 8.6 (1 H, d, *J* 4.5, *H*-6), 8.6 (1 H, dd, *J* 7.4, 1.2, *H*-3), 8.1 (1 H, d, *J* 7.9, *H*-3''), 8.0 (4 H, m, *H*-4, 4', 4'', 5'), 7.5 (2 H, m, *H*-5, 5'') and 7.1 (1 H, s, N-*H*); δ_C (68.7 MHz; DMSO-d_6) 159.9 (*C*ONH), 154.3 (*C*-2), 154.3 (*C*-2'), 150.4, 150.2, 150.0, 149.3, 149.2 (*C*-2'', 6, 6', 6'', *C*NNH), 138.8, 137.3, 137.0 (*C*-4, 4', 4''), 125.0, 124.6 (*C*-5, 5'') and 122.8, 122.4, 121.6, 120.8 (*C*-3, 3', 3'', 5'); *m/z* (APCI) 319 ((M+H), 100 %) and 301 (((M+H)-H_2O), 25 %).

[4 x 4] Ligands

Preparation of 4,6-dicyanopyrimidine (**12**)

To a mixture of 4,6-diiodopyrimidine[66] (25.0 g, 75.3 mmol) and copper(I) cyanide (16.8 g, 188.3 mmol) was added dry DMF (120 ml). This suspension was then heated with efficient stirring at 100 °C until TLC showed the absence of starting material (cyclohexane:DCM:EtOAc (57:40:3)) (~ 1.5 h), whereupon the hot reaction mixture was poured onto ice-cold water (1200 ml) and stirred for a few minutes. To the resulting suspension was added DCM (600 ml), stirred for a further 10 min, filtered *via* a sinter and the resulting cake was washed thoroughly with DCM. The filtrate was separated and aqueous layer extracted with DCM (500 ml). The combined organic extracts were dried over $MgSO_4$, the solvent removed under reduced pressure and the crude material purified by flash column chromatography, eluting with cyclohexane:DCM:EtOAc (57:40:3) to yield 4,6-dicyanopyrimidine (**12**) as a brilliant white solid ($R_f = 0.3$, 6.5 g, 65.4 %) m.p. 98-99 °C. (Found: C, 55.9; H, 1.6; N, 43.0. $C_6H_2N_4$ requires C, 55.4; H, 1.55; N, 43.0%); ν_{max} (KBr)/cm^{-1} 3068 (C-H (arom.)), 1814, 1578 (C=N (arom.)), 1562, 1525, 1457, 1325, 1307, 1171, 985, 910, 893, 878, 771 and 513; δ_H (270 MHz; $CDCl_3$) 9.5 (1 H, s, *H*-5) and 8.0 (1 H, s, *H*-2); δ_C (68.7 MHz; $CDCl_3$) 160.4 (*C*-2), 143.3 (*C*-4, 6), 126.8, (*C*-5) and 113.8 (*C*N); *m/z* (ESI) 131 ((M+H), 100 %).

Preparation of diethyl pyrimidine-4,6-diimidate (**7**)

An ice cold solution of freshly dried 4,6-dicyanopyrimidine (**12**) (0.50 g, 3.9 mmol) in dry ether (30 ml) and dry EtOH, (1.17 ml, 15.4 mmol) was saturated with dry HCl gas for 2 h whilst being maintained at 0 °C. The ice-cold solution was then stoppered and maintained at 0 °C for a further 48 h. The precipitated solid was subsequently collected *via* filtration, washed thoroughly with dry diethyl ether and dried under high vacuum for 1 h. The crude salt was then slurried in ice cold EtOAc (30 ml), neutralised with cold saturated aqueous $NaHCO_3$ solution (~ 15 ml) and the layers rapidly separated. The organic layer was collected, dried ($MgSO_4$) and the solvent removed under reduced pressure to yield a flaky white solid of crude diethyl pyrimidine-4,6-diimidate (**7**) that was used without further purification (0.61 g, 71.4 %) m.p. ~ 70 °C (dec.); ν_{max} (KBr)/cm^{-1} 3294-2983 (NH), 1651 (R-C=NH), 1575 (C=N (arom.)), 1542, 1379, 1338, 1265, 1096, 1022, 873, 739 and 702; δ_H (270 MHz; $CDCl_3$) 9.4 (2 H, s, RCN*H*), 9.3 (1 H, d, *J* 0.7, *H*-2), 8.1 (1 H, s, *H*-5), 4.4 (4

H, q, *J* 7.2, OC*H*$_2$R) and 1.4 (6 H, t, *J* 7.0, RC*H*$_3$); δ_C (68.7 MHz, CDCl$_3$) 163.9 (R*C*NH), 157.9 (*C*-2), 156.4, (*C*-4, 6), 113.3 (*C*-5), 62.9 (O*C*H$_2$R) and 14.1 (R*C*H$_3$).

Preparation of *N*-[bis(2,2'-bipyridine-6'-carboxyamido)]pyrimidine-4'',6''-diamidine (**L2**)

To a hot solution of 6-hydrazido-2,2'-bipyridine (**1**) (3.0 g, 14.0 mmol) and glacial acetic acid (2 drops) in dry MeOH (100 ml) was added, dropwise, diethyl pyrimidine-4,6-dimidate (**7**) (1.4 g, 6.1 mmol) in dry MeOH (50 ml). After heating under reflux for 4 h the precipitated product was collected *via* hot filtration and washed thoroughly with diethyl ether. The pale yellow solid was then dried under vacuum for 6 h at 60 °C to yield (**L2**) (2.9 g, 85.5%) m.p. >250 °C; (Found: C, 59.8; H, 3.95; N, 29.9. $C_{28}H_{22}N_{12}O_2$ requires C, 60.2; H, 4.0; N, 30.1 %); ν_{max} (KBr)/cm^{-1} 3432-3317 (NH, NH$_2$), 1680 (C=O (hydrazide)), 1640, (C=C (arom.)), 1582 (C=N (arom.)), 1519, 1442, 1167, 994 (py. ring) and 756; δ_H (270 MHz; TFA-d$_1$) 9.6 (1 H, s, H-2''), 9.3 (1 H, s, *H*-5''), 8.8 (2 H, d, J 5.4, Ar-*H*), 8.7 (4 H, m, Ar-*H*), 8.5 (4 H, m, Ar-*H*), 8.3 (2 H, d, J 7.9, Ar-*H*) and 8.1 (2 H, t, J 5.9, Ar-*H*); δ_C (67.8 MHz; TFA-d$_1$) 164.3 (*C*ONH), 159.8 (CNNH), 159.5 (*C*-2''), 152.5 (*C*-4'', 6''), 148.6 (*C*-Ar), 147.3 (*C*-Ar), 146.8 (*C*-Ar), 145.4 (*C*-Ar), 142.3 (*C*-Ar), 141.6 (*C*-Ar), 128.1 (*C*-Ar), 127.5 (*C*-Ar), 126.6 (*C*-Ar), 124.6 (*C*-Ar) and 117.6 (*C*-5''); *m/z* (ESI) 559 ((M+H), 95 %).

Preparation of 2,5-dicyanopyrazine (**14**)

In an inert atmosphere of nitrogen, POCl$_3$ (18.5 ml, 153.3 mmol) was added, dropwise, to a stirred cool solution of pyrazine-2,5-dicarboxyamide[67] (10.0 g, 60.2 mmol) in dry DMF (125 ml) and allowed to stir overnight. The reaction mixture was transferred to a separating funnel containing DCM (200 ml) and washed with water (6 x 100 ml). The organic layer collected, dried (MgSO$_4$), concentrated to dryness under vacuum and the crude solid purified *via* flash column chromatography eluting with DCM to give 2,5-dicyanopyrazine (**14**) as a white solid (5.4 g, 69.0 %) m.p. 193 °C (lit.[68] 193 °C); ν_{max} (KBr)/cm^{-1} 3080 (C-H (arom.)), 2246 (CN), 1893, 1466 (C=N (arom.)), 1310, 1158, 1027 and 939; δ_H (270 MHz; CDCl$_3$) 9.1 (2 H, s, *H*-3, 6); δ_C

(68.7 MHz; $CDCl_3$) 147.7 (*C*-3, 6), 131.9 (*C*-2, 5), 113.6 (*C*N); *m/z* (ESI) 131 ((M+H), 100 %).

Preparation of dimethyl pyrazine-2,5-diimidate (**15**)

To an ice cold solution of NaOMe (0.21 g, 3.9 mmol) in dry MeOH (100 ml) was added 2,5-dicyanopyrazine (**14**) (5.0 g, 39 mmol). After warming to room temperature overnight, glacial acetic acid (0.22 ml, 3.9 mmol) was added to the suspension and stirring was continued for a further 10 min. The precipitated solid was collected *via* filtration and dried under vacuum for 6 h at 30 °C to yield a white amorphous solid of dimethyl pyrazine-2,5-diimidate (**15**) (4.8 g, 64.3 %) m.p ~ 110 °C (dec.); ν_{max} (KBr)/cm^{-1} 3277 (NH), 1646 (C=N (imidate ester)), 1445, 1348, 1219, 1195, 1081, 1028, 952 and 897; δ_H (270 MHz; $CDCl_3$) 8.9 (2 H, s, RCN*H*), 8.7 (2 H, s, *H*-3, 6) and 3.8 (6 H, s, ROC*H*$_3$); δ_C (68.7 MHz; $CDCl_3$) 163.9 (R*C*NH), 142.5 (*C*-2, 5), 140.8 (*C*-3, 6) and 53.4 (RO*C*H$_3$).

Preparation of *N*-[bis(2,2'-bipyridine-6'-carboxyamido)]pyrazine-2'',5''-diamidine (**L3**)

To a hot solution of 6-hydrazido-2,2'-bipyridine (**1**) (3.7 g, 17.3 mmol) and glacial acetic acid (2 drops) in dry MeOH (200 ml) was added, dropwise, dimethyl pyrazine-2,5-diimidate (**15**) (1.4 g, 7.2 mmol) in dry MeOH (200 ml). After heating under reflux for 48 h the precipitated product was collected *via* hot filtration and washed thoroughly with diethyl ether. Drying under vacuum at 60 °C for 6 h yielded (**L3**) as a canary yellow solid (3.8 g, 94.4 %) m.p. >250 °C; (Found: C, 58.7; H, 4.1; H, 29.4. $C_{28}H_{22}N_{12}O_2$ +2/3 H_2O requires C, 58.9; H, 4.1; N, 29.5 %); ν_{max} (KBr)/cm^{-1} 3429-3171 (NH, NH_2), 1667 (C=O (hyrazide)), 1621 (C=C (arom.), C=N (imine)), 1582 (C=N (arom.)), 1523, 1482, 1428, 1193, 993 (py.) and 760; δ_H (270 MHz; TFA-d_1) 9.6 (2 H, s, *H*-3'', 6''), 8.8 (2 H, d, J 5.5, *H*-Ar), 8.6 (4 H, d, *H*-Ar), 8.5 (4 H, d, *H*-Ar), 8.3 (2 H, d, J 7.9, *H*-Ar) and 8.0 (2 H, t, J 5.9, *H*-Ar); δ_C (68.7 MHz; TFA-d_1) 164.3 (*C*ONH), 159.5 (*C*NNH), 148.6 (*C*-Ar), 147.3 (*C*-Ar), 146.8 (*C*-Ar), 145.3 (*C*-Ar), 143.4 (*C*-2'', 5''), 142.3 (*C*-Ar), 142.1 (*C*-3'', 6''), 141.6 (*C*-Ar), 128.1 (*C*-Ar), 127.5 (*C*-Ar), 126.5 (*C*-Ar), 124.6 (*C*-Ar); *m/z* (ESI) ((M+H), 100 %).

Preparation of 3,6-dicyanopyridazine (**17**)

To a mixture of 3,6-diiodopyridazine[63] (25.0 g, 75.3 mmol) and copper(I) cyanide (16.8 g, 188.3 mmol) was added dry DMF (120 ml). The suspension was then heated with efficient stirring at 125 °C until TLC showed the absence of starting material (DCM:cyclohexane:EtOAc (5:4:1)) (~ 5 h), whereupon the hot reaction mixture was poured onto ice-cold water (1200 ml) and stirred for a few minutes. DCM (600 ml) was then added, the solution rapidly stirred for 10 min and filtered *via* a sinter. The layers of the filtrate were separated, aqueous layer extracted with DCM (500 ml) and the combined organic phases dried over $MgSO_4$. Removal of the solvent yielded a crude solid which was dissolved in a minimum amount of DCM and purified *via* flash column chromatography, eluting with DCM:cyclohexane:EtOAc (5:4:1) to yield 3,6-dicyanopyridazine (**17**) as a white solid (R_f = 0.3, 7.2 g, 73.6 %) m.p. 133.5-134 °C; (Found: C, 55.4; H, 1.6; N, 42.9. $C_6H_2N_4$ requires C, 55.4; H, 1.55; N, 43.1 %); ν_{max} (KBr)/cm^{-1} 3088-3066 (C-H (arom.)), 1724, 1563 (C=C (arom.)), 1541 (C=N (arom.)), 1394, 1116, 862 and 826; δ_H (270 MHz; $CDCl_3$) 8.1 (2 H, s, *H*-4, 5); δ_C (68.7 MHz; $CDCl_3$) 139.8 (*C*-3, 6), 131.0 (*C*-4, 5), 113.9 (-*C*N); *m/z* (ESI) 131 ((M+H), 100 %).

Preparation of diethyl pyridazine-3,6-diimidate (**18**)

To an ice cold solution of NaOEt (0.29 g, 3.85 mmol) in dry EtOH (40 ml) was added 3,6-dicyanopyridazine (**6**) (0.50 g, 3.85 mmol). After warming to room temperature overnight, glacial acetic acid (0.22 ml, 3.85 mmol) was added to the suspension and stirring was continued for a further 10 min. The solvent was then removed under reduced pressure and the residue partitioned between EtOAc (50 ml) and sat. $NaHCO_3$ solution (20 ml). The layers separated, the aqueous extracted with EtOAc and the combined organic phases washed with sat. $NaHCO_3$, H_2O and brine. The organic layer was dried ($MgSO_4$) and the solvent removed under *vacuo* to yield a flaky solid of (**18**) (0.72 g, 84.3 %) m.p. 103-106 °C; ν_{max} (KBr)/cm^{-1} 3309-2978 (NH), 1643 (C=N (imidate ester)), 1573 (C=N (arom.)), 1327, 1061 and 858; δ_H (270 MHz; $CDCl_3$) 9.5 (2 H, s (br.), RCN*H*), 8.0 (2 H, s, *H*-4, 5), 4.4 (4 H, q, *J* 7.2, OCH_2R) and 1.4 (6 H, t, *J* 6.9, RCH_3); δ_C (68.7 MHz, $CDCl_3$) 163.1 9 (R*C*NH), 150.8 (*C*-3, 6), 125.2 (*C*-4, 5), 62.7 (OCH_2R) and 14.1 (RCH_3).

Preparation of *N*-[bis(2,2'-bipyridine-6'-carboxyamido)]pyridazine-3'',6''-diamidine (**L4**)

To a hot solution of 6-hydrazido-2,2'-bipyridine (**1**) (3.0 g, 14.0 mmol) and glacial acetic acid (2 drops) in dry MeOH (100 ml) was added, dropwise, diethyl pyridazine-3,6-diimidate (**18**) (1.35 g, 6.1 mmol) in dry MeOH (50 ml). After heating under reflux for 4 h the precipitated product was collected *via* hot filtration and washed thoroughly with diethyl ether. The pale yellow solid was dried under vacuum for 6 h at 60 °C to yield (**L4**) (2.9 g, 85.5 %) m.p. >250 °C; (Found: C, 59.5; H, 3.9; N, 29.9. $C_{28}H_{22}N_{12}O_2$ + 1/3 H_2O requires C, 59.6; H, 4.0; N, 29.8 %); ν_{max} (KBr)/cm^{-1} 3427-3317 (NH, NH_2), 1683 (C=O (hydrazide)), 1610 (C=C (arom.), C=N (imine)), 1581 (C=N (arom.)) 1518, 1427, 995 (py.) and 755; δ_H (270 MHz; TFA-d_1) 8.9 (4 H, s, Ar-*H* and *H*-4'',5''), 8.7 (4 H, s, Ar-*H*), 8.5 (4 H, d, Ar-*H*), 8.3 (2 H, d, *J* 7.4, Ar-*H*) and 8.1 (2 H, d, J 6.2, Ar-*H*); δ_C 164.4 (*C*ONH), 159.9 (*C*NNH), 149.3 (*C*-3'', 6''), 148.6 (Ar-*C*), 147.3 (Ar-*C*), 146.8 (Ar-*C*), 145.3 (Ar-*C*), 142.3 (Ar-*C*), 141.6 (Ar-*C*), 128.8 (*C*-4'', 5''), 128.1 (Ar-*C*), 127.4 (Ar-*C*), 126.5 (Ar-*C*) and 124.6 (Ar-*C*); *m/z* (ESI) 559 ((M+H), 100%).

Preparation of 4,6-bis[(6'-methyl)pyrid-2'-yl]pyrimidine (**25**)

To a mixture of crude 2-methyl-6-(tri-n-butyltin)pyridine[69] (~ 90 %) (17.4 g, 41.0 mmol), 4,6-dichloropyrimidine (**24**) (2.9 g, 19.5 mmol) and Pd(II)$(PPh_3)_2Cl_2$ (1.0 g, 1.4 mmol) was added dry DMF (70 ml). The system was flushed with nitrogen and heated at 105 °C for 20 h. Removal of the solvent under high vacuum yielded a dark oil which was subsequently partitioned between saturated KF solution (75 ml) and EtOAc (100 ml), and filtered *via* a sinter. Separation of the layers, extraction of the aqueous layer with EtOAc (2 x 50 ml) followed by drying the organic layers over $MgSO_4$ and evaporation under vacuum gave a dark solid which was purified by column chromatography eluting with EtOAc:Petroleum ether (b.p. 40-60 °C) (1:3). The white solid was used for further reaction without further purification; an analytical sample of (**25**) was obtained as colourless needles by recrystallisation from Petroleum ether (b.p. 40-60 °C) (3.9 g, 76.2 %) m.p. 131.5-133 °C; (Found: C, 73.25; H, 5.5; N, 21.5; $C_{16}H_{14}N_4$ requires C, 73.25; H, 5.4; N, 21.35 %); ν_{max} (KBr)/cm^{-1} 3063 (C-H (arom.)), 1596-1530 (C=N, C=C (arom.)), 1449, 1090, 990 (py. (ring)), 771 and 639; δ_H (270 MHz; $CDCl_3$) 9.3 (1 H, d, *J* 1.2, *H*-5), 9.3 (1 H, d, *J* 1.5, *H*-2), 8.3 (2 H, d, *J* 7.9, *H*-3'), 7.7 (2 H, t, *J* 7.8, *H*-4'), 7.3 (2 H, dd, *J* 6.4 and 1.2, *H*-5') and 2.7 (6 H, s, R-C*H*$_3$); δ_C (68.7 MHz; $CDCl_3$) 164.2 (*C*-4, 6), 158.6 (*C*-2), 158.5 (*C*-6'), 153.6 (*C*-2'), 137.1 (*C*-4'), 124.9 (*C*-5'), 118.8 (*C*-3'), 113.9 (*C*-5) and 24.6 (R*C*H$_3$); *m/z* (ESI) 263 ((M+H), 100 %).

Preparation of 4,6-bis[(6'-ethoxycarbonyl)pyrid-2'-yl]pyrimidine (**27**)

4,6-Bis[(6'-methyl)pyrid-2'-yl]pyrimidine (**25**) (3.0 g, 11.5 mmol) was added in one portion to conc. H_2SO_4 (40 ml) causing an increase in temperature to ca. 50 °C. Freshly ground CrO_3 (3.8 g, 37.8 mmol) was then added in portions in such a manner that the temperature remained at ca. 50 °C, following the addition the temperature was maintained by heating for a further 3 h. The deep green viscous solution was then allowed to cool to room temperature overnight with stirring and subsequently poured onto crushed ice (300 g). The precipitate formed was collected in a sinter, washed with H_2O, EtOH and diethyl ether and dried under vacuum at 50 °C for 8 h to yield the crude diacid (**26**) (1.5 g). The highly insoluble off-white powder was added to dry MeOH (30 ml) and conc H_2SO_4 (3 drops) and heated under reflux for 6 h. The reaction was then cooled in ice and the precipitate formed collected *via* filtration. The solid was dissolved in $CHCl_3$ (20 ml), treated with Fuller's earth (0.5 g), filtered and dried over $MgSO_4$. Evaporation of the solvent under vacuum gave a white solid, which was used for further reactions without purification; an analytical sample of (**27**) was obtained by recrystallisation form toluene (0.5 g, 12.5 %) m.p. 209-210 °C; ν_{max} (KBr)/cm^{-1} 3080 (C-H (arom.)), 3011-2850 (CH_3), 1740 (C=O (ester)), 1564-1527 (C=N, C=C (arom.)), 1443, 1295, 1245, 1142, 994 (py.), 834 and 757; δ_H (270 MHz; $CDCl_3$) 9.4 (1 H, d, *J* 1.2, *H*-5), 9.3 (1 H, d, *J* 1.2, *H*-2), 8.6 (2 H, dd, *J* 7.8 and 1.0, *H*-5'), 8.2 (2 H, dd, *J* 7.7 and 1.0, *H*-3'), 8.0 (2 H, t, *J* 7.6, *H*-4') and 4.0 (6 H, s, RC*H*$_3$); δ_C (68.7 MHz; $CDCl_3$) 165.4 (*C*(O)OEt), 163.4 (*C*-4, 6), 158.5 (*C*-2), 154.4 (*C*-2'), 148.2 (*C*-6'), 138.2 (*C*-4'), 126.4 (*C*-3'), 125.0 (*C*-5'), 114.9 (*C*-5) and 52.9 (R*C*H$_3$); *m/z* (ESI) 351 ((M+H), 100 %).

Preparation of 4,6-bis[(6'-hydrazido)pyrid-2'-yl]pyrimidine (**28**)

Hydrazine monohydrate (1.14 g, 22.9 mmol) was added, dropwise, to a slurry of 4,6-bis[(6'-ethoxycarbonyl)pyrid-2'-yl]pyrimidine (**27**) (0.40 g, 1.14 mmol) in MeOH (40 ml) over a 5 min period. After the reaction was refluxed for 2 d, the white precipitate was collected *via* hot filtration, washed with MeOH and diethyl ether, and dried under vacuum at 50 °C for 8 h to give (**28**) (0.38 g, 95.0 %) m.p. >250 °C; ν_{max} (KBr)/cm^{-1} 3412-3313 (NH, NH$_2$), 1719, 1679 (C=O (hydrazide)), 1573-1522 (C=N, C=C (arom.)), 1440, 996 (py.), 833 and 639; δ_H (270 MHz; DMSO-d$_6$; 100 °C) 10.2 (2 H, s (br.), N-*H*), 9.6 (1 H, d, *J* 1.2, *H*-5), 9.4 (1 H, d, *J* 1.2, *H*-2), 8.6 (2 H, dd, *J* 5.9 and 3.0, *H*-5'), 8.2 (4 H, m, *H*-3', 4') and 5.7 (4 H, s (br.), N*H*$_2$); δ_C (68.7 MHz; DMSO-d$_6$; 100 °C) 162.5 (*C*ONHNH$_2$), 161.7 (*C*-4, 6), 157.9 (*C*-2), 152.2 (*C*-2'), 149.8 (*C*-6'), 138.5 (*C*-4'), 123.2-123.0 (*C*-3', 5') and 113.9 (*C*-5); *m/z* (ESI) 351 ((M+H), 100 %).

Preparation of crude 4,6-bis[6'-(*N*''-pyridine-2''-amidino)-amido]pyrid-2'-yl]pyrimidine (**L5**)

2-Cyanopyridine (0.31 g, 3.0 mmol) was added to a mixture of NaOMe (0.02 g, 0.04 mmol) in dry MeOH (20 ml) to give a clear solution. Upon stirring overnight under anhydrous conditions, 4,6-bis[(6'-hydrazido)pyrid-2'-yl]pyrimidine (**28**) (0.35 g, 1.0 mmol) was added to give a white suspension that turned yellow after being maintained at reflux for 48 h. The suspension was then hot filtered *via* a sinter to give a clear yellow solution that was subsequently evaporated under vacuum. The yellowish residue was washed thoroughly with diethyl ether and dried under vacuum at 50 °C to give (**L5**) as a pale yellow solid (0.10 g, 17.9 %); Sample not suitable for elemental analysis; ν_{max} (KBr)/cm^{-1} 3412-3313 (NH, NH$_2$), 1665 (C=O (hydrazide)), 1573-1522 (C=N, C=C (arom.)), 1440, 996 (py.(ring)) and 641; δ_H (270 MHz; DMSO-d$_6$) 9.9 (1 H, s, *H*-5), 9.5 (1 H, s, *H*-2), 8.7 (2 H, t, *J* 4.7, *H*-6''), 8.6 (2 H, d, *J* 4.5, *H*-4'), 8.4 (2 H, d; *J* 7.9, *H*-4''), 8.3 (4 H, m, *H*-3', 5'), 7.9 (2 H, td, *J* 7.8, 1.7, *H*-5''), 7.5 (2 H, td, *J* 6.1, 1.1, *H*-3'') δ_C (68.7 MHz; DMSO-d$_6$) 162.8 (*C*ONH), 159.3 (*C*-4, 6), 158.6 (*C*-2), 152.4 (*C*-Ar), 152.3 (*C*-Ar), 150.9 (*C*-Ar), 150.0 (*C*-Ar), 148.1 (*C*-Ar), 139.3 (*C*-Ar), 136.9 (*C*-Ar), 125.1 (*C*-Ar), 124.2 (*C*-Ar), 123.9 (*C*-Ar), 121.0 (*C*-Ar) and 114.3 (*C*-5); *m/z* (ESI) 559 ((M+H), 100%).

Preparation of ethyl *N*-(6-ethoxycarbonyl-pyridin-2-amido)amidinoformate(**35**)

Ethylcarboethoxyformimidate (**34**)[70] (6.8 g, 46.9 mmol) was added, dropwise, to a solution of ethyl 6-hydrazidopyridine-2-carboxylate (**33**) (7.0 g, 33.5 mmol) in dry MeOH (280 ml) that contained a few drops of glacial acetic acid over a 10 min period. The solution was heated under reflux for 3 h and the precipitate formed collected *via* hot filtration (3.8 g). Upon cooling in the fridge overnight, the filtrate yielded a second crop (6.1 g) of highly crystalline (**35**) that was used for subsequent analysis even though both crops were identical by NMR (total yield 9.9 g, 96.0 %), m.p. 205-206 °C (MeOH); (Found: C, 50.3; H, 5.1; N, 18.4; $C_{13}H_{16}N_4O_5$ requires C, 50.6; H, 5.2; N, 18.2 %); ν_{max} (KBr)/cm^{-1} 3360-3178 (NH, NH$_2$), 1726 (C=O (ester)), 1721 (C=O (ester)), 1645 (C=O (hydrazide)), 1609, 1530, 1319, 1230, 1130 and 994 (py.); δ_H (270 MHz; DMSO-d$_6$) 10.4 (1 H, s (br.), N-*H*), 8.2-8.1 (3 H, m, *H*-3, 4, 5), 6.9 (2 H, s (br.), N-*H*$_2$), 4.4 (2 H, q, *J* 7.1, OC*H*$_2$R), 4.3 (2 H, q, *J* 6.9, OC*H*$_2$R), 1.4 (3 H, t, *J* 7.9, RC*H*$_3$) and 1.3 (3 H, t, *J* 7.2, RC*H*$_3$); δ_C (68.7 MHz; DMSO-d$_6$) 164.1 (*C*ONH), 162.1 (*C*(O)OEt), 160.2 (*C*(O)OEt), 150.84 (*C*-6), 146.8 (*C*-2), 142.5 (*C*=N), 139.3 (*C*-4), 127.0 (*C*-3), 125.7 (*C*-5), 61.7 (O*C*H$_2$R), 61.5 (O*C*H$_2$R), 14.1 (R-*C*H$_3$) and 14.0 (R-*C*H$_3$); *m/z* (ESI) 309 ((M+H), 100 %).

Preparation of *N*-(6-hydrazidopyridin-2-amido)amidinohydrazide (**36**)

To a slurry of ethyl *N*-(6-ethoxycarbonyl-pyridin-2-amido)amidinoformate (**35**) (9.9 g, 32.1 mmol) in MeOH (900 ml) was added, dropwise, hydrazine monohydrate (32.2 g, 643 mmol) over a 30 min period. The flask was then stoppered and stirred for 3 days. The solid formed collected by filtration washed thoroughly with MeOH and diethyl ether, and dried under vacuum at 60 °C for 6 h to yield (**36**) as a white amorphous solid (8.7 g, 98.1 %), m.p. >250 °C; (Found: C, 37.1; H, 4.65; N, 37.65; $C_9H_{12}N_8O_3$ + 9/10 H_2O requires C, 36.8; H, 4.65; N, 37.8 %); ν_{max} (KBr)/cm^{-1} 3507-

3186 (NH, NH_2), 1683-1662 (C=O), 1622-1588 (C=N), 1512, 1387, 1246, 1000 (py.) and 844; δ_H (270 MHz; DMSO-d_6) 10.9 (2 H, s (br.), N-*H*), 10.6 (1 H, s (br.), N-*H*), 8.2-8.1 (3 H, m, *H*-3, 4, 5), 6.8 (2 H, s (br.), N-*H*NH_2) and 4.6 (4 H, s (br.), NHN-H_2); δ_C (68.7 MHz; DMSO-d_6) 162.1 (*C*ONH), 159.6 (*C*ONH), 158.9 (*C*ONH), 148.9 (*C*-6), 148.4 (*C*-2), 147.9 (*C*NNH), 139.3 (*C*-4), 124.1 (*C*-3) and 132.9 (*C*-5); *m/z* (ESI) 359 ((M+H), 87 %).

Preparation of {N^1-(pyridine-2-carboxyamino)}-[N^4-(pyridine-2'-amido-6'-amidino)pyridine-2''-amidino]amidinoformylhydrazide (**L6**)

To a solution of NaOMe (0.4 g, 7.8 mmol) in dry MeOH (500 ml) was added 2-cyanopyridine (8.1 g, 77.9 mmol). Upon stirring overnight, the solution was cooled to 0 °C and glacial acetic acid (0.5 ml, 7.8 mmol) added. After stirring for 10 min *N*-(6-hydrazidopyridin-2-amido)amidinohydrazide (**36**) (8.6 g, 31.2 mmol) added in one portion to yield a white slurry which turned bright yellow after 6 h under reflux. The solid collected *via* hot filtration, washed thoroughly with diethyl ether and dried under vacuum at 50 °C for 6 h to yield (**L6**) as a bright yellow solid (12.0 g, 78.9 %), m.p. >250 °C; (Found: C, 51.15; H, 4.1; N, 34.2; $C_{21}H_{20}N_{12}O_3$ requires C, 51.25; H, 4.1; N, 34.4 %); ν_{max} (KBr)/cm^{-1} 3403-3213 (NH, NH_2), 1670 (C=O), 1642-1636 (C=N), 1588, 1566, 1523, 1474, 1394 and 998 (py.); δ_H (270 MHz; DMSO-d_6) 11.1 (1 H, s (br.), N-*H*), 11.0 (1 H, s (br.), N-*H*), 10.3 (1 H, s (br.), N-*H*), 8.6 (2 H, m, *H*-6', 6''), 8.2-8.1 (5 H, m, *H*-3, 3', 3'', 4, 5), 7.9 (2 H, m, *H*-4', 4''), 7.5 (2 H, m, *H*-5', 5''), 7.1 (2 H, s (br.), NH_2), 7.0 (2 H, s (br.), NH_2) and 7.0 (2 H, s (br.), NH_2); δ_C (68.7 MHz; DMSO-d_6) 159.1 (*C*ONH), 158.9 (*C*ONH), 157.4 (*C*ONH), 151.9 (*C*-2', 2''), 150.3-149.2 (*C*-6', 6''), 148.8 (*C*-6), 148.7 (*C*NNH), 148.3 (*C*-2), 148.2 (*C*NNH), 148.0 (*C*NNH), 139.3 (*C*-4), 137.1-137.0 (*C*-4', 4''), 125.2-124.9 (*C*-3, 5), 124.2 (*C*-5', 5'') and 121.0-120.8 (*C*-3',3''); *m/z* (ESI) 567 ((M+H+DMSO), 8 %) and 489 ((M+H), 100 %).

Chain Like Ligands

Preparation of dimethyl pyridazine-3,6-diimidate (**38**)

To an ice cold solution of NaOMe (0.21 g, 3.9 mmol) in dry MeOH (100 ml) was added 3,6-dicyanopyridazine (**34**) (5.0 g, 39 mmol). After warming to room temperature overnight, glacial acetic acid (0.22 ml, 3.9 mmol) was added to the suspension and stirring was continued for a further 10 min. The precipitated solid collected *via* filtration and dried under vacuum for 4 h at 30 °C to yield a white amorphous solid of dimethyl pyridazine-3,6-diimidate (**33**) (6.2 g, 83.1 %) m.p. 191-192 °C; ν_{max} (KBr)/cm^{-1} 3310-2954 (NH), 1646 (C=N (imidate ester)), 1575 (C=N (arom.)), 1450, 1341, 1205, 1196, 1181, 1069, 1045, 943, 852 and 705; δ_H (270 MHz; $CDCl_3$) 9.6 (2 H, s, CN*H*), 8.0 (2 H, s, *H*-3, 6) and 4.0 (6 H, s, ROC*H*$_3$); δ_C (68.7 MHz; $CDCl_3$) 163.6 (R*C*NH), 150.5 (*C*-3, 6), 125.3 (*C*-4, 5) and 54.1 (RO*C*H$_3$).

Preparation of *N*-[bis(pyridine-2-amidino)]pyridazine-3',6'-diamidine (**L7**)

To a hot solution of pyridine-2-amidrazone[64] (2.2 g, 16.2 mmol) and glacial acetic acid (2 drops) in dry MeOH (100 ml) was added dimethyl pyridazine-3,6-diimidate (**33**) (1.5 g, 7.7 mmol). After heating under reflux for 4 h the precipitated product was collected *via* hot filtration and washed thoroughly with diethyl ether. The lemon-yellow solid was then dried under vacuum at 60 °C for 6 h to yield (**L7**) (2.8 g, 90.1 %) m.p. 245 °C; (Found: C, 53.5; H, 4.5; N, 41.8. $C_{18}H_{18}N_{12}$ requires C, 53.7; H, 4.5; N, 41.8 %); ν_{max} (KBr)/cm^{-1} 3491-3302 (NH, NH_2), 1615 (C=N (imine), C=C (arom.)), 1560 (C=N (arom.)), 1437 and 998 (py.); δ_H (270 MHz; TFA-d_1) 8.8 (2 H, s, *H*-5', 4'), 8.6 (2 H, d, *J* 4.7, *H*-6), 8.5 (2 H, d, *J* 4.0, *H*-3), 8.4 (2 H, dd, *J* 7.2, 3.0, *H*-4) and 8.0 (2 H, d, *J* 5.4, *H*-5); δ_C (68.7 MHz; TFA-d_1) 154.5 (*C*-2), 149.3 (*C*-6', 3'), 148.8 (*C*NNH), 147.7 (*C*NNH), 143.1 (*C*-6), 141.9 (*C*-4), 129.8 (*C*-4', 5'), 128.3 (*C*-5) and 125.5 (*C*-3); *m/z* (ESI) 403 ((M+H), 100 %).

Preparation of *N*-[bis(pyridine-2-carboxyamido)]pyridazine-3',6'-diamidine (**L7A**)

To a hot solution of pyridine-2-hydrazido[65] (2.2 g, 16.2 mmol) and glacial acetic acid (2 drops) in dry MeOH (100 ml) was added dimethyl pyridazine-3,6-diimidate (1.5 g, 7.7 mmol). After heating under reflux for 8 h the precipitated product was collected *via* hot filtration and washed thoroughly with diethylether. Drying under vacuum for

6 h at 60 °C gave (**L7A**) as a pale yellow solid (2.7 g, 88.0 %) m.p. >250 °C; (Found: C, 52.05; H, 3.9; N, 33.9. $C_{18}H_{16}N_{10}O_2$ + ½ H_2O requires C, 52.3; H, 4.1; N, 33.9 %); ν_{max} (KBr)/cm^{-1} 3421-3296 (NH), 1680 (C=O (hydrazide)), 1610 (C=N (imine)) 1587 (C=C (arom.)), 1570 (C=N (arom.)) 1513, 1431 and 998 (py.); δ_H (270 MHz; TFA-d_1) 8.9 (2 H, d, *J* 5.7, *H*-6), 8.8 (2 H, s, *H*-4', 5'), 8.7 (4 H, d, *H*-3, 4) and 8.2 (2 H, q, *J* 7.2, *H*-5); δ_C (68.7 MHz; TFA-d_1) 157.8 (*C*ONH), 157.6 (*C*-2), 149.2 (*C*-6), 149.1 (*C*NNH), 143.0 (*C*-3', 6'), 140.5 (*C*-4), 130.7 (*C*-4', 5'), 128.7 (*C*-5) and 126.5 (C-3). *m/z* (ESI) 405 ((M+H), 100 %).

Preparation of *N*-[bis(pyridine-2-amidino)]pyrimidine-4',6'-diamidine (**L8**)

To a hot solution of pyridine-2-amidrazone[64] (3.8 g, 28.15 mmol) and glacial acetic acid (2 drops) in dry MeOH (75 ml) was added, dropwise, crude diethyl pyrimidine-4,6-diimidate (**7**) (2.5 g, 11.3 mmol) in dry MeOH (50 ml). After heating under reflux for 4 h the precipitated product was collected *via* hot filtration and washed thoroughly with diethyl ether. After drying under vacuum for 6 h at 60 °C (**L8**) was obtained as a bright yellow solid (3.6 g, 78.9 %) m.p. >250 °C; (Found: C, 52.05; H, 4.3; N, 40.4. $C_{18}H_{18}N_{12}$ + 2/3 H_2O requires C, 52.2; H, 4.6; N, 40.6 %); ν_{max} (KBr)/cm^{-1} 3471-3349 (NH_2, NH), 1619 (C=C (arom.)), C=N (imine)), 1591 (C=N (arom.)), 1522, 1443 and 995 (py.); δ_H (270 MHz; DMSO-d_6) 9.3 (1 H, s, *H*-2'), 9.2 (1 H, s, *H*-5'), 8.6 (2 H, d, *J* 4.7, *H*-6), 8.5 (2 H, d, *J* 7.9, *H*-5), 7.9 (2 H, dd, *J* 5.3 and 1.5, *H*-4), 7.5 (2 H, dd, *J* 6.9 and 1.4, *H*-3) 7.2 (6 H, s (br.), N*H* and N*H*$_2$) and 6.8 (2 H, s (br.), N*H*); δ_C (68.7 MHz; DMSO-d_6) 158.3 (*C*-4'', 6''), 157.3 (*C*-2'), 153.1 (*C*-2), 151.2 (*C*NNH), 151.0 (*C*NNH), 148.2 (*C*-6), 136.5 (*C*-4), 124.8 (*C*-5) and 113.4 (*C*-5'). *m/z* (ESI) 403 ((M+H), 100%).

Preparation of *N*-[bis(pyridine-2-carboxyamido)]pyrimidine-4',6'-diamidine (**L8A**)

To a hot solution of pyridine-2-hydrazido[65] (3.5 g. 25.5 mmol) and glacial acetic acid (2 drops) in dry MeOH (75 ml) was added, dropwise, crude diethyl pyrimidine-4,6-diimidate (**7**) (2.7 g, 12.1 mmol) in dry MeOH (50 ml). After heating under reflux for 4 h the precipitated product was collected *via* hot filtration and washed thoroughly with diethyl ether. After drying under vacuum for 6 h at 60 °C (**L8A**) was obtained as a bright yellow solid (3.8 g, 77.3 %) m.p. > 250 °C; (Found: C, 53.3; H, 4.0; N, 34.6. $C_{18}H_{16}N_{10}O_2$ requires C, 53.5; H, 4.0; N, 34.6 %); ν_{max} (KBr)/cm^{-1} 3442-3199 (NH_2), 1672 (C=O (hydrazide)), 1629 (C=C (arom.), C=N (imine)) 1587 (C=N (arom.)), 1521, 1449, 996 (py.) and 742; δ_H (270 MHz; DMSO-d$_6$; 100 °C) 10.9 (2 *H*, s (br.), N-*H*), 9.3 (1 H, s, *H*-2'), 8.8 (1 H, s, *H*-5'), 8.7 (2 H, s, *H*-6), 8.1 (2 H, s, *H*-3), 8.0 (2 H, s, *H*-4), 7.6 (2 H, s, *H*-5) and 7.2 (4 H, s (br.), N-*H*); δ_C (270 MHz; DMSO-d$_6$; 100 °C) 160.3 (*C*ONH), 158.3 (*C*-4', 6'), 157.3 (*C*-2'), 150.2 (*C*NNH), 148.4 (*C*-2), 146.1 (*C*-6), 137.9 (*C*-4), 126.6 (*C*-5), 122.5 (*C*-3) and 113.1 (*C*-5'); *m/z* (ESI) 809 (2M+H, 80 %), 405 ((M+H), 100 %).

Preparation of crude *N*-[bis(pyridine-2-amidino)]pyrazine-2',5'-diamidine (**L9**)

To a hot solution of pyridine-2-amidrazone[64] (5.3 g, 38.6 mmol) and glacial acetic acid (2 drops) in dry MeOH (175 ml) was added, dropwise, dimethyl pyrazine-2,5-diimidate (**15**) (2.5 g, 12.9 mmol) in dry MeOH (150 ml). After heating under reflux for 24 h the precipitated product was collected *via* hot filtration and washed thoroughly with diethyl ether. Washing with hot DMF (~ 100 °C, 50 ml) and drying under vacuum at 60 °C for 6 h gave crude (**L9**) as a bright red solid of that was relatively pure by NMR, but unsuitable for chemical analysis (3.6 g, 68.8 %) m.p. >250 °C; ν_{max} (KBr)/cm^{-1} 3479-3351 (NH_2, NH), 1625 (C=C (arom.)), C=N (imine)), 1597 (C=N (arom.)), 1443 and 995 (py.); δ_H (270 MHz; TFA-d$_1$) 9.6 (2 H, s, *H*-3', 6'), 8.9 (2 H, d, *J* 5.7, *H*-6), 8.7 (4 H, m, *H*-3, 4) and 8.2 (2 H, d, *J* 4.2, *H*-5).

Preparation of crude *N*-[bis(pyridine-2-carboxyamido)]pyrazine-2',5'-diamidine (**L9A**)

Dimethyl pyrazine-2,5-diimidate (**15**) (2.5 g, 12.9 mmol) was dissolved in dry MeOH (150 ml) and added, dropwise, to a solution of pyridine-2-hydrazido[65] (5.30 g, 32.2 mmol) in dry MeOH (175 ml) that contained a few drops of glacial acetic acid. Once the addition was complete, the reaction was heated under reflux for 24 h and the precipitate formed collected *via* hot filtration. Washing with hot DMF (~ 100 °C, 50 ml) and drying under vacuum at 60 °C for 6 h gave crude (**L9A**) as a yellow solid (3.8 g, 73.2 %); ν_{max} (KBr)/cm^{-1} 3481-3332 (NH_2, NH), 1621 (C=C (arom.)), C=N (imine)), 1585 (C=N (arom.)), 1224, 1445 and 996 (py.); δ_H (270 MHz; TFA-d_1) 9.6 (2 H, s, *H*-3', 6'), 8.9 (2 H, d, *J* 5.7, *H*-6), 8.8 (4 H, m, *H*-3, 4) and 8.2 (2 H, d, *J* 4.1, *H*-5).

[5 x 5] Ligands

Preparation of diethyl pyridine-2,6-dicarboxamidoamidinocarboxylate **(40)**

Ethylcarboethoxyformimidate[70] (8.1 g, 5.7 mmol) was added, dropwise, to a slurry of pyridine-2,6-dihydrazido[71] (4.5 g, 23.3 mmol) in dry MeOH (600 ml) that contained a few drops of glacial acetic acid over a 10 min period. After refluxing for 6 h the white solid was collected *via* hot filtration and washed thoroughly with diethyl ether. After drying under vacuum at 50 °C for 6 h **(36)** was obtained as an off-white solid (8.4 g, 91.9 %) m.p. >250 °C; (Found: C, 45.4; H, 4.9; N, 24.75; $C_{15}H_{19}N_7O_6$ requires C, 45.8; H, 4.9; N, 24.9 %); ν_{max} (KBr)/cm^{-1} 3458-3049 (NH, NH_2), 1719 (C=O (ester)), 1659-1639 (C=N), 1547, 1478, 1420, 1313, 1238, 1171, 1022, 998 (py.), 792 and 646; δ_H (270 MHz; DMSO-d_6) 10.8 (2 H, s (br.), N-*H*), 8.2 (3 H, m, *H*-3, 4, 5), 6.9 (4 H, s (br.), N-H_2), 4.2 (4 H, q, *J* 7.2, OCH_2R) and 1.3 (6 H, t, J 7.1, RCH_3); δ_C (68.7 MHz; DMSO-d_6) 162.1 (*C*ONH), 159.1 (*C*(O)OEt), 148.7 (*C*-2, 6), 144.5 (*C*NNH), 139.4 (*C*-4), 124.6 (*C*-3, 5), 61.8 (OCH_2R) and 13.9 (RCH_3); *m/z* (ESI) 472 (M+H+DMSO, 5 %), 394 ((M+H), 100 %) and ((M-($C_4H_5NO_2$)+H), 12 %).

Preparation of diethyl pyridine-2,6-dicarboxamidoamidinohydrazide **(41)**

To a slurry of diethyl pyridine-2,6-dicarboxamidoamidinocarboxylate **(40)** (7.5 g, 19.1 mmol) in MeOH (1200 ml) was added, dropwise, hydrazine monohydrate (19.1 g, 38.2 mmol) over a 30 min period. Once the addition was complete, the reaction was heated under reflux for 3 d and then cooled to room temperature, whereupon a second addition of hydrazine monohydrate (19.1 g, 38.2 mmol) was made. After refluxing for a further 24 h, the white solid was collected *via* hot filtration, washed with MeOH and diethyl ether and dried under vacuum at 60 °C for 6 h to give **(41)** as a brilliant white solid (5.2 g, 75.5 %) m.p. >250 °C; (Found: C, 36.15; H, 4.15; N, 42.6; $C_{11}H_{15}N_{11}O_4$ requires C, 36.15; H, 4.15; N, 42.2 %); ν_{max} (KBr)/cm^{-1} 3389-3209 (NH, NH_2), 1709, 1680 (C=O), 1640-1546 (C=N and C=C), 1388, 1323, 1247, 1175, 998 (py. ring), 645; δ_H (270 MHz; DMSO-d_6/TFA-d_1) 8.2-8.1 (3 H, m, *H*-3, 4, 5); δ_C (68.7 MHz; DMSO-d_6/TFA-d_1) 162.0 (*C*ONH), 153.3 (*C*-2, 6), 148.9 (*C*NNH), 140.6 (*C*-4), 126.6 (*C*-3, 5); no suitable mass spectrum could be obtained.

[6 x 6] Ligands

Preparation of ethyl 2-hydrazidopyridine-6-carboxylate (**33**)

To a solution of diethyl pyridine-2,6-dicarboxylate (10.0 g, 44.8 mmol) in EtOH (200 ml) was added, dropwise, hydrazine monohydrate (1.1 g, 22.4 mmol) in EtOH (100 ml) over a 2 h period. After stirring for 24 h, the solution was filtered to remove any dihydrazido formed and the filtrate concentrated to dryness under reduced pressure. The desired product was then titriated from the residue with diethyl ether (200 ml), collected *via* filtration and dried under vacuum at 40 °C for 6 h to yield (**33**) (3.10 g, 66.3 %) m.p. 140-141 °C (toluene); (Found: C, 51.45; H, 5.15; N, 20.0. $C_9H_{11}N_3O_3$ requires C, 51.7; H, 5.3; N, 20.1 %); ν_{max} (KBr)/cm^{-1} 3328-2998 (NH, NH_2), 1726 (C=O (ester)), 1677 (C=O (hydrazide)), 1616 (C=N (arom.)), 1508, 1446, 1367, 1312, 1255, 1138, 1023, 998 (py.), 844, 735 and 699; δ_H (270 MHz; $CDCl_3$) 8.1 (1 H, dd, *J* 7.7, 1.0, *H*-4), 8.0 (1 H, dd, *J* 7.7, 1.0, *H*-5), 7.8 (1 H, t, *J* 7.7, *H*-3), 4.2 (2 H, q, *J* 7.2, OCH_2R) and 1.2 (3 H, t, *J* 7.2, RCH_3); δ_C (68.7 MHz; $CDCl_3$) 164.2 (*C*ONH), 163.5 (*C*ONH), 149.3 (*C*-6), 147.0 (*C*-2), 138.5 (*C*-4), 127.4 (*C*-3), 125.0 (*C*-5), 62.0 (OCH_2CH_3) and 14.3 (CH_2CH_3); *m/z* (APCI) 222.2 ((M+Na), 25 %) and 210 ((M+H), 85 %).

Preparation of *N*-(6'-ethoxycarbonylpyridine-2'-amido)pyridine-2-amidine (**42**)

To a solution of NaOMe (0.96 mmol) in MeOH (50 ml) was added 2-cyanopyridine (9.6 mmol, 1.0 g). After stirring overnight the solution was quenched with glacial acetic acid (0.06 ml, 0.96 mmol), ethyl 2-hydrazidopyridine-6-carboxylate (**33**) (2.0 g, 9.6 mmol) added in one portion and the solution heated under reflux for 4 h. The filtrate after this time period was reduced in volume until precipitation occurs and the solid collected by filtration to give a lustrous yellow solid of (**42**) (2.4 g, 78.6 %) m.p. 146-147.5 °C; (Found: C, 54.7; H, 5.2; N, 21.3; $C_{15}H_{15}N_5O_3$ + H_2O requires C, 54.4; H, 5.1; N, 21.15 %); ν_{max} (KBr)/cm^{-1} 3499- 3272 (NH, NH_2), 1718 (C=O (ester)), 1675, 1654, 1526, 1474, 1298, 1246 and 997 (py.); δ_H (270 MHz; DMSO-d$_6$) 8.6 (1 H, dd, *J* 7.7, 1.7, *H*-6), 8.2 (4 H, m, *H*-3, 3', 4', 5'), 7.9 (1 H, ddd, *J* 7.7, 7.5, 1.7, *H*-4) and 7.5 (1 H, ddd, *J* 7.7, 4.9, 1.2, *H*-5); δ_C (68.7 MHz; DMSO-d$_6$) 164.2 (*C*ONH), 159.8 (*C*(O)OEt), 151.3 (*C*NNH), 150.3 (*C*-2), 149.7 (*C*-6), 148.2 (*C*-6'), 146.7 (*C*-2'), 139.2 (*C*-4'), 137.0 (*C*-4), 126.8 (*C*-3'), 125.5 (*C*-5), 125.0 (*C*-5'), 120.9 (*C*-3), 61.6 (O*C*H$_2$R) and 14.0 (R*C*H$_3$); *m/z* (ESI) 300 ((M+H), 100 %).

Preparation of *N*-(6'-hydrazidopyridine-2'-amido)pyridine-2-amidine (**43**)

To a stirred solution of *N*-(6'-ethoxycarbonylpyridine-2'-amido)pyridine-2-amidine (**42**) (10.0 g, 33.4 mmol) in EtOH (250 ml) was added, dropwise, hydrazine monohydrate (6.7 g, 133.8 mmol) and the solution stirred over night at room temperature. The precipitated product was collected *via* filtration, washed with a little cold EtOH and diethyl ether, and dried under vacuum at 40 °C for 8 h to give (**43**) as an off white solid (9.1 g, 86.7 %) m.p. 206-207 °C (MeOH); (Found: C, 51.2; H, 4.4; N, 31.35. $C_{13}H_{13}N_7O_2$ +1/2 MeOH requires C, 51.4; H, 4.7; N, 31.1 %); ν_{max} (KBr)/cm^{-1} 3448-3100 (NH, NH_2), 1701 (C=O (hydrazide)), 1666 (C=O (hydrazide)), 1631 (C=N (arom.)), 1585, 1002 (py.) and 998 (py.); δ_H (270 MHz; DMSO-d$_6$) 8.6 (1 H, ddd, *J* 7.8, 1.7, 1.0 *H*-6), 8.2 (4 H, m, *H*-3, 3', 4', 5'), 7.9 (1 H, ddd, *J* 7.7, 7.5, 1.7, *H*-4), 7.5 (1 H, ddd, *J* 7.5, 4.9, 1.2, *H*-5), 7.0 (2 H, s (br.), RN*H*$_2$) and 4.7 (2 H, s (br.), RN*H*$_2$); δ_C (68.7 MHz; DMSO-d$_6$) 162.3 (*C*ONH), 159.0 (*C*ONH), 151.9 (*C*NNH)), 150.3 (*C*-2), 149.2 (*C*-6), 148.4 (*C*-6'), 148.3 (*C*-2'), 139.3 (*C*-4'), 137.1 (*C*-4), 125.2 (*C*-3'), 124.2 (*C*-5), 123.9 (*C*-5') and 121.0 (*C*-3); *m/z* (APCI) 300 ((M+H, 100 %), 283 (((M-OH)+H), 10 %) and 282 (((M-H_2O)+H), 20 %).

Preparation of *N*-bis[6'-(*N*'-(pyridine-2''-amidino)amidopyridine-2'-amido)]pyrimidine-4'',6''-diamidine (**L11**)

To a hot solution of *N*-(6'-hydrazidopyridine-2'-amido)pyridine-2-amidine (**43**) (8.4 g, 28.1 mmol) and glacial acetic acid (few drops) in dry MeOH (900 ml) was added, dropwise, crude diethyl pyrimidine-4,6-diimidate (**7**) (3.0 g, 13.4 mmol) in dry MeOH (100 ml). After heating under reflux for 6 h the precipitated product was collected *via* hot filtration and washed thoroughly with diethyl ether. Drying under vacuum for 6 h at 60 °C yielded (**L11**) as a bright yellow solid (7.8 g, 79.3 %) m.p. > 250 °C; (Found: C, 50.4; H, 3.8; N, 32.9. $C_{32}H_{28}N_{18}O_4 + 2H_2O$ requires C, 50.3; H, 4.2; N, 33.0 %); ν_{max} (KBr)/cm^{-1} 3430-3218 (NH, NH_2), 1680-1633 (C=O (hyrazide), C=C (arom.), C=N (imine)), 1586 (C=N (arom.)), 1522, 1443, 1389, 1167, 996 (py.) and 748; δ_H (270 MHz; TFA-d$_1$) 9.5 (1 H, s, *H*-2''), 9.2 (1 H, s, *H*-5''), 8.8 (2 H, s, Ar-*H*), 8.5 (4 H, m, Ar-*H*), 8.4 (4 H, m, Ar-*H*), 8.2 (2 H, d, Ar-*H*) and (2 H, d, Ar-*H*); δ_C (270 MHz; TFA-d$_1$) 164.3 (*C*ONH), 160.3 (*C*NNH), 159.8 (*C*NNH), 159.5 (*C*-2''), 152.6 (*C*-4'', 6''), 148.2 (*C*-Ar), 146.0 (*C*-Ar), 145.9 (*C*-Ar), 143.4 (*C*-Ar), 141.0 (*C*-Ar), 139.2 (*C*-Ar), 131.0 (*C*-Ar), 128.5 (*C*-Ar), 126.1 (*C*-Ar) and 117.5 (*C*-5''); *m/z* (ESI) 729 ((M+H), 64 %),

Preparation of *N*-bis[6'-(*N*'-(pyridine-2''-amidino)amidopyridine-2'-amido)]pyrazine-2'',5''-diamidine (**L12**)

To a hot solution of *N*-(6'-hydrazidopyridine-2'-amido)pyridine-2-amidine (**43**) (8.0 g, 26.8 mmol) and glacial acetic acid (few drops) in dry MeOH (850 ml) was added, dropwise, dimethyl pyrazine-2,5-diimidate (**15**) (2.4 g, 12.2 mmol) in dry MeOH (200 ml). After heating under reflux for 24 h the precipitated product was collected *via* hot filtration and washed thoroughly with diethyl ether. Drying under vacuum at 60 °C for 6 h to yield (**L12**) as a orange solid (7.1 g, 78.8 %) m.p. > 250 °C; ν_{max} (KBr)/cm^{-1} 3419-3332 (NH, NH_2), 1690 (C=O (hydrazide)), 1636-1586 (C=C (arom.), C=N (imine)), 1566 (C=N (arom.)), 1512, 1443, 1394, 1159, 998 (py.) and 647; δ_H (270 MHz; TFA-d$_1$) 9.7 (2 H, s, *H*-3'', 6''), 8.9 (2 H, s, *H*-Ar), 8.5-8.4 (12 H, m, *H*-Ar) and 8.3-8.0 (8 H, m, N*H*); δ_C (270 MHz; DMSO-d$_6$) 164.4 (*C*ONH), 161.0 (*C*-Ar), 160.5 (*C*-Ar), 159.5 (*C*-Ar), 148.2 (*C*-Ar), 146.1 (*C*-Ar), 145.9 (*C*-Ar), 143.4 (*C*-Ar), 142.1 (*C*-Ar), 141.0 (*C*-Ar), 139.2 (*C*-Ar), 131.1 (*C*-Ar), 128.5 (*C*-Ar) and 126.1 (*C*-Ar); *m/z* (ESI) 768 (M+K, 45 %) and 729 ((M+H), 65 %).

Preparation of *N*-bis[6'-(*N*'-(pyridine-2''-amidino)amidopyridine-2'-amido)]pyridazine-3'',6''-diamidine (**L13**)

To a hot solution of *N*-(6'-hydrazidopyridine-2'-amido)pyridine-2-amidine (**43**) (8.0 g, 26.8 mmol) and glacial acetic acid (few drops) in dry MeOH (850 ml) was added, dropwise, diethyl pyridazine-3,6-diimidate (**18**) (2.7 g, 12.2 mmol) in dry MeOH (100 ml). After heating under reflux for 6 h the precipitated product was collected *via* hot filtration and washed thoroughly with diethyl ether. Drying under vacuum at 60 °C for 6 h to yield (**L13**) as an orange/ yellow solid (7.4 g, 83.6 %) m.p. > 250 °C; (Found: C, 49.3; H, 4.3; N, 32.65. $C_{32}H_{28}N_{18}O_4$ + $2.7H_2O$ requires C, 49.4; H, 4.3; N, 32.5 %); ν_{max} (KBr)/cm^{-1} 3340-3150 (NH, NH_2), 1680-1635 (C=O (hydrazide), C=C (arom.), C=N (imine)), 1586 (C=N (arom.)), 1566, 1522, 1442, 1240, 998 (py.) and 748; δ_H (270 MHz; DMSO-d_6) 11.2 (2 H, s (br.), N-*H*), 11.1 (2 H, s (br.), N-*H*), 8.6 (2 H, d, *J* 4.2, *H*-6), 8.5 (2 H, s, H-3'', 6''), 8.2 (8 H, m, H-3, 3', 4', 5'), 7.9 (2 H, t, *J* 7.4, *H*-4), 7.5 (2 H, t, *J* 5.7, *H*-5), (2 H, s (br.), N-*H*) and (2 H, s (br.), N-*H*); δ_C (270 MHz; DMSO-d_6) 159.4 (*C*ONH), 159.2 (*C*ONH), 154.0 (*C*-3'', 6''), 151.9 (*C*NNH), 150.2 (*C*NNH), 149.2 (*C*-2), 148.9 (*C*-6), 148.4 (*C*-2', 6'), 139.5 (*C*-4'), 137.2 (*C*-4), 125.7 (*C*-5), 125.3 (*C*-3', 5'), 124.5 (*C*-4'', 5'') and 121.1 (*C*-3); *m/z* (ESI) 767 (M+K, 25 %), 751 ((M+Na), 35 %), 729 ((M+H), 100 %), 711 (((M+H)-H_2O), 16 %).

2.1 Inorganic Synthesis

NMR spectra were measured on a JEOL EX 270 instrument at 270 MHz for ^{1}H, using the residual solvent as internal standard and on a JEOL ECX 400 at 83.4 MHz for ^{207}Pb, using $Pb(OTf)_2$ as reference. FTIR were recorded on a Perkin-Elmer 1600 Series FTIR machine by the preparation of either a KBr disc or nujol mull. Visible spectra were recorded as solutions in MeCN at ~ 10^{-3} mol dm^{-3} using a Lambda 25 instrument. ESI-MS spectra were obtained with the assistance of Dr A. Franklin on a Platform Micromass LC with varying temperatures and cone voltages. X-Ray crystallography was performed externally at both the EPSRC services at Southampton and Daresbury, and solved principally by Dr. P. N. Horton and Prof. W. Clegg, respectively. All samples for X-ray diffraction were kept under solvent prior to mounting and measured at 120 K. Not all the structures presented here have been fully refined and hence, bond lengths and angles for these structures are only quoted to three significant figures with no errors. See supplementary disc for crystallographic files in various forms, *i.e.*, .res .cif and .ins, depending on the level of refinement and the crystallographer. Magnetic measurements were made upon powdered samples at the University of Edinburgh and at the University of St. Johns, Canada on a Quantum Design MPMS5S SQUID Magnetometer with field strengths ranging form 0.2 to 1 T between 2 K and 300 K. Samples were prepared in gelatine capsules and mounted inside straws for attachment to the sample transport rod. Background correction for the sample holder and diamagnetic component of the assemblies were applied. Electrochemical studies were carried out using an AutoLab electrochemical system with Pt working electrode, Ag counter electrode and Ag/AgCl reference electrode. Bulk electrolysis was carried out with a mesh Pt electrode, an Ag counter electrode and Ag/AgCl reference electrode. Acetonitrile was dried by distillation from CaH_2 under an atmosphere of nitrogen. Chemical analyses were performed externally by The University of Nottingham. Note: in most cases good correlation between X-ray data and chemical analysis results allow assignment of the amount of solvent molecules present, however, in some cases X-ray analysis provides little/ no evidence regarding solvent molecules and hence chemical analysis is fitted as best as possible, whilst in other cases no adequate fit could be obtained at all.

Homometallic [2 x 2] Grids

General procedure:

To a hot stirred solution of $M(ClO_4)_{2/3}\cdot 6H_2O$ or $M(OTf)_2$[72] (1.1 mmol) in H_2O (10 ml) was added **L1** (0.32 g, 1.0 mmol) and the resulting suspension heated for 5 min. MeOH (15 ml) and MeCN (15 ml) were added to yield a deep coloured solution, which was subsequently brought to the boil and allowed to cool for approximately 4 h. The solution was then filtered in to a pre-rinsed (MeCN) 100 ml conical flask and after standing for ca. 10 d., the resultant crystals that formed were collected by spotting onto a filter paper. Recrystallisation from PrOH:MeOH:MeCN (1:1:4) yielded high quality crystals suitable for X-ray analysis.

$[Mn_4($**L1**$-H)_4](OTf)_4\cdot 3H_2O$ (**A1**)

(0.43 g, 80.1 %); (Found: C, 40.6; H, 2.4; N, 15.05; $C_{72}H_{58}F_{12}N_{24}O_{19}S_4Mn_4$ requires C, 40.4; H, 2.7; N, 15.7 % (high N content due to high F content)); ν_{max} (KBr)/cm^{-1} 3448 (H_2O), 3325 (NH), 1657 (C=O), 1651 (C=O), 1597-1548 (C=N, C=C), 1253 (CF_3), 1036 (SO_3), 1028, 791 and 636; *m/z* (ESI, 10 V, 70 °C) 893 ($[Mn_4($**L1**$-H)_4(OTf)_2]^{2+}$), 546 ($[Mn_4($**L1**$-H)_4(OTf)]^{3+}$).

$[Cu_4($**L1**$-H)_4](ClO_4)_4\cdot 8H_2O\cdot MeOH$ (**A2**)

(0.35 g, 66.8 %); (Found: C, 39.6; H, 2.8; N, 15.7; $C_{77}H_{72}Cl_4Cu_4N_{24}O_{29}$ requires C, 39.5; H, 3.4; N, 16.0 %); ν_{max} (nujol)/cm^{-1} 3431 (H_2O), 3334 (NH), 1651 (C=O), 1598-1540 (C=N and C=C), 1455, 1083 (ClO_4) and 623; *m/z* (ESI, 0 V, 50 °C) 1434 ($[Cu_{16}($**L1**$-H)_{16}(ClO_4)_{11}]^{5+}$(tetramer)), 1340 ($[Cu_{12}($**L1**$-H)_{12}(ClO_4)_5]^{3+}$ (trimer)), 1180 ($[Cu_8($**L1**$-H)_8(ClO_4)_5]^{3+}$ (dimer)), 1053 ($[Cu_{12}($**L1**$-H)_{12}(ClO_4)_7]^{5+}$ (trimer)), 861 ($[Cu_4($**L1**$-H)_4(ClO_4)_2]^{2+}$), 540 ($[Cu_4($**L1**$-H)_4(ClO_4)]^{3+}$) and 381 ($[Cu_4($**L1**$-H)_4]^{4+}$); λ_{max} (MeCN)/nm 757 (ε/ dm^3 mol^{-1} cm^{-1} 341).

$[Ni_4($**L1**$-H)_4](ClO_4)_4\cdot 3H_2O\cdot 2MeOH$ (**A3**)

(0.34 g, 67.4 %); (Found: C, 41.75; H, 3.0; N, 16.2; $C_{73}H_{66}Cl_4N_{24}Ni_4O_{25}$ requires C, 41.75; H, 3.2; N, 16.7 %); ν_{max} (nujol)/cm^{-1} 3431 (H_2O), 3334 (NH), 1654 (C=O), 1592-1539 (C=N and C=C), 1456, 1377, 1071 (ClO_4) and 622; *m/z* (ESI, 0 V, 50 °C) 1326 ($[Ni_{12}(\mathbf{L1}\text{-}H)_{12}(ClO_4)_8]^{4+}$ (trimer)), 1168 ($[Ni_8(\mathbf{L1}\text{-}H)_8(ClO_4)_5]^{3+}$ (dimer)), 1042 ($[Ni_{12}(\mathbf{L1}\text{-}H)_{12}(ClO_4)_7]^{5+}$ (trimer)), 851 ($[Ni_4(\mathbf{L1}\text{-}H)_4(ClO_4)_2]^{2+}$), 662 ($[Ni_8(\mathbf{L1}\text{-}H)_8(ClO_4)_3]^{5+}$ (dimer)), 534 ($[Ni_4(\mathbf{L1}\text{-}H)_4(ClO_4)]^{3+}$) and 376 ($[Ni_4(\mathbf{L1}\text{-}H)_4]^{4+}$); λ_{max} (MeCN)/nm 924 (ε/ dm^3 mol^{-1} cm^{-1} 249) and ~ 600 (sh.).

$[Co_4(\mathbf{L1}\text{-}H)_4](ClO_4)_4 \cdot 6H_2O \cdot 2MeOH$ (**A4**)

(0.33 g, 63.6 %); (Found: C, 40.6; H, 2.8; N, 16.2; $C_{76}H_{72}Cl_4Co_4N_{24}O_{28}$ requires C, 40.5; H, 3.45; N, 16.2 %); ν_{max} (nujol)/cm^{-1} 3435 (H_2O), 3332 (NH), 1651 (C=O), 1599-1540 (C=N and C=C), 1456, 1361, 1074 (ClO_4) and 623; *m/z* (ESI, 0 V, 50 °C) 1169 ($[Co_8(\mathbf{L1}\text{-}H)_8(ClO_4)_5]^{3+}$ (dimer)), 851 ($[Co_4(\mathbf{L1}\text{-}H)_4(ClO_4)_2]^{2+}$), 535 ($[Co_4(\mathbf{L1}\text{-}H)_4(ClO_4)]^{3+}$) and 386 ($[Co_4(\mathbf{L1}\text{-}H)_4 \cdot MeCN]^{4+}$); λ_{max} (MeCN)/nm ~ 700 (sh).

$[Fe(II)_2Fe(III)_2(\mathbf{L1}\text{-}H)_4](ClO_4)_6 \cdot 4H_2O \cdot MeCN$ (**A5**)

(0.41 g, 74.1 %); (Found: C, 37.45; H, 2.6; N, 15.85; $C_{70}H_{60}Cl_6N_{25}O_{40}Fe_4$ requires C, 37.6; H, 2.85; N, 15.9 %); ν_{max} (nujol)/cm^{-1} 3448 (H_2O), 3319 (NH), 1651 (C=O), 1600-1563 (C=N, C=C), 1460, 1357, 1088 (ClO_4), 790 and 623; *m/z* (ESI, 0 V, 50 °C) 945 ($[Fe_4(\mathbf{L1}\text{-}H)_4(ClO_4)_4]^{+2}$), 423 ($[Fe_4(\mathbf{L1}\text{-}H)_4(ClO_4)_2]^{+4}$) and 346 ($[Fe(\mathbf{L1}\text{-}H)(L1)]^{+2}$) plus other unidentifiable peaks; λ_{max} (MeCN)/nm ~ 600 (sh.).

$[Zn_4(\mathbf{L1}\text{-}H)_4](ClO_4)_4 \cdot 6H_2O \cdot MeCN$ (**A6**)

(0.36 g, 69.3 %); (Found: C, 39.8; H, 2.85; N, 16.7; $C_{69}H_{67}Cl_4N_{25}O_{26}Zn_4$ requires C, 39.9; H, 3.1; N, 16.85 %); ν_{max} (nujol)/cm^{-1} 3436 (H_2O), 3349 (NH), 1658 (C=O), 1597-1542 (C=N and C=C), 1455, 1077 (ClO_4) and 623; *m/z* (ESI, 0 V, 50 °C) 1346 ($[Zn_{12}(\mathbf{L1}\text{-}H)_{12}(ClO_4)_8]^{4+}$ (trimer)), 1183 ($[Zn_8(\mathbf{L1}\text{-}H)_8(ClO_5)_5]^{3+}$ (dimer)), 1057 ($[Zn_{12}(\mathbf{L1}\text{-}H)_4(ClO_4)_7]^{5+}$ (trimer)), 864 ($[Zn_4(\mathbf{L1}\text{-}H)_4(ClO_4)_2]^{2+}$), 672 ($[Zn_8(\mathbf{L1}\text{-}H)_8(ClO_4)_3]^{5+}$ (dimer)), 543 ($[Zn_4(\mathbf{L1}\text{-}H)_4(ClO_4)]^{3+}$) and 393 ($[Zn_4(\mathbf{L1}\text{-}H)_4 \cdot MeCN]^{4+}$).

Heterometallic [2 x 2] Grids

$[Cr(\mathbf{L1})_2](ClO_4)_3\cdot 2H_2O\cdot ½MeCN\cdot MeOH$ (**A7**) (*Precursor*)

To a mixture of $Cr(ClO_4)_3\cdot 6H_2O$ (2.18 g, 4.76 mmol) and **L1** (3.18 g, 10.0 mmol) was added MeOH (30 ml) to give a brown suspension which was subsequently heated under reflux overnight. After cooling the flask in ice, the brown precipitate was collected, washed with diethyl ether and dried under vacuum at room temperature. The sample was then used without further purification; an analytical sample was obtained by the slow evaporation of a saturated solution of MeOH and MeCN (1:1) (4.2 g (crude), 82.1 %); (Found: C, 39.4; H, 2.8; N, 16.1; $C_{35.5}H_{9.5}Cl_3CrN_{12.5}O_{17}$ requires C, 39.6; H, 3.3; N, 16.3 %); ν_{max} (nujol)/cm^{-1} 3559 (H_2O), 3200 (NH), 1678 (C=O), 1606-1570 (C=N, C=C) and 1093 (ClO_4); *m/z* (ESI, 10 V, 70 °C) 1543 ($[Cr_{10}(\mathbf{L1}\text{-}H)_{20}(ClO_4)_{24}]^{6+}$ (decamer)), 1477 ($[Cr_8(\mathbf{L1}\text{-}H)_{16}(ClO_4)_{19}]^{5+}$ (octamer)), 1379 ($[Cr_3(\mathbf{L1}\text{-}H)_6(ClO_4)_7]^{2+}$ (trimer)), 1282 ($[Cr_7(\mathbf{L1}\text{-}H)_{14}(ClO_4)_{16}]^{5+}$ (heptamer)), 1216 ($[Cr_4(\mathbf{L1}\text{-}H)_8(ClO_4)_9]^{3+}$ (tetramer)), 1134 ($[Cr_5(\mathbf{L1}\text{-}H)_{10}(ClO_4)_{11}]^{4+}$ (pentamer)), 1085 ($[Cr_6(\mathbf{L1}\text{-}H)_{12}(ClO_4)_{13}]^{5+}$ (hexamer)), 887 ($[Cr(\mathbf{L1}\text{-}H)_2(ClO_4)_2]^{+}$), 558 ($[Cr_2(\mathbf{L1}\text{-}H)_4(ClO_4)_3]^{3+}$ (dimer)) and 257 ($[Cr(\mathbf{L1}\text{-}H)_2\cdot 2MeCN]^{3+}$).

General Procedure:

To a hot solution of $M(ClO_4)_{2/3}\cdot 6H_2O$ (0.31 mmol) in H_2O (10 ml) was added $[Cr(\mathbf{L1})_2](ClO_4)_3\cdot 2H_2O\cdot ½MeCN\cdot MeOH$ (**A7**) (0.20 g, 0.19 mmol) to give a dark suspension. Heating was continued for a further 5 min whereupon MeCN (25 ml) was added until the suspension dissolved to give a deep dark coloured solution that was allowed to stand for approximately 4 h. The solution was then filtered in to a pre-rinsed (MeCN) 100 ml conical flask and after standing for a period of ca. 10 d, crystals formed that were generally suitable for X-ray analysis.

$[Cr_2Mn_2(\mathbf{L1}\text{-}H)_4](ClO_4)_6\cdot 1.5H_2O$ (**A8**)

(0.20 g, 94.9 %); (Found: C, 39.0; H, 2.6; N, 15.75; $C_{68}H_{55}Cr_2Cl_6Mn_2N_{24}O_{29.5}$ requires C, 38.8; H, 2.6; N, 15.95 %); ν_{max} (nujol)/cm^{-1} 3320-3194 (NH), 1681

(C=O), 1657 (C=O), 1606-1571 (C=N, C=C), 1093 (ClO_4) and 622; *m/z* (ESI, 0 V, 50 °C) 939 ($[Cr_2Mn_2(\mathbf{L1}\text{-}H)_4(ClO_4)_4]^{2+}$, 628 ($[Cr_2(\mathbf{L1}\text{-}H)_2]^+$), 420 ($[Cr_2Mn_2(\mathbf{L1}\text{-}H)_4(ClO_4)_2]^{4+}$) and 247 ($[Cr_2Mn_2(\mathbf{L1}\text{-}H)_4]^{6+}$) plus other unidentifiable peaks.

$[Cr_2Cu_2(\mathbf{L1}\text{-}H)_4](ClO_4)_6{\cdot}4H_2O{\cdot}\frac{1}{2}MeCN$ (**A9**)

(0.18 g, 82.2 %); (Found: C, 37.6; H, 2.7; N, 15.9; $C_{68.5}H_{61.5}Cr_2Cl_6Cu_2N_{24.5}O_{32}$ requires C, 37.85; H, 2.8; N, 15.7 %); ν_{max} (nujol)/cm^{-1} 3315-3193 (NH), 1679 (C=O), 1651 (C=O), 1603-1565 (C=N and C=C), 1064 (ClO_4) and 622; *m/z* (ESI, 0 V, 150 °C) 949 ($[Cr_2Cu_2(\mathbf{L1}\text{-}H)_4(ClO_4)_4]^{2+}$), 600 ($[Cr_2Cu_2(\mathbf{L1}\text{-}H)_4(ClO_4)_3]^{3+}$), 424 ($[Cr_2Cu_2(\mathbf{L1}\text{-}H)_4(ClO_4)_2]^{4+}$), 319 ($[Cr_2Cu_2(\mathbf{L1}\text{-}H)_4(ClO_4)]^{5+}$) and 250 ($[Cr_2Cu_2(\mathbf{L1}\text{-}H)_4]^{6+}$) plus other unidentifiable peaks; λ_{max} (MeCN)/nm 795 (ε/ dm^3 mol^{-1} cm^{-1} 250).

$[Cr_2Ni_2(\mathbf{L1}\text{-}H)_4](ClO_4)_6{\cdot}5H_2O$ (**A10**)

(0.16 g, 72.6 %); (Found: C, 37.1; H, 2.95; N, 15.0; $C_{68}H_{62}Cr_2Cl_6N_{24}Ni_2O_{33}$ requires C, 37.05; H, 2.85; N, 15.25 %); ν_{max} (nujol)/cm^{-1} 3321-3189 (NH), 1659 (C=O), 1652 (C=O), 1603-1556 (C=N and C=C), 1074 (ClO_4) and 621; *m/z* (ESI, 0 V, 120 °C) 944 ($[Cr_2Ni_2(\mathbf{L1}\text{-}H)_4(ClO_4)_4]^{2+}$), 595 ($[Cr_2Ni_2(\mathbf{L1}\text{-}H)_4(ClO_4)_3]3^+$), 421 ($[Cr_2Ni_2(\mathbf{L1}\text{-}H)_4(ClO_4)_2]^{4+}$) and 249 ($[Cr_2Ni_2(\mathbf{L1}\text{-}H)_4]^{6+}$) plus other unidentifiable peaks; λ_{max} (MeCN)/nm 944 (ε/ dm^3 mol^{-1} cm^{-1} 162).

$[Cr_2Co_2(\mathbf{L1}\text{-}H)_4](ClO_4)_6{\cdot}2H_2O$ (**A11**)

(0.16 g, 75.5 %); (Found: C, 38.65; H, 2.7; N, 16.0; $C_{68}H_{56}Cr_2Cl_6Co_2N_{24}O_{30}$ requires C, 38.5; H, 2.65; N, 15.85 %); ν_{max} (nujol)/cm^{-1} 3321-3082 (NH), 1675 (C=O), 1657 (C=O), 1604-1565 (C=C and C=N), 1094 (ClO_4) and 622; *m/z* (ESI, 0 V, 120 °C) 944 ($[Cr_2Co_2(\mathbf{L1}\text{-}H)_4(ClO_4)_4]^{2+}$), 597 ($[Cr_2Co_2(\mathbf{L1}\text{-}H)_4(ClO_4)_3]^{3+}$), 423 ($[Cr_2Co_2(\mathbf{L1}\text{-}H)_4(ClO_4)_2]^{4+}$) and 249 ($[Cr_2Co_2(\mathbf{L1}\text{-}H)_4]^{6+}$) plus other unidentifiable peaks.

$[Cr_2Fe_2(\mathbf{L1}\text{-}H)_4](ClO_4)_6{\cdot}2H_2O{\cdot}MeCN$ (**A12**)

(0.14 g, 69.9 %); (Found: C, 38.35; H, 2.45; N, 16.15; $C_{69}H_{59}Cr_2Cl_6N_{25}O_{30}Fe_2$ requires C, 38.45; H, 2.8; N, 16.25 %); ν_{max} (nujol)/cm^{-1} 3321-3196 (NH), 1681 (C=O), 1656 (C=O), 1540-1562 (C=N, C=C) and 1096 (ClO_4) *m/z* (ESI, 0 V, 120 °C) 940 ($[Cr_2Fe_2(\mathbf{L1}\text{-H})_4(ClO_4)_4]^{2+}$), 595 ($[Cr_2Fe_2(\mathbf{L1}\text{-H})_4(ClO_4)_3]^{3+}$), 421 ($[Cr_2Fe_2(\mathbf{L1}\text{-H})_4(ClO_4)_2]^{4+}$) and 248 ($[Cr_2Fe_2(\mathbf{L1}\text{-H})_4]^{6+}$) plus other unidentifiable peaks.

$[Cr_2Zn_2(\mathbf{L1}\text{-H})_4](ClO_4)_6 \cdot 3H_2O$ (**A13**)

(0.13 g, 60.4 %); (Found: C, 37.85; H, 2.4; N, 15.5; $C_{68}H_{58}Cr_2Cl_6N_{24}O_{31}Zn_2$ requires C, 37.9; H, 2.75; N, 15.6 %); ν_{max} (nujol)/cm^{-1} 3559 (H_2O), 3082 (NH), 1661-1650 (C=O), 1603-1556 (C=N, C=C), 1495, 1332, 1094 (ClO_4), 722 and 622; *m/z* (ESI, 0 V, 120 °C) 950 ($[Cr_2Zn_2(\mathbf{L1}\text{-H})_4(ClO_4)_4]^{2+}$), 601 ($[Cr_2Zn_2(\mathbf{L1}\text{-H})_4(ClO_4)_3]^{3+}$), 426 ($[Cr_2Zn_2(\mathbf{L1}\text{-H})_4(ClO_4)_2]^{4+}$) and 250 ($[Cr_2Zn_2(\mathbf{L1}\text{-H})_4]^{6+}$) plus other unidentifiable peaks.

Mixed Oxidation [2 x 2] and [3 x 3] Grids: Controlled Potential Electrolysis (CPE)

General Procedure:

Experiments were carried out in dry acetonitrile that contained 0.1 M TEAP. This solution was then added to the cell starting from the silver counter electrode end making sure that this level of solution was higher than the bulk cell. The assembly to be oxidised (~ 0.15 mmol) was then added to the bulk cell and the solution thoroughly purged with nitrogen gas. The solution was then held at a set potential until the residual current was less than 0.1 μA (~ 5 h). The darkened solution was then evaporated and repeatedly extracted with boiling DCM. The residue was then crystallised from aqueous acetonitrile and used for further study.

$[Mn(II)_5Mn(III)_4(L(N)\text{-}2H)_6](ClO_4)_{10} \cdot 4MeOH \cdot MeCN$ (**A14**)

(0.57 g, 93.5 %); (Found: C, 35.7; H, 2.4; N, 19.05; $C_{120}H_{109}Cl_{10}N_{55}O_{56}Mn_9$ requires C, 34.45; H, 2.70; N, 18.95 %); ν_{max} (nujol)/cm^{-1} 3541 (H_2O), 3199 (NH), 1689

(C=O), 1654-1560 (C=N, C=C) and 1096 (ClO_4); λ_{max} (MeCN)/nm 996 (ε/ dm^3 mol^{-1} cm^{-1} 795) and 695 (ε/ dm^3 mol^{-1} cm^{-1} 800).

[4 x 4] Grids

$[Pb_{16}$(**L2**-2H)$_8$(OTf)$_6$(H_2O)$_5$](OTf)$_{10}$·23H_2O (**A15**)

To a solution of Pb(OTf)$_2$ (0.27 g, 0.53 mmol) in MeCN (25 ml) was added **L2** (0.14 g, 0.25 mmol) and after stirring for a few moments all the ligand dissolves. Further stirring causes precipitation of a red powder, which dissolved by the addition of H_2O, dropwise. The resulting solution was subsequently stirred overnight. Removal of the solvent under reduced pressure on a water bath and drying under high vacuum for 6 h yields a red solid. Addition of the solid to mixture of H_2O (15 ml) and MeCN (25 ml) gives a deep red solution that yields rod-shaped crystals of [Pb_{16}(**L2**-2H)$_8$(OTf)$_6$(H_2O)$_5$](OTf)$_{10}$·23H_2O upon standing for a period of one week that were suitable for X-ray analysis (0.26 g, 78.8 %); (Found: C, 27.05; H, 1.55; N, 12.45; $C_{240}H_{216}F_{48}N_{96}O_{92}S_{16}Pb_{16}$ requires C, 27.05; H, 2.05; N, 12.6 %); δ_{Pb} (83.4 MHz, CD_3CN/D_2O) 2049 (1 Pb (corner)), 1991 (1 Pb (corner)), 1947 (1 Pb (corner)), 1855 (8 Pb (sides)), 1823 (1 Pb (corner)) and 1651 (4 Pb (inner)); ν_{max} (KBr)/cm^{-1} 3425 (H_2O), 3300-3092 (NH), 1631 (C=O), 1591-1527 (C=C, C=N), 1448, 1252 (CF_3), 1160, 1030 (SO_3) and 639 (SO_3); *m/z* (ESI, 10 V, 120 °C) 1539 ([Pb_{16}(**L2**-2H)$_8$(OTf)$_{10}$]$^{+6}$), 1300 ([Pb_{16}(**L2**-2H)$_8$(OTf)$_9$]$^{+7}$), 1120 ([Pb_{16}(**L2**-2H)$_8$(OTf)$_8$]$^{+8}$), 979 ([Pb_{16}(**L2**-2H)$_8$(OTf)$_7$]$^{+9}$), 866 ([Pb_{16}(**L2**-2H)$_8$(OTf)$_6$]$^{+10}$), 774 ([Pb_{16}(**L2**-2H)$_8$(OTf)$_5$]$^{+11}$) and 697 ([Pb_{16}(**L2**-2H)$_8$(OTf)$_4$]$^{+12}$).

[Mn_{12}(**L2**-2H)$_4$(**L2**)$_4$](OTf)$_{16}$·14H_2O (**A16**)

To a solution of Mn(OTf)$_2$ (0.27 g, 0.76 mmol) in EtOH (50 ml) was added **L2** (0.14 g, 0.25 mmol) and the resulting suspension heated until the volume was reduced to approximately 25 ml. MeOH (20 ml) was added and again, with heating, the volume was reduced to 25 ml. Thereafter, MeCN (20 ml) was added and the dark red solution allowed to stand for approximately 4 h before being filtered into a pre-rinsed (MeCN) 100 ml conical. Upon standing for 3 weeks very small crystals of

$[Mn_{12}($**L2**$-2H)_4($**L2**$)_4](OTf)_{16}\cdot14H_2O$ formed that were only suitable for a synchrotron source (0.14 g, 59.3 %); (Found: C, 37.05; H, 2.3; N, 18.75; $C_{240}H_{196}F_{48}N_{96}O_{78}S_{16}Mn_{12}$ requires C, 37.15, H, 2.5; N, 17.3 % (found N high due to high F content)). ν_{max} (KBr)/cm^{-1} 3442 (H_2O), 1696 (C=O), 1654 (C=O), 1599-1550 (C=C and C=N), 1459, 1255 (CF_3), 1030 (SO_3) and 639 (SO_3); *m/z* (ESI, 0 V, 70 °C) 1352 ($[Mn_{12}($**L2**$-2H)_4($**L2**$)_4(OTf)_{11}]^{+5}$), 1102 ($[Mn_{12}($**L2**$-2H)_4($**L2**$)_4(OTf)_{10}]^{+6}$), 922 ($[Mn_{12}($**L2**$-2H)_4($**L2**$)_4(OTf)_9]^{+7}$), 789 ($[Mn_{12}($**L2**$-2H)_4($**L2**$)_4(OTf)_8]^{+8}$) and 685 ($[Mn_{12}($**L2**$-2H)_4($**L2**$)_4(OTf)_7]^{+9}$).

$[Mn_{16}($**L2**$-2H)_8](OTf)_{16}\cdot2H_2O\cdot10MeOH$ (**A17**)

L2 (0.20 g, 0.36 mmol) was added to a solution of $Mn(OTf)_2$ (0.38 g, 1.07 mmol) in H_2O (10 ml), after stirring for a few moments MeCN (25 ml) was added to give a dark solution with a tint of red. TEA (0.05 ml, 0.36 mmol) was added to the solution causing a slight darkening followed by a small amount of heat to bring the temperature to approximately 40 °C. Upon standing for approximately 4 h, the solution was filtered into a pre-rinsed (MeCN) 100 ml conical and allowed to stand. After 2 weeks the powder formed was collected by filtration and washed with Et_2O. Crystallisation of the solid was achieved by evaporation of a solution of PrOH (30 ml), MeCN (10 ml), MeOH (10 ml) and H_2O (5 ml) to yield $[Mn_{16}($**L2**$-2H)_8](OTf)_{16}\cdot2H_2O\cdot10MeOH$ that was suitable for synchrotron analysis (0.21 g, 58.1 %); (Found: C, 37.2; H, 2.25; N, 16.55; $C_{250}H_{204}F_{48}N_{96}O_{76}S_{16}Mn_{16}$ requires C, 37.2; H, 2.55; N, 16.65 %); ν_{max} (KBr)/cm^{-1} 3424 (H_2O), 1663 (C=O), 1584-1560 (C=N, C=C), 1459, 1258 (CF_3), 1031 (SO_3) and 637 (SO_3).

$[Mn_{12}($**L3**$-2H)_4($**L3**$)_4](OTf)_{16}\cdot6H_2O\cdot8MeOH$ (**A18**)

To a hot solution of $Mn(OTf)_2$ (0.27 g, 0.76 mmol) in MeOH (20 ml) was added **L3** (0.14 g, 0.25 mmol) and once all the ligand had dissolved, H_2O (5 ml) was added and the solution brought to the boil. After standing for approximately 4 h, the solution was then filtered into a pre-rinsed (MeOH) 100 ml conical and allowed to stand. Upon standing for a period of two weeks X-ray quality crystals of $[Mn_{12}($**L3**$-2H)_4($**L3**$)_4](OTf)_{16}\cdot6H_2O\cdot8MeOH$ formed (0.19 g, 77.0 %); (Found: C, 37.85; H, 2.35; N, 17.10; $C_{248}H_{228}F_{48}N_{96}O_{78}S_{16}Mn_{12}$ requires C, 37.85; H, 2.90; N, 17.10 %); ν_{max} (KBr)/cm^{-1} 3412 (H_2O), 3350-3149 (NH), 1684 (C=O), 1646 (C=O), 1600-1563 (C=C, C=N)), 1458, 1255 (CF_3), 1160, 1031 (SO_3), 786, 757 and 639 (SO_3); *m/z* (ESI, 0 V, 50 °C) 1351 ([Mn_{12}(**L3**-2H)$_4$(**L3**)$_4$(OTf)$_{11}$]$^{+5}$), 1102 ([Mn_{12}(**L3**-2H)$_4$(**L3**)$_4$(OTf)$_{10}$]$^{+6}$), 923 ([Mn_{12}(**L3**-2H)$_4$(**L3**)$_4$(OTf)$_9$]$^{+7}$), 789 ([Mn_{12}(**L3**-2H)$_4$(**L3**)$_4$(OTf)$_8$]$^{+8}$), 685 ([Mn_{12}(**L3**-2H)$_4$(**L3**)$_4$(OTf)$_7$]$^{+9}$).

[Pb_4(**L4**-2H)(OTf)$_5$(H_2O)$_2$](OTf) (**A19**)

To a hot solution of Pb(OTf)$_2$ (0.73 g, 1.43 mmol) in H_2O (10 ml) was added **L4** (0.20 g, 0.36 mmol) to give a yellow suspension that dissolved upon the addition of MeOH (20 ml) and MeCN (20 ml). Upon standing the orange solution deposited a powder that was collected *via* filtration and crystallised from PhMe: MeCN (1:3) to give orange plates of [Pb_4(**L4**-2H)(OTf)$_5$(H_2O)$_2$](OTf) (0.62 g, 74.7 %); (Found: C, 17.8; H, 0.8; N, 6.9; $C_{34}H_{24}F_{18}N_{12}O_{22}S_6Pb_4$ requires C, 17.65; H, 1.05; N, 7.25 %); ν_{max} (KBr)/cm^{-1} 3446 (H_2O), 3290 (NH), 1641 (C=O), 1627-1560 (C=C, C=C), 1528, 1251 (CF_3), 1173, 1034 (SO_3) and 642 (SO_3); *m/z* (ESI, 0 V, 70 °C) 1370 ([Pb_8(**L4**-2H)$_2$(OTf)$_9$]$^{+3}$ (dimer)), 991 ([Pb_4(**L4**-2H)(OTf)$_4$]$^{+2}$), 611 ([Pb_4(**L4**-2H)(OTf)$_3$]$^{+3}$) and 423 ([Pb_4(**L4**-2H)(OTf)$_2$]$^{+4}$).

[Mn_4(**L4**-H)$_4$](ClO_4)$_4$·16H_2O (**A20**)

To a hot solution of Mn(ClO_4)$_2$·6H_2O (0.27 g, 0.75 mmol) in H_2O (30 ml) was added **L4** (0.14 g, 0.25mmol), after heating for 5 min MeCN (15 ml) was added to give a scarlet solution. Upon standing for approximately 4 h, the solution was filtered into a pre-rinsed (MeCN) 100 ml conical and allowed to stand. Large rod-like crystals of [Mn_4(**L4**-H)$_4$](ClO_4)$_4$·16H_2O formed after a 2 week period that were only suitable for synchrotron analysis (0.16 g, 82.9 %); (Found: 42.7; H, 3.0; N, 21.3; $C_{112}H_{120}Cl_4N_{48}O_{40}Mn_4$ requires C, 42.9; H, 3.7; N, 21.45 %); ν_{max} (KBr)/cm^{-1} 3415 (H_2O), 3315-3128 (NH, NH_2), 1690 (C=O), 1654 (C=O), 1650-1547 (C=N, C=C), 1378, 1080 (ClO_4) and 622; *m/z* (ESI, 0 V, 70 °C) 1323 ([Mn_4(**L4**-H)$_4$(ClO_4)$_2$]$^{+2}$), 850 ([Mn_4(**L4**-H)$_4$(ClO_4)]$^{+3}$ and 612 ([Mn_4(**L4**-H)$_4$]$^{+4}$).

$[Pb_{16}(\mathbf{L6}\text{-}3H)_8](OTf)_8 \cdot 58H_2O \cdot 8MeOH$ (**A21**)

L6 (0.20 g, 0.41 mmol) was added to a hot solution of $Pb(OTf)_2$ (0.62 g, 1.23 mmol) in MeOH, once all the ligand had dissolved H_2O (7 ml) was added and the yellow solution brought to the boil. After standing for approximately 4 h, the solution was filtered in to a pre-rinsed (MeOH) 100 ml conical and allowed to stand. Large crystals of $[Pb_{16}(\mathbf{L6}\text{-}3H)_8](OTf)_8 \cdot 58H_2O \cdot 8MeOH$ formed after 10 d that were suitable for X-ray analysis (0.41 g 82.6 %) (Found: C, 22.8; H, 1.35; N, 13.75; $C_{184}H_{284}F_{24}N_{96}O_{98}S_8Pb_{16}$ requires C, 22.8; H, 2.9; N, 13.85 %); ν_{max} (KBr)/cm^{-1} 3446 (H_2O), 3336 (NH), 1635 (C=O), 1553 (C=C, C=N), 1284 (CF_3), 1172, 1031 (SO_3) and 640 (SO_3); *m/z* (ESI, 10 V, 70 °C) 1531 ($[Pb_{16}(\mathbf{L6}\text{-}3H)_8(OTf)_3]^{+5}$), 1249 ($[Pb_{16}(\mathbf{L6}\text{-}3H)_8(OTf)_2]^{+6}$) and 1049 ($[Pb_{16}(\mathbf{L6}\text{-}3H)_8(OTf)]^{+7}$).

$[Mn_{16}(\mathbf{L6}\text{-}3H)_8](OTf)_{16} \cdot 27H_2O \cdot 10MeOH$ (**A22**)

To a hot solution of $Mn(OTf)_2$ (0.46 g, 1.23 mmol) in MeOH was added **L6**, the red solution was then heated until boiling, H_2O added (7 ml) and again brought to boil. Upon cooling the solution was filtered in to a pre-rinsed (MeOH) conical flask and allowed to stand. Large crystals of $[Mn_{16}(\mathbf{L6}\text{-}3H)_8](OTf)_{16} \cdot 27H_2O \cdot 10MeOH$ formed after 10 d that were suitable for synchrotron analysis (0.29 g, 83.4 %), (Found: C, 33.0; H, 2.35; N, 19.85; $C_{186}H_{230}F_{24}N_{96}O_{69}S_8Mn_{16}$ requires C, 33.05; H, 3.4; N, 19.9 %); ν_{max} (KBr)/cm^{-1} 3434 (H_2O), 3338 (NH), 1687 (C=O), 1660 (C=O), 1583-1547 (C=N, C=C), 1470, 1256 (CF_3), 1171, 1030 (SO_3), 751 and 642 (SO_3); *m/z* (ESI, 0 V, 70 °C) 1339 ($[Mn_{16}(\mathbf{L6}\text{-}3H)_8(OTf)_4]^{+4}$), 1042 ($[Mn_{16}(\mathbf{L6}\text{-}3H)_8(OTf)_3]^{+5}$), 843 ($[Mn_{16}(\mathbf{L6}\text{-}3H)_8(OTf)_2]^{+6}$) and 701 ($[Mn_{16}(\mathbf{L6}\text{-}3H)_8(OTf)]^{+7}$).

Pyridazine Bridged Helical Chains

$[Cu_4(\mathbf{L7})_3](ClO_4)_8 \cdot 14H_2O$ (**A23**)

To a hot solution of $Cu(ClO_4)_2 \cdot 6H_2O$ (0.30 g, 8.0 mmol) in H_2O (10 ml) was added **L7** (0.20 g, 0.50 mmol). Heating was continued for 5 min with stirring followed by the addition of MeCN (20 ml), which yielded a dark brown solution. After standing for approximately 4 h, the solution was filtered into a pre-rinsed (MeCN) 100 ml conical flask and upon standing for 14 d crystals of $[Cu_4(\mathbf{L7})_3](ClO_4)_8\cdot 14H_2O$ formed that were suitable for X-ray analysis (0.29 g, 77.4 %); (Found: C, 26.1; H, 2.9; N, 19.8. $C_{54}H_{72}Cl_8N_{36}O_{46}Cu_4$ requires C, 25.9; H, 3.3; N, 20.0 %) ν_{max} (nujol)/cm^{-1} 3584 (H_2O), 3331 (NH), 1659 (C=N and C=C)), 1074 (ClO_4); *m/z* (ESI, 0 V, 50 °C) 1402 ($[Cu_8(\mathbf{L7})_6(ClO_4)_{13}]^{+3}$), 1253 ($[Cu_{12}(\mathbf{L7})_9(ClO_4)_{19}]^{+5}$), 1190 ($[Cu_{16}(\mathbf{L7})_{12}(ClO_4)_{25}]^{+7}$), 1028 ($[Cu_4(\mathbf{L7})_3(ClO_4)_6]^{+2}$), 803 ($[Cu_8(\mathbf{L7})_6(ClO_4)_1]^{+5}$), 652 ($[Cu_4(\mathbf{L7})_3(ClO_4)_5]^{+}$), 474 ($[Cu_4(\mathbf{L7})_3(ClO_4)_4]^{+4}$) and 376 ($[Cu_4(\mathbf{L7})_3(ClO_4)_3]^{+5}$); λ_{max} (MeCN)/nm 780 (ε/ dm^3 mol^{-1} cm^{-1} 602);

$[Mn_4(\mathbf{L7})_3](ClO_4)_8\cdot MeCN\cdot 10H_2O$ (**A24**)

L7 (0.20 g, 0.50 mmol) was added to a solution of $Mn(ClO_4)_2\cdot 6H_2O$ (0.24 g, 0.67 mmol) in MeCN (30 ml) to give a deep red solution that was subsequently stirred overnight. The solvent was then removed on a water bath under reduced pressure and dried under high vacuum for 6 h. The solid was then redissolved in MeCN (20 ml) along with a few drops of water and diethyl ether was allowed to diffuse slowly into the solution. After ca. 10 d crystals formed along with a small amount of yellow powder that was decanted away, filtration of the remaining solution gave $Mn_4(\mathbf{L7})_3(ClO_4)_8\cdot MeCN\cdot 10H_2O$ which were also suitable for X-ray analysis (0.34 g, 85.3 %); (Found: C, 28.35; H, 2.4; N, 21.1; $C_{56}H_{77}Cl_8N_{37}O_{32}Mn_4$ requires C, 28.5; H, 3.1; N, 21.2 %); ν_{max} (nujol)/cm^{-1} 3331-3186 (NH), 1661 (C=N), 1633 (C=N), 1581-1557 (C=N, C=C), 1377 and 1081 (ClO_4); *m/z* (ESI, 0 V, 50 °C) 1011 ($[Mn_4(\mathbf{L7})_3(ClO_4)_6]^{+2}$), 641 ($[Mn_4(\mathbf{L7})_3(ClO_4)_5]^{+3}$) and 466 ($[Mn_4(\mathbf{L7})_3(ClO_4)_4\cdot MeCN]^{+4}$).

$[Ni_4(\mathbf{L7})_3](OTf)_8\cdot 2H_2O$ (**A25**)

To a hot solution of $Ni(OTf)_2$ (0.28 g, 0.80 mmol) in H_2O (10 ml) was added **L7** (0.20 g, 0.50 mmol), heating was continued until the ligand dissolved to give a dark solution with a tint of red and then MeCN (20 ml) was added. The solution was allowed to stand for approximately 4 h, subsequently filtered into a pre-rinsed (MeCN) 100 ml conical flask and allowed to stand. X-ray quality crystals of

$[Ni_4(\mathbf{L7})_3](OTf)_8\cdot 2H_2O$ formed after standing for around 10 d (0.30 g, 66.1 %); (Found: C, 28.05; H, 2.00; N, 18.6; $C_{62}H_{58}F_{24}N_{36}O_{26}S_8Ni_4$ requires C, 27.9; H, 2.15; N, 18.9); ν_{max} (KBr)/cm^{-1} 3336-3194 (NH), 1694-1656 (C=N), 1589-1560 (C=N, C=C), 1257 (CF_3), 1031 (SO_3) and 640 (SO_3); *m/z* (ESI, 10 V, 50 °C) 1176 ($[Ni_4(\mathbf{L7})_3(OTf)_6\cdot H_2O]^{+2}$), 912 ($[Ni_8(\mathbf{L7})_6(OTf)_{11}\cdot 2H_2O]^{+5}$ (dimer)), 735 ($[Ni_4(\mathbf{L7})_3(OTf)_5\cdot H_2O]^{+3}$) and 514 ($[Ni_4(\mathbf{L7})_3(OTf)_4\cdot H_2O]^{+4}$); λ_{max} (MeCN)/nm 776 (ε/ dm^3 mol^{-1} cm^{-1} 921).

$[Zn_4(\mathbf{L7})_3](OTf)_8\cdot 3H_2O$ (**A26**)

To a hot solution of $Zn(OTf)_2$ (0.29 g, 0.80 mmol) in H_2O (10 ml) was added **L7** (0.20 g, 0.50 mmol) followed by heating for 5 min. MeOH (20 ml) was then added to give a golden solution, which was allowed to cool to room temperature. Filtration into a pre-rinsed (MeOH) 100 ml conical yielded upon standing for 3 weeks, X-ray quality crystals of $[Zn_4(\mathbf{L7})_3](OTf)_8\cdot 3H_2O$ (0.38 g, 84.4 %); (Found: C, 27.2; H, 2.05; N, 18.70; $C_{62}H_{60}F_{24}O_{27}N_{36}S_8Zn_4$ requires C, 27.4; H, 2.2; N, 18.55) ν_{max} (KBr)/cm^{-1} 3341-3198 (NH), 1668-1646 (C=N), 1588-1566 (C=N, C=C), 1442, 1248 (CF_3), 1168, 1031 (SO_3) and 640 (SO_3) δ_H (270 MHz; CD_3CN) 8.8 (2 H, s, *H*-4', 5'), 8.7 (2 H, dd, *J* 4.2 and 0.7, *H*-6), 8.4 (2 H, td, *J* 7.9 and 1.4, *H*-4), 8.2 (2 H, d, *J* 7.9, *H*-3), 7.9 (2 H, ddd, *J* 7.7, 5.2 and 1.0, *H*-5) and 7.6-6.8 (8 H, s (br.). RN*H*$_2$). *m/z* (ESI, 0 V, 70 °C) 1160 ($[Zn_4(\mathbf{L7})_3(OTf)_6]^{+2}$), 723 ($[Zn_4(\mathbf{L7})_3(OTf)_5]^{+3}$) and 505 ($[Zn_4(\mathbf{L7})_3(OTf)_4]^{+4}$).

$[Cu_5(\mathbf{L7A}\text{-}3H)_2(H_2O)_5](ClO_4)_4\cdot{\sim}10H_2O\cdot 2MeCN$ (**A27**)

To a stirred solution of $Cu(ClO_4)_2\cdot 6H_2O$ (0.73 g, 1.98 mmol) in MeCN (20 ml) was added **L7A** (0.20g, 0.50 mmol) and the suspension stirred until all the ligand had dissolved. TEA (0.14 ml, 0.99 mmol) was added causing darkening of the solution that was subsequently stirred for a further 10 min. H_2O (10 ml) was added and the solution allowed to stand for approximately 4 h, whereupon it was filtered into a pre-rinsed (MeCN) 100 ml conical and allowed to stand. This yielded large dark crystals of $[Cu_5(\mathbf{L7A}\text{-}3H)_2(H_2O)_5](ClO_4)_4\cdot{\sim}10H_2O\cdot 2MeCN$ suitable for X-ray analysis (0.37 g, 79.7 % (based upon crystal structure)). No satisfactory elemental analysis could be obtained; ν_{max} (nujol mull)/cm^{-1} 3378 (NH), 1665 (C=O), 1630-1525 (C=N, C=C), 1455, 1376, 1096 (ClO_4) and 622; λ_{max} (MeCN)/nm ~ 700 (sh.).

Pyrimidine Bridged Helical Assemblies

$[Cu_8$(**L8**)$_4(H_2O)_8](ClO_4)_{16}\cdot 6H_2O\cdot MeCN$ (**A28**)

To a hot solution of $Cu(ClO_4)_2\cdot 6H_2O$ (0.55 g, 1.49 mmol) in H_2O (10 ml) was added in one portion, **L8** (0.20 g, 0.50 mmol). After heating for a further five min MeCN (25 ml) was added to give a dark brown solution, which was allowed to stand for approximately 4 h. The solution was then filtered into a pre-rinsed 100 ml conical and upon standing for a period of one week a green powder formed that was collected *via* filtration. Suitable crystals were grown from a concentrated mixture of $MeNO_2$ and MeCN (1:2) (0.38 g (powder), 76.3 %); (Found: C, 21.85; H, 2.65; N, 17.45; $C_{74}H_{103}Cl_{16}N_{49}O_{78}Cu_8$ requires C, 22.2; H, 2.60; N, 17.15 %); ν_{max} (nujol mull)/cm^{-1} 3414 (H_2O), 3333-3198 (NH), 1672-1645 (C=N), 1459, 1377, 1101 (ClO_4) and 623; *m/z* (ESI, 20 V, 50 °C) 1136 ([Cu_8(**L8**)$_4(ClO_4)_{13}]^{+3}$), 827 ([Cu_8(**L8**)$_4(ClO_4)_{12}]^{+4}$) and 642 ([Cu_8(**L8**)$_4(ClO_4)_{11}]^{+5}$); λ_{max} (MeCN)/nm 666 (ε/ dm^3 mol^{-1} cm^{-1} 1596).

$[Mn_6$(**L8**)$_4Cl_{12}]6H_2O\cdot 2MeOH$ (**A29**)

L8 (0.20 g, 0.50 mmol) was dissolved in a minimum amount DMF (~ 7 ml) and added to a hot solution of $MnCl_2\cdot 4H_2O$ (1.99 mmol, 0.39 g) in MeOH (20 ml). Upon cooling, the deep red solution deposited a small amount of an orange powder that was removed by filtration into a pre-rinsed (MeOH) 100 ml conical flask. Large block like red crystals of $[Mn_6$(**L8**)$_4Cl_{12}]6H_2O\cdot 2MeOH$ formed after standing overnight that were suitable for X-ray analysis (0.21 g, 66.6 %); (Found: C, 35.2; H, 3.45; N, 26.45; $C_{74}H_{92}Cl_{12}N_{48}O_8Mn_6$ requires C, 35.0; H, 3.60; N, 26.5 %); ν_{max} (KBr)/cm^{-1} 3304 (NH), 1626-1525 (C=N, C=C), 1413, 1300, 1014, 797 and 748.

$[Cu_{20}$(**L8A**-2H)$_4$(**L8A**-4H)$_4(H_2O)_{16}](ClO_4)_{16}\cdot 14H_2O$ (**A30**)

L8A (0.10 g, 0.25 mmol) was added to a solution of $Cu(ClO_4)_2{\cdot}6H_2O$ (0.37 g, 1.00 mmol) in MeCN (20 ml) and allowed to stir until all the ligand dissolved whereupon TEA (0.07 ml, 0.50 mmol) was added. The resulting dark solution was stirred for 5 min and EtOH (10 ml) and H_2O (2 ml) were added followed by a further 30 min of stirring. Upon standing for around 4 h, the solution was filtered into a pre-rinsed 100 ml conical (MeCN) and allowed to evaporate at room temperature. Very small square red plates of (**A30**) formed after standing for 2 weeks that were suitable for X-ray analysis (0.08 g, 39 %) (Found: C, 26.2; H, 1.85; N, 16.75; $C_{144}H_{164}Cl_{16}N_{80}O_{110}Cu_{20}$ requires C, 26.15; H, 2.50; N, 16.95 %); ν_{max} (nujol mull)/cm^{-1} 3549 (H_2O), 1668 (C=O), 1581-1537 (C=C, C=N), 1376, 1098 (ClO_4) and 722.

Other Characterised Assemblies

$[Pb_4($**L9A**$-2H)(OTf)_6(H_2O)_2]_n$ (**A31**)

To a stirred solution of $Pb(OTf)_2$ (1.00 g, 1.98 mmol) in H_2O (10 ml) was added **L9A** (0.20 g, 0.50 mmol) to give a suspension which dissolved to give a red solution upon the addition of MeOH (20 ml) and MeCN (20 ml). Upon standing for a period of 3 weeks the almost dry solution deposited large red blocks of $[Pb_4($**L9A**$-2H)(OTf)_6(H_2O)_2]_n$ that were suitable for X-ray analysis (0.59 g, 55.1 %); (Found: C, 13.6; H, 0.6; N, 6.3; $C_{24}H_{18}F_{18}N_{10}O_{22}S_6Pb_4$ requires C, 13.3; H, 0.8; N, 6.4 %); ν_{max} (KBr disc)/cm^{-1} 3436 (H_2O), 3305 (NH), 1618 (C=O), 1594-1533 (C=N, C=C), 1470, 1346, 1253 (CF_3), 1178, 1034 (SO_3) and 642 (SO_3).

$\{[Pb_5($**L13**$-(4H + H_2O))(OTf)_5(H_2O)_5](OTf)(H_2O)_6\}_n$ (**A32**)

L13 (0.20 g, 0.27 mmol) was added to a stirred solution of $Pb(OTf)_2$ in H_2O (10 ml) to give an suspension which dissolved upon the addition of MeOH (10 ml) and MeCN (20 ml). The orange solution deposited crystals of $\{[Pb_5($**L13**$-(4H + H_2O))(OTf)_5(H_2O)_5](OTf)(H_2O)_6\}_n$ suitable for X-ray analysis upon standing for 3 weeks (0.08 g, 10.3 % (based upon M.W. from X-ray data)); no satisfactory elemental analysis could be obtained; ν_{max} (KBr disc)/cm^{-1} 3504 (H_2O), 3306 (NH), 1630 (C=O), 1557-1540 (C=N, C=C), 1257 (CF_3), 1177, 1033 (SO_3), 744 and 642 (SO_3).

Chapter Three

Homometallic [2 x 2] Grids

3.0 Introduction

There are a variety of [2 x 2] grids reported in the literature with most examples covered in chapter 1, however most of these assemblies have their metal centres separated by long bridges that hinder magnetic exchange. Those bridged by a single atom, in particular alkoxide, are better suited to promote magnetic exchange due to short metal-metal separations.

Thompson and Matthews have used the alkoxide bridge to form a variety of [2 x 2] grids with the general formula $[M_4(L(F))_4X_4]^{+4}$ X = anion or solvent.[4] These are viewed as non-homoleptic systems because the ligand (L(F)) does not satisfy the coordination requirements of the octahedral metal ion. Hence, the ligand undergoes a step-wise self-assembly process to produce non-homoleptic [2 x 2] grids, and a strict self-assembly process to produce $[M_5(L(F)_6]A_4$ (A = anion) pentanuclear homoleptic assemblies.[45] This suggests a mixture of species could exist in solution. In contrast, L(F) forms a homoleptic [2 x 2] grid when reacted with Cu(II) because of its variety of coordination preferences and adopts a trigonal based pyramidal geometry in this case.[4c] Lehn's work with a single atom bridge is limited to a single phenoxide example.[44b] Importantly the ligand (L(E)) provides two tridentate pockets that satisfy the coordination requirements of an octahedral metal ion. The only reported assembly is $[Cu_4(L(E)\text{-}H)_4](PF_6)_4$ that displays very little magnetic exchange due to the orthogonality of the magnetic orbitals.

Ligand Design

L1 was designed to provide two contiguous tridentate pockets built around a single alkoxide bridge to promote both magnetic and electrochemical behaviour (Fig. 24). The two tridentate pockets are composed of different coordinating groups, which renders the ligand unsymmetrical but favours the exclusive formation of homoleptic [2 x 2] square grids of the type $[M_4(\mathbf{L1}\text{-}H)_4]A_4$ when self-assembled with transition metal ions that prefer an octahedral geometry. It was envisaged that the resulting [2 x 2] grids would be stable in solution, which would allow for the observation of reversible electronic communication between metal centres and perhaps the preparation of mixed valent species by bulk eletrolysis (chapter 5). The unsymmetrical nature of the ligand has also been exploited in the preparation of heterometallic [2 x 2] grids, which are discussed in chapter 4.

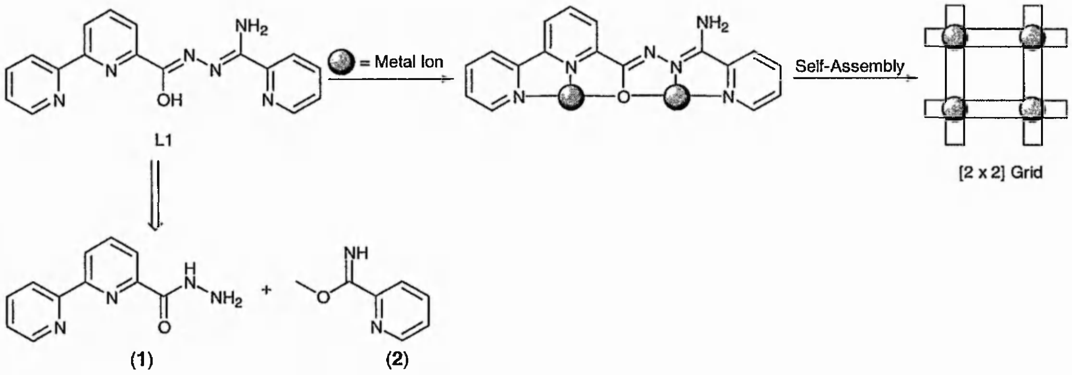

Figure 24 Complexation and disconnection of **L1**.

Ligand Synthesis

A reasonable disconnection of **L1** gives 6-hydrazido-2,2'-bipyridine (**1**) and methyl-pyridine-2-imidate (**2**). This methodology has been reported for the synthesis of similar diazine based ligands and gives high yields.[4a] 6-Hydrazido-2,2'-bipyridine was prepared in 54 % yield from 2,2'-bipyridine (**3**) in four steps (see Fig. 25). Initially, statistical mono oxidation of 2,2'-bipyridine in chloroform with *m*-CPBA according to a standard literature procedure[73] gave the desired mono-*N*-oxide (**4**). Conversion to the nitrile (**5**) was then pursued using a preparation reported by Heirtlzer[62], however the reaction did not proceed as reported and gave low yields together with various by-products that were not analysed further. In addition, the reaction required large quantities of TMSCN that is expensive and highly toxic. An alternative route was attempted using the mono-*N*-oxide in water along with potassium cyanide.[74] Unfortunately this gave low yields with a mixture of both 4- and 6- substituted 2,2'-bipyridines. Hodgson has reported[75] a similar methodology to that of Heirtlzer that only uses a small excess of TMSCN and gave exclusively the 6-cyano-2,2'-bipyridine (**5**) in high yields. This was used to furnish the methyl imidate ester in dry methanol followed by acidic hydrolysis to the ester, methyl 2,2'-bipyridine-6-carboxylate (**6**) in excellent yields.[62] Addition of an excess of hydrazine monohydrate to the ester in dry methanol gave the novel 6-hydrazido-2,2'-bipyridine (**1**) after recrystallisation from methanol. Reaction of this novel compound with methyl pyridine-2-imidate (**2**) [4a] (generated *in situ* from 2-cyanopyridine and a catalytic amount of NaOMe in methanol) in methanol with a small amount of glacial acetic acid gave **L1** in excellent yields and high purity.

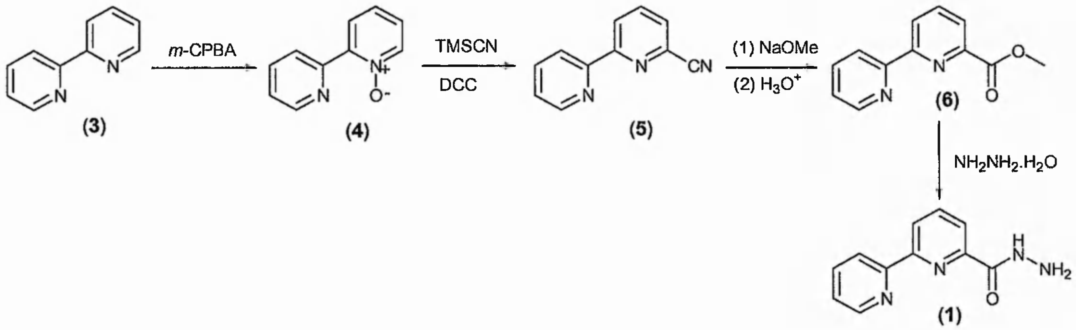

Figure 25 Synthesis of 6-hydrazido-2,2'-bipyridine (**1**) from 2,2'-bipyridine (**3**).

Complexation

Addition of **L1** to a slight excess of a selected first row transition metal salt (perchlorate or triflate) in water followed by the addition of methanol and/ or acetonitrile gave clear solutions. Upon standing at ambient conditions these solutions yielded crystals suitable for further analysis in the cases of Mn(II) (**A1**), Cu(II) (**A2**), Ni(II) (**A3**), Co(II) (**A4**), Fe(II), Fe(III) (**A5**) and Zn(II) (**A6**). The Mn(II) assembly was originally prepared from the perchorlate salt that has been almost fully characterised, however crystals suitable for X-ray analysis could not be obtained.

3.1 Solution Studies

Electrospray ionisation is a particularly soft technique that is ideal for the detection of multiply charged high molecular weight compounds. In addition the successive loss of anions can yield patterns that can be used to determine the molecular weight of large molecular assemblies. Spectra were obtained in acetonitrile with cone voltages ranging from 0 to 20 V at temperatures between 50 and 70 °C.

In the cases of Mn(II) (**A1**), Cu(II) (**A2**), Ni(II) (**A3**), Co(II) (**A4**) and Zn(II) (**A6**) extremely clean spectra were obtained that display a series of peaks that are attributed to the successive loss of the perchlorate anion from a species with an overall charge of +4 and a molecular weight in accord with $[M_4(\mathbf{L1}\text{-}H)_4(ClO_4)_4]$ along with various adducts formed between the cation and acetonitrile that is typical of this type of system.[76] Furthermore, these examples show the formation of intermolecular adducts of the grids such that dimers and trimers are observed in solution (Fig. 26), which is particularly interesting in terms of surface applications. The formation of adducts would be a distinct advantage in producing uniform surfaces.[77]

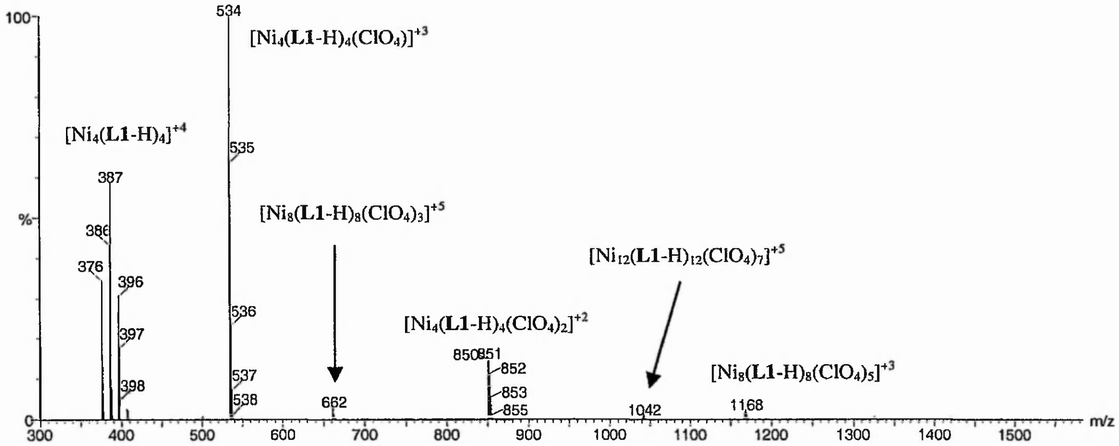

Figure 26 ESI-MS spectrum of $[Ni_4(\mathbf{L1}\text{-}H)_4](ClO_4)_4$ (**A3**) in acetonitrile at a cone voltage of 10 V.

It would appear that a change in attendant anion to triflate in the case of $[Mn_4(\mathbf{L1}\text{-}H)_4](OTf)_4$ stops the formation of any adducts between itself and acetonitile. However, it does yield a clean spectrum with both the +2 and +3 states prominent.

The spectra of the Fe(II) and Fe(III) assemblies are less conclusive, since a mixture of identifiable and unidentifiable peaks are observed. The Fe(II) is approximately correct with peaks associated with the +2 and +3 states along with small amounts of other species with one identified as the "corner species" made up from two ligands and one metal centre (Fig. 27). The Fe(III) example shows no peaks that correlate with the desired $Fe(III)_4(\mathbf{L1}\text{-}H)_4$ cation, however there are a number of identifiable peaks that can be assigned to a mixed oxidation $Fe(II)_2Fe(III)_2$ motif along with a corner species depicted in Fig. 27.

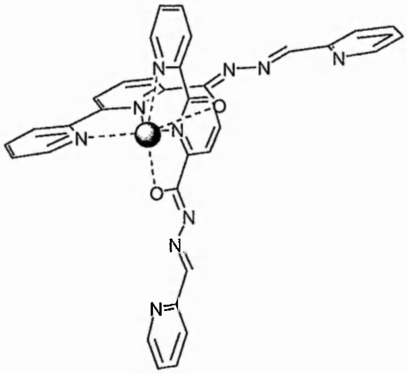

Figure 27 Schematic representation of corner piece. No charge is indicated and the overall geometry of the motif is assumed. Note: NH_2 groups are omitted for clarity.

Electrochemical methods especially cyclic voltametry (CV) can be used to give a clear indication of separate redox processes occurring in solution, whilst differential pulse voltammtery (DPV) can be used to resolve minute differences in oxidative potentials.[78] Electrochemical methods were carried out in dry acetonitrile at approximately 1.0 mmol with TEAP as a supporting electrolyte with a typical three electrode set-up (Chapter One). Saturated Ag/ AgCl was used as reference electrode and in each case the addition of ferrocene introduced a reversible peak at $E_p = + 0.44$ V.

CV studies on solutions of the crystalline solids indicate a number of peaks exhibited at a negative potential between -2.0 and -1.4 V and can be attributed to the reduction of the 2,2'-bipyridine group along with other functionalities present within the ligand framework, similar to that reported by other authors.[79] The Mn(II) (**A1**), Co(II) (**A4**) and Fe(II) assemblies show similar types of oxidative behaviour exhibiting a series of one electron processes in both the cathodic and anodic sweeps. The peak observed in the cathodic sweep at the highest potential can be attributed to the formation of $M(III)_4$, whilst the Fe(III) assembly displays more complex reversible behaviour. The Ni(II) (**A3**) assembly shows no reversible peaks over the range of –2 and 2 V with three irreversible peaks (no return) at 1.10, 1.16 and 1.60 V that could be attributed to the formation of Ni(III). The Zn(II) (**A6**) assembly shows one irreversible peak at 1.50 V which would be expected to be associated with ligand oxidation. There are some more specific details covered in the following section for the cases of Mn(II) (**A1**), Co(II) (**A4**), Fe(II) and Fe(III) (**A5**).

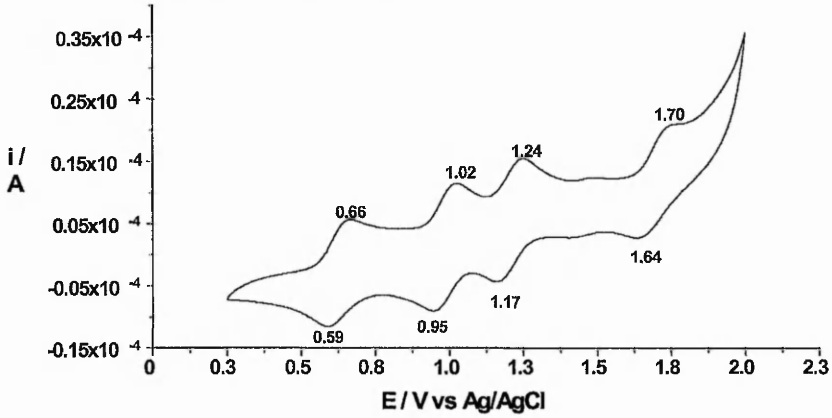

Figure 28 CV scan of $[Mn_4(\mathbf{L1}\text{-}H)_4](ClO_4)_4$ (**A1**). Scan rate = 100 mVs^{-1}.

The CV scans of $[Mn_4(\mathbf{L1}\text{-}H)_4](ClO_4)_4$ (**A1**) are consistent over the range 50 to 500 mV and indicates that the system has some reversibility (Fig. 28). Comparison of the potentials between the cathodic and anodic sweeps confirms reversibility with peak separation, ΔE_p between 60 and 70 mV (Table 1).

Table 1 Electrochemical data of $[Mn_4(\mathbf{L1}\text{-}H)_4](ClO_4)_4$ (**A1**) in MeCN.

Oxidation step	Cathiodic peak, E_{pc}/ V	Aniodic peak, E_{pa}/ V	ΔE_p / mV
1	0.66	0.59	70
2	1.02	0.95	70
3	1.24	1.17	70
4	1.70	1.64	60

Cathodic sweep DPV analysis shows the expected four peaks with similar intensities (Fig. 29). Also there is clear indication of a peak at approximately 1.4 V that is not particularly visible from the CV scan. The origins of this peak are unclear; the $[Zn_4(\mathbf{L1}\text{-}H)_4](ClO_4)_4$ (**A5**) assembly shows a single irreversible peak at 1.50 V in the CV scan that could possibly be observed here, however the peak observed in the CV scan appears to have some type of reversibility (Fig. 28). Also, this peak occurs in other electrochemically active species at different potentials discussed later in this chapter. Other authors have reported that small amounts of water present from crystallisation can be detected[80] (E_{pc} in acetonitrile ~ 1.45 V versus Ag/AgCl[81]), but further addition of water to the solution under investigation causes no increase in the peak at 1.42 V.

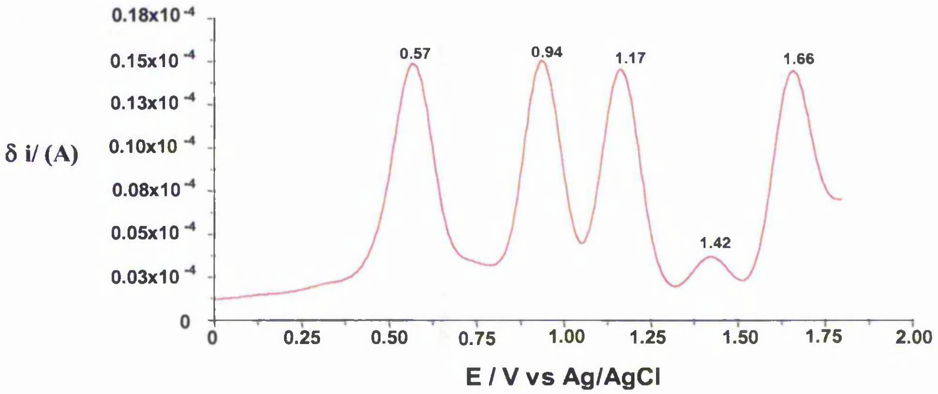

Figure 29 DPV of $[Mn_4(\mathbf{L1}\text{-}H)_4](ClO_4)_4$ (**A1**). Scan rate = 20 mV s^{-1}, oxidative sweep.

Further analysis using methodology set out by Taube[82] allows calculation of the comproportionation constant, K_c. This methodology assumes a reaction of type:

$$A \xrightarrow{n_1,\, E_1^0} B \xrightarrow{n_2,\, E_2^0} C \qquad (7)$$

The relationship of the concentrations of A and B to C at equilibrium is expressed by the comproportionation constant:

$$K_c = \frac{[B]^{n_1+n_2}}{[C]^{n_1}[A]^{n_2}} = e^{(\Delta E^0 n_1 n_2 F)/(RT)} \qquad (8)$$

Where ΔE^o is the change in standard potential of the step under investigation, F = Faraday constant. Thus for a one electron process $n_1 = n_2 = 1$ at 298 K, K_c is simplified to:

$$K_c = e^{\Delta E^0/25.69} \qquad (9)$$

ΔE^o is assumed to have the same value of $\Delta E_{1/2}$, the latter can be obtained from both CV and DPV analysis. The latter technique appears to be more favoured because of better resolution of the peaks with the simple conversion of E_p to $E_{1/2}$ *via*:

$$E_p = E_{1/2} - \frac{E_{pul}}{2} \qquad (10)$$

These values of K_c are similar to those reported for a number of di-phenoxide bridged complexes [$LM_2(\mu\text{-}O)_2$] complexes (M = Mn, Cu) with values in order of $10^{10\text{-}11}$ and 10^6 respectively (Table 2).[83] The values obtained here indicate reasonable stability of the mixed valent species however, whether the peak between the last two pairs of peaks at 1.42 V is causing a chemical change in solution is unclear. This may make the comparison of the $Mn(II)Mn(III)_3$ species unreasonable.

Table 2 Comproportionation constants for mixed oxidation Mn(II)Mn(III) species.

Species	$\Delta E_{1/2}$/ mV	Comproportionation constant, K_c
$Mn(II)_3Mn(III)$	370	1.8×10^6
$Mn(II)_2Mn(III)_2$	230	7.7×10^3
$Mn(II)\ Mn(III)_3$	490	1.9×10^8

The $[Co_4(\mathbf{L1}\text{-}H)_4](ClO_4)_4$ (**A4**) spectrum is not consistent with varying sweep rates between 50 and 500 mV with the first two peaks becoming more broad and shifting in position with increasing scan rate (Fig. 30). Examination between the cathodic and anodic sweeps at 100 mVs^{-1} indicates that the first two peaks have large separations of 90 and 130 mV (Table 3). This is caused by slow exchange of the oxidant/ reductant at the surface electrode and is termed quasi reversible. The latter two peaks are reversible (ΔE_p = 60-70 mV) with a K_c value of 8.3×10^5, which was obtained from DPV analysis.

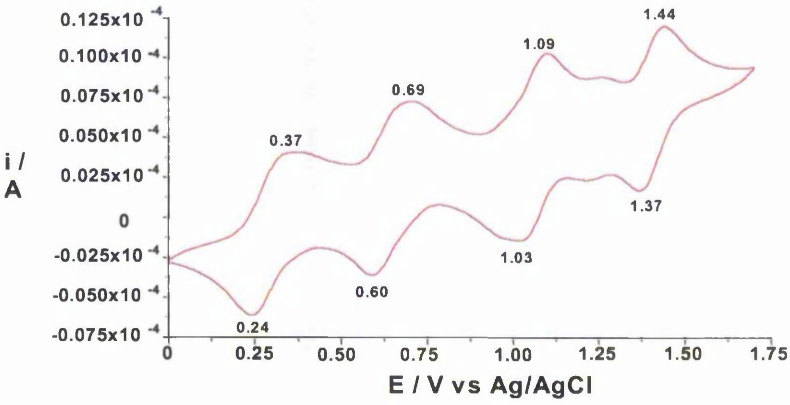

Figure 30 CV of $[Co_4(\mathbf{L1}\text{-}H)_4](ClO_4)_4$ (**A4**) at 100 mVs^{-1}.

There is a distinct shift in potential from ~ 1.5 V in $[Mn_4(\mathbf{L1}\text{-}H)_4](ClO_4)_4$ (**A1**) to ~ 1.2 V in $[Co_4(\mathbf{L1}\text{-}H)_4](ClO_4)_4$ of the unidentifiable peak. This may be associated with a ligand oxidation process that would obviously shift depending on the nature of the metal ion to which it was bound.

Table 3 Electrochemical data for $[Co_4(\mathbf{L1}\text{-}H)_4](ClO_4)_4$ (**A4**) in MeCN at 100 mVs^{-1}.

Oxidation step	E_{pc}/ V	E_{pa}/ V	ΔE_p / mV
1	0.37	0.24	130
2	0.69	0.60	90
3	1.09	1.03	60
4	1.44	1.37	70

The CV of $[Fe_4(\mathbf{L1}\text{-}H)_4](ClO_4)_4$ shows four near reversible waves (peak separation, (ΔE_p = 60-70 mV, Table 4). Examination of the CV shows that the peaks are not particularly well defined with a number of shoulders present (Fig. 31). This is likely to be caused by a mixture of minor species in solution that are evident from the ESI-MS spectrum.

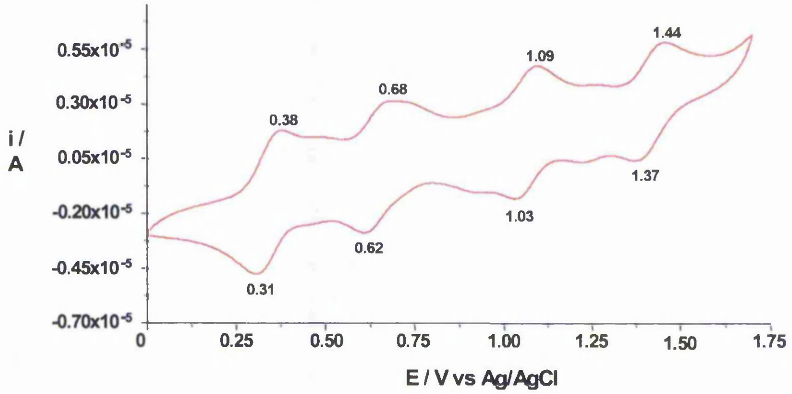

Figure 31 CV of $[Fe_4(\mathbf{L1}\text{-}H)_4](ClO_4)_4$ at 100 mVs^{-1}.

Table 4 Electrochemical data of $[Fe_4(\mathbf{L1}\text{-}H)_4](ClO_4)_4$ in MeCN at 100 mVs^{-1}.

Oxidation step	E_{pc}/ V	E_{pa}/ V	ΔE_p / mV
1	0.38	0.31	70
2	0.68	0.62	60
3	1.09	1.03	60
4	1.44	1.37	70

The Fe(III) (**A5**) motif displays very interesting electrochemical behaviour. The CV shows six reasonably reversible waves (peak separation, ΔE_p = 50-80 mV, Table 5) between 0.4 and 1.47 V on the cathodic sweep in approximately 2:1:1:1:1:2 ratio of peak area (Fig. 32). The spectrum is consistent over a range of sweep rates from 50 to 500 mV. Attempts to hold the sample at a negative potential before running the scan give exactly the same results.

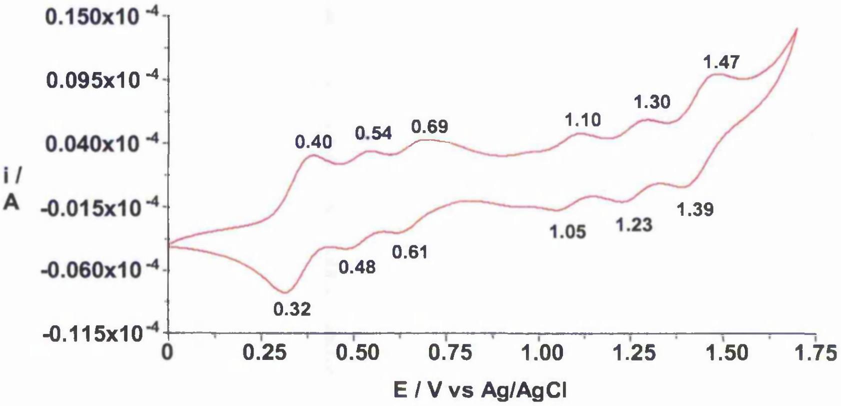

Figure 32 CV of **A5** at 100 mVs^{-1}.

Assignment of these processes has been unsuccessful, but it is most likely that there is a mixture of species present in solution, which is supported by ESI-MS. Also it is currently thought that the Fe(III) motif might be adopting different ligand configurations in solution, but still has a $Fe_4(\mu\text{-}O)_4$ core. To overcome this problem, another source of Fe(III) was used, the results of this are discussed later.

Table 5 Electrochemical data of **A5** in MeCN at 100 mVs^{-1}

Oxidation step	E_{pc}/ V	E_{pa}/ V	ΔE_p / mV
1	0.40	0.32	80
2	0.54	0.48	60
3	0.69	0.61	80
4	1.10	1.05	50
5	1.30	1.23	70
6	1.47	1.39	80

UV and visible spectroscopy ranging from 190-1100 nm can identify electronic transitions between weakly bonded species with certain transitions being indicative of a particular metal ion.[84] All spectra were recorded in acetonitrile at concentrations between 10^{-3} and 10^{-5} mol dm^{-3} for visible and UV regions, respectively. Those recorded in the UV region were dominated by metal to ligand charge transfer bands (MLCT) at 190-500 nm. Therefore the following section will be concerned with *d-d* transitions that occur in the visible range from 500 to 1100 nm. Both Mn(II) and Zn(II) have half and full *d* orbitals respectively and thus do not exhibit any *d-d* transitions.

The Cu(II) assembly (**A2**) shows a single absorption at approximately 757 nm (ε = 341 dm^3 mol^{-1} cm^{-1}). This absorption is typical of Cu(II) complex, however interpretation of this is not straightforward even though only one electron is involved. This is because of the low level of symmetry of the Cu(II) environment and the broad peak observed is likely to be a mixture of overlapping transitions.[85]

Octahedral Ni(II) complexes generally exhibit three spin allowed transitions that are expected for a d^8 ion ranging from approximately 350 to 1100 nm. In the case of [Ni$_4$(**L1**-H)$_4$](ClO$_4$)$_4$ (**A3**) only two peaks are observed at about 600 and 924 nm (ε = 249 dm^3 mol^{-1} cm^{-1}) with the former being a shoulder. These transitions are assigned as $^3A_{2g}\rightarrow{}^3T_{1g}(F)$ and $^3A_{2g}\rightarrow{}^3T_{2g}$ respectively. This is in accord with that for an octahedral Ni(II) species with one peak being completely hidden underneath the MLCT.[85]

The Co(II) assembly (**A4**) shows only a shoulder at approximately 600 nm which is in accord with a d^7 ion in an octahedral geometry with the transition being associated with ${}^4T_{1g}(F) \rightarrow {}^4T_{1g}(P)$. There can be a further absorbance at a higher wavelength associated with ${}^4T_{1g}(F) \rightarrow {}^4T_{2g}$ transition, which is not observed for this assembly.[85]

The iron assemblies show very similar spectra that are dominated in the region of ~600 nm by low energy charge transfer absorptions. The Fe(II) assembly has a shorter wavelength, ~ 520 nm, than the Fe(III) assembly, ~ 600 nm. These absorptions are in accord with similar species reported in the literature.[38]

3.2 Solid-State Studies

In most cases the crystals obtained from the initial reaction solutions were not suitable for single crystal X-ray analysis except in the case of $[Mn_4(\mathbf{L1}\text{-H})_4](OTf)_4$ (**A1**). Recrystallisation from n-propanol, methanol and acetonitrile yielded large crystals suitable for single crystal analysis in all cases. Examination of these crystals demonstrated that the [2 x 2] motif had been formed; however there appeared to be a problem with most of the structures. It was soon discovered that in most cases two of the ligands were disordered causing large errors in the final refinements of the structures. This disorder is created by the ligand adopting different configurations around each metal centre so that there are mixtures of N_{bipy}/N_{bipy}, $N_{bipy}/N_{py/\,diazine}$ and $N_{py/\,diazine}/N_{py/\,diazine}$ coordination pockets. Consequently, in the solid-state there are a variety of different structural isomers, with two possibilities presented in Fig. 33. The most common type of geometry is that observed in Fig. 33 where each metal ion has its coordination geometry made up from one N_{bipy} and one $N_{py/\,diazine}$. The disorder means that there are numerous bond lengths and angles, however the following structural discussion will be limited to the most common geometry to allow structural comparisons.

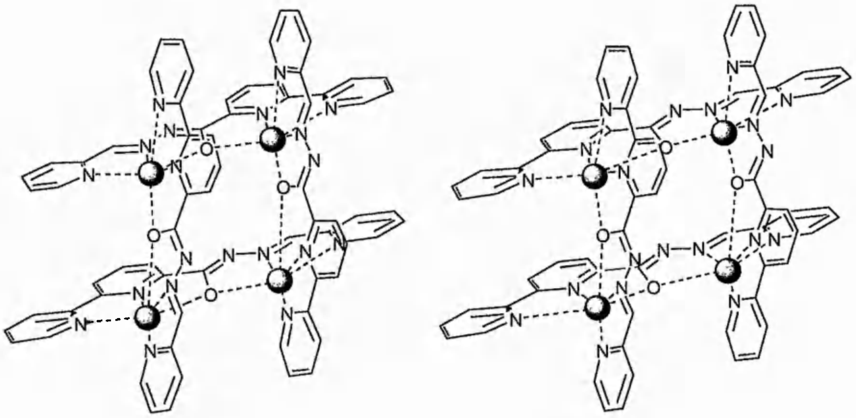

Figure 33 Schematic representations of different geometry configurations in homonuclear [2 x 2] grids. Note: NH_2 groups have been omitted for clarity.

As expected the structures are very similar and the discussion will be limited to a selected example of $[Mn_4(\mathbf{L1}\text{-}H)_4](OTf)_4$ **(A1)** followed by a number of generalisations common to each assembly.

The $[Mn_4(\mathbf{L1}\text{-}H)_4]^{+4}$ cation is shown in Fig. 34 without any ligand disorder and relevant bond angles and distances are given in Tables 6 and 7, respectively. The cation is made up from four parallel sets of ligands that coordinate in two distinct sets above and below the mean plane of Mn(II) ions. The ligands stack in a head-to-toe fashion so that the bipy rings are opposed by py rings and *vice-versa*. The cation has an overall size of approximately 13.6 x 13.6 Å, with aromatic ring separation < 4.0 Å suggesting π-π interactions which is typical of grid like structures.[4,61] Surrounding the central cation are the expected four triflate anions, some disordered, and a number of water molecules.

Removal of the bulk of the organic structure reveals the alkoxide bridged metal core with metal-metal separations of Mn1-Mn2, 3.90 Å; Mn2-Mn3, 3.88 Å; Mn3-Mn4, 3.88 Å; and Mn4-Mn1, 3.92 Å (Fig. 34). Each Mn(II) centre has its coordination environment made from two alkoxy donors and four nitrogen donors in a distorted *cis*-N_4O_2 octahedral environment. Further investigation of the bond angles around the Mn(II) centres indicate that each distorted octahedral environment has a basal plane composed of two terminal N_{py} and two alkoxy donors, which lie within the same plane of the grid-like array.

Table 6 Selected bond angles/ ° of $[Mn_4(\mathbf{L1}\text{-}H)_4]^{+4}$ cation.

O41B-Mn1-N3	118.5(6)	N5-Mn2-N63B	168.1(7)	O21-Mn3-N21	144.0(3)
O41B-Mn1-N45B	74.5(7)	O61B-Mn2-N6	96.0(6)	N23-Mn3-N21	71.9(3)
N3-Mn1-N45B	166.9(5)	O1-Mn2-N6	143.6(2)	O61B-Mn3-N21	97.3(6)
O41B-Mn1-O1	94.7(13)	N5-Mn2-N6	71.3(3)	N66B-Mn3-N21	96.5(10)
N3-Mn1-O1	71.4(2)	N63B-Mn2-N6	97.7(8)	N65B-Mn3-N21	107.8(9)
N45B-Mn1-O1	107.3(8)	O61B-Mn2-N61B	140.0(7)	O21-Mn4-N25	72.7(3)
O41B-Mn1-N46B	145.1(8)	O1-Mn2-N61B	96.2(6)	O21-Mn4-O41B	94.4(10)
N3-Mn1-N46B	96.0(6)	N5-Mn2-N61B	109.1(5)	N25-Mn4-O41B	109.3(7)
N45B-Mn1-N46B	70.9(7)	N63B-Mn2-N61B	66.8(7)	O21-Mn4-N26	143.5(3)
O1-Mn1-N46B	91.6(8)	N6-Mn2-N61B	96.9(6)	N25-Mn4-N26	70.8(3)
O41B-Mn1-N1	96.9(12)	O21-Mn3-N23	72.4(3)	O41B-Mn4-N26	97.5(13)
N3-Mn1-N1	70.7(2)	O21-Mn3-O61B	93.7(7)	O21-Mn4-N43B	119.0(10)
N45B-Mn1-N1	111.3(8)	N23-Mn3-O61B	114.9(6)	N25-Mn4-N43B	167.7(10)
O1-Mn1-N1	141.4(2)	O21-Mn3-N66B	93.3(10)	O41B-Mn4-N43B	68.1(7)
N46B-Mn1-N1	99.3(9)	N23-Mn3-N66B	99.2(7)	N26-Mn4-N43B	97.4(11)
O61B-Mn2-O1	95.5(7)	O61B-Mn3-N66B	145.7(9)	O21-Mn4-N41B	97.6(6)
O61B-Mn2-N5	110.9(6)	O21-Mn3-N65B	108.2(9)	N25-Mn4-N41B	114.5(4)
O1-Mn2-N5	72.3(2)	N23-Mn3-N65B	172.9(6)	O41B-Mn4-N41B	136.2(8)
O61B-Mn2-N63B	74.0(8)	O61B-Mn3-N65B	72.1(8)	N26-Mn4-N41B	97.3(6)
O1-Mn2-N63B	118.7(8)	N66B-Mn3-N65B	73.8(9)	N43B-Mn4-N41B	69.3(6)

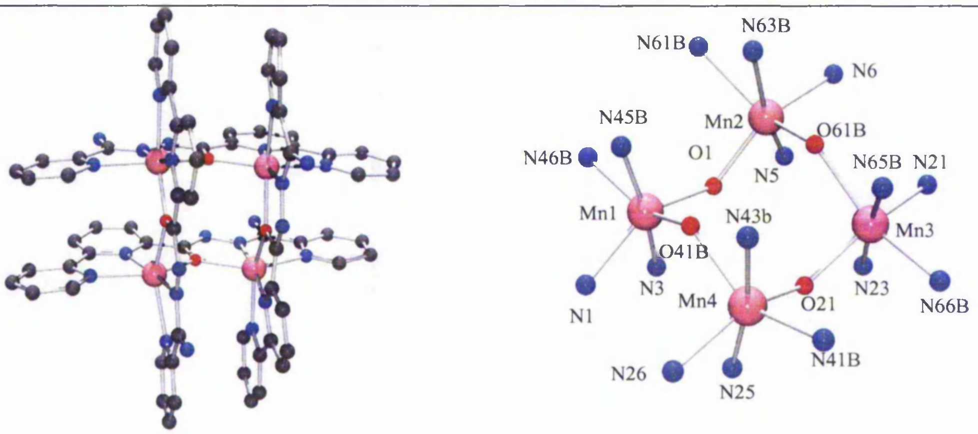

Figure 34 POV-Ray representation of $[Mn_4(\mathbf{L1}\text{-}H)_4]^{+4}$ cation and $Mn_4(\mu\text{-}O_4)$ inner core.

Table 7 Selected bond lengths of $[Mn_4(\mathbf{L1}\text{-}H)_4]^{+4}$ cation including all disordered sites/ Å.

Mn1-N43A	2.12(2)	Mn2-N65A	2.110(18)	Mn3-N63A	2.09(2)	Mn4-O41A	2.11(3)
Mn1-O41B	2.13(3)	Mn2-O61B	2.15(2)	Mn3-O61A	2.113(19)	Mn4-N45A	2.13(2)
Mn1-N3	2.162(7)	Mn2-O1	2.160(5)	Mn3-O21	2.158(5)	Mn4-O21	2.158(6)
Mn1-O41A	2.18(3)	Mn2-N5	2.175(7)	Mn3-N23	2.163(9)	Mn4-N25	2.225(8)
Mn1-N45B	2.18(2)	Mn2-O61A	2.187(19)	Mn3-O61B	2.19(2)	Mn4-N46A	2.233(16)
Mn1-O1	2.184(4)	Mn2-N66A	2.195(14)	Mn3-N66B	2.21(2)	Mn4-O41B	2.25(3)
Mn1-N46B	2.227(18)	Mn2-N63B	2.27(2)	Mn3-N65B	2.26(2)	Mn4-N26	2.265(7)
Mn1-N1	2.296(6)	Mn2-N6	2.310(6)	Mn3-N21	2.301(7)	Mn4-N43B	2.30(2)
Mn1-N41A	2.379(17)	Mn2-N61B	2.447(16)	Mn3-N61A	2.383(18)	Mn4-N41B	2.407(16)

The following discussion about bond lengths will only be concerned with those formed around the two ordered ligands (Table 7). Each Mn(II) ion is in a similar geometry with axial contacts to N_{py} and $N_{diazine}$ ranging from 2.162(7) to 2.30(2) Å and longer N_{py} equatorial contacts ranging from 2.227(18) to 2.447(16) Å which could be associated with the rigidity of the ligand. Two alkoxy donors fall into the range 2.13(3) to 2.25(3) Å, completing the remaining coordination and create a bond angle between each Mn(II) centre with an average value of 127°. The Mn(II) bond lengths are unextraordinary and can be rationalised in terms of ligand restraint rather than any metal ion coordination preference.

From examination of the Mn(II) (**A1**), Cu(II) (**A2**), Ni(II) (**A3**), Co(II) (**A4**) and Zn(II) (**A6**) structures formed there are a number of similar structural properties:

(1). The most favoured ligand configuration is that where each metal ion receives one tridentate N_{bipy} and one tridentate $N_{py/\ diazine}$ chelating sub-unit.

(2). The average size of the cations is approximately 13.6 x 13.6 Å.

(3). The ligands stack in a head-to-toe fashion with π-π separations < 4.0 Å.

(4). The $M_4(\mu^2\text{-}O)_4$ core gives small metal-metal separations less than 4.1 Å with averages Mn(II) = 3.90 Å, Cu(II) = 4.06 Å, Ni(II) = 3.94 Å, Co(II) = 3.92 Å and Zn(II) = 3.92 Å

(5). Angles formed between adjacent metal centres around the alkoxide bridges have a value ~ 134° with averages in accord with their metal-metal separations, Mn(II) = 127°, Cu(II) = 140°, Ni(II) = 137°, Co(II) = 134° and Zn(II) = 133°.

(6). Torsion angles between four metal ions have a range from 12.7° to 19.2° indicating that the grids are reasonably flat.

(7). Each metal ion has a distorted octahedral *cis*-N_4O_2 coordination environment with the basal plane composed of two terminal N_{py} and two bridging alkoxy donors. The axial sites are composed from a mixture of N_{py} and $N_{diazine}$.

(8). The bond lengths appear to show very little variation across the series of transition metal ions except for the Cu(II) assembly that is axially compressed due to the Jahn-Teller effect.

Table 8 Selected bond angles/ ° of $[Cu_4(\mathbf{L1}\text{-}H)_4]^{+4}$ cation.

N2-Cu1-N44	174.8(8)	O1-Cu2-N5	157.6(4)	N42-Cu3-N65	108.0(9)
N2-Cu1-O41	98.3(7)	N4-Cu2-O21	112.6(14)	N64-Cu3-N65	76.0(6)
N44-Cu1-O41	80.2(5)	N22-Cu2-O21	72.8(4)	O41-Cu3-N65	92.8(5)
N2-Cu1-N45	103.3(7)	O1-Cu2-O21	94.1(4)	O61-Cu3-N65	154.0(4)
N44-Cu1-N45	78.5(5)	N5-Cu2-O21	87.1(5)	N41-Cu3-N65	92.9(6)
O41-Cu1-N45	158.4(4)	N4-Cu2-N21	98.8(14)	N62-Cu4-N24	177.2(14)
N2-Cu1-N1	77.9(5)	N22-Cu2-N21	75.8(5)	N62-Cu4-N25	103.7(14)
N44-Cu1-N1	97.1(7)	O1-Cu2-N21	92.6(5)	N24-Cu4-N25	79.1(5)
O41-Cu1-N1	90.1(5)	N5-Cu2-N21	98.0(5)	N62-Cu4-O21	98.0(14)
N45-Cu1-N1	96.4(5)	O21-Cu2-N21	148.6(5)	N24-Cu4-O21	79.2(5)
N2-Cu1-O1	73.5(4)	N42-Cu3-N64	174.7(13)	N25-Cu4-O21	157.9(5)
N44-Cu1-O1	111.5(7)	N42-Cu3-O41	77.0(5)	N62-Cu4-N61	75.9(6)
O41-Cu1-O1	95.3(4)	N64-Cu3-O41	106.5(17)	N24-Cu4-N61	103.7(5)
N45-Cu1-O1	88.8(5)	N42-Cu3-O61	97.9(8)	N25-Cu4-N61	97.7(6)
N1-Cu1-O1	151.4(4)	N64-Cu3-O61	78.2(5)	O21-Cu4-N61	91.6(5)
N4-Cu2-N22	174.4(14)	O41-Cu3-O61	91.7(4)	N62-Cu4-O61	73.9(5)
N4-Cu2-O1	79.8(4)	N42-Cu3-N41	78.5(5)	N24-Cu4-O61	106.5(5)
N22-Cu2-O1	101.7(5)	N64-Cu3-N41	98.0(17)	N25-Cu4-O61	87.5(5)
N4-Cu2-N5	79.0(5)	O41-Cu3-N41	155.5(4)	O21-Cu4-O61	94.6(4)
N22-Cu2-N5	100.1(5)	O61-Cu3-N41	93.5(5)	N61-Cu4-O61	149.7(4)

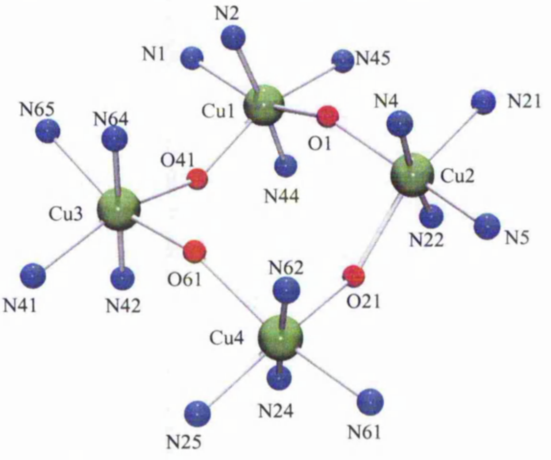

Figure 35 POV-Ray representation of $[Cu_4(\mathbf{L1}\text{-}H)_4]^{+4}$ inner core.

Table 9 Selected bond lengths/ Å of $[Cu_4(\mathbf{L1}\text{-}H)_4]^{+4}$ cation.

Cu1-N2	1.908(12)	Cu2-N4	1.889(12)	Cu3-N42	1.878(19)	Cu4-N24	1.907(12)
Cu1-N1	2.133(11)	Cu2-N5	2.057(11)	Cu3-O61	2.149(10)	Cu4-N25	2.092(12)
Cu1-O1	2.224(9)	Cu2-O1	2.060(9)	Cu3-N41	2.176(12)	Cu4-O21	2.083(10)
Cu1-N44	1.894(16)	Cu2-N22	1.910(12)	Cu3-O41	2.146(10)	Cu4-N62	1.92(2)
Cu1-N45	2.122(12)	Cu2-N21	2.249(14)	Cu3-N64	1.92(2)	Cu4-N61	2.248(13)
Cu1-O41	2.079(10)	Cu2-O21	2.261(10)	Cu3-N65	2.227(13)	Cu4-O61	2.271(10)

Table 10. Selected bond angles/ ° of $[Ni_4(\mathbf{L1}\text{-}H)_4]^{+4}$ cation.

O1-Ni1-N1	154.3(2)	N6-Ni2-O2	91.63(19)	N5-Ni2-O2	109.16(19)
O1-Ni1-O4	93.46(16)	N6-Ni2-N9	101.9(2)	N5-Ni2-N9	174.4(2)
O1-Ni1-N24	90.43(18)	O2-Ni2-N9	76.4(2)	N6-Ni2-N7	95.5(2)
N1-Ni1-O4	90.2(2)	O2-Ni3-N11	77.0(2)	O2-Ni2-N7	153.7(2)
N1-Ni1-N24	96.6(2)	O2-Ni3-O3	93.86(16)	N7-Ni2-N9	77.4(2)
N3-Ni1-N23	175.7(2)	O2-Ni3-N15	102.3(2)	O2-Ni3-N12	154.0(2)
O4-Ni1-N23	78.2(2)	N11-Ni3-O3	108.0(2)	O2-Ni3-N13	91.51(19)
N23-Ni1-N24	77.7(3)	N11-Ni3-N15	174.4(2)	N11-Ni3-N12	77.7(3)
O1-Ni1-N3	77.4(2)	N12-Ni3-N13	98.3(2)	N11-Ni3-N13	99.0(3)
O1-Ni1-N23	106.9(2)	O3-Ni3-N13	153.0(3)	N12-Ni3-O3	88.24(18)
N1-Ni1-N3	77.0(3)	N13-Ni3-N15	75.5(3)	N12-Ni3-N15	103.4(2)
N1-Ni1-N23	98.7(3)	O3-Ni4-N18	155.4(3)	O3-Ni3-N15	77.5(2)
N3-Ni1-O4	101.9(2)	O3-Ni4-N19	93.98(18)	O3-Ni4-N17	78.5(2)
N3-Ni1-N24	102.4(2)	N17-Ni4-N18	77.1(3)	O3-Ni4-O4	90.50(16)
O4-Ni1-N24	155.6(2)	N17-Ni4-N19	97.6(2)	O3-Ni4-N21	99.9(2)
O1-Ni2-N5	77.51(19)	N18-Ni4-O4	93.6(2)	N17-Ni4-O4	107.5(2)
O1-Ni2-N6	154.6(2)	N18-Ni4-N21	104.7(3)	N17-Ni4-N21	175.0(2)
O1-Ni2-N7	92.89(18)	O4-Ni4-N21	77.2(2)	N18-Ni4-N19	92.6(2)
N5-Ni2-N6	77.7(2)	O1-Ni2-O2	91.33(16)	O4-Ni4-N19	154.9(2)
N5-Ni2-N7	97.1(2)	O1-Ni2-N9	103.3(2)	N19-Ni4-N21	77.7(2)

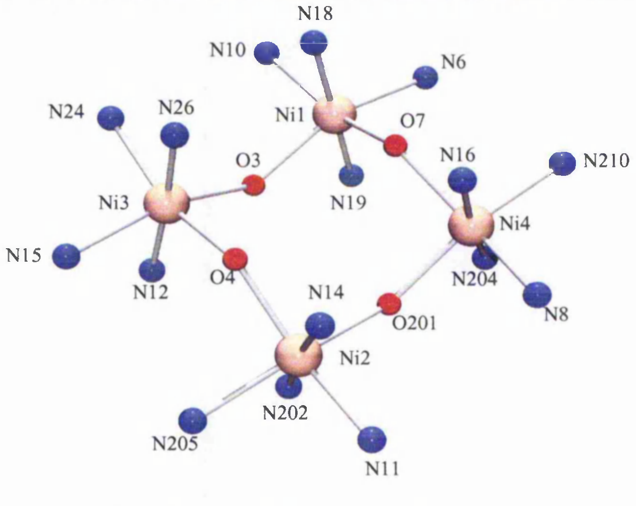

Figure 36 POV-Ray representation of $[Ni_4(\mathbf{L1}\text{-}H)_4]^{+4}$ inner core.

Table 11 Selected bond lengths/ Å of $[Ni_4(\mathbf{L1}\text{-}H)_4]^{+4}$ cation.

Ni1-O1	2.087(4)	Ni2-O1	2.110(4)	Ni3-O2	2.092(4)	Ni4-O3	2.121(4)
Ni1-N3	1.965(6)	Ni2-N6	2.121(6)	Ni3-N12	2.091(5)	Ni4-N18	2.139(7)
Ni1-N23	1.972(6)	Ni2-N7	2.125(5)	Ni3-N13	2.170(6)	Ni4-N19	2.108(6)
Ni1-N1	2.145(6)	Ni2-N5	1.980(6)	Ni3-N11	1.986(6)	Ni4-N17	1.961(6)
Ni1-O4	2.113(4)	Ni2-O2	2.123(4)	Ni3-O3	2.134(4)	Ni4-O4	2.101(4)
Ni1-N24	2.117(5)	Ni2-N9	1.966(6)	Ni3-N15	1.965(6)	Ni4-N21	1.966(6)

Table 12 Selected bond angles/ ° of $[Co_4(\mathbf{L1}\text{-H})_4]^{+4}$ cation.

O1-Co1-N1	151.2(4)	N6-Co2-O2	94.3(4)	N10-Co3-N12	75.0(4)		
O1-Co1-O4	94.9(3)	N6-Co2-N8	95.5(5)	N10-Co3-N13	102.9(4)		
O1-Co1-N24	93.8(4)	O2-Co2-N8	75.2(4)	N12-Co3-O3	91.0(4)		
N1-Co1-O4	88.2(4)	O1-Co2-O2	93.2(3)	N12-Co3-N14	99.7(5)		
N1-Co1-N24	98.0(4)	O1-Co2-N8	113.4(4)	O3-Co3-N14	75.8(4)		
N2-Co1-N22	172.1(5)	N4-Co2-O2	108.6(5)	O3-Co4-N18	151.8(4)		
O4-Co1-N22	75.2(4)	N4-Co2-N8	170.7(4)	O3-Co4-N19	94.0(4)		
N22-Co1-N24	74.4(5)	N6-Co2-N7	95.9(4)	N16-Co4-N18	75.8(4)		
O1-Co1-N2	75.6(4)	O2-Co2-N7	149.4(4)	N16-Co4-N19	107.8(5)		
O1-Co1-N22	101.7(4)	N7-Co2-N8	75.2(4)	N18-Co4-O4	94.7(4)		
N1-Co1-N2	76.8(5)	O2-Co3-N10	75.0(3)	N18-Co4-N20	99.2(4)		
N1-Co1-N22	106.7(5)	O2-Co3-O3	96.0(3)	O4-Co4-N20	76.8(4)		
N2-Co1-O4	112.2(4)	O2-Co3-N14	110.3(4)	O3-Co4-N16	76.2(3)		
N2-Co1-N24	98.2(5)	N10-Co3-O3	104.9(4)	O3-Co4-O4	93.7(3)		
O4-Co1-N24	149.5(5)	N10-Co3-N14	174.7(5)	O3-Co4-N20	108.9(4)		
O1-Co2-N4	75.3(4)	N12-Co3-N13	97.1(4)	N16-Co4-O4	101.1(4)		
O1-Co2-N6	151.2(4)	O3-Co3-N13	152.2(4)	N16-Co4-N20	174.5(4)		
O1-Co2-N7	91.6(4)	N13-Co3-N14	76.7(4)	N18-Co4-N19	91.4(4)		
N4-Co2-N6	75.9(4)	O2-Co3-N12	150.0(4)	O4-Co4-N19	151.1(4)		
N4-Co2-N7	101.8(5)	O2-Co3-N13	90.1(4)	N19-Co4-N20	74.4(4)		

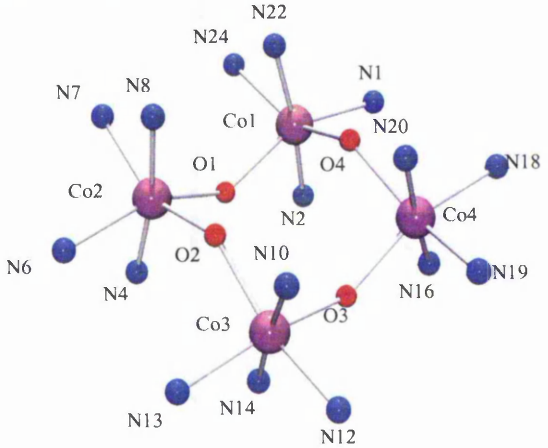

Figure 37 POV-Ray representation of $[Co_4(\mathbf{L1}\text{-H})_4]^{+4}$ inner core.

Table 13 Selected bond lengths/ Å for $[Co_4(\mathbf{L1}\text{-H})_4]^{+4}$ cation.

Co1-O1	2.119(8)	Co2-O1	2.149(9)	Co3-O2	2.113(9)	Co4-O3	2.098(8)
Co1-N2	2.020(13)	Co2-N6	2.207(10)	Co3-N12	2.192(11)	Co4-N18	2.176(10)
Co1-N22	2.009(13)	Co2-N7	2.167(10)	Co3-N13	2.166(10)	Co4-N19	2.191(11)
Co1-N1	2.127(11)	Co2-N4	1.973(12)	Co3-N10	2.022(11)	Co4-N16	2.007(11)
Co-O4	2.139(8)	Co2-O2	2.109(8)	Co3-O3	2.119(8)	Co4-O4	2.137(8)
Co1N24	2.214(12)	Co2-N8	2.062(11)	Co3-N14	2.020(11)	Co4-N20	2.027(11)

Table 14 Selected bond angles/ ° for $[Zn_4(\mathbf{L1}\text{-}H)_4]^{+4}$ cation.

N21-Zn1-N5	173	N3-Zn2-N17	173	N15-Zn3-N11	173	N9-Zn4-O2	75
N21-Zn1-O4	74	N3-Zn2-O1	74	N15-Zn3-O2	103	N9-Zn4-N23	172
N21-Zn1-O1	105	N3-Zn2-O3	105	N15-Zn3-O3	73	N9-Zn4-O4	106
N21-Zn1-N6	104	N3-Zn2-N18	104	N15-Zn3-N12	105	N9-Zn4-N24	105
N21-Zn1-N19	75	N3-Zn2-N1	76	N15-Zn3-N13	74	N9-Zn4-N7	76
N5-Zn1-O4	113	N17-Zn2-O1	113	N11-Zn3-O2	75	O2-Zn4-N23	113
N5-Zn1-O1	74	N17-Zn2-O3	74	N11-Zn3-O3	114	O2-Zn4-O4	93
N5-Zn1-N6	77	N17-Zn2-N18	77	N11-Zn3-N12	77	O2-Zn4-N24	91
N5-Zn1-N19	97	N17-Zn2-N1	97	N11-Zn3-N13	99	O2-Zn4-N7	151
O4-Zn1-O1	96	O1-Zn2-O3	96	O2-Zn3-O3	95	N23-Zn4-O4	73
O4-Zn1-N6	92	O1-Zn2-N18	94	O2-Zn3-N12	152	N23-Zn4-N24	77
O4-Zn1-N19	149	O1-Zn2-N1	150	O2-Zn3-N13	93	N23-Zn4-N7	96
O1-Zn1-N6	151	O3-Zn2-N18	151	O3-Zn3-N12	90	O4-Zn4-N24	149
O1-Zn1-N19	89	O3-Zn2-N1	92	O3-Zn3-N13	147	O4-Zn4-N7	94
N6-Zn1-N19	99	N18-Zn2-N1	94	N12-Zn3-N13	98	N24-Zn4-N7	97

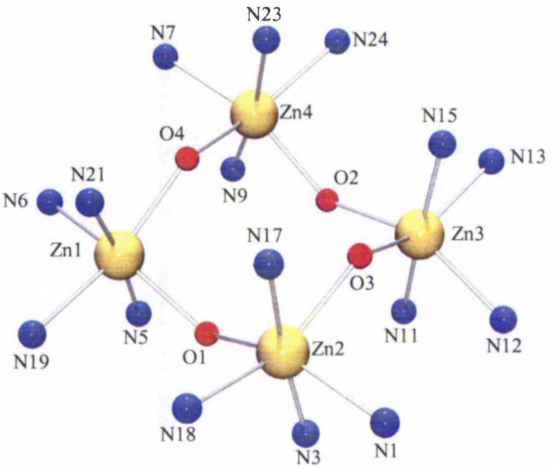

Figure 38 POV-Ray representation of $Zn_4(\mu^2\text{-}O)_4$ core.

Table 15 Selected bond lengths/ Å for $[Zn_4(\mathbf{L1}\text{-}H)_4]^{+4}$ cation.

Zn1-N21	2.02	Zn2-N3	1.98	Zn3-N15	2.03	Zn4-N9	1.97
Zn1-N5	2.08	Zn2-N17	2.09	Zn3-N11	2.04	Zn4-O2	2.11
Zn1-O4	2.11	Zn2-O1	2.13	Zn3-O2	2.14	Zn4-N23	2.12
Zn1-O1	2.14	Zn2-O3	2.17	Zn3-O3	2.16	Zn4-O4	2.14
Zn1-N6	2.21	Zn2-N18	2.21	Zn3-N12	2.19	Zn4-N24	2.20
Zn1-N19	2.24	Zn2-N1	2.23	Zn3-N13	2.25	Zn4-N7	2.25

From the literature examples previously discussed a number of comparisons can be made. The [2 x 2] grids, $[M_4(L(F))_4X_4]^{+4}$, of Thompson and Matthews[4c] have virtually identical metal ion geometries considering all the factors mentioned above. Obviously when comparing to heterocyclic bridged [2 x 2] grids the separations between metal centres are considerably larger than those observed here. For example grids reported by Lehn[41], Brooker[46] and Glass[54] have separation of approximately 6.6, 7.1 and 8.5 Å, respectively. Lehn's phenoxide bridged, $[Cu_4(L(E)\text{-}H)_4](PF_6)_4$ [44b], has metal-metal separations and bond angles around 4.1 Å and 141° respectively that are similar to the analogous Cu(II) motif prepared here. Considering the information obtained from the crystallography here and that reported in the literature, there appears to be very little deviation between the structures.

No crystals suitable for X-ray diffraction were ever obtained for the Fe(II) motif and from a combination of characterisation techniques it is suggested that the sample is likely to be a combination of various mixed oxidation Fe(II) and Fe(III) [2 x 2] grids. Attempts to overcome this by preparation with ascorbic acid and addition of the ligand to a methalonic solution of the $Fe(BF_4)_2{\cdot}6H_2O$ followed by immediate collection of the precipitate gave samples that appeared to be impure as suggested by ESI-MS, CV and chemical analysis. Consequently, no further discussion will be concerned with these samples.

*$[Fe_4(\mathbf{L1}\text{-}H)_4](ClO_4)_6$ (**A5**)*

Examination of the structure indicated that the cation was not disordered and surrounded by six anions along with water and acetonitrile molecules. Considering the evidence provided by X-ray crystallography, ESI-MS, variable temperature magnetisation studies (Page 100) and chemical analysis results, this assembly is assigned as being an $Fe(II)_2Fe(III)_2$ mixed oxidation [2 x 2] grid. The cation has an external dimension of approximately 13.6 x 13.6 Å and π-π separations < 4.0 Å. Close examination of the central cation shows a stark difference from the other [2 x 2] grids discussed previously. There are two distinct iron coordination environments; Fe2 and Fe4 have two N_{bipy} tridentate donors and Fe1 and Fe3 receive two $N_{py/\ diazine}$ tridentate donors (Fig. 39).

Table 16 Bond angles/ ° for Fe(II)/ Fe(III) ions in [Fe$_4$(**L1**-H)$_4$]$^{+6}$ cation.

O1-Fe1-N1	151.1(3)	N6-Fe2-N18	93.8(3)	N13-Fe3-N15	74.1(4)
O1-Fe1-O2	93.9(3)	O3-Fe2-N18	148.8(3)	N13-Fe3-N19	92.6(3)
O1-Fe1-N9	109.9(3)	O1-Fe2-N5	74.1(3)	N15-Fe3-O4	113.0(3)
N1-Fe1-O2	93.2(3)	O1-Fe2-O3	96.5(3)	N15-Fe3-N21	170.8(3)
N1-Fe1-N9	99.0(3)	O1-Fe2-N18	95.4(3)	O4-Fe3-N21	75.6(3)
N3-Fe1-N7	102.3(3)	N5-Fe2-O3	110.7(3)	O2-Fe4-N12	150.1(3)
O2-Fe1-N7	149.6(3)	N5-Fe2-N18	100.3(4)	O2-Fe4-N23	114.4(3)
N7-Fe1-N9	74.8(3)	N6-Fe2-N17	101.1(4)	N11-Fe4-N12	75.1(4)
O1-Fe1-N3	76.0(3)	O3-Fe2-N17	74.4(3)	N11-Fe4-N23	170.4(3)
O1-Fe1-N7	91.6(3)	N17-Fe2-N18	74.4(4)	N12-Fe4-O4	91.0(3)
N1-Fe1-N3	75.1(3)	O3-Fe3-N13	150.1(3)	N12-Fe4-N24	95.9(3)
N1-Fe1-N7	96.2(3)	O3-Fe3-O4	93.6(3)	O4-Fe4-N24	150.0(3)
N3-Fe1-O2	108.0(3)	O3-Fe3-N21	106.9(3)	O2-Fe4-N11	75.0(3)
N3-Fe1-N9	173.3(3)	N13-Fe3-O4	93.3(3)	O2-Fe4-O4	96.7(3)
O2-Fe1-N9	75.2(3)	N13-Fe3-N21	103.0(3)	O2-Fe4-N24	91.8(3)
O1-Fe2-N6	148.3(3)	N15-Fe3-N19	97.0(3)	N11-Fe4-O4	106.6(3)
O1-Fe2-N17	110.6(3)	O4-Fe3-N19	149.9(3)	N11-Fe4-N24	103.4(3)
N5-Fe2-N6	74.4(4)	N19-Fe3-N21	74.3(3)	N12-Fe4-N23	95.5(3)
N5-Fe2-N17	172.9(3)	O3-Fe3-N15	76.4(3)	O4-Fe4-N23	75.0(3)
N6-Fe2-O3	91.0(3)	O3-Fe3-N19	95.7(3)	N23-Fe4-N24	75.3(3)

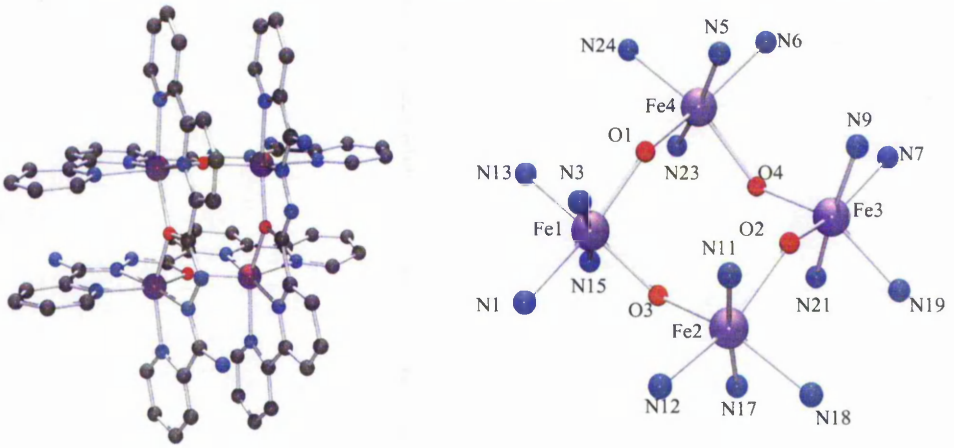

Figure 39 Left: POV-Ray representation of Fe(II)$_2$Fe(III)$_2$ cation and right POV-Ray representation of Fe(II)$_2$Fe(III)$_2$ inner core.

Table 17 Bond lengths/ Å of mixed oxidation Fe(II)$_2$Fe(III)$_2$ assembly.

Fe1-O1	2.025(7)	Fe2-O1	2.174(7)	Fe3-O3	2.008(7)	Fe4-O2	2.154(7)
Fe1-N3	1.995(8)	Fe2-N6	2.187(10)	Fe3-N15	2.012(9)	Fe4-N12	2.188(9)
Fe1-N7	2.131(8)	Fe2-N17	2.097(9)	Fe3-N19	2.136(9)	Fe4-N23	2.092(8)
Fe1-N1	2.150(9)	Fe2-N5	2.106(9)	Fe3-N13	2.143(9)	Fe4-N11	2.079(9)
Fe1-O2	2.007(7)	Fe2-O3	2.191(7)	Fe3-O4	2.008(7)	Fe4-O4	2.170(7)
Fe1-N9	2.025(8)	Fe2-N18	2.204(10)	Fe3-N21	2.020(8)	Fe4-N24	2.168(9)

The ligand configuration could explain the origins of the mixed oxidation state species. Initially in solution the formation of the most stable chelate would take place and this is tentatively assigned as being the corner piece type structure (Fig. 40) with the Fe(III) coordination environment made up from two tridentate N_{bipy} donors. Following this, two possible mechanisms are proposed; the binding of a second Fe(III) ion in the $N_{py/\ diazine}$ pocket which is subsequently reduced either by the diazine group or other species present in solution. Self-assembly with an equivalent unit would yield the structure observed (Fig. 40). Alternatively, due to the relative inertness of Fe(III) binding of this cation in the $N_{py/\ diazine}$ might be unfavourable. However, two corner pieces could combine simultaneously if they encountered two labile Fe(II) ions that have formed in solution. This configuration appears to be unstable in solution as indicated by ESI-MS and electrochemical studies, however solid-state studies indicate one structural type. This result is further supported by a series of heterometallic [2 x 2] grids with the same ligand configuration and the same solution instability, which are discussed in chapter 4.

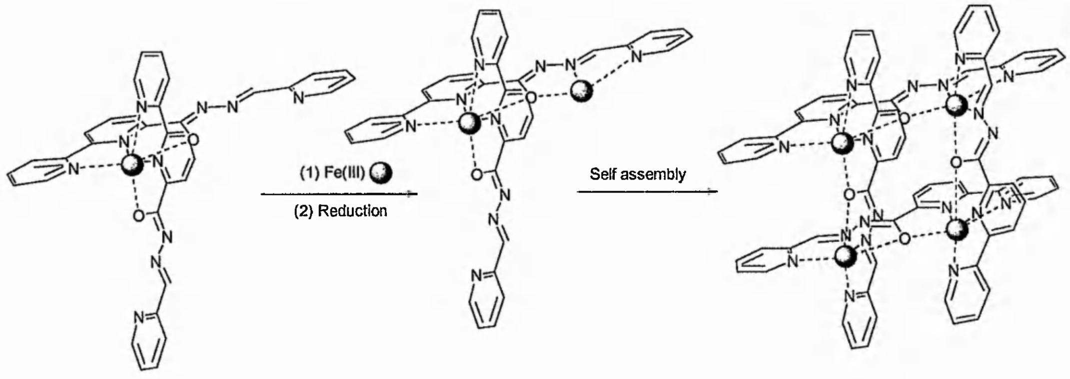

Figure 40 Possible mechanism for the formation of the mixed Fe(II)$_2$Fe(III)$_2$ grid.

Analysis of the central core shows that each iron centre has a distorted octahedral *cis*-N_4O_2 geometry. The basal plane of the distorted octahedron is assigned as being in the same plane as the alkoxide bridged iron core. Therefore Fe1 has its basal plane is made up from N1, N13, O1 and O3. The geometries of the metal ions appear to be restrained by the ligand and from crystallographic evidence no assignment can be made to a particular oxidation state. Thus the assignment is made according to the self-assembly process observed for the heterometallic structures in chapter 4 rather than any other evidence.

Attempts to use $Fe(III)(NO_3)_3$ in place of $Fe(III)(ClO_4)_3$ yielded a completely different structure. Reaction of $Fe(III)(NO_3)_3$ with **L1** in water followed by the addition of methanol gave a dark brown solution that yielded crystals upon standing for a period of 14 days along with a small amount of lightly coloured powder, which dissolved upon further standing. The dark orange crystals were only obtained in a low yield (28 %) and the structure of the cation is not the expected grid motif but a mononuclear species that contains a seven coordinate Fe(III) ion (Fig. 41). The ligand appears to have been cleaved between the carbonyl and diazine bond by the nucleophilic attack of water, giving 2,2'-bipyridine-6-carboxylate and pyridyl-2-amidrazone (Fig. 42). The later of these could have been the pale powder observed briefly as a precipitate. The ligand hydrolysis could also be facilitated by the protonation of the terminal pyridyl ring by the acidic $Fe(III)(NO_3)_3$ consequently stopping this group from further binding. Similar ligands have also been reported to undergo this type of reduction when reacted with $Fe(III)(NO_3)_3$.[38] In addition, the occupance of the Fe(III) ion in the N_{bipy} pockets supports the assignment of the metal ions in $[Fe(II)_2Fe(III)_2(\mathbf{L1}\text{-}H)_4](ClO_4)_6$.

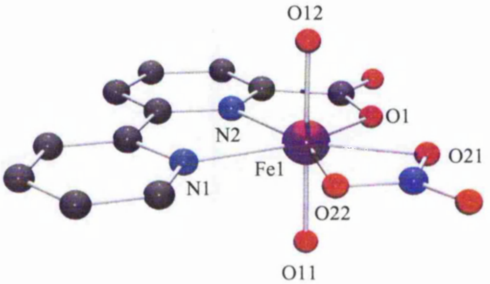

Figure 41 POV-Ray representation of $Fe(6\text{-carboxylate-}2,2'\text{-bipyridine})(H_2O)_2(NO_3)$.

Table 18 Bond lengths/ Å and angles/ ° for $[Fe(6\text{-carboxylate-}2,2'\text{-bipyridine})(H_2O)_2(NO_3)](NO)_3$.

Fe1-N1	2.221(3)	O12-Fe1-O11	175.54(9)	O11-Fe1-O22	88.57(9)
Fe1-N2	2.121(3)	O12-Fe1-O1	94.70(10)	O1-Fe1-O22	132.69(9)
Fe1-O1	2.067(2)	O11-Fe1-O1	88.52(10)	N2-Fe1-O22	152.57(10)
Fe1-O11	2.003(3)	O12-Fe1-N2	90.55(10)	O21-Fe1-O22	59.54(9)
Fe1-O12	2.001(3)	O11-Fe1-N2	93.27(10)	O12-Fe1-N1	91.49(10)
Fe1-O21	2.142(2)	O1-Fe1-N2	74.73(10)	O11-Fe1-N1	87.47(11)
Fe1-O22	2.160(2)	O12-Fe1-O21	87.39(10)	O1-Fe1-N1	146.82(9)
		O11-Fe1-O21	90.59(10)	N2-Fe1-N1	72.64(10)
		O1-Fe1-O21	73.29(9)	O21-Fe1-N1	139.65(9)
		N2-Fe1-O21	147.66(10)	O22-Fe1-N1	80.12(9)
		O12-Fe1-O22	86.98(10)		

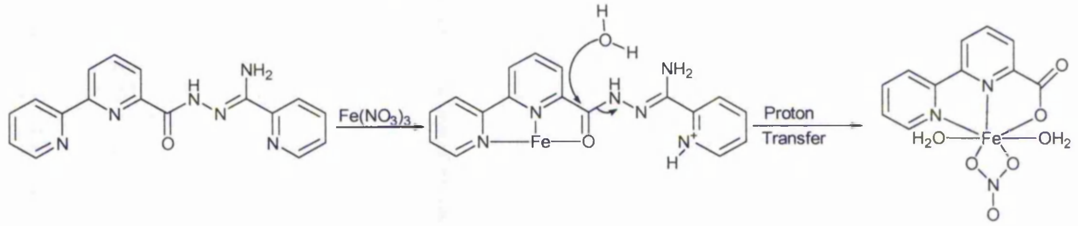

Figure 42 Fe(III)$(NO_3)_3$ catalytic hydrolysis of **L1**.

Magnetism

Variable temperature magnetic susceptibility measurements were made on powdered samples of the previously discussed homometallic [2 x 2] grids except the Zn(II) assembly that is purely diamagnetic. The raw data obtained from the SQUID were manipulated to give values of χ'_m that have been diamagnetically corrected for both sample holder and organic components of the structure. Determination of the magnitude of the exchange integral can be achieved by modelling the susceptibility data, which requires the use of a suitable Hamiltonian expression (11). In the case of a [2 x 2] grid, the geometry is similar to a square (D_{4h}) or distorted square (D_{2d}) with two exchange integrals 2*J*1 and 2*J*2 for the sides and 2*J*3 to represent any diagonal interaction (Fig. 43).[4c]

$$H_{ex} = -2J1\{S_2 \cdot S_3 + S_1 \cdot S_4\} - 2J2\{S_1 \cdot S_2 + S_3 \cdot S_4\} - 2J3\{S_1 \cdot S_3 + S_2 \cdot S_4\} \quad (11)$$

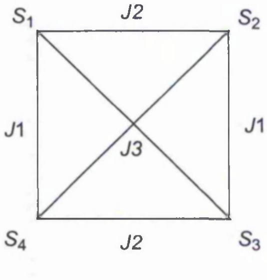

Figure 43 Exchange model for a tetranuclear square.

A number of simplifications can be made to the model; the diagonal term *J*3 can be set to zero because it is assumed that there is very little interaction *via* such a long pathway and it is also assumed that each [2 x 2] grid is a perfect square thus, *J*1 = *J*2. Using this symmetry (D_{4h}) along with the addition rules of spin-vector coupling[14] each of the energy terms can be calculated at a particular temperature. Substituting the appropriate energy term in to the van Vleck[12] equation gives a value of χ_m at a particular temperature. During this thesis, this was achieved by initially using a program called ow0L that calculates the energy spectrum according to the inputted model.[86] This is then opened by a separate program, MAGMUN, which performs fitting of the data in accord with the van Vleck equation taking in to account TIP, paramagnetic impurities and Wiess like corrections.[86] Also MAGMUN takes in to account the standard deviation of the value of χ_m and outputs a goodness of fit (10^2 R) between 0 and 100 with values closer to zero being the better fit (12).

$$R = \left(\frac{\sum(\chi_{obsd} - \chi_{calcd})^2}{\sum \chi_{obsd}^{\ 2}} \right)^{1/2} \qquad (12)$$

The following discussion will deal with the magnetic properties of each assembly.

*[Mn$_4$(**L1**-H)$_4$](OTf)$_4$* (**A1**)

The room temperature value of effective magnetic moment of 10.9 μb is in approximate agreement with 11.8 μb for four spin only Mn(II) centres. Close examination of the T versus χ_m plot shows a steady increase in magnetic susceptibility with decreasing temperature with a sharp shoulder at approximately 30 K that is indicative of antiferromagnetic exchange (Fig. 45). This exchange process is expected when the M-O-M bond angles are large (~ 127 °) and consequently promotes Anderson antiferromagnetic behaviour. Following this decrease in magnetic susceptibility there is a sharp increase at ~ 10 K, which is indicative of a substantial paramagnetic impurity.

Modelling of the data between 300 and 5 K as a tetranuclear square with four spins of S = 5/2 and only one exchange integral yields a reasonable fit of the data with 10^2 R = 0.97. Values of g = 1.97 and J = -3.79 cm^{-1} are similar to that reported for other Mn(II) square motifs linked *via* alkoxy bridges with large Mn-O-Mn bond angles (Fig 46).[4c] TIP is set at zero for an Mn(II) system in octahedral geometry in accord with other examples in the literature[4] and θ also set at zero demonstrating that there is no intermolecular exchange, *i.e.*, all the magnetism is derived from within the individual assemblies. Of interest, is that the fitting of the low temperature data relies on the inclusion of a rather large value of paramagnetic impurity, $\rho = 0.015$, when compared to other values in the literature, typically, $\rho \sim 0.0001$.[4c] This could be associated with the sample being slightly impure or maybe a different type of exchange mechanism occurring at low temperatures.

*$[Cu_4(\mathbf{L1}\text{-}H)_4](ClO_4)_4$ (**A2**)*

Initial investigation of this sample *via* a T versus $\chi_m T$ shows an almost horizontal line that would indicate very little exchange (Fig. 45). Consequently the data obtained is fitted to the Curie-Weiss law that only assumes very weak intermolecular interactions. Thus a plot of χ^{-1} versus T yields a straight line with $C = 0.35$ cm^{3}mol^{-1}K and $\theta = -4.91$ K, these values are similar to other uncoupled Cu(II) species.[44b] Structural considerations can be used to explain why there is insignificant coupling. Each of the Cu(II) ions are axially Jahn-Tellar compressed and therefore the one unpaired electron resides in the d_{z^2} that points axially. As a result the unpaired electrons are orthogonal to the superexchange pathway provided by the alkoxy bridges (Fig. 44).

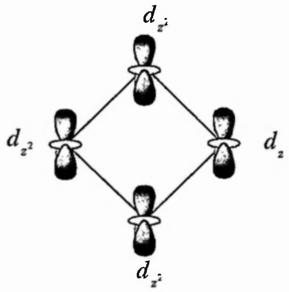

Figure 44 Proposed arrangement of magnetic orbital in $[Cu_4(\mathbf{L1}\text{-}H)_4](ClO_4)_4$ (**A2**).

*$[Ni_4(\mathbf{L1}\text{-}H)_4](ClO_4)_4$ (**A3**)*

The room temperature effective magnetic moment of 5.66 μ_b is in excellent agreement with 5.66 μ_b for four spin only Ni(II) centres. Examination of the T versus χ_m plot shows a steady increase of magnetic susceptibility with decreasing temperature followed by a sharp turn downwards at approximately 30 K that is

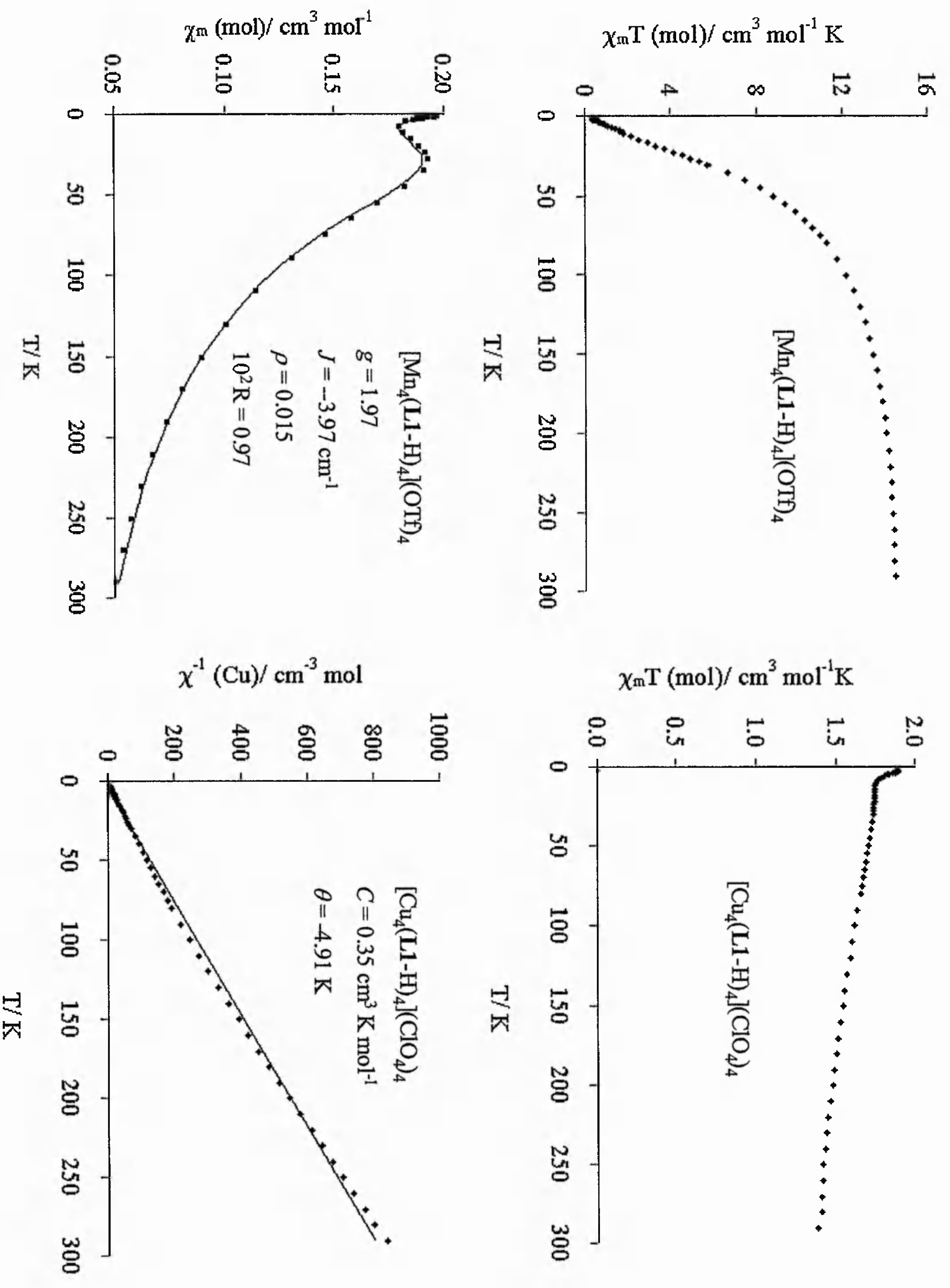

Figure 45 Top right: **A1** demonstrating antiferromagnetic behaviour, top left: fit for **A1**, bottom right: **A2** displaying little intramolecular exchange and bottom left: Curie plot for **A2**. Note: In all examples squares = experimental and solid line = calculated.

indicative of intramolecular antiferromagnetic exchange (Fig. 46). This process would be expected as with **(A1)** because of the large Ni-O-Ni bond angles ~ 137°.

Fitting of the data as a tetranuclear square between 300 and 5 K with four spin values of $S = 1$ and only one exchange integral gives a reasonable fit of the data with $10^2R = 1.28$. The values $g = 2.14$ and $J = -8.71$ cm^{-1} are in accord with previously reported alkoxide bridged Ni(II) tetranuclear grids (Fig 46).[4c,47] The inclusion of other parameters, particularly TIP that is regularly included for Ni(II) assemblies[87] only reduced the quality of the fit. The inclusion of zero field splitting, *D*, cannot be modelled with the programs available, but has been quoted as an important parameter by other authors and may reflect the reasonable fit of the data.[11]

*$[Co_4($**L1**$-H)_4](ClO_4)_4$ (**A4**)*

Variable temperature magnetic studies on a powdered sample of the Co(II) grid indicate a decrease in effective magnetic moment with decreasing temperature from 7.24 μ_b at 300 K down to 3.5 μ_b at 1.92 K (Fig. 47). The room temperature value is rather low for four spin only Co(II) (~ 7.7 μ_b). Furthermore, the intrinsic spin orbit contribution associated with octahedral Co(II) should increase the experimental value even higher. Why such a low value is observed is unclear, it may be due to the presence of low spin Co(II) with $S = 1/2$ that has been observed in pyridazine Schiff base macrocycles.[88] Attempts to model the data with various combinations of $S = 1/2$ and $S = 3/2$ do not yield reasonable results.

*$[Fe(II)_2Fe(III)_2($**L1**$-H)_4](ClO_4)_6$ (**A5**)*

Upon cooling the sample in a homogeneous magnetic field there is a steady decrease in effective magnetic moment with temperature from 9.62 μ_b at 300 K down to 3.51 at 1.8 K (Fig. 46). The room temperature value of 9.62 μ_b is in broad agreement with two $S = 5/2$ and two $S = 2$ spins, $\mu_{eff} = 10.86$ μ_b. The behaviour observed is typical of these grid systems because of the large M-O-M bond angles that in this case promote antiferromagnetic interactions.

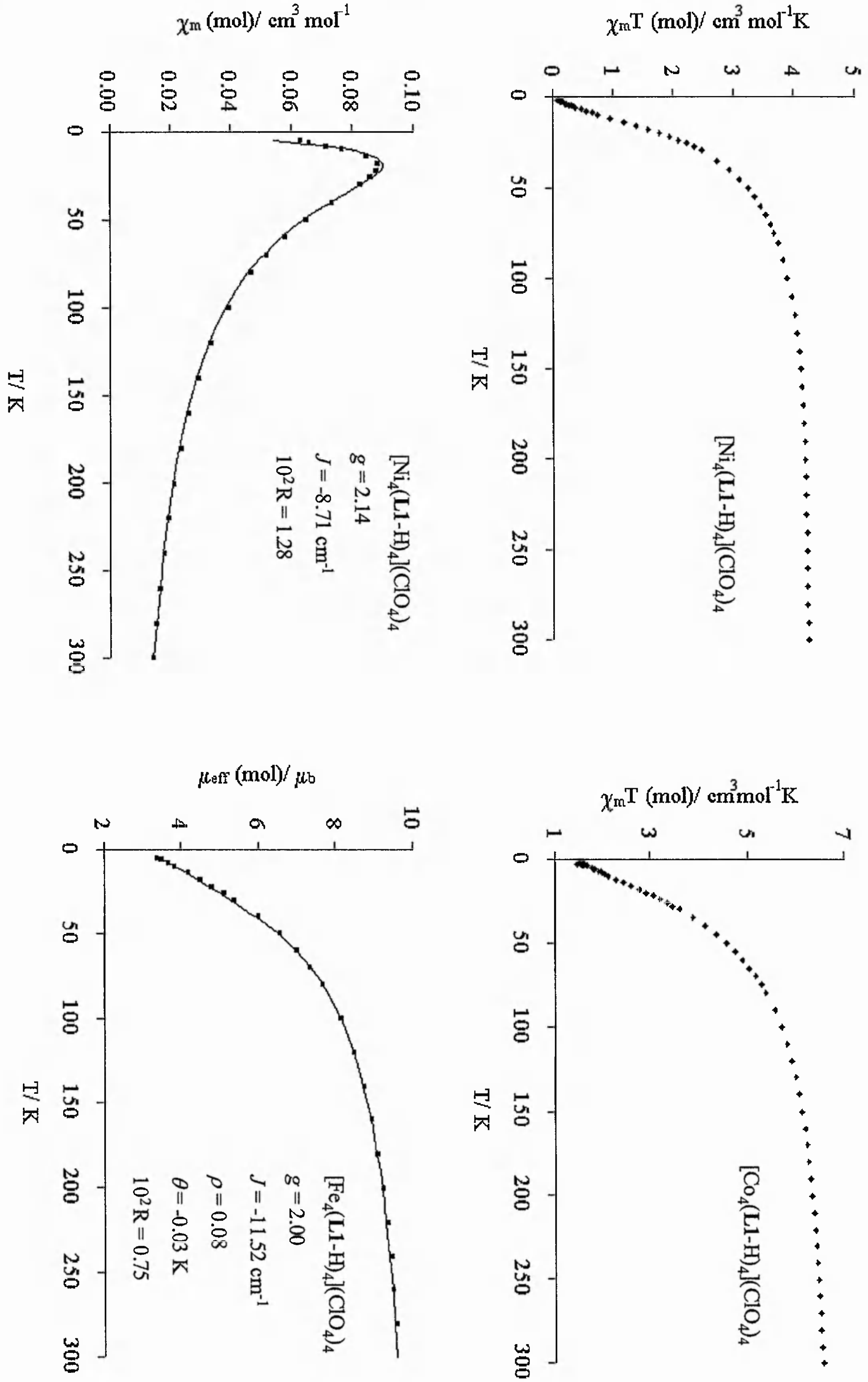

Figure 46 Top right: **A3** displaying antiferromagnetic behaviour, top right: **A3** fit, bottom right: **A4** exhibiting antiferromagnetic behaviour and bottom left: fit for mixed oxidation $Fe(II)_2Fe(III)_2$ grid (**A5**).

Fitting of the experimental data between 300 and 5 K as a tetranuclear square with spins of $S = 5/2$ and $S = 2$ assuming that both Fe(II) are high spin which is likely in this type of system yields a good correlation. However, this does require the inclusion of a rather large paramagnetic impurity, which could represent the impure nature of the sample or may indicate some zero-field splitting is occurring that is common in the case of iron assemblies.[23] Fitting gave the following parameters; $g = 2.00$, $J = -11.52$ cm^{-1}, $\rho = 0.08$, $\theta = -0.03$ K and 10^2 R = 0.75 (Fig. 46).

Comparing the data obtained here with similar motifs in the literature a number of similarities are observed in the cases of Mn(II) and Ni(II). For example the J values of -3.97 and -8.71 cm^{-1} respectively have similar values to those reported from Mn(II) and Ni(II) [2 x 2] grids reported by Thompson and Matthews, -2.85 and -13.60 cm^{-1} respectively.[4c] $[Co_4(\mathbf{L1}\text{-H})_4](ClO_4)_4$ does not appear to agree with any similar or even mononuclear assemblies reported in the literature, which generally have high g values associated with a spin-orbit coupling contribution. Lehn's phenoxide bridged Cu(II) [2 x 2] grid has comparable insignificant intramolecular exchange to the analogous motif observed here.[44b] Both of these have their magnetic properties explained in terms of the orientation of the relevant magnetic orbitals. The mixed valent iron grid provides an interesting example; there is a report of a similar mixed oxidation species with a thiolate bridge, however detailed variable temperature magnetisation studies are not reported.[53]

Other Metal Ions

L1 has shown its ability to form novel homometallic of [2 x 2] grids with various first row transition metal ions in the +2 oxidation state and one example of a mixed oxidation $Fe(II)_2Fe(III)_2$ has been observed. Incorporation of the inert Cr(III) has been attempted by firstly reducing $Cr(III)(ClO_4)_3$ to give the labile Cr(II), followed by self-assembly with the ligand and then oxidation back up to Cr(III).[85] An alternative route starting from $Cr(II)(OTf)_2$[89] has also been attempted. Both routes have yielded crystalline material, which have proven to be unsuitable for single crystal X-ray analysis. ESI-MS does not support the formation of a [2 x 2] grid, which could be a limitation of the technique.

The formation of a Mn(III) assembly is particularly attractive because compounds incorporating this ion regularly display SMM behaviour. This was attempted initially by using a direct source of Mn(III), $Mn(OAc)_3$, followed by addition of another anion to effect precipitation but no crystalline material could be obtained. Following this, methodology set out by Christou[90] was attempted. This starts with a Mn(II) salt which is then oxidised in solution with tetra(n-buty)lammonium permanganate (13). The ligand is then added and the solution allowed to stand, in this case it gave crystals that were unsuitable for X-ray analysis with no evidence from ESI-MS to support grid formation.

$$4\mathbf{L1} + 3.2\ Mn(ClO_4)_2 + 0.8\ KMnO_4 + 0.8\ NaClO_4 + \rightarrow [Mn(III)_4(\mathbf{L1}\text{-}H)_4](ClO_4)_8 \qquad (13)$$

3.3 Conclusion

The syntheses of a novel series of homometallic [2 x 2] grids have been reported and the compounds are characterised in both solution and the solid-state. Solution studies generally indicate grid stability, with some examples displaying reversible electronic communication between metal centres due to the nature of the bridging ligand. Solid-state characterisation generally shows high levels of ligand disorder making detailed discussion difficult, however the bond lengths and angles are typical of grid-like systems. The mixed oxidation $Fe(II)_2Fe(III)_2$ [2 x 2] grid is an interesting example indicating that serendipitous approach can play a role in the designed approach. This subsequently led to the formation of a mononuclear Fe(III) complex due to ligand hydrolysis which supports the assignment of the metal ions within $[Fe(II)_2Fe(III)_2(\mathbf{L1}\text{-}H)_4](ClO_4)_6$. The magnetic data obtained for each [2 x 2] grid are consistent with the structures observed demonstrating the ability of the designed approach to produce discrete assemblies with predictable intramolecular magnetic interactions.

Chapter Four

Heterometallic [2 x 2] Grids

4.0 Introduction

There are limited numbers of mixed metal grids reported in the literature,[42a, 4c] which is to be expected, because of the length and complexity of any synthetic strategy. Mixed metal systems are particularly attractive because of their potential to show both novel electrochemical and magnetic behaviour. There are no reports in the literature of a controlled mixed metal grid being formed by the addition of two labile transition metal ions with an octahedral coordination preference to a particular ligand. This strategy would probably yield various mixtures of homometallic and heterometallic grids. Lehn has used a logical approach to produce mixed metal grids as previously discussed in Chapter One, however this requires protection/ deprotection of the ligand, leading to a total of four synthetic steps. More importantly, the metal ions are diamagnetic and bridged by pyrimidine heterocycles giving long metal-metal separations (~ 6.6 Å).[42] Thompson and Matthews have reported a single example of a mixed $[Cu_3Fe(III)(L(F))_4(NO_3)]_2(ClO_4)_4(NO_3)_4$ assembly by reaction of a mononuclear Fe(III) species with $Cu(NO_3)_2$ which one would have expected to from a species in a 1:1 ratio of Cu(II) and Fe(III).[91a] This demonstrates that the starting complex is not stable enough and consequently scrambles in solution to form the assembly observed.

Synthetic Strategy

To reduce the number of synthetic steps and increase the stability of potential precursors, the Cr(III) ion was investigated. This cation is particularly inert with a water exchange rate constant of approximately 10^{-6} s^{-1} compared with 10^{-2} s^{-1} for Co(III) and 10^{10} s^{-1} for Cu(II).[85] Consequently, it was envisaged that when **L1** was reacted with Cr(III) under suitable conditions and the correct stoichiometry it could form a "corner piece" that would be stable under ambient conditions due to the relative inertness of Cr(III) (Fig. 47). The formation of the corner piece will be favoured by the unsymmetrical nature of **L1** which was designed to accommodate the single Cr(III) ion in the bipyridine tridentate pocket. Reaction of the corner piece under mild conditions with a suitably labile transition metal ion should yield a heterometallic grid in a controlled manner involving only two synthetic steps (Fig. 47).

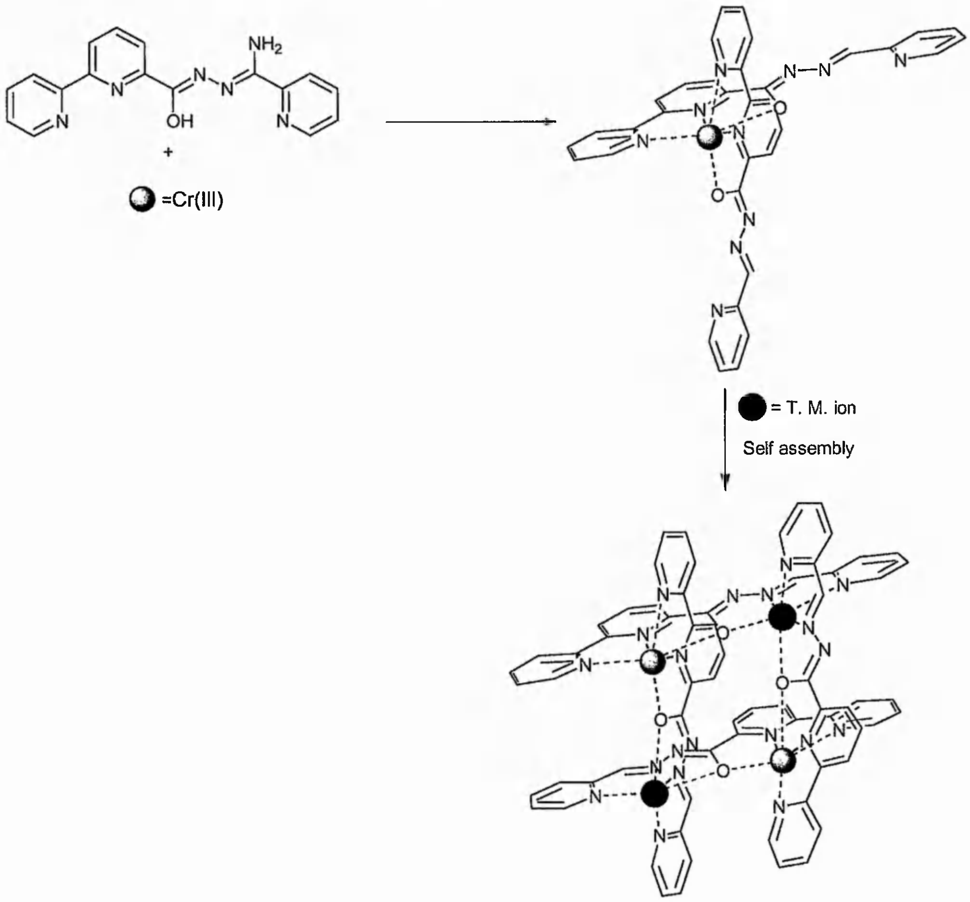

Figure 47 Controlled formation of the "corner piece" and controlled self-assembly to form a heterometallic [2 x 2] grid. Note: NH_2 groups have been omitted for clarity.

Synthesis: Corner Piece

Reaction of one equivalent $Cr(ClO_4)_3 \cdot 6H_2O$ with two equivalents of **L1** in methanol followed by maintaining at reflux overnight yielded a brown powder. Recrystallisation of the powder from a mixture of methanol and acetonitrile yielded crystals suitable for X-ray analysis.

4.1 Solid-State Studies: Corner Piece

The dimeric structure, Fig 48, is not fully refined however; it consists of two individual cations surrounded by a number of water, methanol and acetonitrile molecules and six perchlorate anions. Removal of these shows the two cations in a very similar arrangement to those observed with the homometallic [2 x 2] grids, however closer investigation indicates that there are only two metal ions present with an *anti* configuration with respect to each other (Fig. 48). The six anions present suggest that each Cr(III) is held in a formally neutral ligand. The two separate cations are held together by π-π stacking with the likelihood of hydrogen bonding between N donors and the protons, associated with neutral alkoxy bridge, within the vacant coordination pockets. Each Cr(III) ion is held in two tridentate N_{bipy} pockets suggesting this is the most stable chelate.

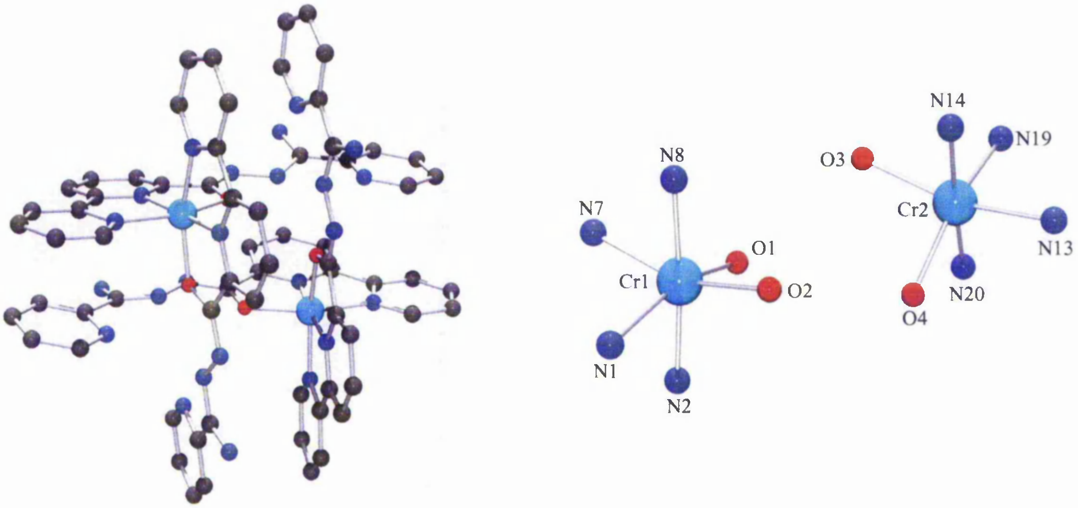

Figure 48 Right: POV-Ray representation of $[Cr_2(\mathbf{L1})_4]^{+6}$ cation and left: POV-Ray representation of $[Cr_2(\mathbf{L1})_4]^{+6}$ inner core.

Table 19 Selected bond angles/ ° and lengths/ Å for $[Cr_2(\mathbf{L1})_4]^{+6}$ cation.

O1-Cr1-N2	80	O4-Cr2-O3	93	Cr1-O1	1.97
O1-Cr1-N8	105	O4-Cr2-N14	105	Cr1-N2	1.98
O1-Cr1-O2	93	O4-Cr2-N20	79	Cr1-N8	1.98
O1-Cr1-N7	90	O4-Cr2-N19	157	Cr1-O2	1.98
O1-Cr1-N1	158	O4-Cr2-N13	92	Cr1-N7	2.04
N2-Cr1-N8	175	O3-Cr2-N14	80	Cr1-N1	2.10
N2-Cr1-O2	102	O3-Cr2-N20	101	Cr2-O4	1.97
N2-Cr1-N7	100	O3-Cr2-N19	92	Cr2-O3	1.98
N2-Cr1-N1	78	O3-Cr2-N13	157	Cr2-N14	1.98
N8-Cr1-O2	79	N14-Cr2-N20	176	Cr2-N20	1.99
N8-Cr1-N7	78	N14-Cr2-N19	98	Cr2-N19	2.08
N8-Cr1-N1	97	N14-Cr2-N13	77	Cr2-N13	2.08
O2-Cr1-N7	158	N20-Cr2-N19	78		
O2-Cr1-N1	93	N20-Cr2-N13	102		
N7-Cr1-N1	92	N19-Cr2-N13	92		

Removal of the bulk of organic ligand yields the inner core with the distorted octahedral *cis*-N_4O_2 Cr(III) ions separated by long through space distance of ~ 5.5 Å. Examination of the bond angles around the individual Cr(III) ions indicate that the basal plane consists of two terminal N_{py} donors and two bridging alkoxy donors. The bond lengths (Table 19) formed around each Cr(III) ion are not particularly interesting with a range between ~ 1.97 to ~ 1.99 Å for those contacts to either axial N_{py} or alkoxy bridges and slightly longer contacts to equatorial N_{py} ranging from ~ 2.04 to ~ 2.10 Å which is associated with the rigidity of the ligand (Table 19).

4.2 Solution Studies: Corner Piece

Further evidence for this motif is provided by ESI-MS in acetonitrile at cone voltages between 0 and 20 V. This displays a series of peaks that are associated with the successive loss of three perchlorate anions from the mononuclear species. As expected there are peaks associated with the dimer, which is observed in the solid state and in addition, there are a series of other peaks observed that are associated with higher geometric species with up to the decamer evident. No reversible electrochemical behaviour is observed in either acetonitrile or DMF over the range – 2 to 2 V, only a number of peaks at a negative potential associated with reduction of the ligand framework. Visible spectroscopy in acetonitrile between 500 to 1100 nm at 10^{-3} mol dm^{-3} only shows poorly resolved shoulders.

Complexation

Addition of the Cr(III) corner piece to an aqueous solution of the perchlorate salt of a labile first row transition metal ion, followed by a small amount of heat and the addition of acetonitrile yielded dark clear solutions. No base was added and upon standing the solutions yielded polycrystalline solids that were suitable for further analysis.

4.3 Solution Studies: Heterometallic [2 x 2] Grids

ESI-MS in acetonitrile of each sample at low cone voltages indicated the desired [2 x 2] motif present with an overall charge of +6; however a number of further peaks were observed some of which correspond to the starting corner piece. In addition, there is no evidence to suggest the formation of $[Cr_2Fe(III)_2(\mathbf{L1}\text{-}H)_4](ClO_4)_8$ assembly. On closer inspection of the spectrum there are a series of peaks that actually correspond to the Fe(II) species, $[Cr_2Fe(II)_2(\mathbf{L1}\text{-}H)_4](ClO_4)_6$, suggesting either the Fe(III) species is reduced in solution or even the Fe(III) ion is reduced before the self-assembly process. Interestingly, this reduction has also been observed in a mixed oxidation $Fe(II)_2Fe(III)_2$ homometallic [2 x 2] grid in Chapter Three with the Fe(II) ion again accommodated in the $N_{py/\ diazine}$ pocket.

Electrochemical studies in acetonitrile or DMF ranging from –2 to 2 V show no peaks associated with any reversible oxidation processes. A series of irreversible peaks is observed at a negative potential and are associated with functionalities present within the ligand framework.

Visible spectroscopy from 500 to 1100 nm in acetonitrile provides a small amount of evidence to suggest that labile transition metal ions are present. Both the Mn(II) and Zn(II) mixed metal assemblies show no further absorbances within the visible range due to their half/ full *d* orbitals respectively. Also, there are poorly resolved absorbances associated with Cr(III) in all cases and by comparison with the spectrum of the starting corner piece and the spectra of the homometallic [2 x 2] grids (Chapter Three) an assignment of the peaks associated with the labile transition metal ions has been made.

The Cu(II) assembly has one broad peak at 795 nm ($\varepsilon = 250$ dm^3 mol^{-1} cm^{-1}) that is difficult to assign to a particular transition due to the lack of symmetry associated with the normally highly distorted Cu(II) ion.[85] The absorbance observed is similar to that observed in the homonuclear [2 x 2] grid, 757 nm ($\varepsilon = 341$ dm^3 mol^{-1} cm^{-1}), with the shift associated with the different coordination geometries. The Ni(II) assembly shows a single absorbance at 944 ($\varepsilon = 162$ dm^3 mol^{-1} cm^{-1}) which is similar to that seen in the homonuclear species that has an absorbance at 924 ($\varepsilon = 249$ dm^3 mol^{-1} cm^{-1}). The absorbance is assigned as with the homometallic grid for the transition $^3A_{2g} \rightarrow {}^3T_{1g}(F)$. The Co(II) assembly shows no absorbances within the visible range. This is not unexpected when the homonuclear species is examined that only displays a single shoulder at ~ 600 nm. Both of the iron assemblies also show no absorbances in the visible range because any transitions are likely to be hidden under MLCT bands.[43, 78]

4.4 Solid-State Studies: Heterometallic [2 x 2] Grids

Only three out of the potential seven assemblies have been characterised by single crystal X-ray crystallography. The three that have been structurally characterised are $[Cr_2Mn_2(\mathbf{L1}\text{-H})_4](ClO_4)_6 \cdot 1.5H_2O$, $[Cr_2Cu_2(\mathbf{L1}\text{-H})_4](ClO_4)_6 \cdot 4H_2O \cdot 1/2MeCN$ and $[Cr_2Zn_2(\mathbf{L1}\text{-H})_4](ClO_4)_6 \cdot 3H_2O$. Attempts with the other labile first row transition metal ions did yield attractive looking crystals after recrystallisation, however these all gave poor data sets.

Investigation of these structures yielded a rather unexpected result. It was envisaged that due to the high inertness of the Cr(III) ion that no scrambling would occur in solution and thus the structures observed should not be disordered unlike the homometallic [2 x 2] grids. However, the heterometallic grids appear to be disordered. This would imply scrambling of the inert corner piece in solution and thus a mixture of products, but the crystal structure appears to contain the desired number of anions with the metal ions in the correct *anti* configuration. It is currently felt that the overall configuration of the metal ions is correct and it is suggested that the whole cation is rotationally disordered by a two-fold symmetry, which implies that the Cr(III) precursor has not scrambled in solution.[91b]

Structures: General

Removal of the disorder gives the desired cation surrounded by six perchlorate anions and a number of water and acetonitrile molecules. The number of perchlorate anions would suggest a formal charge of –1 on the ligand in accord with the homometallic [2 x 2] grids. Close examination of the cations indicates the desired metal binding coordination pockets have formed. Thus, there are two coordination pockets made up from two tridentate $N_{py/\ diazine}$ that contain the labile metal ion and another two made from two tridentate N_{bipy} donors that contain the inert Cr(III) ion (Fig. 49).

Table 20 Bond angles/ ° for $[Cr_2Mn_2(\mathbf{L1}\text{-}H)_4]^{+6}$ cation. Note any atoms labelled with _ are related by symmetry.

N5A-Cr1-N5A_	175	021_-Cr2-021	94	N23A-Mn1-N3A	176
N5A-Cr1-O1_a	105	021_-Cr2-N25A	104	N23A-Mn1-O1	110
N5A-Cr1-O1	79	021_-Cr2-N25A	78	N23A-Mn1-021	74
N5A-Cr1-N6	78	021_-Cr2-N26	90	N23A-Mn1-N21	71
N5A-Cr1-N6_a	99	021_-Cr2-N26_	157	N23A-Mn1-N1	106
N5A_-Cr1-O1_a	79	021-Cr2-N25A	78	N3A-Mn1-O1	72
N5A_-Cr1-O1	105	021-Cr2-N25A	104	N3A-Mn1-021	110
N5A_-Cr1-N6	99	021-Cr2-N26	157	N3A-Mn1-N21	105
N5A_-Cr1-N6_a	78	021-Cr2-N26_	90	N3A-Mn1-N1	72
O1_a-Cr1-O1	95	N25A-Cr2-N25A	177	O1-Mn1-021	93
O1_a-Cr1-N6	89	N25A-Cr2-N26	79	O1-Mn1-N21	98
O1_a-Cr1-N6_a	156	N25A-Cr2-N26_	99	O1-Mn1-N1	144
O1-Cr1-N6	156	N25A-Cr2-N26	99	021-Mn1-N21	144
O1-Cr1-N6_a	89	N25A-Cr2-N26_	79	021-Mn1-N1	97
N6-Cr1-N6_a	97	N26-Cr2-N26_	96	N21-Mn1-N1	93

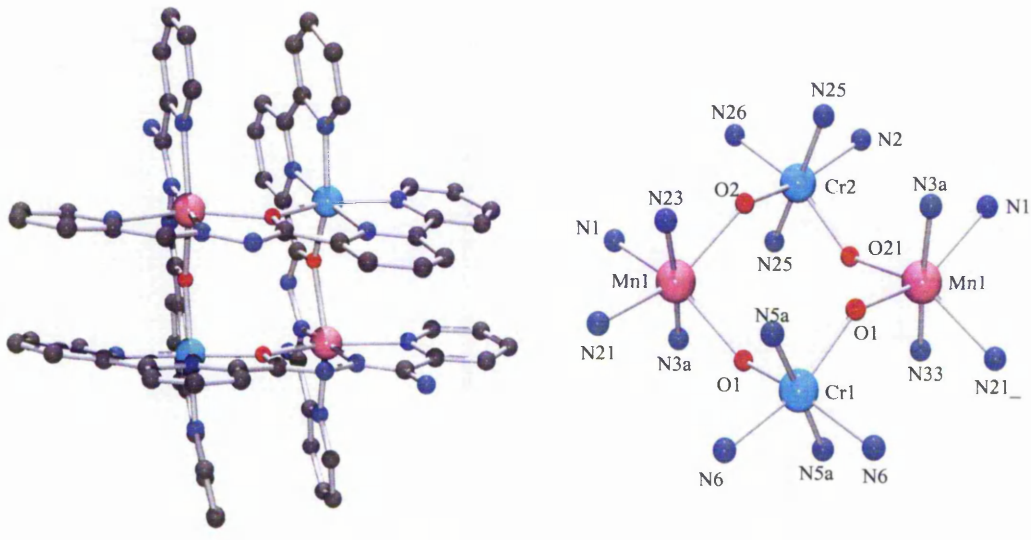

Figure 49 Left: POV-Ray representation of $[Cr_2Mn_2(\mathbf{L1}\text{-}H)_4]^{+6}$ cation and right: POV-Ray representation of $[Cr_2Mn_2(\mathbf{L1}\text{-}H)_4]^{+6}$ inner core.

Table 21 Bond distances/ Å for $[Cr_2Mn_2(\mathbf{L1}\text{-}H)_4]^{+6}$.

Cr1-N5A	1.96	Cr2-021_	2.00	Mn1-N23A	2.05
Cr1-N5A_	1.96	Cr2-021	2.00	Mn1-N3A	2.12
Cr1-O1_a	2.01	Cr2-N25A	2.05	Mn1-O1	2.24
Cr1-O1	2.01	Cr2-N25A	2.05	Mn1-021	2.25
Cr1-N6	2.07	Cr2-N26	2.07	Mn1-N21	2.28
Cr1-N6_a	2.07	Cr2-N26_	2.07	Mn1-N1	2.28

$[Cr_2Mn_2(\mathbf{L1}\text{-}H)_4](ClO_4)_6{\cdot}1.5H_2O$

The following structural discussion will be concerned with the Mn(II) assembly with all the disorder removed. The structure has *C2/c* space group thus each of the Mn(II) ions are crystallographically identical and the Cr(III) ions are symmetrical about the mean plane of the grid. The pairs of parallel ligands stack in a head-to-toe fashion with bipy rings opposed by pyridine rings and *visa versa.* This gives rise to close aromatic ring separations, < 4.1 Å, implying π-π interactions. The cation has a long dimension of approximately 13.6 Å and an internal dimension (*i.e.*, metal-metal separation) of ~ 3.91 x ~ 3.91 Å implying the central alkoxide bridged core is essentially a perfect square (Fig. 49).

Removal of the bulk of the organic ligand reveals the central coordination core of the cation (Fig. 49). Close examination of the bond angles around the Mn(II) centres and the Cr(III) centres suggest that the basal plane of the distorted octahedron consist of two alkoxy donors and two terminal N_{py} donors that are all in the mean plane of the grid. Bridging bond angles that separate the different ions, M-O-M, have an average value of ~ 134°. The Cr(III) ions have very similar geometry to that seen in the corner piece precursor with a general increase in distortion. This is likely to be associated with the ligands being more sterically strained to allow grid formation. The bond lengths around the single Mn(II) ion are unsurprising with slightly longer bonds to equatorial N_{py} probably due to ligand restraint.

From a combination of the three structures obtained a number of similarities are observed:

(1) Each labile first row transition metal ions has a coordination geometry made from two tridentate $N_{py/\ diazine}$ donors while the inert Cr(III) has two tridentate N_{bipy} donors.

(2) The cations have external dimensions of approximately 13.6 x 13.6 Å.

(3) Side by side aromatic rings of the ligands have π-π separations less than 4.1 Å.

(4) The $Cr_2M_2(\mu^2\text{-}O)_4$ cores have similar metal-metal separations with average $(\mu^2\text{-}O)_4$ values, Mn(II) = 3.91 Å, Cu(II) = 3.97 Å and Zn(II) = 4.01 Å.

(5) The angles formed between each metal ion *via* the alkoxide bridge have average values Mn(II) = 134°, Cu(II) = 138° and Zn(II) = 137°.

(6) The torsion angles around the plane of metal ions are reasonably flat particularly the Mn(II) and Zn(II) motif that have values of τ = 0° and τ = 0.7°, respectively. While the Cu(II) motif has a distortion of 11.1° which is still considerably smaller than that observed in the homometallic grid (19.2°).

(7) Each metal ion has a distorted octahedral geometry with the basal plane consisting of two terminal N_{py} donors and two alkoxy bridges all of which lie in the mean plane of the grid of metal ions.

(8) Bond lengths for the Cr(III) ion vary very little across the selected series indicating retention of configuration. The labile anions appear to have to adapt to the remaining coordination pockets. The $Cr(III)_2Cu(II)_2$ assembly unlike the homometallic $Cu(II)_4$ assembly appears to be dynamically Jahn-Teller distorted with a variety of bond lengths.

The numbers of heterometallic [2 x 2] grids reported in the literature restricts comparison of these assemblies. Lehn's heterometallic [2 x 2] grids all contain two diamagnetic metals to provide inertness of intermediates and pyrimidine bridges giving large metal-metal separations, however not even a brief crystallographic discussion is given.[42c] $[Cu_3Fe(III)(L(F))_4(NO_3)]_2(ClO_4)_4(NO_3)_4$ displays close metal-metal separations, around 4.0 Å with the single Fe(III) ion receiving an octahedral coordination geometry consisting of two tridentate donors, whilst each of the Cu(II) ions have a square based pyramidal type geometry consisting of mixtures of tri-, bi- and monodentate donors.[91a] The bond angles formed between adjacent metal centres have a range of 134-142°, which are in a similar order to those observed here.

Table 22 Bond angles/ ° for $[Cr_2Cu_2(\mathbf{L1}\text{-}H)_4]^{+6}$ cation.

N14-Cr3-N23	175	N20-Cr4-N22	175	N12-Cu1-N10	178	N21-Cu2-N34	177
N14-Cr3-O3	104	N20-Cr4-O5	102	N12-Cu1-N8	81	N21-Cu2-N17	103
N14-Cr3-O4	79	N20-Cr4-O6	78	N12-Cu1-N15	101	N21-Cu2-N26	77
N14-Cr3-N11	101	N20-Cr4-N19	79	N12-Cu1-O6	77	N21-Cu2-O5	75
N14-Cr3-N16	78	N20-Cr4-N7	102	N12-Cu1-O3	106	N21-Cu2-O4	102
N23-Cr3-O3	77	N22-Cr4-O5	79	N10-Cu1-N8	101	N34-Cu2-N17	80
N23-Cr3-O4	106	N22-Cr4-O6	107	N10-Cu1-N15	77	N34-Cu2-N26	102
N23-Cr3-N11	79	N22-Cr4-N19	97	N10-Cu1-O6	102	N34-Cu2-O5	106
N23-Cr3-N16	98	N22-Cr4-N7	77	N10-Cu1-O3	76	N34-Cu2-O4	76
O3-Cr3-O4	93	O5-Cr4-O6	92	N8-Cu1-N15	103	N17-Cu2-N26	100
O3-Cr3-N11	155	O5-Cr4-N19	94	N8-Cu1-O6	155	N17-Cu2-O5	89
O3-Cr3-N16	91	O5-Cr4-N7	156	N8-Cu1-O3	88	N17-Cu2-O4	153
O4-Cr3-N11	90	O6-Cr4-N19	156	N15-Cu1-O6	91	N26-Cu2-O5	152
O4-Cr3-N16	156	O6-Cr4-N7	93	N15-Cu1-O3	153	N26-Cu2-O4	94
N11-Cr3-N16	95	N19-Cr4-N7	91	O6-Cu1-O3	89	O5-Cu2-O4	89

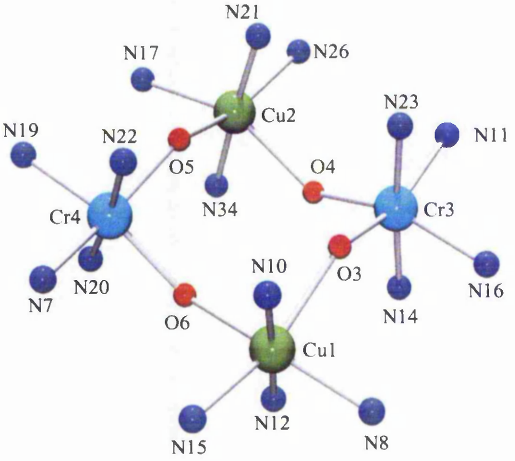

Figure 50 POV-Ray representation of $[Cr_2Cu_2(\mathbf{L1}\text{-}H)_4]^{+6}$ inner core.

Table 23 Bond lengths/ Å for $[Cr_2Cu_2(\mathbf{L1}\text{-}H)_4]^{+6}$ cation.

Cr3-N14	1.94	Cr4-N20	1.95	Cu1-N12	1.94	Cu2-N21	1.94
Cr3-N23	1.97	Cr4-N22	1.99	Cu1-N10	1.95	Cu2-N34	1.97
Cr3-O3	2.00	Cr4-O5	2.01	Cu1-N8	2.12	Cu2-N17	2.15
Cr3-O4	2.02	Cr4-O6	2.03	Cu1-N15	2.14	Cu2-N26	2.15
Cr3-N11	2.07	Cr4-N19	2.09	Cu1-O6	2.23	Cu2-O5	2.25
Cr3-N16	2.09	Cr4-N7	2.09	Cu1-O3	2.23	Cu2-O4	2.26

Table 24 Bond angles/ ° for $[Cr_2Zn_2(\mathbf{L1}\text{-}H)_4]^{+6}$ cation.

N2-Cr1-O1	78.8(3)	N22-Cr2-O21	78.4(3)	N64-Zn1-O41	103.3(11)
N2-Cr1-O41	104.7(4)	O61-Cr2-N21	93.1(11)	N44-Zn1-O41	72.6(4)
O1-Cr1-O41	93.6(5)	N62-Cr2-N21	97.9(11)	N66-Zn1-O41	88.8(5)
N2-Cr1-N42	176.8(4)	N22-Cr2-N21	78.7(3)	N46-Zn1-O41	149.6(3)
O1-Cr1-N42	102.5(7)	O21-Cr2-N21	156.9(3)	O61-Zn1-O41	94.9(10)
O41-Cr1-N42	78.2(4)	O61-Cr2-N61	157.2(5)	N24-Zn2-N4	177.6(3)
N2-Cr1-N41	99.2(3)	N62-Cr2-N61	77.7(4)	N24-Zn2-N26	77.3(3)
O1-Cr1-N41	92.8(3)	N22-Cr2-N61	99.1(4)	N4-Zn2-N26	104.7(3)
O41-Cr1-N41	156.1(4)	O21-Cr2-N61	92.3(3)	N24-Zn2-N6	102.2(3)
N42-Cr1-N41	77.9(4)	N21-Cr2-N61	94.3(4)	N4-Zn2-N6	76.3(3)
N2-Cr1-N1	79.0(3)	N64-Zn1-N44	174.0(17)	N26-Zn2-N6	98.2(3)
O1-Cr1-N1	157.7(3)	N64-Zn1-N66	78.2(4)	N24-Zn2-O1	106.6(3)
O41-Cr1-N1	90.2(6)	N44-Zn1-N66	106(2)	N4-Zn2-O1	74.9(3)
N42-Cr1-N1	99.7(7)	N64-Zn1-N46	107.1(11)	N26-Zn2-O1	90.1(3)
N41-Cr1-N1	92.5(4)	N44-Zn1-N46	77.1(3)	N6-Zn2-O1	151.2(3)
O61-Cr2-N62	80.0(5)	N66-Zn1-N46	98.2(3)	N24-Zn2-O21	73.4(2)
O61-Cr2-N22	103.5(4)	N64-Zn1-O61	73.3(4)	N4-Zn2-O21	104.6(3)
N62-Cr2-N22	175.2(9)	N44-Zn1-O61	102(2)	N26-Zn2-O21	150.7(2)
O61-Cr2-O21	89.2(11)	N66-Zn1-O61	151.4(4)	N6-Zn2-O21	89.1(3)
N62-Cr2-O21	105.2(11)	N46-Zn1-O61	92.9(9)	O1-Zn2-O21	97.1(2)

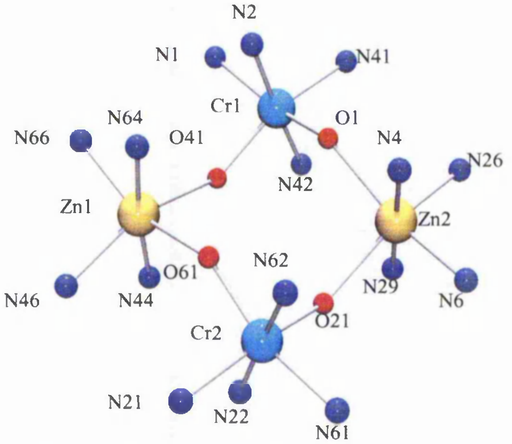

Figure 51 POV-Ray representation of $[Cr_2Zn_2(\mathbf{L1}\text{-}H)_4]^{+6}$ inner core.

Table 25 Bond lengths/ Å for $[Cr_2Zn_2(\mathbf{L1}\text{-}H)_4]^{+6}$ cation.

Cr1-N2	1.965(8)	Cr2-O61	1.967(11)	Zn1-N64	1.973(14)	Zn2-N24	1.987(7)
Cr1-O1	2.008(6)	Cr2-N62	1.963(14)	Zn1-N44	2.006(13)	Zn2-N4	2.021(8)
Cr1-O41	2.004(10)	Cr2-N22	1.987(8)	Zn1-N66	2.132(7)	Zn2-N26	2.162(7)
Cr1-N42	2.000(13)	Cr2-O21	2.010(6)	Zn1-N46	2.134(7)	Zn2-N6	2.176(7)
Cr1-N41	2.084(8)	Cr2-N21	2.072(8)	Zn1-O61	2.340(11)	Zn2-O1	2.238(6)
Cr1-N1	2.078(8)	Cr2-N61	2.128(8)	Zn1-O41	2.348(10)	Zn2-O21	2.287(6)

Magnetism

Even though each sample has not been structurally characterised there is reasonable evidence to support heterometallic grid formation from ESI-MS, IR and visible spectroscopy and chemical analysis. Consequently, variable temperature magnetisation measurements were made on each sample. The data obtained were fitted to a simple exchange model virtually identical to that used for the homometallic grids. Here the symmetry is again assumed to be D_{4h} therefore only one value of J is necessary leading to the same Hamiltonian expression, but with two different spins to accommodate the different types of paramagnetic ion present. Attempts to fit the data as more complicated systems (Fig. 52 and (14)) with interacting diagonal spins does not improve the fit of the data in all cases and simply reduces the magnitude of the predominant exchange integral.

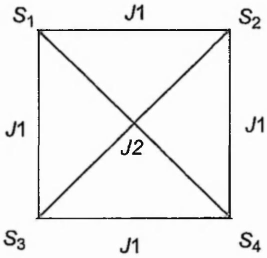

Figure 52 Exchange model for a heterometallic square with D_{4h} symmetry and interacting diagonal spins

$$\begin{aligned} H_{ex} &= -2J1(S1 \cdot S2 + S2 \cdot S4 + S4 \cdot S3 + S3 \cdot S1) \\ &\quad - 2J2(S1 \cdot S4 + S2 \cdot S3) \end{aligned} \qquad (14)$$

*[Cr_2Mn_2(**L1**-H)$_4$](ClO_4)$_6$* (**A8**)

The room temperature value of effective magnetic moment for this assembly is 9.81 μ_b, which is in sound agreement with the spin-only value of 10.00 μ_b and shows a steady decrease with decreasing temperature down to a final value of 4.09 μ_b at 2 K (Fig. 53). This decrease in effective magnetic moment is indicative of antiferromagnetic exchange that would be expected from examination of the bond angles formed across the alkoxy bridge between adjacent metal centres.

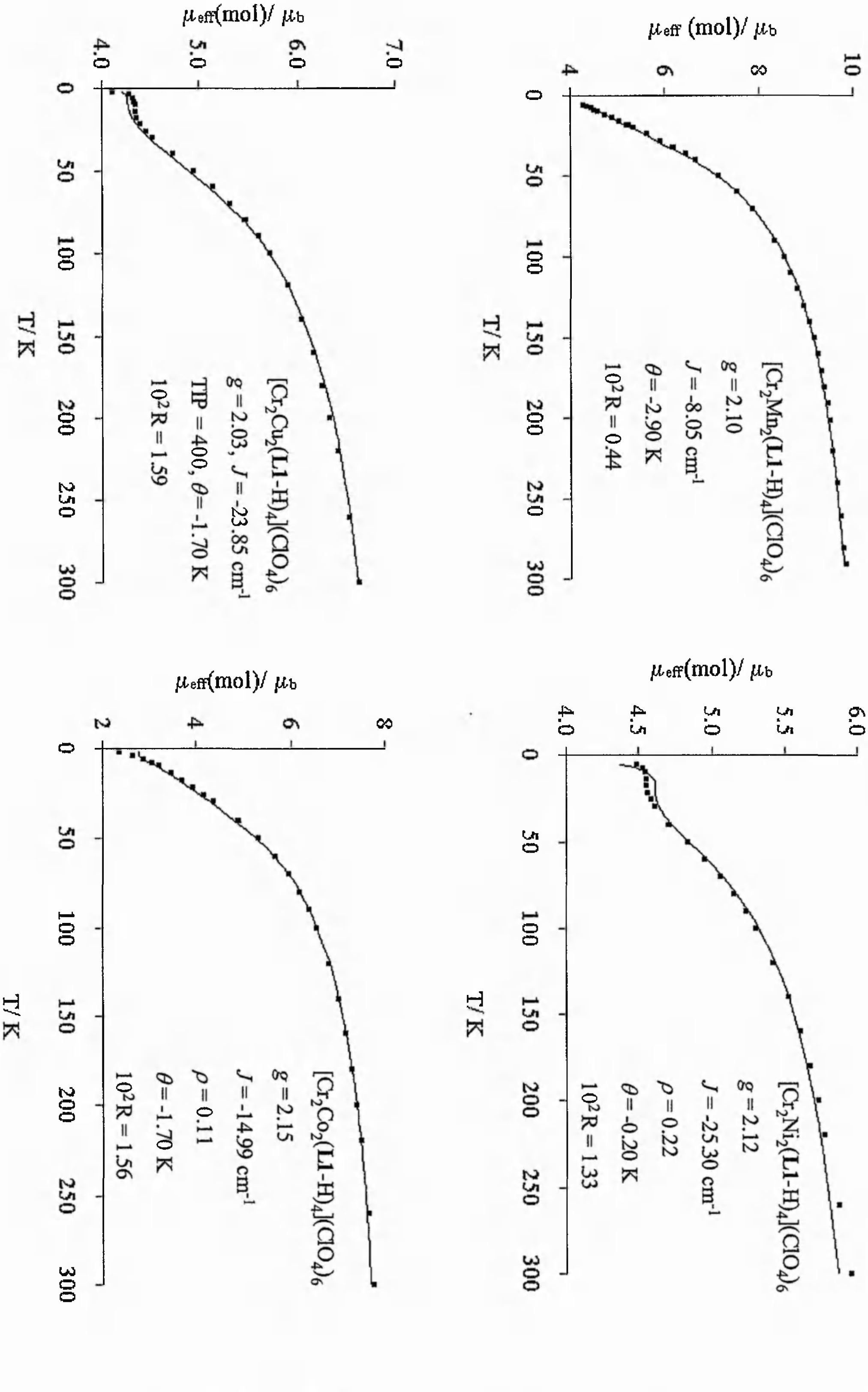

Figure 53 Top right: $[Cr_2Mn_2(\mathbf{L1}\text{-}H)_4](ClO_4)_6$ (**A8**) displaying antiferromagnetic exchange, top left: $[Cr_2Cu_2(\mathbf{L1}\text{-}H)_4](ClO_4)_6$ (**A9**) displaying antiferroamgnetic exchange, bottom right: $[Cr_2Ni_2(\mathbf{L1}\text{-}H)_4](ClO_4)_6$ (**A10**) and bottom left: $[Cr_2Co_2(\mathbf{L1}\text{-}H)_4](ClO_4)_6$ (**A11**).

Modelling of the data between 300 and 5 K as described above with two spins of S = 3/2 and S = 5/2 yields a good fit. Leading to g = 2.10, J = -8.05 cm^{-1}, θ = -2.90 K and 10^2 R = 0.44 (Fig. 53). Unfortunately the fit is heavily dependent of the incorporation of a rather large value of θ which takes account of weak intermolecular interactions. Why this is necessary is unclear, but other authors have reported values of θ up to -9.6 K suggesting that it is a consequence of competing exchange mechanisms.[92]

*[Cr$_2$Cu$_2$(**L1**-H)$_4$](ClO$_4$)$_6$* (**A9**)

In contrast to the homometallic Cu(II) grid that displays little or no exchange there appears to be a reasonable antiferromagnetic interaction because the effective magnetic moment decreases from 5.95 μ_b (spin-only value = 6.00 μ_b) at 290 K to 4.48 μ_b at 6 K with decreasing temperature (Fig. 53). This is a consequence of the Cu(II) ions geometry that both appear to be dynamically Jahn-Teller distorted rather than axially compressed, as observed for the homometallic Cu(II)$_4$ grid.[93] The former distortion implies that both the $d_{x^2-y^2}$ and the d_{z^2} are occupied by the unpaired electron in a statistical manner with the d_{z^2} magnetic orbital orthogonal to the diamagnetic bridge. Fitting of the data between 290 and 6 K with two spin of S = 3/2 and two S = 1/2 yields a reasonable fit of the data. Giving values of g = 2.03, J = -23.85 cm^{-1}, TIP = 400 x 10^{-6} emu mol^{-1}, θ = -1.70 K and 10^2 R = 1.59.

*[Cr$_2$Ni$_2$(**L1**-H)$_4$](ClO$_4$)$_6$* (**A10**)

Upon cooling, this sample shows a steady decrease in effective magnetic moment from a room temperature value of 6.62 μ_b down to 4.27 μ_b at 2 K, which is indicative of an antiferromagnetic interaction (Fig. 53). Modelling of the data becomes rather difficult even though the room temperature value of effective magnetic moment is similar to the expected spin-only value of 6.93 μ_b. However, an adequate fit of the data, 10^{2}R = 1.33, can be obtained when a very large value of ρ (0.22) is introduced with other parameters having acceptable values of g = 2.12, J = -25.30 cm^{-1} and θ = -0.20 K. This extremely large ρ value could be associated with zero field splitting that is often observed in Ni(II) assemblies[28] which MAGMUN cannot suitably model. Alternatively it could even represent a fraction of incomplete grids which may well be associated with the relatively inert nature of the Ni(II) ion (water exchange constant = ~ 10^4 s^{-1}).[85] A similar effect has been observed in an octanuclear Ni(II) assembly with a value of ρ around 0.1.[94]

*$[Cr_2Co_2($**L1**$-H)_4](ClO_4)_6$ (**A11**)*

The room temperature value of effective magnetic moment shows a steady decrease upon cooling from 7.74 μ_b down to 2.62 μ_b at 4 K that is indicative of antiferromagnetic exchange (Fig. 53). The spin-only value of 7.75 μ_b is in excellent agreement with the room temperature value. Interestingly fitting of the data, as with the equivalent Ni(II) species, requires the introduction of a very large ρ value of 0.11. Again, this may represent zero field splitting or a fraction of incomplete grid.[94] The other parameters are in the region of previously discussed samples with values g = 2.15, J = -14.99 cm^{-1} and 10^2R = 1.56. This fit when compared to the homometallic Co(II) [2 x 2] grid appears not to be significantly affected by a spin orbit contribution.

*$[Cr_2Fe(II)_2($**L1**$-H)_4](ClO_4)_6$ (**A12**)*

The effective magnetic moment shows a steady decrease from 7.59 μ_b at room temperature of down to 2.31 μ_4 at 2 K which is indicative of antiferromagnetic exchange (Fig. 54). The room temperature value is extremely low when compared to the spin-only value of 8.83 μ_b and consequently attempts to fit the data with spins of S = 3/2 and S = 2 have been unsuccessful. However, an adequate fit of the data can be obtained when one of the Fe(II) ions is assigned as having S = 0 suggesting that a fraction of this ion is adopting a of low spin configuration, but without structural analysis in depth discussion of this observation is inappropriate.

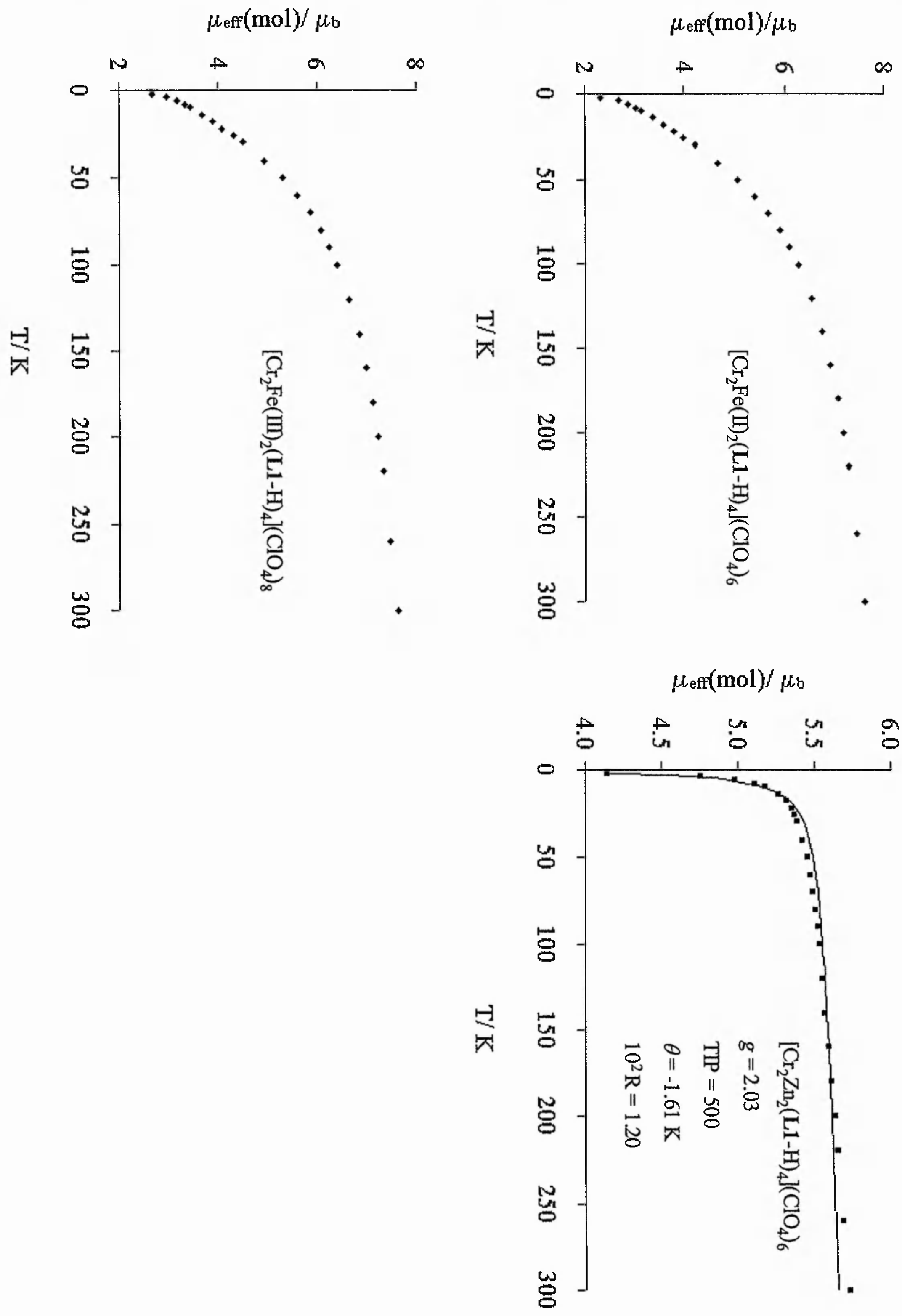

Figure 54 Top left and right: $[Cr_2Fe_2(\mathbf{L1}\text{-}H)_4](ClO_4)_6$ **(A12)** and $[Cr_2Fe_2(\mathbf{L1}\text{-}H)_4](ClO_4)_8$ displaying very similar profiles suggesting similar composition and bottom $[Cr_2Zn_2(\mathbf{L1}\text{-}H)_4](ClO_4)_6$ **(A13)** displaying weak intermolecular antiferromagnetic exchange.

*[Cr_2Zn_2(**L1**-H)$_4$](ClO_4)$_6$* (**A13**)

Despite the fact that the Zn(II) ion is diamagnetic this example provides an interesting case where the two spins (S = 3/2) are separated by an O-Zn-O diamagnetic bridge. The magnetic moment shows a decrease from a room temperature value of 5.72 μ_b down to 4.13μ_b at 2 K that is indicative of very weak antiferromagnetic exchange (Fig. 54). The room temperature value is in good agreement with a spin-only value of 5.48 μ_b. Fitting of the data gives a good fit when including a reasonable value of TIP (~ 500 x 10^{-6} emu mol^{-1}) that is probably present within other systems observed here but is not a significant effect. Interestingly, the weak antiferromagnetic interaction can be modelled by either the use of intramolecular exchange (J) or intermolecular exchange (θ). From examination of the previous examples in this chapter they all require the introduction of a θ value to give a fit of the data that is not generally necessary for the homometallic [2 x 2] grids. Therefore, it is suggested that this interaction is intermolecular in nature and fitting on this basis gives g = 2.03, TIP = 500 x 10^{-6} emu mol^{-1}, θ = -1.61 K and 10^2R = 1.20.

*[Cr_2Fe(III)$_2$(**L1**-H)$_4$](ClO_4)$_8$*

Examination of the effective magnetic moment shows a steady decrease from a room temperature of 7.61 μ_b down to 2.67 μ_b at 2 K that is indicative of antiferromagnetic exchange (Fig. 54). Interestingly, the profile of this plot is very similar to that observed in the analogous Fe(II) species (see above). This would suggest that these two assemblies have similar composition and in this case, can be compared to the mixed oxidation Fe(II)$_2$Fe(III)$_2$ grid that is observed in chapter 3 which is formed by the reduction of Fe(III) to Fe(II) that occupies a $N_{py/\ diazine}$ pocket. Consequently it is proposed that a similar reduction is occurring here yielding [Cr_2Fe(II)$_2$(L1-H)$_4$](ClO_4)$_6$. As with the analogous Fe(II) assembly no adequate fit of the data could be obtained.

4.5 Conclusion

A series of heterometallic [2 x 2] grids has been synthesised in a controlled manner in only two synthetic steps from the starting ligand. In solution they show no reversible electrochemical behaviour and only fractional amounts present by ESI-MS, whilst visible spectroscopy confirms the presents of labile transition metal ions in most cases with reasonable absorbances in accord with their homometallic parent [2 x 2] grids. Structural characterisation is achieved for selected transition metal ions and displays the desired [2 x 2] grids with pairs of the same metal ion in the desired *anti* geometry, however these structures appear to be two-fold rotationally disordered.

The magnetic studies are more complicated for those observed for the homometallic [2 x 2] grids and probably require more detailed investigation including the possibilities of spin frustration and zero field splitting.[15] However, some interesting conclusions can be made. Those heterometallic [2 x 2] grids which have been structurally characterised, *i.e,* Mn(II), Cu(II) and Zn(II) all appear to give acceptable fits of the experimental data without the need for large paramagnetic impurities suggesting these samples are minimally contaminated with incomplete grids. The Ni(II) assembly requires a large paramagnetic impurity associated with the relatively inert nature of the Ni(II) ion and it is likely to contain a reasonable fraction of incomplete grid. As for the Co(II) assembly, which again requires a large paramagnetic impurity, the relatively labile nature of the Co(II) ion (water exchange rate = ~ 10^7 s^{-1}) would suggest a smaller amount of incomplete grid and hence, as observed, a smaller paramagnetic impurity, however, this may be associated with a mixture of high and low spin configurations for the Co(II) ion as observed with the homometallic [2 x 2] in Chapter Three. This latter effect could also explain why only adequate fits of the Fe(II) assembly can be obtained when one Fe(II) ion is assumed to be low spin.

Chapter Five

Mixed Oxidation [2 x 2] and [3 x 3] Grids

5.0 Introduction

The formation of mixed oxidation state assemblies is particularly attractive because many exhibit interesting magnetic properties such as SMM behaviour with reasonably high blocking temperatures.[6] The formation of these relies on a serendipitous approach that chemically oxidises the participating metal ions before formation of the assembly.[18] Alternatively, a mixed oxidation sate assembly can be formed *via* simple aerial oxidation of the metal ion, which can be accompanied by a reduction or oxidation of the organic ligand used in the self-assembly process. Consequently pre-determined results using these approaches are unlikely and often, low yields are obtained.[18] To overcome this problem, preformed homovalent assemblies have been oxidised with a stoichiometric amount of chemical oxidant, but this has also led to the formation of various mixtures of heterovalent assemblies.[95]

A logical way to circumvent these problems is to apply controlled potential electrolysis (CPE) to a preformed homovalent assembly that displays reversible/ quasi-reversible electrochemical behaviour. This should allow the exclusive formation of one mixed oxidation species in high yields in a relatively simple manner. Christou has applied this technique to form mixed oxidation tetranuclear $Co(III)_3Co(IV)$[96] and $Mn(III)_3Mn(IV)$[97] assemblies with the former being the first example of Co(IV) to exist in a polynuclear species.

Consequently, we have applied this technique to both [2 x 2] and [3 x 3] homovalent square grids that display reversible electrochemical behaviour and, for the first time, report mixed valence grids formed in a controlled manner by means of CPE.

CPE as its name suggests simply holds the potential of a electrode at set value whilst monitoring the current. Once the current has reached a negligible level the potential is withdrawn. The magnitude of the potential is generally obtained from a CV by examination of the region separating pairs of peaks. The solution contains a known amount of an assembly along with an anion that acts as a supporting electrolyte allowing charge to flow through the solution.

The Electrochemical Cell[98]

A three-electrode set-up was employed with a Pt mesh-working electrode, Ag/AgCl reference electrode and silver counter electrode. Fig. 55 represents the electrochemical cell, which has a number of significant differences from a typical CV cell. The compartment in which the oxidation takes place is considerably larger (~ 300 ml) allowing reasonable amounts of mixed valent assembly to be prepared. The solution in this compartment is stirred rapidly to ensure diffusion of all of the material to the working electrode surface. The silver counter electrode is separated from the bulk solution by two fine frits. This arrangement minimises the danger of mixing of the products formed at the working and counter electrodes.

Once the residual current reaches a minimal level the potential is withdrawn and the solvent removed by evaporation under reduced pressure. The remaining solid contains large amounts of TEAP, which is removed by repeated extraction with hot DCM, to give the desired mixed valent assembly in good yields (~ 80 %).

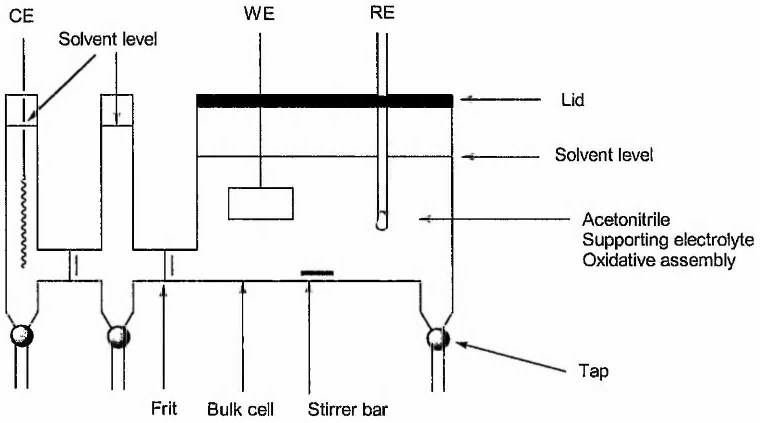

Figure 55 Schematic representation of bulk electrochemical cell.

5.1 Mixed Oxidation Manganese [2 x 2] Grids

Examination of the CV scan of $[Mn_4(\mathbf{L1}\text{-}H)_4](ClO_4)_4$ (chapter 3) shows four reversible waves with large separations between them and consequently large conproportionation constants, making this system an ideal candidate for the preparation of mixed oxidation assemblies *via* CPE. Therefore, three mixed oxidation state species were prepared by the methodology set out in the inorganic experimental section to give $Mn(II)_3Mn(III)$, $Mn(II)_2Mn(III)_2$ and $Mn(II)Mn(III)_3$

assemblies which were generated at voltages of 0.75 V, 1.13 V and 1.35 V, respectively (Ref. Ag/AgCl).

Solution Studies

Analysis of these sample by ESI-MS in acetonitrile at 70 °C with ranging cone voltages only display peaks associated with the parent Mn(II) [2 x 2] assembly except for the Mn(II)Mn(III)$_3$ assembly that shows one (893 *m/z*, +2) peak associated with the opposite species, Mn(II)$_3$Mn(III). However, detection of higher oxidation (> +2) species by ESI-MS under these conditions appears to be unfavourable and suggests that these species are not stable in the vapour phase, reverting back to the parent homovalent species. This could be occurring due to the large potential applied across the cone to effect ion formation.

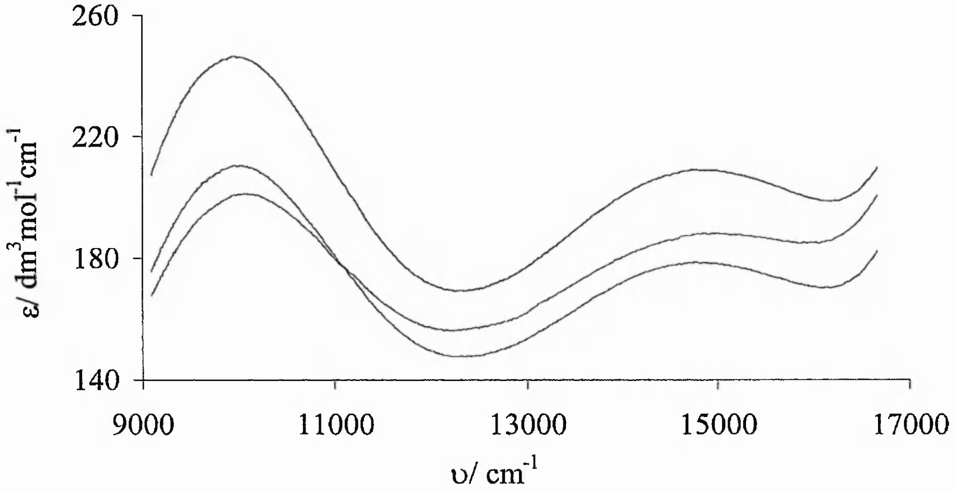

Figure 56 Visible spectra of mixed oxidation Mn$_4$ [2 x 2] grids. Green = [Mn(II)$_3$Mn(III)(**L1**-H)$_4$](ClO$_4$)$_5$, blue = [Mn(II)$_2$Mn(III)$_2$(**L1**-H)$_4$](ClO$_4$)$_6$ and red [Mn(II) Mn(III)$_3$(**L1**-H)$_4$](ClO$_4$)$_7$.

In contrast, visible spectroscopy confirms the presence of Mn(III) in all three samples with peaks that increase in intensity as more Mn(III) is present, whilst the parent Mn(II) assembly shows no absorbance within the visible region (Fig. 56). Of interest are the [Mn(II)$_3$Mn(III)(**L1**-H)$_4$](ClO$_4$)$_5$ and [Mn(II)$_2$Mn(III)$_2$(**L1**-H)$_4$](ClO$_4$)$_6$ that have very similar absorbance spectra which suggests that these samples may be similar in composition. This suggestion is supported by CV studies (chapter 3) where a smaller comproportionation is observed for the Mn(II)$_2$Mn(III)$_2$ state (~ 7.7 x 10^3) implying that this particular species is not as stable as the others.

The two transitions observed at ~ 10000 cm^{-1} (1000 nm) and ~ 14400 cm^{-1} (660 nm) are similar to those observed by other authors in mixed oxidation Mn(II)/Mn(III) species.[95a] On this basis, the absorbance at ~ 10000 cm^{-1} is likely to be LMCT ((μ-O) $\rightarrow$ Mn(III)) in nature while the absorbance at ~ 14400 cm^{-1} is an inter-valence charge transfer band associated with fast electron transfer between the Mn(II) and Mn(III) ions.[95a]

Solid-State Studies

Crystals of these compounds could be easily obtained from a number of different solvents that become progressively darker as the potential at which they were prepared was stepped in a more positive direction, which would suggested increased conversion of Mn(II) to Mn(III). The crystals obtained for single crystal X-ray analysis gave poor data sets, which could not be solved, even after repeating the controlled potential experiment several times and using different crystallisation solvents and techniques.

Due to a lack of structural characterisation no further studies have been carried out on these samples and no attempts to prepare [2 x 2] mixed oxidation species containing other first row transition metal ions have been investigated.

5.2 Mixed Oxidation State Manganese [3 x 3] Grids

Thompson and Matthews have prepared a complete [3 x 3] Mn(II) grid that displays a wealth of electrochemistry.[4a] Preparation of this assembly according to the literature procedure followed by CV studies in acetonitrile reproduced those reported. Examination of the cathodic section of the CV scan at 100 mVs^{-1} showed one large and four smaller peaks, which have been previously assigned to four and one electron processes respectively. Consequently, the most oxidised grid is $Mn(II)Mn(III)_8$ and it is suggested from the communication that the individual Mn(II) ion occupies the central cavity.[4a]

From these results, the preparation of two mixed oxidation species was attempted using the same procedure employed to form the [2 x 2] grids. The potential was held at 0.80 V, which was expected to remove four electrons from the system implying the formation of four Mn(III) ions. For another sample, the potential was held at 1.65 V to remove eight electrons from the assembly to give the almost fully oxidised $[Mn(II)Mn(III)_8(L(N)\text{-}2H)_6](ClO_4)_{14}$ (see page 26 for L(N) structure).

Solid-State Studies

Crystals obtained in both cases were suitable for X-ray analysis, however examination of these structures indicated that they were essentially identical with only ten anions present. This would imply that both species contained only four Mn(III) ions and repeated attempts to prepare the higher order mixed oxidation species always gave $[Mn(II)_5Mn(III)_4(L(N)\text{-}2H)_6](ClO_4)_{10}$ according to X-ray crystallographic studies.

$[Mn(II)_5Mn(III)_4(L(N)\text{-}2H)_6](ClO_4)_{10}$ (**A14**)

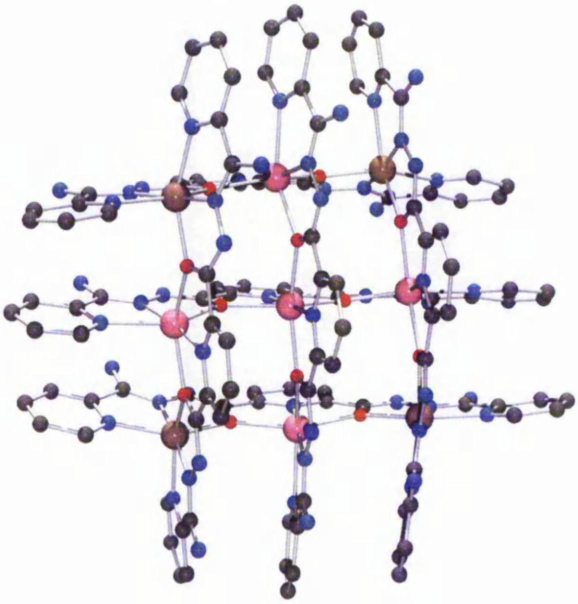

Figure 57 POV-Ray representation of mixed oxidation $[Mn(II)_5Mn(III)_4(L(N)\text{-}2H)_6]^{+10}$ cation. Brown = Mn(III).

This structure has recently been published and consists of a central cation surrounded by ten perchlorate anions and various solvent molecules.[95b] The cation has an external long dimension of ~ 17.1 Å with an internal metal grid dimension around 7.9 Å (Fig. 57). The six ligand strands can be divided into to two groups of three that lie above and below the mean plane of metal ions with separation less than 4.0 Å between parallel aromatic rings. The structure is highly symmetrical with *I4* space group with three crystallographically different manganese cations that all have a distorted octahedral environment with their basal planes assigned as being in the mean plane of the grid of metal ions. The three separate ions make up the sides, the centre and corners with coordination geometries of *mer*-N_3O_3, *trans*-N_2O_4 and *cis*-N_4O_2, respectively. The separation between metal ions *via* the alkoxy bridge is around 4.0 Å with the bond angle created averaging around 132°.

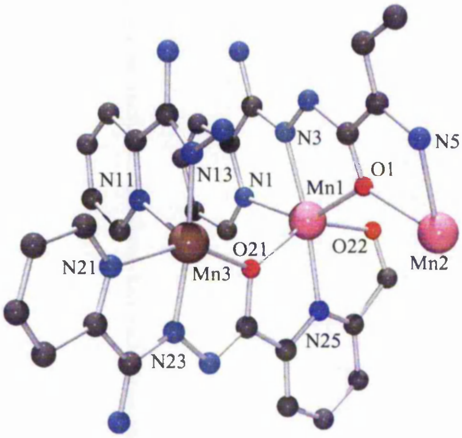

Figure 58 POV-Ray representation of $[Mn(II)_5Mn(III)_4(L(N))_6]^{+10}$ asymmetric unit.

Table 26 Selected bond lengths/ Å and angles/ ° for $[Mn(II)_5Mn(III)_4(L(N))_6]^{+10}$ cation.

Mn1-N1	2.353(10)	N3-Mn1-O1	73.7(3)	O1-Mn2-N5	71.2(2)
Mn1-N3	2.120(8)	N3-Mn1-N25	172.3(4)	N5iii-Mn2-N5	180.000(2)
Mn1-N25	2.177(10)	O1-Mn1-N25	113.2(3)	N13-Mn3-N23	171.0(5)
Mn1-O1	2.160(8)	N3-Mn1-O21	104.1(4)	N13-Mn3-O22iii	75.9(4)
Mn1-O21	2.221(8)	O1-Mn1-O21	93.1(3)	N23-Mn3-O22iii	104.9(4)
Mn1-O22	2.243(8)	N25-Mn1-O21	72.8(4)	N13-Mn3-O21	113.0(4)
Mn2-N5	2.262(15)	N3-Mn1-O22	111.4(3)	N23-Mn3-O21	76.0(4)
Mn2-O1	2.220(8)	O1-Mn1-O22	95.8(3)	O22iii-Mn3-O21	97.6(3)
Mn3-N11	2.176(10)	N25-Mn1-O22	72.1(3)	N13-Mn3-N11	75.3(4)
Mn3-N13	1.947(13)	O21-Mn1-O22	144.5(3)	N23-Mn3-N11	104.7(4)
Mn3-N21	2.213(11)	N3-Mn1-N1	72.0(4)	O22iii-Mn3-N11	150.4(4)
Mn3-N23	1.988(12)	O1-Mn1-N1	145.2(4)	O21-Mn3-N11	87.4(4)
Mn3-O21	2.132(9)	N25-Mn1-N1	101.4(4)	N13-Mn3-N21	96.7(5)
		O21-Mn1-N1	100.6(3)	N23-Mn3-N21	74.3(5)
		O22-Mn1-N1	91.3(4)	O22iii-Mn3-N21	90.1(3)
		O1-Mn2-O1i	142.4(4)	O21-Mn3-N21	150.3(4)
		O1-Mn2-O1ii	95.97(12)	N11-Mn3-N21	100.0(4)
		O1-Mn2-N5iii	108.8(2)		

Examination of the bond lengths around the metal centres provides information for the assignment of the Mn(III) ion (Table 26). Mn3 that occupies the corner of the grid has four reasonable bonds ranging from 2.132(9) to 2.213(11) Å to equatorial N_{py} and alkoxide, whilst the axial bonds to $N_{diazine}$ are relatively short having values of 1.947(13) and 1.988(12) Å (Fig. 58). These shorter bonds are typically associated with Jahn-Teller compression that is observed for the homometallic Cu(II) [2 x 2] grid. Mn(III) that has a d^4 configuration and also undergoes this type of distortion and consequently Mn3 is assigned as the Mn(III) ion. Examination of the coordination geometries around Mn1 and Mn2 confirms these have a range of bond lengths typically associated with Mn(II) (Table 26).

Solution Studies

As with the [2 x 2] assemblies no evidence for the formation of mixed-valent assemblies is provided by ESI-MS which only indicates the presence of the homovalent Mn(II) grid. However, evidence for the presence of Mn(III) is provided by visible spectroscopy in acetonitrile that displays two peaks with similar intensities and thus similar extinction coefficients (~ 800 cm dm^3 mol^{-1}) at ~ 10000 cm^{-1} and 14400 cm^{-1}. As with the [2 x 2] mixed oxidation state grids, the absorbance at ~ 10000 cm^{-1} is likely to be LMCT ((μ-O) → Mn(III)) in nature while the absorbance at ~ 14400 cm^{-1} is an inter-valence charge transfer band associated with fast electron transfer between the Mn(II) and Mn(III) ions.[95a]

Magnetism

Upon cooling, $[Mn(II)_5Mn(III)_4(L(N)\text{-}2H)_6](ClO_4)_{10}$ **(A14)** shows a steady decrease in effective magnetic moment from a room temperature value of 15.5 μ_b down to 2.4 μ_b at 2 K, whilst a plot of χ_m versus T shows a steady increase down to ~ 50 K whereupon a brief decrease is observed followed by a steep increase at ~ 20 K (Fig. 59). Both of these observed plots are indicative of antiferromagnetic exchange which is observed in the analogous Mn(II) [3 x 3] grid. Typically this process is caused by large Mn-O-Mn bond angles (~ 130°) and is not particularly affected by a change in metal ion oxidation state.

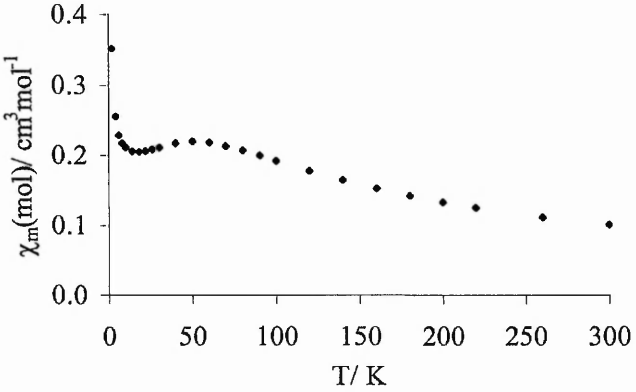

Figure 59 Magnetic profile for $[Mn(II)_5Mn(III)_4(L(N))_6](ClO_4)_{10}$ (**A14**) with a brief plateau at ~ 50 K indicating antiferromagnetic exchange.

Modelling of the data even at the simplest level becomes extremely complicated due to two different spins states and two different exchange integrals. Fig. 60 represents a suggested model for fitting of the experimental data, along with the resulting Hamiltonian expression (15).

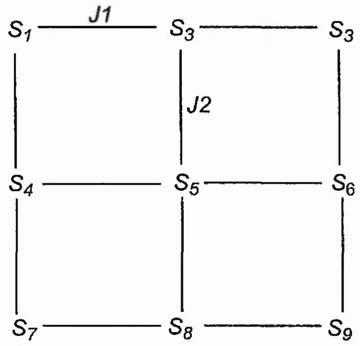

Figure 61 Simplified exchange model for $[Mn(II)_5Mn(III)_4(L(N))_6](ClO_4)_{10}$ (**A14**).

$$\begin{aligned} H_{ex} = -J1\{&S_1 \cdot S_2 + S_2 \cdot S_3 + S_3 \cdot S_6 + S_6 \cdot S_9 + S_9 \cdot S_8 + S_8 \cdot S_7 + S_7 \cdot S_4 + S_4 \cdot S_1\} \\ -J2\{&S_2 \cdot S_5 + S_6 \cdot S_5 + S_8 \cdot S_5 + S_4 \cdot S_5\} \end{aligned} \qquad (15)$$

5.3 Conclusion

The attempted preparation of mixed oxidation manganese [2 x 2] grids has been reported. The presence of Mn(III) is confirmed by visible spectroscopy in acetonitrile. In contrast a mixed oxidation species [3 x 3] grid is reported that appears stable under atmospheric conditions with magnetic properties in accord with the structure observed. However, the higher order mixed oxidation species, Mn(II)Mn(III)$_8$, could not be isolated probably owing to its poor stability. This poor stability could be associated with the lack of flexibility found within the rigid grid framework, which would need to undergo significant 'flexing' to accommodate eight Mn(III) ions undergoing Jahn-Teller distortion.

Chapter Six

[4 x 4] Grids

6.0 Introduction

The formation of higher order grids (> [3 x 3]) is limited to a few examples, which are covered in Chapter One. Higher order grids are particularly attractive because they demonstrate the ability of supramolecular coordination chemistry to build molecules with nanometre dimensions. Furthermore, the introduction of paramagnetic transition metal ions renders these motifs both magnetically and electrochemically active. These functional grids could find applications in the field of magnetic data storage with the ability to potentially store one bit of information per single grid molecule.[55]

The synthesis and structural characterisation of higher order grids with complete metal ion coordination has so far remained a synthetic challenge.[58] Consequently, there are relatively few ligands reported to date capable of ordering transition metal ions into grid-like assemblies. However, a family of ligands, developed by Lehn, based around sequences of pyridine and pyrimidine or pyridazine heterocycles have proven to be successful in generating [2 x 2] and [3 x 3] grids with tetrahedral and octahedral transition metal ions. More recently ligand L(P) has led to a complete $Pb(II)_{16}$ [4 x 4] grid which was originally characterised in solution by ESI-MS and ^{207}Pb NMR[99] and more recently the structure confirmed by single crystal X-ray diffraction.[60] Yet, a detailed investigation of L(P) (Fig. 61) by ESI-MS with varying first row transition metal ions provided no evidence to suggest [4 x 4] grid formation or any other structural motif.[100] From examination of the ligand strand it has been suggested that it is too rigid and hence the linear array of tridentate pockets cannot "pinch" sufficiently to incorporate smaller transition metal ions in a [4 x 4] grid-like manner.[95] This implies that large cations, particularly Pb(II), are ideal candidates for [4 x 4] grid formation and in addition, assemblies formed with this cation can be characterised in solution by both ^{1}H and ^{207}Pb NMR.

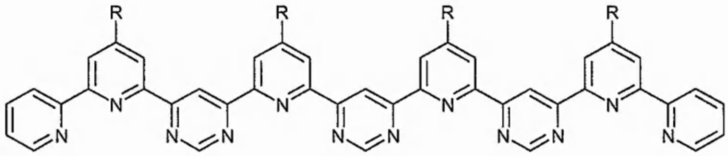

L(P)

Figure 61 L(P) provides a linear array of tridentate pockets capable of forming [4 x 4] molecular grid. R = S^{n}Pr.

6.1 Heterocyclic Bridged [4 x 4] Grids

Design: ***L2***

L2 was designed to provide four contiguous tridentate pockets built around a single pyrimidine ring and two alkoxide bridges to promote both magnetic and electrochemical exchange (Fig. 62). All these bridging functionalities have a proven record at promoting grid formation and providing suitable pathways for electronic communication.[4] More importantly, the incorporation of two diazine links on both sides of the central pyrimidine ring renders the ligand flexible, potentially allowing the binding of the smaller transition metal ions. These diazine links reduce the need for bridging heterocycles, hence reducing the need for lengthy synthetic strategies and allowing large amounts, ~ 10 g, of ligand to be prepared.

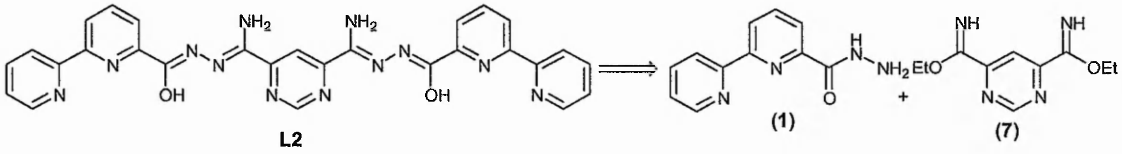

Figure 62 L2 contains a linear array of tridentate donors that have the potential to form a [4 x 4] grid.

Synthesis

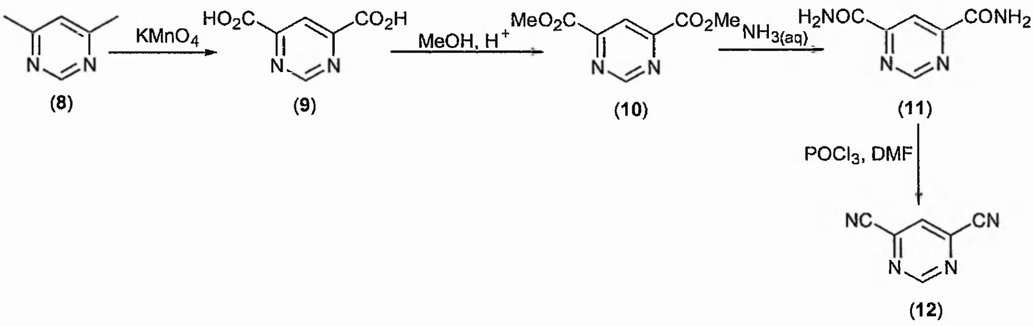

Figure 63 Preparation of 4,6-dicyanopyrimidine (**12**).

The synthesis of such a large molecule requires a strategy that expolits its symmetry. The most sensible disconnection of **L2** yields 6-hydrazido-2,2'-bipyridine (**1**) and diethyl pyrimidine-4,6-diimidate (**7**). The synthesis of 6-hydrazido-2,2'-bipyridine

(Chapter Three) has been previously discussed and the following discussion will cover the synthesis of 4,6-dicyanopyrimidine (**12**), diethyl pyrimidine-4,6-diimidate (**7**) and **L2**.

The formation of diethyl pyrimidine-4,6-diimidate (**7**) requires the corresponding dinitrile compound (**12**). However, there is only one reference to 4,6-dicyanopyrimidine (**12**), which indicated that it had been prepared by dehydration of the amide (Fig. 63).[101] The synthesis of the amide was achieved according to Hunt,[102] by basic aqueous oxidation of 4,6-dimethylpyrimidine (**8**) with potassium permanganate to give the diacid (**9**), followed by esterification in methanol. Addition of dimethyl pyrimidine-4,6-dicarboxylate (**10**) to a concentrated ammonium solution yields the desired diamide (**11**). Dehydration of the diamide was subsequently effected using Vilsmeier reagent according to Gorbyleva[103] and furnishes 4,6-dicyanopyrimidine (**12**) (Fig. 63). Nevertheless, this could not be justified as a viable method due to the length of the synthetic route, the low yields obtained (~ 17 % over four steps) and the expense of 4,6-dimethylpyrimidine (**8**). A thorough literature search found that a similar compound, 1,4-dicyanophthalazine, had been prepared by taking the corresponding diiodo compound and reacting it with copper(I) cyanide in boiling pyridine.[122] Application of this methodology gave the desired compound, but in low yields (~ 20 %). The yield was improved (67 %) by employing different reaction conditions and workup. Principally these were using dry DMF as solvent and extending the reaction time.

Formation of the diimidate ester was attempted by the addition of 4,6-dicyanopyrimidine (**12**) to a 10 % solution of NaOMe in dry MeOH. After work up the product was identified by ^{1}H and ^{13}C NMR as a mixture that principally contained methyl 6-methoxypyrimidine-4-imidate (**13**). This product is formed because of the high nucleophilicity of the methoxide ion, which displaced the nitrile group at room temperature. This phenomenon was also observed at low temperatures (Fig. 64). The only other reported technique to form imidate esters requires the use of hydrogen chloride gas in a suitable solvent (usually ether, benzene or petroleum ether) along with a stoichiometric amount of an alcohol.[104]

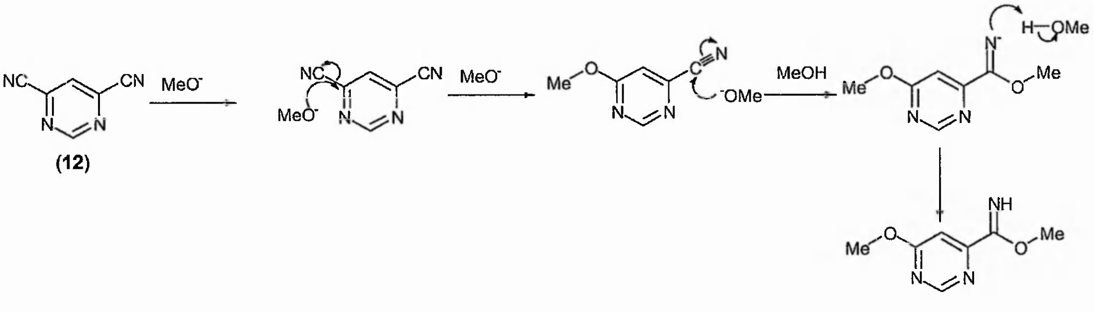

(13)

Figure 64 Proposed mechanism for the displacement of one nitrile group by the methoxide ion to form 4,6-dicyanopyrimidine (**12**).

The diethyl imidate ester (**7**) was initially prepared rather than the dimethyl derivative and this proved to be advantageous (see page 154). Development of this reaction was tedious and frequently produced the decomposition product, the diester, even when strict anhydrous conditions were enforced. Further investigation has noted that the reaction works particularly well when the dinitrile has been freshly dried suggesting the compound is hygroscopic. The diethyl imidate ester obtained is only about 80 % pure and attempts to purify it caused hydrolysis to the ester and consequently it was used crude. Addition of freshly prepared crude diethyl pyrimidine-4,6-dimidate (**7**) in dry methanol to hot solution of 6-hydrazido-2,2'-bipyridine (**1**) in dry methanol along with a catalytic amount of acetic acid gives **L2** in high purity and good yields after four hours under reflux.

Complexation: General

Due to large amounts of **L2** that can be synthesised a large number of complexation reactions in a variety of manners have been attempted, nevertheless only those that gave single crystals can be conclusively structurally characterised. Unfortunately, this has only been achieved for a limited number of examples; however, evidence relating to other samples will be presented. To test the ligand design, reaction with the Pb(II) ion was initially examined because of its proven track record to form higher order grids and its ability to be characterised in solution by NMR. The following discussion will deal with the assemblies formed with **L2**.

*Complexation: **L2** (Pb(II))*

Addition of **L2** to the correct stoichiometry (1:2) of $Pb(OTf)_2$ in acetonitrile yielded a scarlet solution which was subsequently stirred overnight. Upon removal of the solvent and crystallisation from aqueous acetonitrile large single crystals formed that were suitable for further analysis.

*Solution Studies: **L2** (Pb(II))*

Examination of the crystals by ESI-MS in acetonitrile with ranging cone voltages (0-20V) at 70 °C indicated one species present with a molecular weight over 10,000 units and following further analysis the peaks were assigned to the species $[Pb_{16}(\mathbf{L2}\text{-}2H)_8(OTf)_n]^{16-n}$ ($n = 4$-10) (Fig. 65).

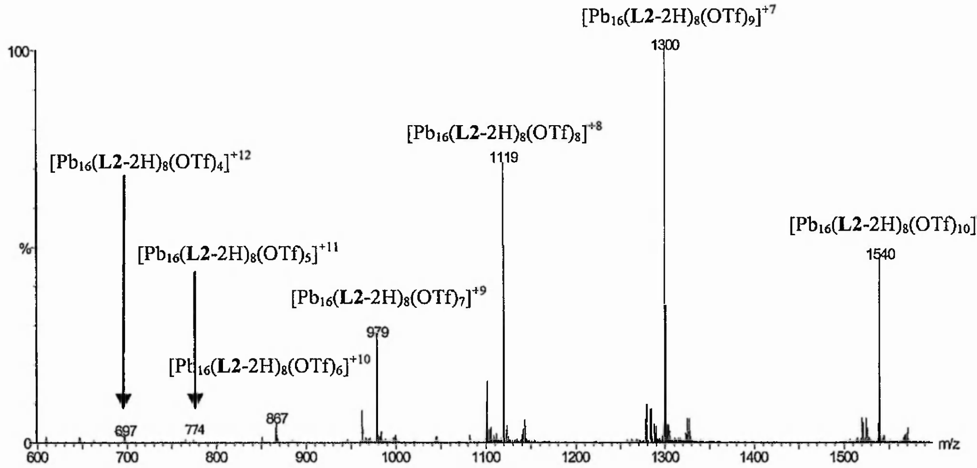

Figure 65 ESI-MS of $[Pb_{16}(\mathbf{L2}\text{-}2H)_8(OTf)_{16}]$ in acetonitrile at 70 °C with a cone voltage of 10 V.

However, examination of the same crystals in deuterated acetonitrile and dimethyl sulfoxide by ^1H NMR between 238 and 303 K only gave broad and poorly resolved spectra. This could be attributed to the individual ligand strands all being in a different magnetic environment and therefore in solution up to 128 different proton environments maybe observed. This is supported by ^{207}Pb NMR which was performed at JEOL Ltd. on a 400 MHz spectrometer and indicated a total of six different Pb(II) nuclei present in approximately a 1:1:1:1:4:8 ratio within the range of 1650 to 2050 ppm (referenced to $Pb(OTf)_2$) (Fig. 66).

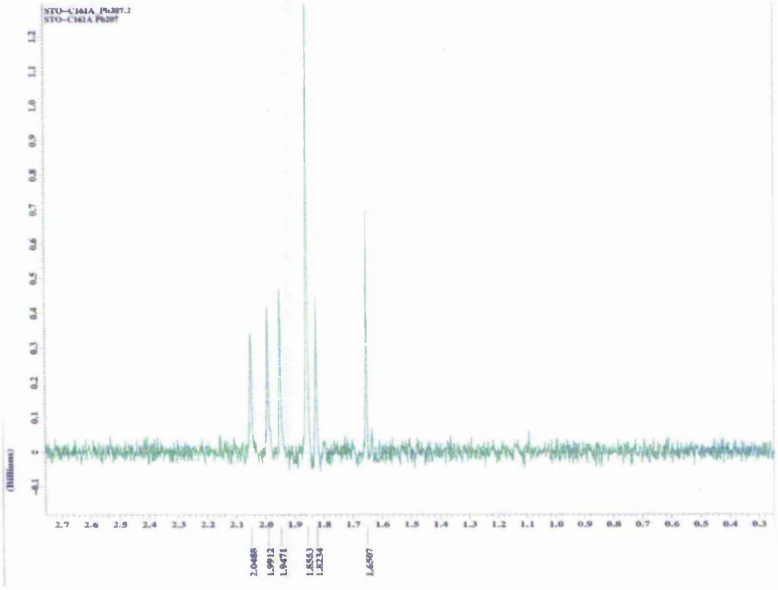

Figure 66 ^{207}Pb NMR of [Pb_{16}(**L2**-2H)$_8$(OTf)$_{16}$] indicating six Pb(II) environments.

The nature of the donors in the binding site and the number of neighbouring ^{207}Pb(II) nuclei determines the sequence of chemical shifts in the ^{207}Pb NMR spectrum. The ^{109}Ag NMR signals of a [3 x 3] Ag(I)$_9$ assembly of a grid-type structure indicated a decreasing shift (lower ppm values) with increasing numbers of less basic donors and neighbouring ions.[55a] On this basis, it is suggested that the four individual peaks are assigned to the corner Pb(II) ions because they receive the hardest donors and consequently appear furthest down field. The large peak is thus associated with the eight side Pb(II) ions and the peak furthest upfield assigned to the central ions because of the low donor power of the N_{pym}.

*Solid-State Studies: [Pb_{16}(**L2**-2H)$_8$(H_2O)$_5$(OTf)$_6$](OTf)$_{10}$·(H_2O)$_{23}$ (**A15**)*

The crystals examined in solution were also suitable for X-ray analysis and indicated the desired motif had been formed, and was communicated recently as the first ever complete [4 x 4] grid to be structurally characterised.[105a] The structure is made from a central cation surrounded by ten uncoordinated triflate anions and a number of water molecules.

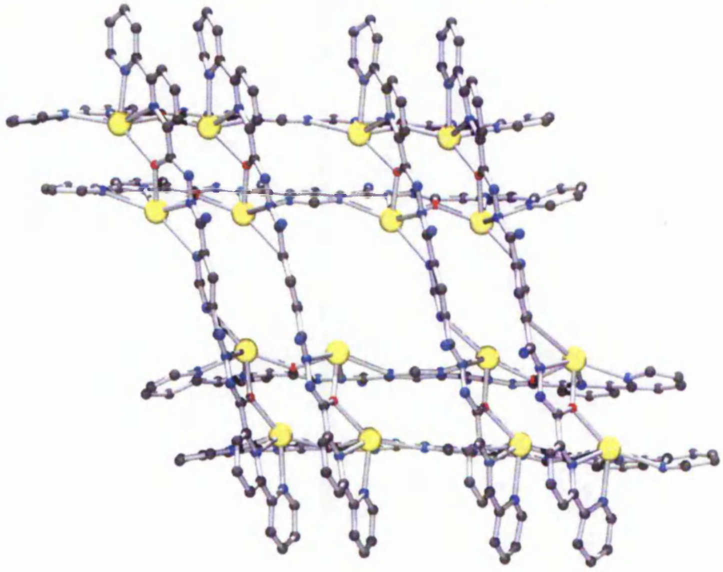

Figure 67 POV-Ray representation of $[Pb_{16}(\mathbf{L2}\text{-}2H)_8]^{+16}$ cation. All anions and solvent molecules have been omitted for clarity.

The cation is represented in Fig. 67 with external and internal dimensions of ~ 25.8 Å and ~ 16.2 Å, respectively. The grid is best described as a complete [4 x (2 x 2)] grid of grids due to the bridging pyrimidine rings rather than a true [4 x 4] grid. The ligand strands can be divided into pairs, within each pair the aromatic ring separation is less than 4.0 Å, suggesting π-π interactions. This staggering causes the whole grid to adopt a rhombohedral shape rather than a square. This distortion is accounted for because of the large size of the Pb(II) ion that protrudes from the tridentate pockets provided by the ligand, allowing additional molecules of water and triflate anions to coordinate. This gives a mixture of six, seven and eight coordinate Pb(II) ions. However, the distribution of donors around the cations is not symmetrical which is clearly indicated by Fig. 67. This void in coordination is attributed to the presence of the $6s^2$ stereochemically active lone pair of electrons that are frequently observed in Pb(II) structures[105b] and is likely to contribute to the overall distortion of the grid. Interestingly, the plane of sixteen Pb(II) ions is essentially flat with a torsion angle between the four corner ions (Pb1, Pb4, Pb13, Pb16) of 6° and consequently the individual [2 x 2] grids have an average torsion angle of 1.4°.

Table 27 Selected bond lengths/ Å for $[Pb_{16}(\mathbf{L2}\text{-}2H)_8(OTf)_6(H_2O)_5]^{+16}$ cation.

Pb1-O1	2.420(15)	Pb2-N4	2.428(19)	Pb5-O121	2.272(14)	Pb6-O151	2.482(15)
Pb1-N121	2.451(19)	Pb2-N151	2.474(18)	Pb5-O31	2.370(15)	Pb6-N34	2.503(18)
Pb1-N122	2.625(19)	Pb2-N6	2.555(17)	Pb5-N124	2.498(19)	Pb6-N36	2.535(17)
Pb1-N2	2.664(19)	Pb2-O1	2.556(15)	Pb5-N32	2.595(17)	Pb6-O31	2.567(14)
Pb1-O301	2.668(18)	Pb2-N152	2.622(19)	Pb5-N31	2.823(18)	Pb6-N154	2.72(2)
Pb1-O121	2.771(14)	Pb2-O151	2.772(15)	Pb5-N126	2.891(18)	Pb6-O319	2.756(17)
Pb1-N1	2.804(19)					Pb6-N156	2.949(18)

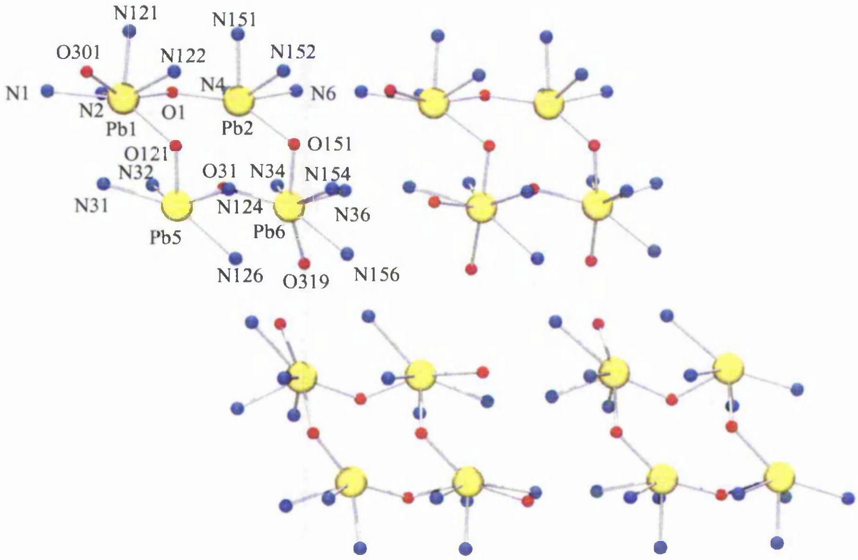

Figure 68 POV-Ray representation of $[Pb_{16}(\mathbf{L2}\text{-}2H)_8]^{+16}$ inner core.

The subsets of [2 x 2] grids have separations ranging from ~ 7.0 to ~ 7.8 Å. This variation is due to the unsymmetrical distortion of the grid, *i.e.*, one set of ligands is more staggered than the other. The μ-O alkoxide separations have a range from ~ 4.1 to ~ 4.4 Å and a bridge angle ranging from ~ 111 to ~ 119° (Table 28). The separations are considerably larger than those seen with first row transition metal ions and consequently the bond angles are considerably smaller. The bond lengths do not show any real pattern except that the shortest are associated with the alkoxide ions (~ 2.3 Å) and the longest with the less basic N_{pym} (~ 3.0 Å) (Table 27).

Table 28 Selected bond angles/ ° for $[Pb_{16}(\mathbf{L2}\text{-}2H)_8]^{+16}$ cation.

O1-Pb1-N121	81.7(8)	N4-Pb2-N152	136.3(7)	N32-Pb5-0331	151.3(5)
O1-Pb1-N122	81.6(7)	N151-Pb2-N152	63.6(5)	N31-Pb5-0331	95.5(6)
N121-Pb1-N122	64.1(5)	N6-Pb2-N152	81.4(7)	N126-Pb5-0331	64.5(6)
O1-Pb1-N2	64.0(5)	O1-Pb2-N152	135.7(6)	0151-Pb6-N34	88.2(6)
N121-Pb1-N2	88.3(7)	N4-Pb2-0151	126.9(6)	0151-Pb6-N36	82.1(7)
N122-Pb1-N2	139.0(6)	N151-Pb2-0151	121.7(6)	N34-Pb6-N36	63.5(5)
O1-Pb1-0301	148.9(6)	N6-Pb2-0151	74.1(6)	0151-Pb6-031	82.9(6)
N121-Pb1-0301	70.7(7)	O1-Pb2-0151	151.3(6)	N34-Pb6-031	61.8(5)
N122-Pb1-0301	73.9(7)	N152-Pb2-0151	59.7(5)	N36-Pb6-031	123.4(5)
N2-Pb1-0301	127.0(6)	0121-Pb5-031	84.2(6)	0151-Pb6-N154	59.8(5)
O1-Pb1-0121	81.1(6)	0121-Pb5-N124	67.0(5)	N34-Pb6-N154	139.3(6)
N121-Pb1-0121	123.6(6)	031-Pb5-N124	79.9(6)	N36-Pb6-N154	86.2(6)
N122-Pb1-0121	60.5(4)	0121-Pb5-N32	87.2(6)	031-Pb6-N154	129.5(5)
N2-Pb1-0121	129.0(6)	031-Pb5-N32	65.2(5)	0151-Pb6-0319	154.2(6)
0301-Pb1-0121	102.4(5)	N124-Pb5-N32	138.7(6)	N34-Pb6-0319	74.8(6)
O1-Pb1-N1	122.2(6)	0121-Pb5-N31	74.4(6)	N36-Pb6-0319	73.1(6)
N121-Pb1-N1	88.4(7)	031-Pb5-N31	120.9(5)	031-Pb6-0319	104.9(5)
N122-Pb1-N1	141.7(6)	N124-Pb5-N31	133.9(6)	N154-Pb6-0319	123.7(5)
N2-Pb1-N1	59.0(5)	N32-Pb5-N31	59.4(5)	0151-Pb6-N156	112.7(5)
0301-Pb1-N1	71.9(6)	0121-Pb5-N126	125.0(5)	N34-Pb6-N156	132.3(5)
0121-Pb1-N1	144.5(6)	031-Pb5-N126	82.7(6)	N36-Pb6-N156	77.1(6)
N4-Pb2-N151	86.9(7)	N124-Pb5-N126	58.1(5)	031-Pb6-N156	157.0(6)
N4-Pb2-N6	63.9(5)	N32-Pb5-N126	132.5(6)	N154-Pb6-N156	55.6(5)
N151-Pb2-N6	85.6(8)	N31-Pb5-N126	152.8(6)	0319-Pb6-N156	68.8(5)
N4-Pb2-O1	63.2(5)	0121-Pb5-0331	99.9(6)	N24-Pb5-0331	68.2(6)
N151-Pb2-O1	83.0(7)	031-Pb5-0331	142.8(6)		
N6-Pb2-O1	126.3(6)				

*Complexation: **L2**(Mn(II))*

Working with Mn(II) salts having non-coordinating anions (*i.e.*, perchlorate, tetrafluoroborate, triflate and nitrate), solvents and stoichiometries initially only gave powders which could not be crystallised. After numerous attempts very small almost black crystals were obtained when **L2** was reacted with excess $Mn(OTf)_2$ in a mixture of ethanol, methanol and acetonitrile which were used for subsequent analysis.

Solution Studies: ***L2*** *(Mn(II))*

Examination of the crystals by ESI-MS in acetonitrile at 70 °C with a range of cone voltages (0-20 V) gave a relatively clean spectrum with a distinct series of peaks (Fig. 69). Analysis of these peaks suggested an assembly with a molecular weight of approximately 7500 units with a charge of +16. While the charge would indicate an assembly with sixteen metal ions the molecular weight would only suggest twelve Mn(II) ions present. No reversible electrochemical behaviour was observed in acetonitrile over the range -2 to 2 V, in addition, irreversible peaks typically associated with ligand reduction were absent.

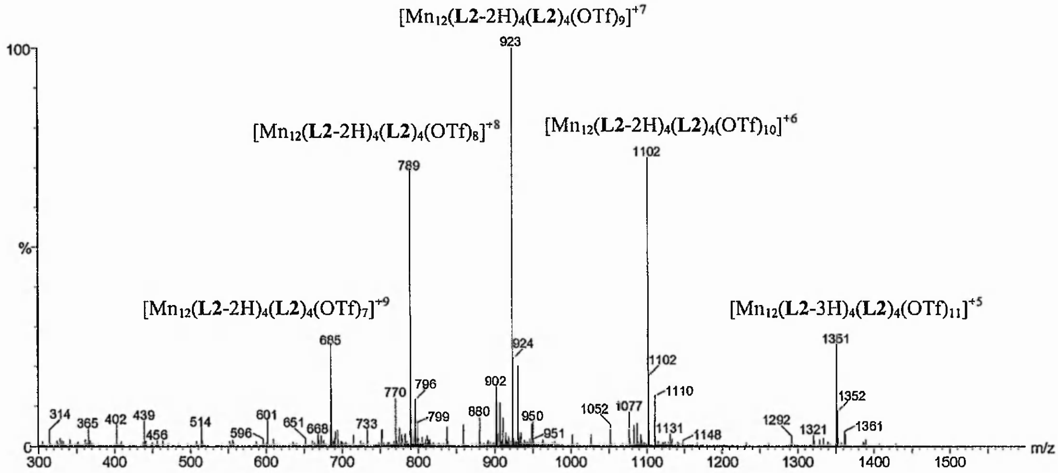

Figure 69 ESI-MS of $[Mn_{12}(\mathbf{L2}\text{-}2H)_4(\mathbf{L2})_4(OTf)_{16}]$ in acetonitrile at 10 V and 70 °C.

Solid-State Studies: $[Mn_{12}(\mathbf{L2}\text{-}2H)_4(\mathbf{L2})_4](OTf)_{16}\cdot 14H_2O$ *(**A16**)*

Examination of the crystals used for the solution studies *via* a synchrotron X-ray source indicated that a [4 x 4] grid motif had been formed, however the structure only contained twelve Mn(II) with the four central potential coordination sites vacant. The structure, even though not fully occupied, is only the second structure ever reported to contain twelve Mn(II)[106] ions and is best described as a [4 x (3)] grid of triangles.

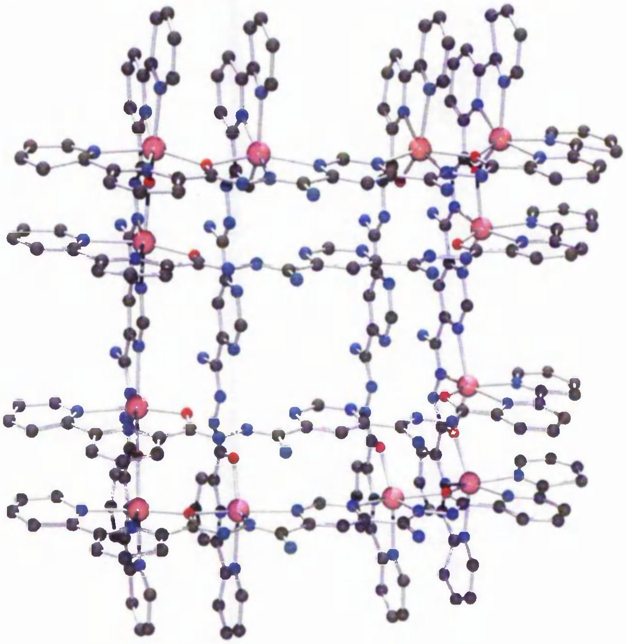

Figure 70 POV-Ray representation of $[Mn_{12}(\mathbf{L2}\text{-}2H)_4(\mathbf{L2})_4]^{+16}$ cation.

Table 29 Bond angles/ ° and lengths/ Å for $[Mn_{12}(\mathbf{L2}\text{-}2H)_4(\mathbf{L2})_4]^{+16}$ cation.

O6-Mn1-N13	121	N12-Mn1-O5	102	O5-Mn2-O5	101	Mn1-O6	2.11
O6-Mn1-N12	74	N12-Mn1-N2	116	O5-Mn2-N11	73	Mn1-N13	2.14
O6-Mn1-O5	97	N12-Mn1-N20	72	O5-Mn2-N11	124	Mn1-N12	2.20
O6-Mn1-N2	97	O5-Mn1-N2	142	O5-Mn2-N19	93	Mn1-O5	2.22
O6-Mn1-N20	146	O5-Mn1-N20	93	O5-Mn2-N19	143	Mn1-N2	2.34
N13-Mn1-N12	163	N2-Mn1-N20	96	N11-Mn2-N11	156	Mn1-N20	2.35
N13-Mn1-O5	71			N11-Mn2-N19	93	Mn2-O5	2.16
N13-Mn1-N2	72			N11-Mn2-N19	70	Mn2-N11	2.16
N13-Mn1-N20	93			N19-Mn2-N19	96	Mn2-N19	2.28

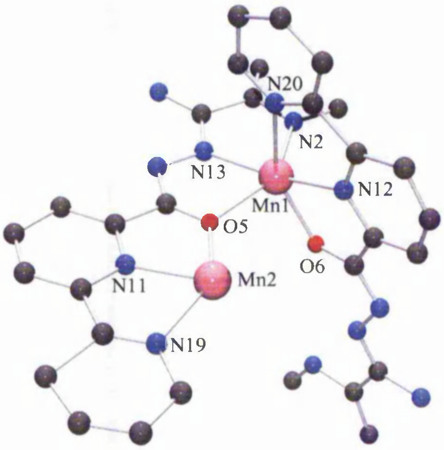

Figure 71 POV-Ray representation of $[Mn_{12}(\mathbf{L2}\text{-}2H)_4(\mathbf{L2})_4]^{+16}$ asymmetric unit.

The structure obtained is of low precision with only the central cation being clear (Fig. 70). The cation has an *I4* space group with each of the four identical corners consisting of three Mn(II) ions and in addition, there is a plane of symmetry running diagonal from the centre of the side of the grid to the opposing side. The cation has a long dimension in the region of 24.3 Å with an internal metal square dimension of approximately 14.2 Å. The four parallel pairs of ligands lie above and below the mean plane of Mn(II) ions with π-π separations between individual ligands less than 3.8 Å. Each triangular subunit of Mn(II) ions that are separated by a pyrimidine bridge giving long metal-metal distances around 6.6 Å, similar to those observed in [2 x 2][41] and [3 x 3][46] (~ 6.5 Å) grids. Within the triangular subunit the metal-metal separations are typical for Mn(II) bridged by alkoxide with a value around 3.9 Å.[4c] All the alkoxide bridges create a bond angle between the metal centres around 128° that again is typical of Mn(II) in this type of structure.[4c] The Mn(II) ions have a distorted octahedral *cis*-N_4O_2 coordination geometry with the basal plane in the mean plane of the square of Mn(II) ions, for example the corner ion has its basal plane consisting of two terminal N_{py} donors and two alkoxide bridges. The bond lengths formed around each ion are not particularly interesting, with slightly longer bonds around ~ 2.34 Å associated with the less basic N_{pym} (Table 29).

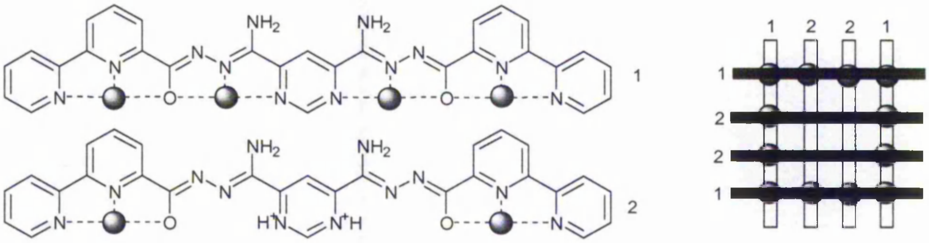

Figure 72 Proposed ligand binding modes in $[Mn_{12}(\mathbf{L2}\text{-}2H)_4(\mathbf{L2})_4](OTf)_{16}$.

From the combination of ESI-MS, IR and preliminary X-ray crystallography it is suggested that a total of eight protons associated with the ligands have been retained by the cation increasing its charge to +16 rather than the expected +8. From this information it is proposed that the outer four ligands have a charge of -2 because they are fully coordinated and the inner four ligands that make up the hash structure are still neutral (see Fig. 72: hash = 2, 2, 2, 2). The protons associated with this second set of ligands could be bound to the central N_{pym} consequently stopping the binding of further cations. Examination of the IR spectrum indicates two distinct carbonyl stretches, one of which was been shifted downfield from the free ligand implying it has more single bond character (1680 to 1654 cm^{-1}) therefore it is acting as an alkoxide bridge, whilst the second peak appears in a very similar position to that observed in the free ligand (1680 to 1694 cm^{-1}) suggesting no metal binding. As a result, the structural formula is proposed to be $[Mn_{12}(\mathbf{L2}\text{-}2H)_4(\mathbf{L2})_4](OTf)_{16}$.

*Magnetism: $[Mn_{12}(\mathbf{L2}\text{-}2H)_4(\mathbf{L2})_4](OTf)_{16}$ (**A16**)*

Variable temperature magnetic susceptibility measurements were made on a powdered sample of $[Mn_{12}(\mathbf{L2}\text{-}2H)_4(\mathbf{L2})_4](OTf)_{16}\cdot 14H_2O$. The raw data obtained from the SQUID were manipulated to give values of χ_m that were diamagnetically corrected for both sample holder and organic components of the structure. Determination of the magnitude of the exchange integral can be achieved by modelling of the susceptibility data, which requires the use of a suitable Hamiltonian expression (16).

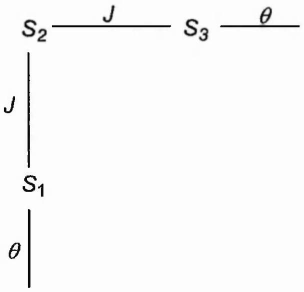

Figure 73 Exchange model for $[Mn_{12}(\mathbf{L2}\text{-}2H)_4(\mathbf{L2})_4](OTf)_{16}\cdot 14H_2O$.

$$H_{ex} = -2J\{S_1 \cdot S_2 + S_2 \cdot S_3\} \qquad (16)$$

Modelling of this data as a ring of twelve Mn(II) ions with two exchange integrals to represent coupling across the alkoxide bridge and the pyrimidine ring exceeds the capability of most modern day computers because of the size of the matrix generated.[4c] The largest example of a modelled assembly with individual metal spins of $S = 5/2$ is for a ring of eight with only one exchange integral.[107] However, a simpler model can be used by, dividing the structure into four separate trinuclear subunits and accommodating the interaction across the pyrimdine ring by the incorporation of a θ value (Fig 73). This assumption is reasonable because the pyrimidine heterocycle has only been shown to propagate exchange in the order $J = -0.2\ \mathrm{cm}^{-1}$.[108]

Examination of a plot of effective magnetic moment versus temperature shows a steady decrease with decreasing temperature from a room temperature of 10.06 μ_b down to 4.65 μ_b at 5 K (Fig. 78). This decrease is indicative of antiferromagnetic exchange and the room temperature value of effective magnetic moment, per trimer, is in good agreement with the spin-only value for three spins of $S = 5/2$, 10.25 μ_b. Modelling of the data as previously discussed and applying the Hamiltonian (16) yields a fit a good fit of the data with $g = 2.03$, $J = -3.15\ \mathrm{cm}^{-1}$, $\theta = -2.91$ K and $10^2 R = 0.91$ between 5 and 300 K. These values are in good agreement with similar Mn(II) alkoxide bridged systems.[4c]

*Complexation: **L2** (Mn(II) + base)*

To overcome the incomplete coordination observed in $[\mathrm{Mn}_{12}(\mathbf{L2}\text{-}2\mathrm{H})_4(\mathbf{L2})_4](\mathrm{OTf})_{16}$ numerous bases were added in different stoichiometries in a number of different manners. However, this frequently led to the formation of oils or insoluble precipitates. After numerous attempts, it was discovered that after addition of **L2** to excess $\mathrm{Mn(OTf)_2}$ in aqueous acetonitrile, the solution could tolerate one equivalent of triethylamine. Upon standing, a dark solid precipitated which was crystallised by the slow evaporation of a concoction of n-propanol, methanol, acetonitrile and a small amount of water (10:3:6:1) .

*Solution Studies: **L2** (Mn(II) + base)*

Examination of the crystals formed above by ESI-MS in acetonitrile with a range of cone voltages (0-20 V) at 70 °C produced spectra that contained numerous clusters of peaks that could not be assigned. No reversible electrochemical behaviour was observed in acetonitrile over the range -2 to 2 V, in addition, irreversible peaks typically associated with ligand reduction were absent.

Solid-State Studies: $[Mn_{16}(\mathbf{L2}\text{-}2H)_8](OTf)_{16}\cdot 2H_2O\cdot 10MeOH$ (**A17**)

Analysis of the crystals *via* a synchrotron X-ray source structurally characterised the assembly. The structure has a large central cation surrounded by sixteen triflate anions and probably numerous solvent molecules (Fig. 74). The cation consists of eight parallel ligands that are subdivided into pairs; two pairs situated above the mean plane of sixteen Mn(II) ions and the other two pairs below the mean plane of Mn(II) ions. The cation appears to be essentially the same as $[Mn_{12}(\mathbf{L2}\text{-}2H)_4(\mathbf{L2})_4](OTf)_{16}$ but, due to the addition of base, this structure is completely metallated with the four central cavities being occupied by Mn(II) ions. This is the first ever example of a complete [4 x 4] grid containing paramagnetic metal ions. However, the grid is subdivided into four individual [2 x 2] grids, a consequence of the pyrimidine linker and therefore is more suitably described as a [4 x (2 x 2)] grid of grids and is analogous to the Pb_{16} assembly.

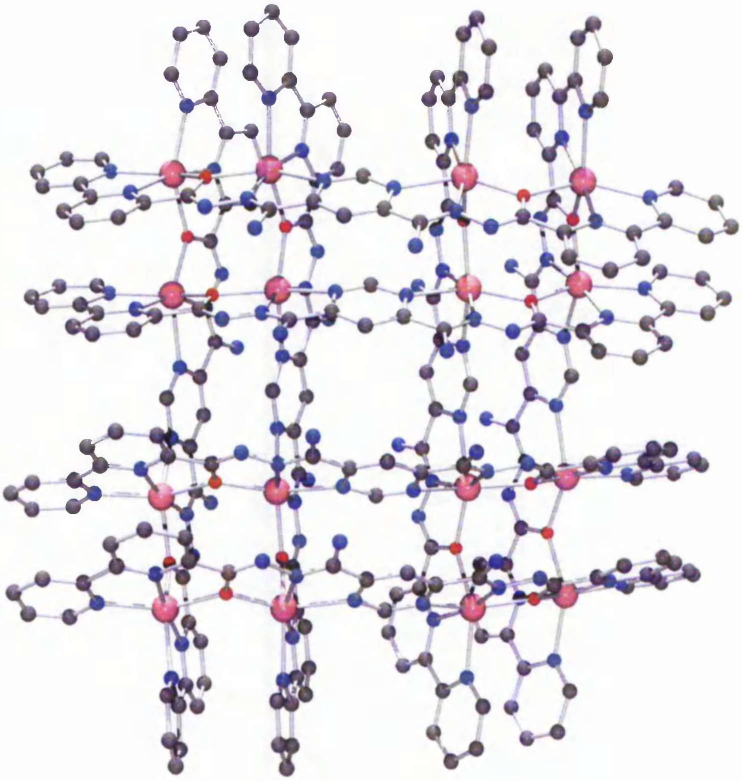

Figure 74 POV-Ray representation of $[Mn_{16}(\mathbf{L2}\text{-}2H)_8]^{+16}$ cation.

Table 30 Selected bond lengths/ Å for $[Mn_{16}(\mathbf{L2}\text{-}2H)_8]^{+16}$ cation.

Mn1-O1	2.178(5)	Mn2-O1	2.159(5)	Mn5-O3	2.139(5)	Mn6-O3	2.195(5)
Mn1-N2	2.195(6)	Mn2-N6	2.344(6)	Mn5-N14	2.179(6)	Mn6-N18	2.329(6)
Mn1-N49	2.286(7)	Mn2-N61	2.276(7)	Mn5-N52	2.130(6)	Mn6-N64	2.201(6)
Mn1-N1	2.286(7)	Mn2-N4	2.116(6)	Mn5-N13	2.229(7)	Mn6-N16	2.205(6)
Mn1-O9	2.213(5)	Mn2-O11	2.180(5)	Mn5-O9	2.166(5)	Mn6-O11	2.180(5)
Mn1-N50	2.178(6)	Mn2-N62	2.165(6)	Mn5-N54	2.423(7)	Mn-N66	2.336(6)

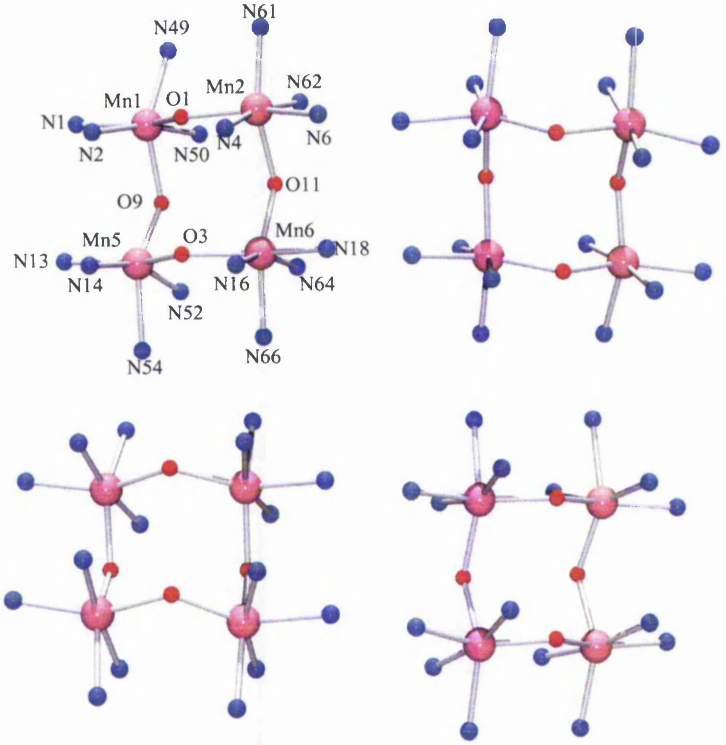

Figure 75 POV-Ray representation of $[Mn_{16}(\mathbf{L2}\text{-}2H)_8]^{+16}$ inner core.

Examination of cation reveals very similar details to $[Mn_{12}(\mathbf{L2}\text{-}2H)_4(\mathbf{L2})_4](OTf)_{16}$ with an external and internal dimension of ~ 24.0 Å and ~ 14.1 Å respectively. However, adjacent aromatic rings are not parallel to each other because of the overall grid distortion. This is best observed by examining a single ligand strand (Fig. 76), which indicates each ligand is severely bent to allow complete binding within the tridentate pockets. This bending occurs because of the flexible nature of the diazine link and could explain the downfall of other ligand designs.

Table 31 Selected bond angles/ ° for $[\mathrm{Mn}_{16}(\mathbf{L2}\text{-}2\mathrm{H})_8]^{+16}$ cation.

O1-Mn1-N1	142.3(2)	O11-Mn2-N62	74.0(2)	N14-Mn5-N54	87.7(2)
O1-Mn1-O9	94.66(18)	O1-Mn2-O11	95.37(18)	O9-Mn5-N54	142.9(2)
O1-Mn1-N50	109.0(2)	O1-Mn2-N62	116.1(2)	O3-Mn5-N13	144.3(2)
N1-Mn1-O9	97.8(2)	N4-Mn2-O11	96.9(2)	O3-Mn5-O9	98.42(19)
N1-Mn1-N50	108.7(2)	N4-Mn2-N62	167.3(2)	O3-Mn5-N54	92.6(2)
N2-Mn1-N49	120.3(2)	N6-Mn2-N61	100.1(2)	N16-Mn6-N64	159.2(2)
O9-Mn1-N49	144.4(2)	O11-Mn2-N61	146.3(2)	N18-Mn6-O11	94.9(2)
N49-Mn1-N50	71.8(2)	N61-Mn2-N62	72.5(2)	N18-Mn6-N66	98.2(2)
O1-Mn1-N2	72.1(2)	N6-Mn2-O11	88.67(19)	O11-Mn6-N66	139.6(2)
O1-Mn1-N49	94.1(2)	N6-Mn2-N62	99.8(2)	O3-Mn6-N16	70.6(2)
N1-Mn1-N2	71.4(2)	N14-Mn5-O9	129.4(2)	O3-Mn6-O11	102.41(19)
N1-Mn1-N49	96.0(2)	N13-Mn5-O9	96.2(2)	O3-Mn6-N66	91.6(2)
N2-Mn1-O9	95.3(2)	N13-Mn5-N54	95.1(2)	N16-Mn6-O11	127.1(2)
N2-Mn1-N50	168.0(2)	N14-Mn5-N52	156.8(2)	N16-Mn6-N66	93.3(2)
O9-Mn1-N50	72.7(2)	O9-Mn5-N52	73.8(2)	N18-Mn6-N64	100.0(2)
O1-Mn2-N4	72.9(2)	N52-Mn5-N54	69.1(2)	O11-Mn6-N64	70.6(2)
O1-Mn2-N6	143.54(19)	O3-Mn5-N14	73.8(2)	N64-Mn6-N66	69.5(2)
O1-Mn2-N61	96.4(2)	O3-Mn5-N52	107.1(2)	O3-Mn6-N18	139.8(2)
O1-Mn1-N2	142.3(2)	O11-Mn2-N63	74.0(2)	N14-Mn5-N55	87.7(2)
O1-Mn1-O10	94.66(18)	O1-Mn2-O12	95.37(18)	O9-Mn5-N55	142.9(2)

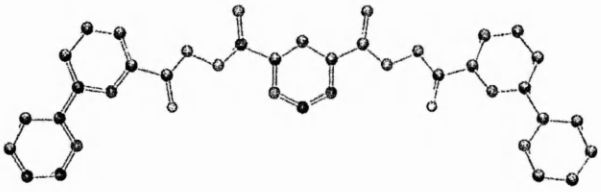

Figure 76 POV-ray representation of (**L2**-2H) in $[\mathrm{Mn}_{16}(\mathbf{L2}\text{-}2\mathrm{H})_8]^{+16}$ cation.

Furthermore, this bending causes considerable distortion between the individual [2 x 2] grids demonstrated by the torsion angle between the corner Mn(II) ions (Mn1, Mn4, Mn13, Mn16) which has a value ~ 31°. Whilst, within each subset, the torsion angle between the Mn(II) ions has an average value of 9.3° which is similar to that observed in the homonuclear [2 x 2] grid, 12.7°. The separation *via* the pyrimidine rings between adjacent subsets has an average distance around 6.5 Å with only a very small deviation around 0.1 Å between the outer and inner bridge Mn(II) ions. Within each subset the average metal-metal separation is ~ 3.9 Å giving bridging bond angles around 128°, both of which are typical for this type of system (Table 30 and

31).[4c] The Mn(II) ions have a distorted *cis*-N_4O_2 octahedral configuration with their basal planes consisting of two alkoxide donors and two $N_{py/pym}$ donors which all lie in the mean plane of Mn(II) ions. The bond lengths and angles are not extraordinary, however, there are a number of long bonds to bridging N_{pym} donors ranging from 2.306(6) to 2.423(7) Å which are associated with its low donor power.

*Magnetism: [Mn$_{16}$(**L2**-2H)$_8$](OTf)$_{16}$ (**A17**)*

Variable temperature magnetic susceptibility measurements were made on a powdered sample of $[Mn_{16}(\mathbf{L2}\text{-}2H)_8](OTf)_{16}\cdot 2H_2O\cdot 10MeOH$. The raw data obtained from the SQUID were manipulated to give values of χ_m that have been diamagnetically corrected for both sample holder and organic components of the structure.

Modelling of the data becomes complicated with a total of sixteen Mn(II) ions and even with a very simplified view a minimum of two separate J values are required. Consequently a simplified model (Fig. 77) based upon the $[Mn_{12}(\mathbf{L2}\text{-}2H)_4(\mathbf{L2})_4](OTf)_{16}$ example discussed previously is introduced where the motif is assumed to be four separate [2 x 2] grids (Chapter Three) with a θ accounting for weak interactions across the bridging pyrimidine rings.

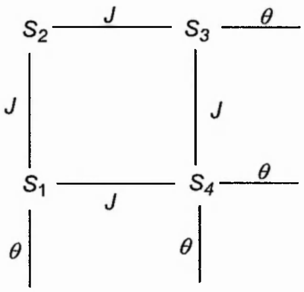

Figure 77 Exchange model for $[Mn_{16}(\mathbf{L2}\text{-}2H)_8](OTf)_{16}$.

Upon cooling the magnetic susceptibility shows a steady increase until approximately 25 K where a slight decrease is observed, which is indicative of antiferromagnetic exchange. Upon further cooling down to 2 K there is a rapid

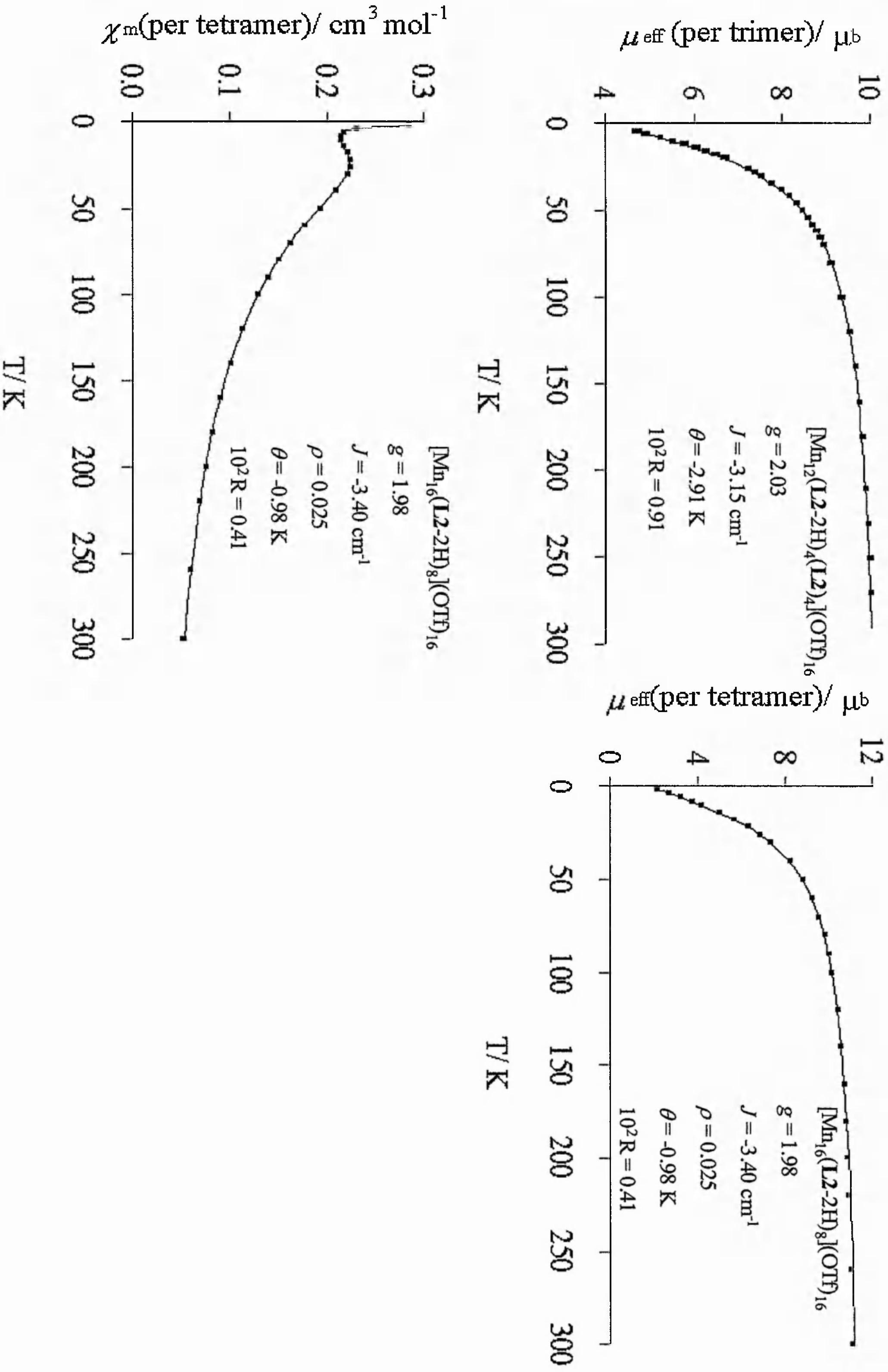

Figure 78 Top right: [Mn_{12}(**L2**-2H)$_4$(**L2**)$_4$](OTf)$_{16}$ (**A16**) displaying antiferromagnetic exchange, top left: [Mn_{16}(**L2**-2H)$_8$](OTf)$_{16}$ (**A17**) displaying large paramagnetic impurity and bottom right [Mn_{16}(**L2**-2H)$_8$](OTf)$_{16}$ (**A17**) displaying antiferromagnetic exchange.

increase in magnetic susceptibility that appears to be associated with all completely coordinated grid-like Mn(II) motifs. The room temperature effective magnetic moment, per tetramer, has a value of 11.02 μ_b which is in acceptable agreement with four spin-only Mn(II) ions, 11.80 μ_b. Accordingly, fitting as a homometallic [2 x 2] grid with four spins of $S = 5/2$ yields an excellent fit of the data with $g = 1.98$, $J = -3.40$ cm^{-1}, $\rho = 0.025$, $\theta = -0.93$ K and 10^2 R = 0.41 (Fig. 78).

Other Metal Ions

The characterisation of grid-like assemblies is heavily dependent on the formation of single crystals suitable for X-ray analysis. For other first row transition metal ions this has not been achieved, even after numerous attempts with different anions, solvents, bases and reaction conditions. The powders obtained were analysed by ESI-MS in acetonitrile at ranging cone voltages at 70 °C and produced relatively weak spectra that contained numerous peaks suggesting that the powders are mixtures of species.

*Design: **L3***

L3, analogous to **L2**, provides a linear array of four tridentate pockets that are bridged by a single pyrazine ring and two alkoxy bridges (Fig. 79). These bridging elements should promote electronic communication between metal centres and specifically the pyrazine ring should favour the formation of an interwoven style grid similar to that observed with ligand L(K) (Chapter One).

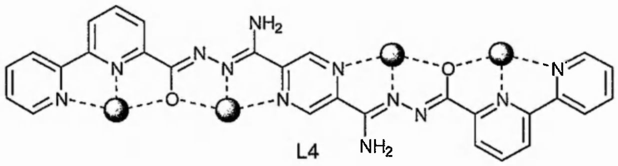

Figure 79 **L3** should promote the formation of an interwoven style [4 x 4] grid.

*Synthesis: **L3***

The synthesis of **L3** requires dimethyl pyrazine-2,5-diimidate (**15**) which can only be prepared from the corresponding dicyano compound (**14**). The latter was easily prepared from the readily available 2,5-dimethylpyrazine *via* acidic oxidation with CrO_3[109] followed by applying the same methodology initially used to prepare 4,6-dicyanopyrimidine (**12**) (*i. e.*, ester to amide to nitrile). This gave a considerably better yield (37 %) for this heterocycle over four steps. No attempt was made to prepare 2,5-dicyanopyrazine (**14**) from the corresponding diiodo compound by reaction with copper(I) cyanide because of the simplicity of the initial scheme.

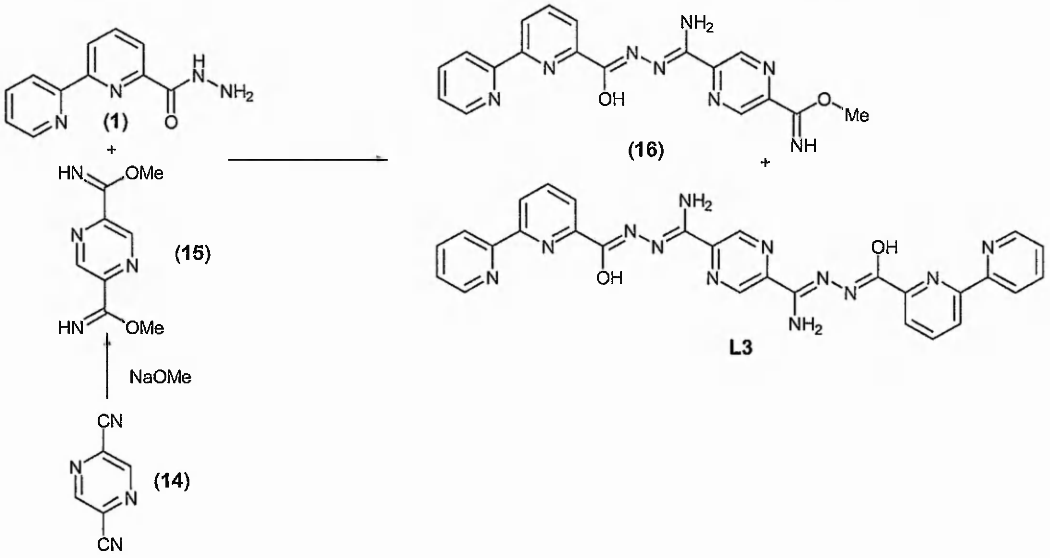

Figure 80 Formation of **L3** and the half product (**15**).

Conversion of 2,5-dicyanopyrazine (**14**) to dimethyl pyrazine-2,5-diimidate (**15**) was achieved using a solution of sodium methoxide in dry MeOH and was easily isolated by filtration as a stable solid. Subsequent reaction of this with 6-hydrazido-2,2'-bipyridine (**1**) in dry methanol yielded a mixture of products that contained the desired **L3** and the half product where only one bipy group has been attached (Fig. 80). It was observed that the preparation of **L2** had worked very cleanly, which had been prepared from the diethyl imidate derivative rather than the dimethyl imidate suggesting greater solubility and therefore reactivity. Attempts to make diethyl pyrazine-2,5-diimidate were unsuccessful because in solution it appears to decompose instantly to the ester (as indicated by TLC and, ^1H and ^{13}C NMR) . Preparation of **L3** was eventually successful using the dimethyl imidate along with larger volumes of methanol and a considerably increased reaction time (~ 48 h, 94 %).

Complexation: ***L3*** *Pb(II)*

Attempts to prepare an interwoven style Pb_{16} grid were unsuccessful. A variety of reaction conditions were employed that generally yielded red powders, which would not crystallise. Analysis of these by ESI-MS in acetonitrile with a range of cone voltages and temperatures, yielded spectra of very low intensity making assignment between observed peaks and any background noise difficult.

Complexation: ***L3*** *Mn(II)*

Addition of **L3** to an excess of $Mn(OTf)_2$ in methanol followed by the addition of water yielded large dark red rods upon standing that were suitable for further analysis.

Solution Studies: ***L3*** *Mn(II)*

Examination of the redissolved crystals in acetonitrile at 70 °C using a range of cone voltages by ESI-MS revealed a series of peaks that correspond to the species $[Mn_{12}(\mathbf{L3}\text{-}H)_8(OTf)_n]^{16-n}$ (n = 7-11). This would suggest that the square Mn_{12} assembly formed with **L2** has been formed here with **L3**. No reversible electrochemical behaviour was observed in acetonitrile over the range -2 to 2 V, in addition, irreversible peaks typically associated with ligand reduction were absent.

Solid-State Studies: $[Mn_{12}(\mathbf{L3}\text{-}2H)_4(\mathbf{L3})_4](OTf)_{16}\cdot 6H_2O\cdot 8MeOH$ *(***A18***)*

The structure is at a higher level of refinement compared to $[Mn_{12}(\mathbf{L2}\text{-}2H)_4(\mathbf{L2})_4](OTf)_{16}$ and it is indicated that there are approximately sixteen anions present confirming the previous assignment for $[Mn_{12}(\mathbf{L2}\text{-}2H)_4(\mathbf{L2})_4](OTf)_{16}$. Therefore it is suggested that not all ligand strands are fully deprotonated with those occupying the central hash structure formally neutral and the likelihood that the remaining protons are associated with the inner pyrazine heterocycle.

The central cation has no internal crystallographic symmetry, with each triangular subunit being slightly different. The external long dimension of the incomplete [4 x

4] grid is around 25.1 Å and the internal square of twelve Mn(II) ions has a dimension around 15.3 Å (Fig. 81). Both these values are larger than those observed with $[Mn_{12}(\mathbf{L2}\text{-}2H)_4(\mathbf{L2})_4](OTf)_{16}$ and is an influence of the central pyrazine ring. Within the parallel pairs of ligands that are observed there are close π-π interactions with separations less than 3.8 Å. The ligands, as designed, interweave through the structure because of the arrangement of substituents on the central pyrazine ring. This bridging ring causes large metal-metal separations between adjacent trinuclear subunits with distances around 8.0 Å, considerably longer than those observed with the pyrimidine ligand. However, this separation is typical, for example the interwoven [2 x 2] grid formed with L(K) has metal-metal separations around 7.6 Å.[52] The longer distances are rationalised here in terms of the steric restraints of the larger [4 x 4] grid.

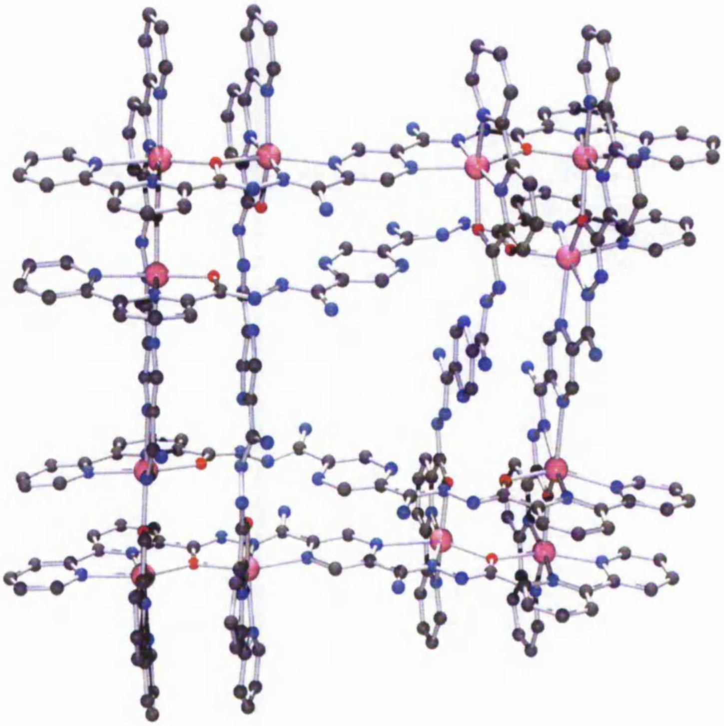

Figure 81 POV-Ray representation of $[Mn_{12}(\mathbf{L3}\text{-}2H)_4(\mathbf{L3})_4]^{+16}$ cation.

Within each triangular subunit the metal-metal separations and bond angles are not particularly different from other motifs with average values of 3.93 Å and 129°, respectively (Table 33). The distorted *cis*-N_4O_2 octahedral Mn(II) ions have their basal planes consisting of two alkoxy donors and two N donors made up from

Table 32 Selected bond lengths/ Å for $[Mn_{12}(\mathbf{L3}\text{-}2H)_4(\mathbf{L3})_4]^{+16}$ cation.

Mn1-N2	2.128(13)	Mn2-O151	2.136(11)	Mn5-N124	2.139(13)
Mn1-O1	2.142(10)	Mn2-N4	2.135(14)	Mn5-O121	2.154(10)
Mn1-N122	2.165(13)	Mn2-N152	2.159(13)	Mn5-O31	2.161(10)
Mn1-O121	2.236(9)	Mn2-O1	2.187(10)	Mn5-N32	2.204(13)
Mn1-N121	2.269(12)	Mn2-N151	2.283(12)	Mn5-N31	2.307(12)
Mn1-N1	2.320(12)	Mn2-N6	2.340(12)	Mn5-N126	2.532(11)

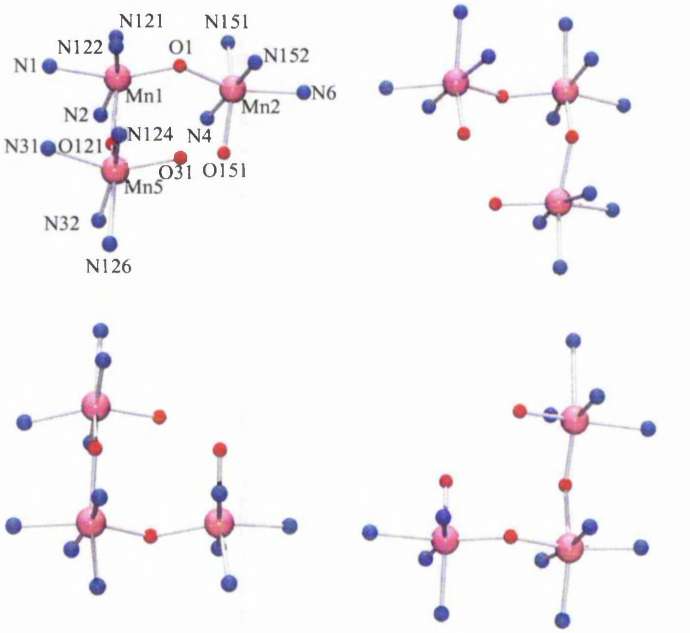

Figure 82 POV-Ray representation of $[Mn_{12}(\mathbf{L3}\text{-}2H)_4(\mathbf{L3})_4]^{+16}$ inner core.

Table 33 Selected bond angles/ ° for $[Mn_{12}(\mathbf{L3}\text{-}2H)_4(\mathbf{L3})_4]^{+16}$ cation.

N2-Mn1-O1	74.5(4)	O151-Mn2-N4	102.4(5)	N124-Mn5-O121	72.8(4)
N2-Mn1-N122	162.1(5)	O151-Mn2-N152	74.0(4)	N124-Mn5-O31	119.2(5)
O1-Mn1-N122	121.7(5)	N4-Mn2-N152	174.2(5)	O121-Mn5-O31	97.3(4)
N2-Mn1-O121	96.3(5)	O151-Mn2-O1	95.3(4)	N124-Mn5-N32	157.4(5)
O1-Mn1-O121	99.7(4)	N4-Mn2-O1	72.7(4)	O121-Mn5-N32	127.3(5)
N122-Mn1-O121	74.3(4)	N152-Mn2-O1	102.8(5)	O31-Mn5-N32	72.4(4)
N2-Mn1-N121	117.5(5)	O151-Mn2-N151	145.0(5)	N124-Mn5-N31	99.5(5)
O1-Mn1-N121	95.1(5)	N4-Mn2-N151	112.6(5)	O121-Mn5-N31	96.8(5)
N122-Mn1-N121	71.6(4)	N152-Mn2-N151	71.2(5)	O31-Mn5-N31	141.2(5)
O121-Mn1-N121	145.6(5)	O1-Mn2-N151	95.7(5)	N32-Mn5-N31	70.3(4)
N2-Mn1-N1	71.2(5)	O151-Mn2-N6	94.8(4)	N124-Mn5-N126	66.7(4)
O1-Mn1-N1	145.4(5)	N4-Mn2-N6	69.7(4)	O121-Mn5-N126	139.2(4)
N122-Mn1-N1	92.9(5)	N152-Mn2-N6	114.8(5)	O31-Mn5-N126	98.6(4)
O121-Mn1-N1	88.0(4)	O1-Mn2-N6	142.4(5)	N32-Mn5-N126	93.4(5)
N121-Mn1-N1	97.0(5)	N151-Mn2-N6	96.4(5)	N31-Mn5-N126	93.8(5)

combinations of N_{py} and N_{pyz}, all of which lie in the mean plane of the square of twelve Mn(II) ions. The bond distances are not unusual, however, there are number of very long bonds towards the N_{pyz} donor, ranging from 2.340(12) to 2.658(13) Å, associated with its low donor power and the rigidity of the ligand (Table 32).

Magnetism: $[Mn_{12}(\mathbf{L3}\text{-}2H)_4(\mathbf{L3})_4](OTf)_{16}\cdot$(**A18**)

Variable temperature magnetic susceptibility measurements were made on a powdered sample of $[Mn_{12}(\mathbf{L3}\text{-}2H)_4(\mathbf{L3})_4](OTf)_{16}\cdot 6H_2O\cdot 8MeOH$. The raw data obtained from the SQUID are manipulated to give values of χ_m that have been diamagnetically corrected for both sample holder and organic components of the structure.

This structure is particularly interesting because it allows comparisons between the central heterocycles and how they affect magnetic exchange. The simplification that allows for the fitting of experimental data of the pyrimidine analogue can also be applied here because pyrazine has been shown to undergo similar weak exchange, $J \sim -0.2$ cm^{-1}.[108] As would be expected, this motif has a similar profile to $[Mn_{12}(\mathbf{L2}\text{-}2H)_4(\mathbf{L2})_4](OTf)_{16}\cdot 14H_2O$ that is a consequence of the alkoxide bridged Mn(II) ion dominating the magnetic interactions. The effective magnetic moment, per trimer, shows a steady decrease from a room temperature value of 9.83 μ_b down to 5.60 μ_b at 5 K and the room temperature value is in good agreement with the spin-only of 10.25 μ_b (Fig. 78). Fitting of the data in the same manner as $[Mn_{12}(\mathbf{L2}\text{-}2H)_4(\mathbf{L2})_4](OTf)_{16}\cdot 14H_2O$ yields an excellent fit with $g = 1.99$, $J = -3.51$ cm^{-1}, $\theta = -0.67$ K and 10^2 R = 0.15. This indicates that in these systems the pyrimidine heterocycle provides a better exchange pathway than the pyrazine ring because of the magnitude of the θ value. This may well be explained by simple structural considerations, because the Mn(II) ions in the pyrimidine motif are separated by an average distance of 6.6 Å, whilst those in the pyrazine have a separation around 8.0 Å. It should be noted that the differences in the exchange integral could also be used to explain the large differences in θ, however to directly compare the two systems by applying the same value of J only led to poor fits of the data.

Complexation: ***L3*** *(Mn(II) + base)*

In an attempt to produce a completely metalated interwoven [4 x (2 x 2)] grid of grids a base, particularly triethylamine, was added in different stoichiometries to a mixture of the ligand and non-coordinating Mn(II) metal salts (*i.e.*, perchlorate, tetrafluoroborate, triflate and nitrate). No single crystals were ever formed but numerous powders were isolated and examined systematically by ESI-MS.

Solution Studies

Examination of the solids by ESI-MS in acetonitrile using varying cone voltages and temperatures generally yielded poor quality spectra that could not be interpreted. However, one example did reveal a relatively clean spectrum, which was prepared by reaction of excess $Mn(BF_4)_2{\cdot}6H_2O$ with **L3** in a aqueous acetonitrile followed by the addition of two equivalents of triethlyamine. The spectrum appears to be a mixture of assemblies all with a charge of +16 and are assigned as $[Mn_{13}(\mathbf{L3}\text{-}2H)_4(\mathbf{L3})_4(BF_4)_n]^{16-n}$ (n = 6-11) and $[Mn_{14}(\mathbf{L3}\text{-}2H)_4(\mathbf{L3})_4(BF_4)_n]^{16-n}$ (n=6-11) (Fig. 83). This vacant coordination could be associated with the low donor power of the central N_{pyz} and ligand restraint both of which cause very long bonds in the analogous Mn_{12} motif. Also the overall charge would suggest that the four central ligands are still protonated blocking complete metal coordination.

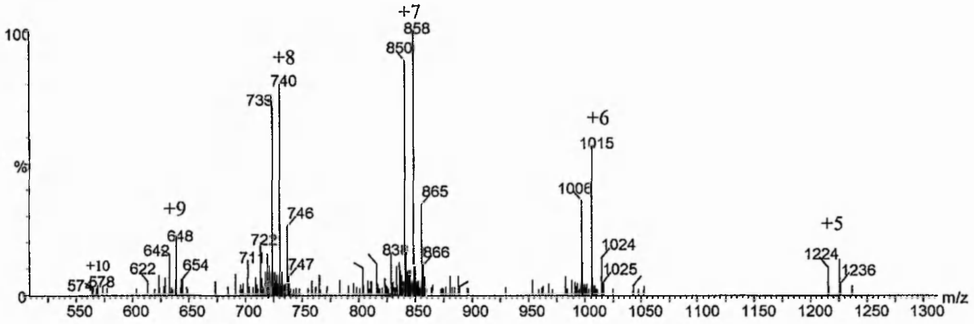

Figure 83 ESI-MS of product formed by reaction of excess $Mn(BF_4)_2$ with **L3** in aqueous acetonitrile followed by the addition of two equivalents of triethylamine at 70 °C and 10 V.

Other Metal Ions

Reaction of **L3** with other first row transition metal ions yielded numerous powders that when examined by ESI-MS in acetonitrile at 70 °C with ranging cone voltages only displayed weak signals similar to those observed with **L2**.

*Design: **L4***

L4 incorporates four tridentate coordination pockets in a bent array that are separated by a mixture of a single pyridazine ring and two alkoxy bridges (Fig. 84). The change in heterocycle does not appear to provide ideal geometry to produce a [4 x 4] grid, however it has been used by Matthews to form an incomplete Cu_{12} square.[62]

*Synthesis: **L4***

L4 was synthesised easily by the reaction of diethyl pyridazine-3,6-diimidate **(18)** and with 6-hydrazido-2,2'bipyridine (1) in boiling dry methanol along with a catalytic amount of glacial acetic acid. Diethyl pyridazine-3,6-diimidate **(18)** was prepared by reaction of 3,6-dicyanopyridazine **(17)** with sodium ethoxide in ethanol (Fig. 84) and 3,6-dicyanopyridazine **(17)** was prepared from 3,6-dichloropyridazine under similar reaction conditions used for 4,6-dicyanopyrimidine **(12)**.

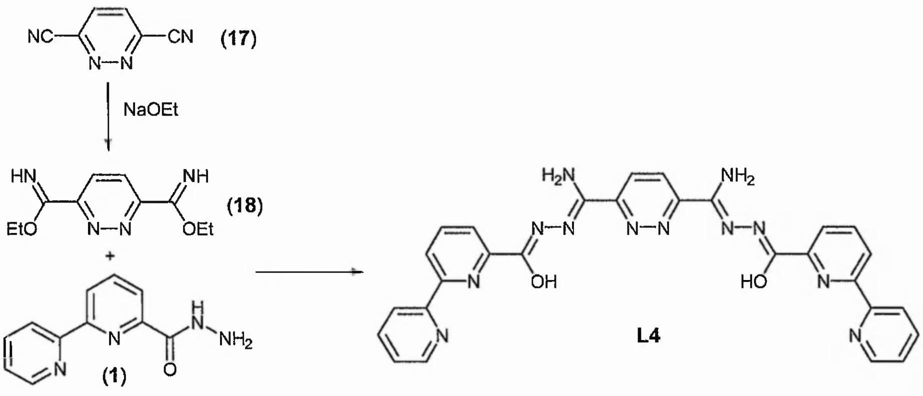

Figure 84 **L4** has bent chain of tridentate pockets that is unlikely to form [4 x 4] grids with transition metal ions that display an octahedral coordination preference.

*Complexation: **L4** Pb(II)*

Examination of the first two ligands, **L2** and **L3**, would suggest that reaction of **L4** with Pb(II) would be unlikely to form a [4 x 4] grid. This is indeed the case. Reaction with of **L4** with $Pb(OTf)_2$ would only yield crystals from a mixture of toluene and acetonitrile when a large excess of metal salt was used.

Solution-Studies: ***L4*** *Pb(II)*

Examination of the redissolved crystals in acetonitrile at 70 °C using a range of cone voltages by ESI-MS revealed a series of peaks that correspond to the species $[Pb_4(\mathbf{L4}\text{-}2H)(OTf)_n]^{6-n}$ (n = 2-4) along with their acetonitrile adducts. Evidence for dimer formation is also observed.

Solid-State Studies: $[Pb_4(\mathbf{L4}\text{-}2H)(OTf)_5(H_2O)_4(MeCN)_3](OTf)$ **(A19)**

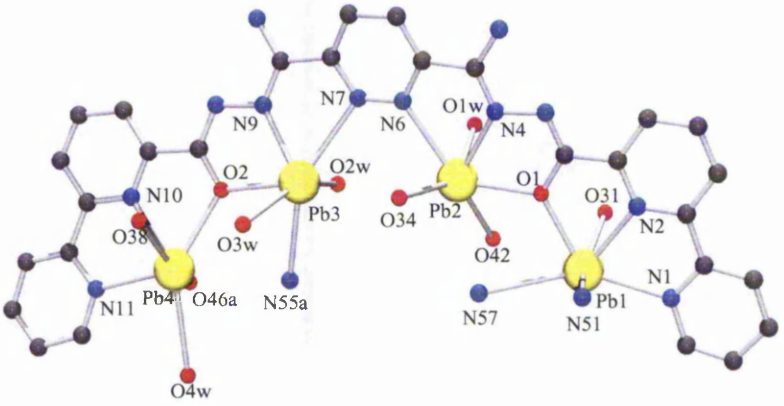

Figure 85 POV-Ray representation of $[Pb_4(\mathbf{L4}\text{-}2H)(OTf)_5(H_2O)_4(MeCN)_3]^+$ cation.

Table 34 Bond lengths/ Å and angles/ ° for $[Pb_4(\mathbf{L4}\text{-}2H)(OTf)_5(H_2O)_4(MeCN)_3]^+$ cation.

Pb1-O1	2.42	Pb2-N4	2.38	Pb3-O2	2.39	Pb4-N11	2.46
Pb1-N2	2.47	Pb2-O1	2.39	Pb3-N9	2.40	Pb4-N12	2.50
Pb1-N51	2.54	Pb2-O1w	2.50	Pb3-O2w	2.55	Pb4-O2	2.52
Pb1-N1	2.55	Pb2-N6	2.64	Pb3-O3w	2.60	Pb4-O38	2.63
Pb1-O31	2.69	Pb2-O34	2.72	Pb3-N7	2.79	Pb4-O46a	2.65
Pb1-N57	3.06	Pb2-O42	2.90	Pb3-N55a	2.83	Pb4-O4w	2.96

The pale orange crystals obtained were suitable for X-ray analysis and the structure obtained was a linear array of four Pb(II) ions with a single ligand strand. The coordination geometry of the Pb(II) ions is completed by a mixture of triflate, water and acetonitrile molecules giving four six coordinate Pb(II) ions. The cation has an external and internal dimension of ~ 21.1 and ~ 11.4 Å respectively and metal-metal separations around 4.3 Å (Fig. 85). The chain of Pb(II) ions is obviously not linear due to steric effects of the ligand with angles for Pb1-Pb2-Pb3 ~ 145° and Pb2-Pb3-Pb4 ~ 144°. The metal ions have a highly distorted geometry similar to that observed in $[Pb_{16}(\mathbf{L2}\text{-}2H)_8(OTf)_6(H_2O)_5](OTf)_{10}(H_2O)_{23}$ due to the presence of a stereochemically active lone pair.[105b] Interestingly, upon drying the chemical analysis results only fit for $[Pb_4(\mathbf{L4}\text{-}2H)(OTf)_5(H_2O)_2](OTf)$ suggesting a change in geometry after drying due to the loss of acetonitrile. Consequently, this result suggested that this particular ligand design is unsuitable for grid formation for those metal ions that display an octahedral coordination preference.

*Complexation: **L4** Mn(II)*

Addition of **L4** to excess $Mn(ClO_4)_2{\cdot}6H_2O$ or $Mn(OTf)_2$ in water followed by the addition of acetonitrile yielded dark red solutions which produced red rod-like crystals upon standing. Interestingly, it was observed that a large amount of water was necessary to cause crystal formation. The following discussion will be concerned with the perchlorate analogue.

*Solution Studies: **L4** Mn(II)*

Examination of the redissolved crystals in acetonitrile at 70 °C using a range of cone voltages by ESI-MS revealed a series of peaks that correspond to the species $[Mn_4(\mathbf{L4}\text{-}H)_4(ClO_4)_n]^{4-n}$ (n = 2-4) along with their acetonitrile adducts. Electrochemical studies in acetonitrile proved difficult due to low solubility, which can be improved by the addition of water that subsequently dominates the spectra. Changing to more polar solvents, for example DMF, does not generate any reversible peaks over the range -2 to 1.4 V.

*Solid-State Studies: $[Mn_4(L4\text{-}H)_4](ClO_4)_4{\cdot}16H_2O$ (**A20**)*

X-Ray analysis indicated a pseudo [2 x 2] grid where tails of the ligand are protruding from the grid core and are surrounded by numerous molecules of water that appear to be necessary to effect crystallisation. It is likely that these tails are held together by various hydrogen bonds and π-π interactions. Consequently the "L" shaped structure has a long dimension around 21.2 Å, which is shorter than **L2** and **L3** because half of the ligand is bound up by hydrogen bonding (Fig. 86).

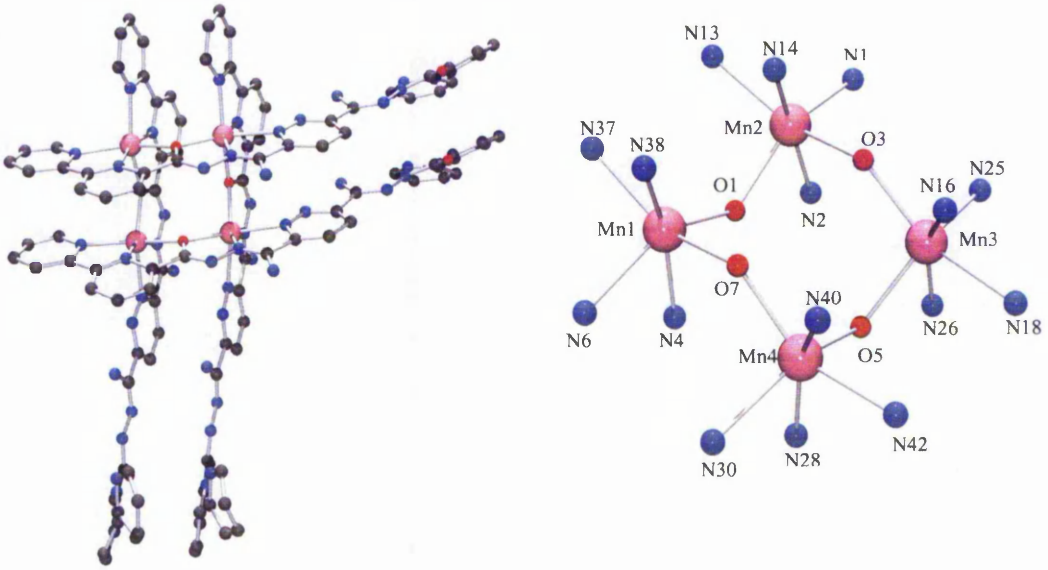

Figure 86 Right: POV-Ray representation of $[Mn_4(\mathbf{L4}\text{-}H)_4]^{+4}$ cation and left: POV-Ray representation of $[Mn_4(\mathbf{L4}\text{-}H)_4]^{+4}$ inner core.

Table 35 Bond lengths/ Å for $[Mn_4(\mathbf{L4}\text{-}H)_4]^{+4}$ cation.

Mn1-N4	2.16	Mn2-N14	2.15	Mn3-O3	2.13	Mn4-N28	2.14
Mn1-O1	2.17	Mn2-O1	2.16	Mn3-N16	2.14	Mn4-O7	2.15
Mn1-N38	2.18	Mn2-N2	2.16	Mn3-N26	2.18	Mn4-N40	2.18
Mn1-O7	2.22	Mn2-O3	2.20	Mn3-O5	2.22	Mn4-O5	2.20
Mn1-N37	2.26	Mn2-N13	2.25	Mn3-N25	2.28	Mn4-N42	2.31
Mn1-N6	2.35	Mn2-N1	2.28	Mn3-N18	2.35	Mn4-N30	2.39

The mean plane of Mn(II) ions are separated by an average distance of 3.92 Å with M-O-M bond angles averaging around 128° with a torsion angle (Mn1-Mn2-Mn3-Mn4) of approximately 1°. This torsion angle is considerably smaller than that observed in the homometallic [2 x 2] grids (~ 12.7°) demonstrating that this assembly is particularly flat. The bond lengths and angles are not extraordinary and rationalised in terms of lower donor power for long bonds associated with the pyridazine ring and ligand restraint (Table 35).

Magnetism: *$[Mn_4(\mathbf{L4}\text{-}H)_4](ClO_4)_4$* (**A20**)

Variable temperature magnetic susceptibility measurements were made on a powdered sample of $[Mn_4(\mathbf{L4}\text{-}H)_4](ClO_4)_4\cdot16H_2O$. The raw data obtained from the SQUID were manipulated to give values of χ_m that have been diamagnetically corrected for both sample holder and organic components of the structure.

This can be seen as a [2 x 2] grid analogous to that prepared in chapter 3. Upon cooling the sample showed a steady increase in magnetic susceptibility until approximately 12 K where a brief plateau occurs that is indicative of antiferromagnetic exchange (Fig. 87). Upon further cooling down to ~ 2 K there is a rapid increase in magnetic susceptibility probably associated with a large paramagnetic impurity (Fig. 87). The effective magnetic moment has a room temperature value of 11.49 μ_b that is in good agreement with the spin-only value for four $S = 5/2$ ions, 11.83 μ_b.

Applying a simple tetranuclear square model as used in chapter 3 with only one exchange integral and with four spins of $S = 5/2$ gives a reasonable fit of the data obtained between 5 and 300 K. This model gives values of $g = 2.01$, $J = -2.71$ cm^{-1}, $\rho = 0.033$ and $10^2R = 1.18$. The inclusion of such a large value of paramagnetic impurity, ρ, is required to fit the data at low temperatures similar to that observed in the homometallic Mn(II) [2 x 2] grid. The values of other parameters are similar in magnitude to other [2 x 2] grids reported here and by others.[4c]

Other Metal Ions

The formation of the Mn(II) [2 x 2] grid with **L4** might suggest other first row transition metal ions forming similar motifs. ESI-MS does not suggest this, however, in the case of a Cu(II) motif prepared by reaction of **L4** with excess $Cu(OTf)_2$ in water and methanol a mixture of peaks are observed with some assigned as the complete Cu_{16} [4 x 4] grid. Unfortunately, attempts to produce suitable crystals or a cleaner spectrum, from samples prepared in various ways, were all unsuccessful.

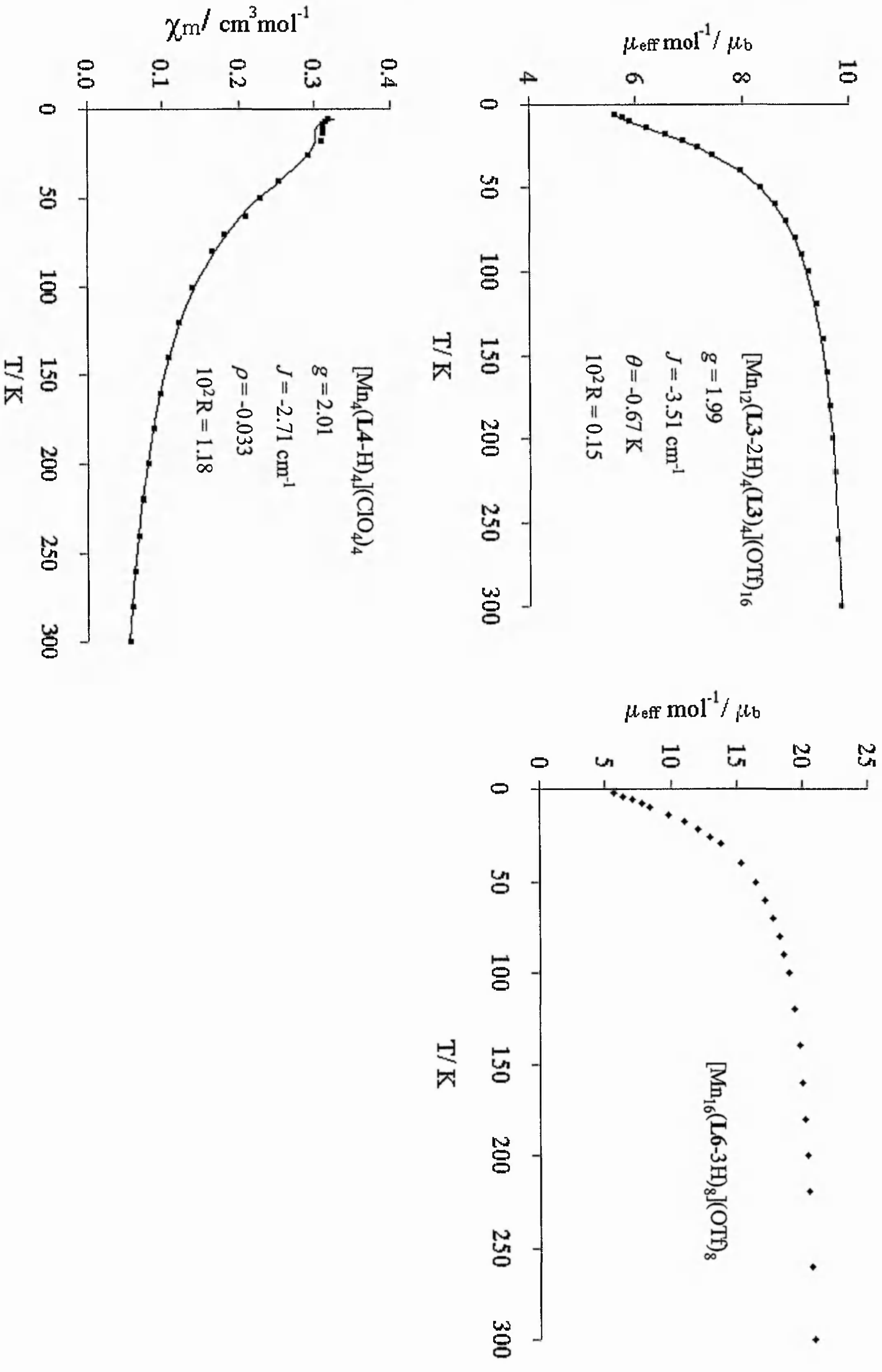

Figure 87 Top right: [Mn$_{12}$(**L3**-2H)$_4$(**L4**)$_4$](OTf)$_{16}$ (**A18**) displaying antiferromagnetic behaviour, top left: [Mn$_4$(**L4**-H)$_4$](ClO$_4$)$_4$ (**A20**) displaying antiferromagnetic behaviour and large paramagnetic impurity and bottom right: [Mn$_{16}$(**L6**-3H)$_8$](OTf)$_8$ (**A22**) displaying antiferromagnetic exchange.

6.2 Further Heterocyclic Bridged Systems

Design: ***L5***

To overcome the lack of assemblies observed with other transition metal ions, rather than just Mn(II), **L2** was redesigned in a logical manner so that the most ideal chelating units are located towards the centre of the ligand strand. As with **L2, L5** provides a linear array of tridentate pockets that are linked by a mixture of a single pyrimidine ring and two alkoxy donors (Fig. 88). However, locating the most ideal chelates towards the centre of the ligand strand should, during the self-assembly process, promote occupation of these inner sites and stop vacant coordination as observed in **(A16)** and **(A17)**.

Synthesis: ***L5***

A reasonable disconnection of **L5** gives the dihydrazide **(19)** and methyl pyridine-2-imidate **(2)** (Fig. 88). The latter of these can be prepared as described previously. There is very little in the literature about substituted 4,6-bis(2-pyridyl)-pyrimidines. The parent heterocycle has been prepared by Case *via* the condensation of the corresponding 1,3-dione with formamide, however the reaction gives low yields.[110] This pathway was considered unsuitable due to the number of synthetic steps and the low yield reported.

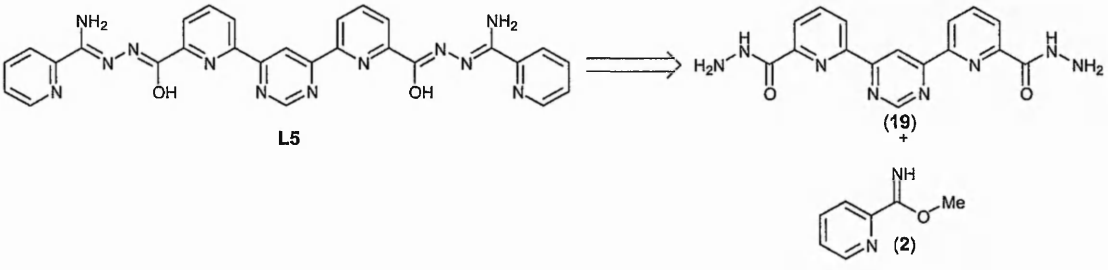

Figure 88 L5 provides a linear array of tridentate pockets with the most ideal chelating groups located towards the centre of the ligand strand. And disconnection of **L5**.

Typical methods for the synthesis of linked aromatic rings include both Suzuki[111] and Stille[112] cross coupling. The former method was initially attempted. Various attempts were made to form the boronic acid including one specific literature example for the methylpyridyl derivative **(22)**[113] and were all unsuccessful (Fig. 89). It appears that the introduction of the alkyl borate is feasible however **(21)**; subsequent hydrolysis even under very mild conditions causes spontaneous deboronation. Other authors have experienced similar problems regarding the introduction of the boronic acid group to the two position on pyridine.[114]

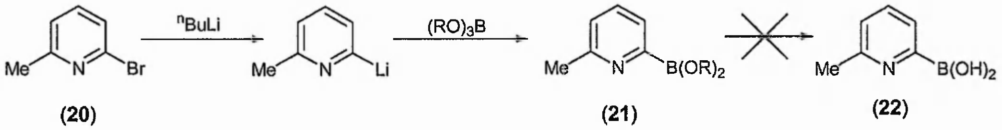

Figure 89 Attempted synthetic scheme for the preparation of six substituted pyridine-2-boronic acid.

Consequently, methodology set out by Stille was followed (Fig. 90). This approach has been used extensively by Lehn to produce similar systems.[69] Lithium-halogen exchange of 2-bromo-6-methylpyridine **(20)** followed by quenching with tri-n-butyltin chloride yields the desired Stille donor **(23)** in good yields after standard workup.[69] Symmetrical coupling of this with 4,6-dichloropyrimidine **(24)** in the presence of $Pd(PPh_3)_2Cl_2$ in DMF gives the dimethyl derivative **(25)** in good a yield (72 %). Attempts to oxidise this compound to give the diacid **(26)** only gave low yields when using CrO_3 in conc. H_2SO_4. However, an improved synthesis has recently been published.[115] At the time this improved synthesis was unpublished and consequently numerous other methods of oxidation were attempted including reactions in non-aqueous solvents using the oxidants selenium dioxide and tetrabutylammonium permanganate, but with no success. A logical way around this is to introduce the desired ester functionality to the Stille donor before the cross coupling **(31)**. There is one example of this in the literature and it is prepared by reaction of a halogenated heteroaromatic ester with hexabutylditin along with a palladium catalyst (Fig. 90).[116] However, applying this methodology and variations on it, only yielded very small quantities of the desired Stille donor.

As a result, the small quantities of diacid obtained were converted to the methyl ester **(27)** by heating in methanol along with a catalytic amount of conc. H_2SO_4. Addition of an excess of hydrazine monohydrate to the diester **(27)** in methanol followed by boiling for two days gave the desired dihydrazide **(28)**. Reaction of this with methyl pyridine-2-imidate (**2**) in methanol along with a catalytic amount of glacial acetic acid gave **L5** in low yields and low purity. Attempts to refine the reaction, including working in other solvents, were not successful.

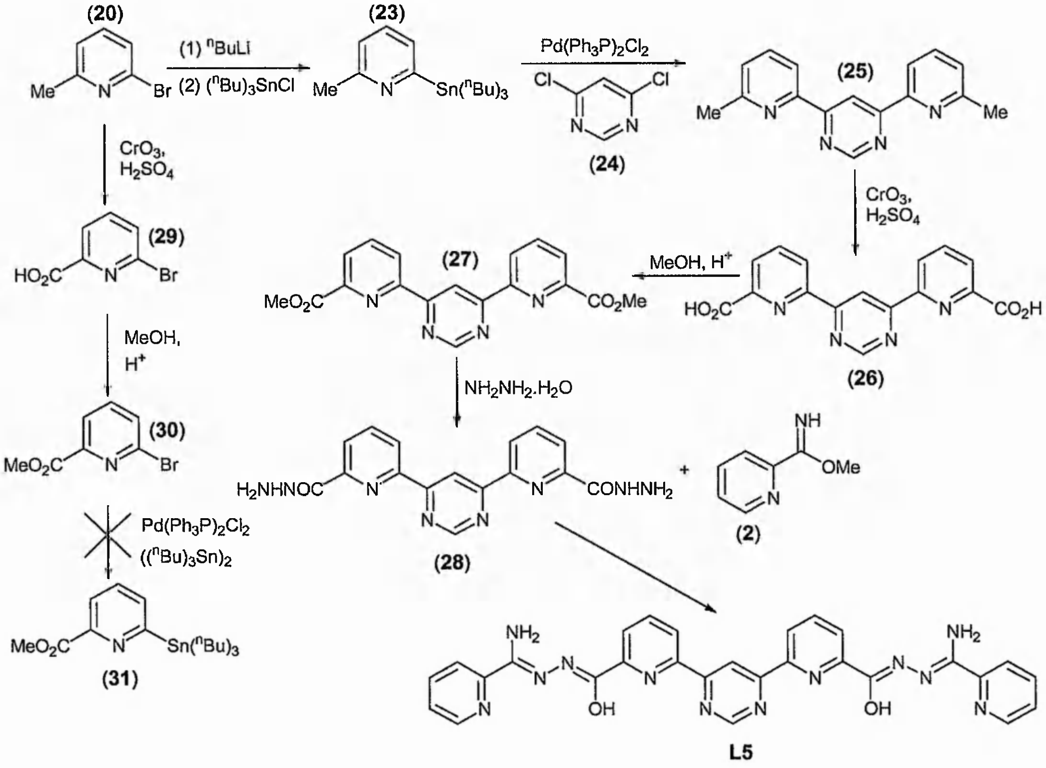

Figure 90 Synthetic scheme for **L5**.

Complexation: L5

Reaction with the small amounts of **L5** obtained gave crystalline material with $Mn(ClO_4)_2{\cdot}6H_2O$, however the crystals were not suitable for X-ray analysis and no evidence *via* ESI-MS was provided to support grid formation or any other structural motif. Furthermore, similar results were observed for the other first row transition metal ions, suggesting that the impure nature of the ligand is hindering the formation of [4 x 4] grids.

6.3 Alkoxy Bridged [4 x 4] Grids

Design: ***L6***

Designing purely alkoxide bridged [4 x 4] ligands is considerably more challenging than those which contain bridging heterocycles. The advantage of such systems is that all metal ions are brought in close proximity causing stronger magnetic and electrochemical exchange with an overall smaller sized grid. During this project a number of ligands were designed based upon purely alkoxide bridged systems, however the majority required the inclusion of phenoxide based systems and the incorporation of hydrolytically sensitive imine bonds (**32**) (Fig. 91).

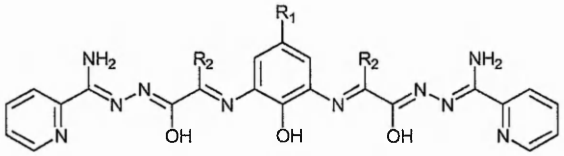

(32)

Figure 91 Example of a [4 x 4] ligand design that contains a phenoxide bridge and hydrolytically sensitive imine bonds.

To overcome these problems an unsymmetrical ligand, **L6**, was designed that contains a linear array of tridentate pockets that are all alkoxide bridged in a similar manner to L(N) which forms homoleptic [3 x 3] grids with selected first row transition metal ions.[4c] However, there were a number of concerns associated with the overall rigidity of the ligand, which may allow the formation of other motifs. Setting these worries aside the synthesis of **L6** was attempted.

Synthesis: ***L6***

The preparation of **L6** was straightforward and yielded large amounts of ligand suitable for further study. Accordingly, reaction of the unsymmetrical ethyl 2-hydrazidopyridine-6-carboxylate (**33**) with ethyl carboethoxyformimidate (**34**) [70] in dry methanol along with a catalytic amount of glacial acetic acid yielded the diester (**35**). Conversion to the dihydrazido (**36**) was achieved by reaction with an excess of hydrazine monohydrate in methanol. Boiling (**36**) with methyl pyridine-2-imidate (**2**) in methanol along with a catalytic amount of glacial acetic acid yielded **L6** (Fig. 92).

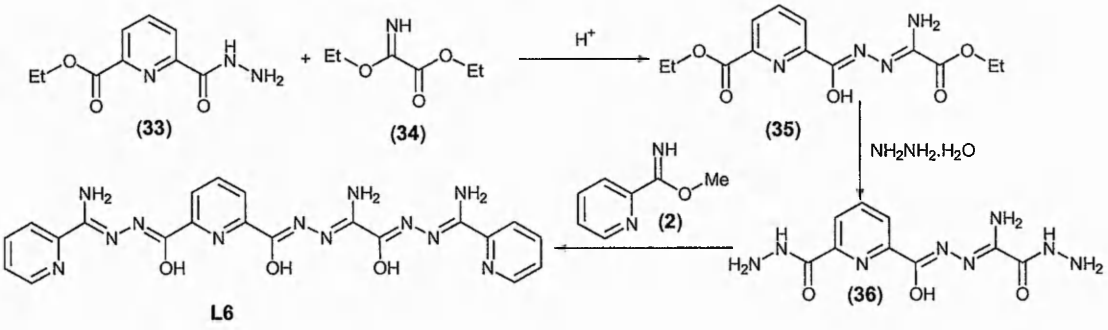

Figure 92 Synthetic pathway applied to form **L6.**

*Complexation: **L6** Pb(II)*

Reaction of **L6** with an excess of $Pb(OTf)_2$ in methanol followed by the addition of water yielded, upon standing, large yellow rod-like crystals suitable for further analysis.

*Solution-Studies: **L6** Pb(II)*

Examination of the crystals in acetonitrile by ESI-MS at 70 °C with a range of cone voltages yielded three peaks that are assigned as $[Pb_{16}(\mathbf{L6}\text{-}3H)_8(OTf)_n]^{n-8}$ (n = 5-7). Interestingly, there are further peaks around both the +6 and +5 charge states that are separated by a mass to charge ratio of ~ 150 and are assigned as the same compound but with an integer increase in anion content (Fig. 93).

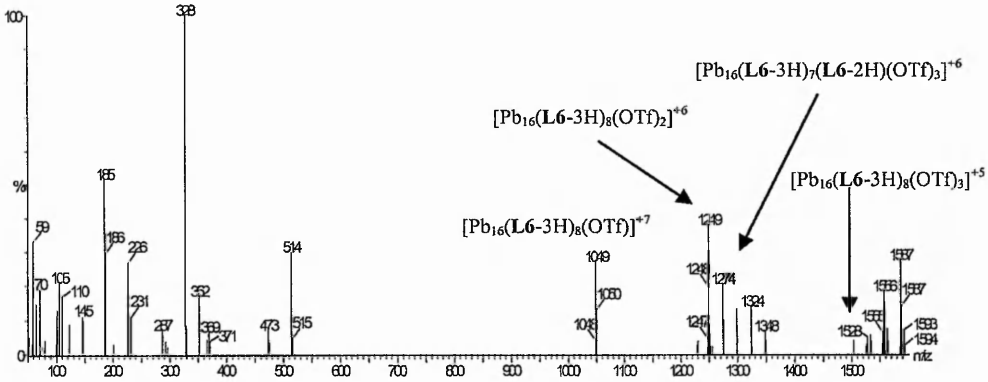

Figure 93 ESI-MS in acetonitrile at 70 °C and 10 V of $[Pb_{16}(\mathbf{L6}\text{-}3H)_8](OTf)_8$.

*Solid-State Studies: $[Pb_{16}(\mathbf{L6}\text{-}3H)_8](OTf)_8\cdot 8MeOH\cdot 58H_2O$ (**A21**)*

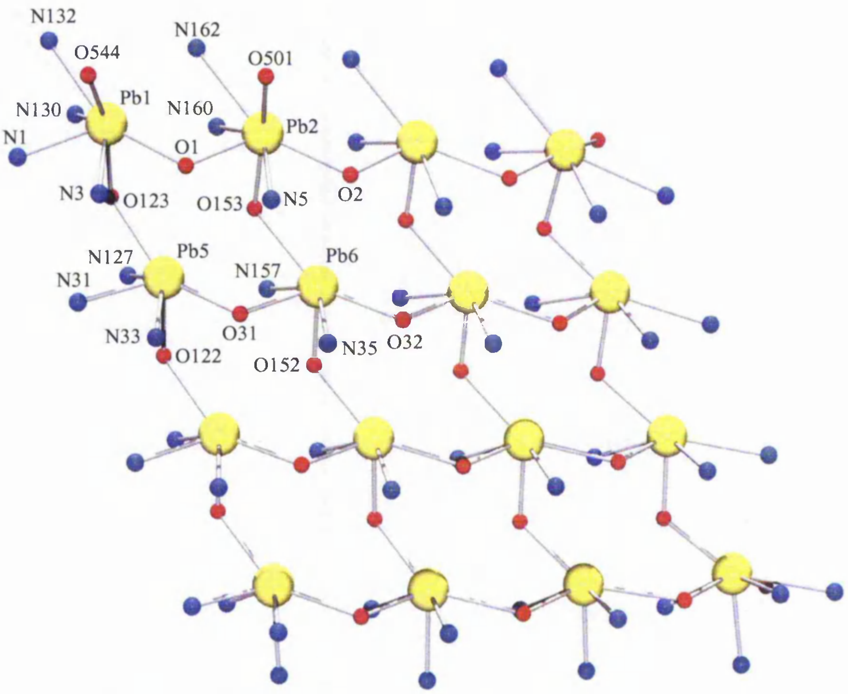

Figure 94 POV-Ray representation of $[Pb_{16}(\mathbf{L6}\text{-}3H)_8]^{+8}$ inner core.

Table 36 Selected bond angles/° of $[Pb_{16}(\mathbf{L6}\text{-}3H)_8]^{+8}$ cation.

N3-Pb1-O1	62	O1-Pb2-O153	80	N33-Pb5-O31	63	O152-Pb6-O31	84
N3-Pb1-O123	83	O1-Pb2-N5	66	N33-Pb5-O122	81	O152-Pb6-N35	82
N3-Pb1-N1	65	O1-Pb2-N160	83	N33-Pb5-N31	65	O152-Pb6-N157	64
N3-Pb1-O544	75	O1-Pb2-O2	124	N33-Pb5-N127	133	O152-Pb6-O32	82
N3-Pb1-N130	133	O1-Pb2-O501	87	N33-Pb5-O123	138	O152-Pb6-O153	120
N3-Pb1-N132	137	O1-Pb2-N162	80	O31-Pb5-O122	82	O31-Pb6-N35	66
O1-Pb1-O123	82	O153-Pb2-N5	83	O31-Pb5-N31	127	O31-Pb6-N157	81
O1-Pb1-N1	126	O153-Pb2-N160	60	O31-Pb5-N127	132	O31-Pb6-O32	125
O1-Pb1-O544	93	O153-Pb2-O2	84	O31-Pb5-O123	151	O31-Pb6-O153	78
O1-Pb1-N130	129	O153-Pb2-O501	158	O122-Pb5-N31	84	N35-Pb6-N157	135
O1-Pb1-N132	154	O153-Pb2-N162	115	O122-Pb5-N127	62	N35-Pb6-O32	59
O123-Pb1-N1	83	N5-Pb2-N160	136	O122-Pb5-O123	117	N35-Pb6-O153	135
O123-Pb1-O544	158	N5-Pb2-O2	59	N31-Pb5-N127	83	N157-Pb6-O32	136
O123-Pb1-N130	58	N5-Pb2-O501	76	N31-Pb5-O123	79	N157-Pb6-O153	58
O123-Pb1-N132	114	N5-Pb2-N162	138	N33-Pb5-O213	102	O32-Pb6-O153	151
N1-Pb1-O544	82	N160-Pb2-O2	131				
N1-Pb1-N130	82	N160-Pb2-O501	136				
N1-Pb1-N132	78	N160-Pb2-N162	57				
O544-Pb1-N130	135	O2-Pb2-O501	90				
O544-Pb1-N132	79	O2-Pb2-N162	153				
N130-Pb1-N132	57	O501-Pb2-N162	79				

Single crystal X-ray diffraction confirms the expected [4 x 4] grid structure, however, the structure is at a low level of refinement with only the central core clearly visible (Fig. 94). This is associated with the unsymmetrical nature of the ligand that causes some disorder within the structure. The grid has approximately external and internal dimensions of ~ 22.9 and ~ 13.0 Å with a distorted central core, which has a rhombohedral shape. Undoubtedly, this is caused as with $[Pb_{16}(\mathbf{L2}\text{-}2H)_8(OTf)_6(H_2O)_5](OTf)_{10}\cdot 23H_2O$ by a combination of the $6s^2$ stereochemically active lone pair,[105b] identifiable by the large void around the Pb(II) ion, along with the cations large size.

Table 37 Selected bond lengths/ Å for $[Pb_{16}(\mathbf{L6}\text{-}3H)_8]^{+8}$ cation.

Pb1-N3	2.48	Pb2-O1	2.39	Pb5-N33	2.42	Pb6-O152	2.43
Pb1-O1	2.55	Pb2-O153	2.50	Pb5-O31	2.48	Pb6-O31	2.46
Pb1-O123	2.57	Pb2-N5	2.51	Pb5-O122	2.48	Pb6-N35	2.54
Pb1-N1	2.61	Pb2-N160	2.66	Pb5-N31	2.51	Pb6-N157	2.56
Pb1-O544	2.68	Pb2-O2	2.68	Pb5-N127	2.72	Pb6-O32	2.60
Pb1-N130	2.71	Pb2-O501	2.77	Pb5-O123	2.84	Pb6-O153	2.84
Pb1-N132	2.87	Pb2-N162	3.01				

The $Pb_{16}O_{24}$ core has a true [4 x 4] grid structure with nine fused Pb_4O_4 subunits, which lead to both consistent metal-metal separations and Pb-O-Pb bond angles that have values averaging around 4.34 Å and 117°, respectively (Table 36). The plane of sixteen Pb(II) ions appears essentially flat with a torsion angle for Pb1-Pb4-Pb13-Pb16 of 0°. The Pb(II) ions have a substantial spread of bond lengths with no real pattern, along with a mixture of twelve six coordinate and four seven coordinate cations (Table 37).

*Complexation: **L6** Mn(II)*

Considering those examples reported in the literature[4c] and the results discussed in this chapter it is obvious to see that Mn(II) favours grid formation, probably due to its lack of CFSE. Reaction of **L6** with excess $Mn(ClO_4)_2\cdot 6H_2O$ or $Mn(OTf)_2$ in various mixtures of water, methanol and acetonitrile all yielded large crystals with the latter used for further study.

*Solution Studies: **L6** Mn(II)*

Examination of redissolved crystals in acetonitrile by ESI-MS at 70 °C with a range of cone voltages revealed a series of peaks between 701 to 1339 *m/z* that represent $[\mathrm{Mn_{16}}(\mathbf{L6}\text{-}3\mathrm{H})_8(\mathrm{OTf})_n]^{8-n}$ (n = 4-7) (Fig. 95). Closer examination shows that the most predominant peaks actually represent a species where only fifteen Mn(II) ions are present with an overall charge of +8, also a species with only fourteen Mn(II) ions is observed. CV studies in acetonitrile and DMF show no reversible peaks over the range of -2 to 2 V, which could be attributed to vacant metal ion coordination, observed in solution.

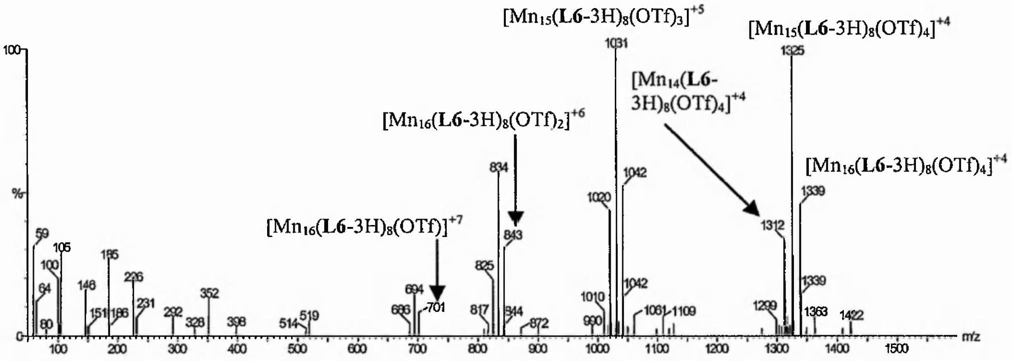

Figure 95 ESI-MS in acetonitrile at 70 °C and 10 V of $[\mathrm{Mn_{16}}(\mathbf{L6}\text{-}3\mathrm{H})_8](\mathrm{OTf})_8$.

*Solid-State Studies: $[\mathrm{Mn_{16}}(\mathbf{L6}\text{-}3\mathrm{H})_8](\mathrm{OTf})_8\cdot10\mathrm{MeOH}\cdot27\mathrm{H_2O}$ (**A22**)*

Examination of the solid-state by X-ray diffraction indicates a fully metalated grid with a total of sixteen Mn(II) ions (Fig. 96). The large structure is made up of a cation surrounded by eight triflate anions and almost certainly numerous solvent molecules that have not been crystallographically located. The cation has an external length of ~ 22.2 Å and an internal dimension of ~ 12.1 Å along with a small amount of ligand disorder because of its unsymmetrical nature. The grid of Mn(II) ions is reasonably flat with a torsion angle between the four corner ions of only ~ 1°, however this is slightly misleading when the ligand strand is examined which has a distinct bend to allow donation (Fig. 98). This demonstrates a successful design due to the flexibility of the diazine link that is highly suited to grid formation. The eight ligands fall into two parallel subsets of four which occupy separate sets above and

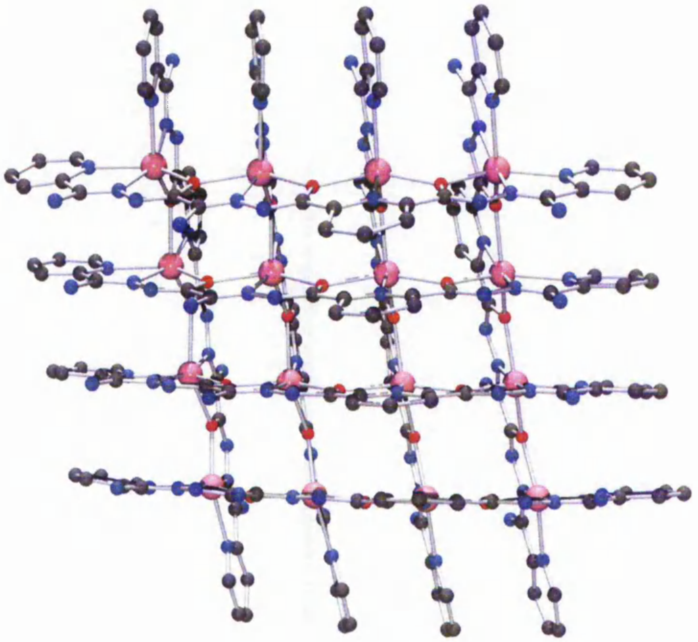

Figure 96 POV-Ray representation of $[Mn_{16}(\mathbf{L6}\text{-}3H)_8]^{+8}$ cation..

Table 38 Selected bond lengths/ Å for $[Mn_{16}(\mathbf{L6}\text{-}3H)_8]^{+8}$ cation.

Mn1-N1	2.335(9)	Mn2-O1	2.250(7)	Mn5-N15	2.116(8)	Mn6-O4	2.227(6)
Mn1-O1	2.198(6)	Mn2-O2	2.194(6)	Mn5-O14	2.158(6)	Mn6-O5	2.201(5)
Mn1-N58	2.057(10)	Mn2-N63	2.118(9)	Mn5-O15	2.253(7)	Mn6-N66	2.152(7)
Mn1-N3	2.095(9)	Mn2-N6	2.145(8)	Mn5-N13	2.354(9)	Mn6-N18	2.143(7)
Mn1-O15	2.165(6)	Mn2-N61	2.377(8)	Mn5-O4	2.171(6)	Mn6-O16	2.227(6)
Mn1-N60	2.335(9)	Mn2-O16	2.154(5)	Mn5-N56	2.133(9)	Mn6-O17	2.221(5)

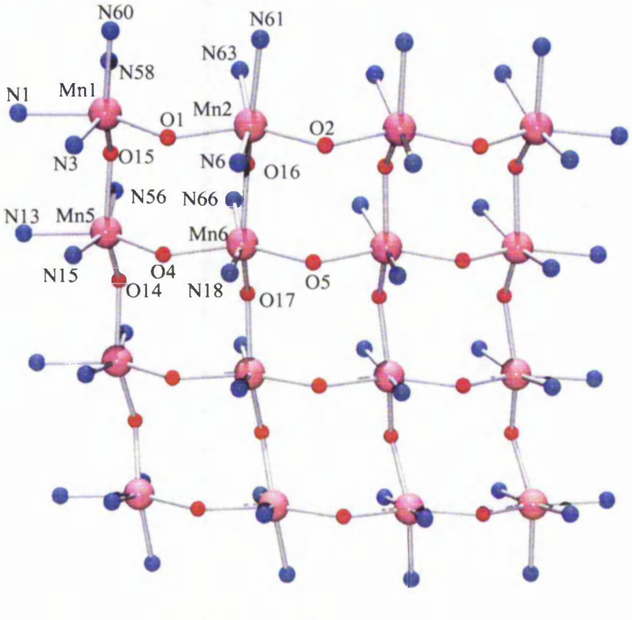

Figure 97 POV-Ray representation of $[Mn_{16}(\mathbf{L6}\text{-}3H)_8]^{+8}$ inner core.

below the mean plane of Mn(II) ions with aromatic ring separation of less than 4.0 Å suggesting π-π interactions.

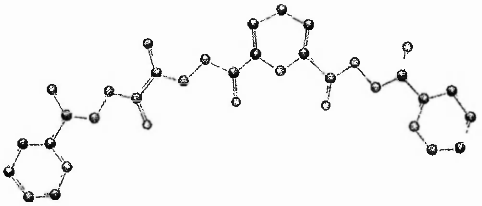

Figure 98 POV-Ray representation of **L6**-3H displaying the bent nature of the ligand strand.

Table 39 Selected bond angles/ ° for [Mn$_{16}$(**L6**-3H)$_8$]$^{+8}$ cation.

N1–Mn1–N3	71.2(3)	N61–Mn2–O16	141.1(3)	N15–Mn5–O4	72.4(3)
N1–Mn1–O15	90.2(3)	O1–Mn2–N61	101.8(3)	N15–Mn5–N56	156.8(3)
N1–Mn1–N60	95.6(3)	O1–Mn2–O16	88.7(2)	O4–Mn5–O14	100.3(2)
N3–Mn1–O15	123.3(3)	N6–Mn2–N61	95.6(3)	O4–Mn5–O15	92.2(2)
N3–Mn1–N60	92.6(4)	N6–Mn2–O16	123.2(3)	O14–Mn5–O15	143.8(3)
O1–Mn1–N58	125.2(3)	O2–Mn2–N63	123.3(3)	O4–Mn6–O5	143.6(2)
O15–Mn1–N58	73.1(3)	N61–Mn2–N63	69.8(3)	O4–Mn6–N66	93.0(3)
N58–Mn1–N60	70.8(3)	N63–Mn2–O16	72.5(2)	N18–Mn6–O5	72.3(2)
N1–Mn1–O1	143.2(4)	O2–Mn2–N61	88.8(3)	N18–Mn6–N66	160.0(3)
N1–Mn1–N58	90.0(4)	O2–Mn2–O16	104.3(2)	O5–Mn6–O16	92.9(2)
N3–Mn1–O1	72.1(3)	N13–Mn5–N15	70.3(3)	O5–Mn6–O17	96.4(2)
N3–Mn1–N58	153.9(3)	N13–Mn5–O14	94.2(3)	O16–Mn6–O17	143.2(2)
O1–Mn1–O15	108.6(2)	N13–Mn5–O15	96.3(3)	O4–Mn6–N18	72.4(2)
O1–Mn1–N60	87.7(3)	N15–Mn5–O14	122.6(3)	O4–Mn6–O16)	99.1(2)
O15–Mn1–N60	143.4(3)	N15–Mn5–O15	93.5(3)	O4–Mn6–O17	94.3(2)
O1–Mn2–N6	72.3(3)	O4–Mn5–N56	125.8(3)	N18–Mn6–O16	96.2(3)
O1–Mn2–O2	144.3(3)	O14–Mn5–N56	72.1(3)	N18–Mn6–O17	120.6(3)
O1–Mn2–N63	92.1(3)	N56–Mn5–O15	73.1(3)	O5–Mn6–N66	123.3(3)
N6–Mn2–O2	72.8(3)	N13–Mn5–O4	142.2(3)	O16–Mn6–N66	72.2(2)
N6–Mn2–N63	156.5(3)	N13–Mn5–N56	91.9(4)	N66–Mn6–O17	73.0(2)

Within the core of Mn(II) ions three different distorted octahedral Mn(II) ion environments are found; the corner ions have *cis*-N_4O_2 donor arrangements, the side Mn(II) centres have a *mer*-N_3O_3 donor arrangements and the central Mn(II) ions have a *trans*-N_2O_4 donor arrangement. The $Mn_{16}O_{24}$ core is made up from nine directly fused Mn_4O_4 subunits that have very similar geometries. Averaging through these groups gives an average metal-metal separation of 4.0 Å and an M-O-M bond angle average of 131° which are similar to those observed in other Mn(II) grids formed here and reported by others.[4c] This consistent metal-metal separation is associated with the continuous alkoxide giving the cation a true [4 x 4] structure rather than a [4 x (2 x 2)] structure. The bonds lengths are typical (Table 38) however, a number of the longer bonds are associated with the terminal N_{py} and are likely to be a consequence of the steric restraint of the ligand.

*Magnetism: $[Mn_{16}$(**L6**-3H)]$(OTf)_8$ (**A22**)*

This structure is purely alkoxide bridged implying that each Mn(II) ion will be interacting strongly with neighbouring ions and as a result cannot be modelled by dividing into four separate subunits. Therefore, a suitable model even at the very simplest level, will be based upon a three exchange model (Fig. 98) with sixteen spins of S = 5/2 giving the Hamiltonian expression (17). Nevertheless, magnetic measurements have been made between 2 and 300 K, which show a steady decrease in effective magnetic moment with decreasing temperature, indicating antiferromagnetic exchange. The room temperature effective magnetic moment of 20.91 μ_b is in approximate agreement with the spin-only value for sixteen Mn(II) ions of 23.72 μ_b and may represent a percentage of incomplete grid which is observed in solution.

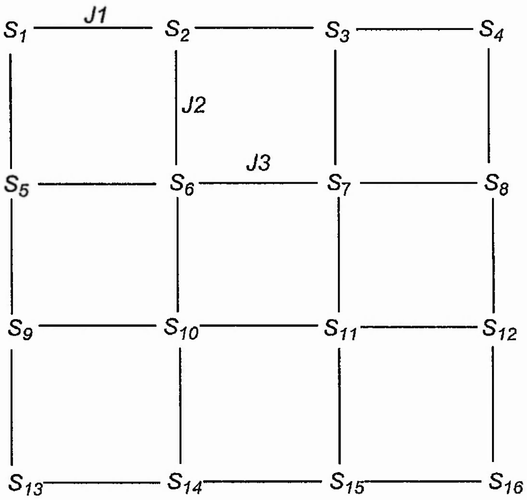

Figure 98 Proposed model for purely alkoxide bridged [4 x 4] grids.

$$\begin{aligned} H_{ex} = -J1\{&S_1 \cdot S_2 + S_2 \cdot S_3 + S_3 \cdot S_4 + S_4 \cdot S_8 + S_8 \cdot S_{12} + S_{12} \cdot S_{16} \\ &+ S_{16} \cdot S_{15} + S_{15} \cdot S_{14} + S_{14} \cdot S_{13} + S_{13} \cdot S_9 + S_9 \cdot S_5 + S_5 \cdot S_1\} \\ &- J2\{S_2 \cdot S_6 + S_3 \cdot S_7 + S_8 \cdot S_7 + S_{12} \cdot S_{11} + S_{15} \cdot S_{11} + S_{14} \cdot S_{10} + S_9 \cdot S_{10} + S_5 \cdot S_6\} \\ &- J3\{S_6 \cdot S_7 + S_7 \cdot S_{11} + S_{11} \cdot S_{10} + S_{10} \cdot S_6\} \end{aligned}$$

(17)

Other Metal Ions

Various powders were obtained by reaction of **L6** with first row transition metal ions. A thorough study by ESI-MS in acetonitrile at various temperatures and cone voltages did not suggest grid formation with the triflate and perchlorate analogues of Cu(II), Ni(II), Co(II), Fe(II), Fe(III) and Zn(II) that generally produced spectra of weak intensity.

6.4 Conclusion

This chapter has demonstrated that [4 x 4] grids can be formed and structurally characterised incorporating both diamagnetic and paramagnetic metal ions. These were limited to Pb(II) and Mn(II) with little evidence to suggest grid formation with other transition metal ions. Interestingly, varying the heterocycle in the cases of **L2** and **L3** produced the desired ligand framework where both suffer from incomplete metal ion coordination. **L2** can be fully metallated on the addition of base, whilst the addition of base to reactions involving **L3** only increased the metal nuclearity by one or two Mn(II) ions as suggested by ESI-MS. This persistent vacant coordination is could be associated with the interwoven nature of the grid that reduces its overall flexibility. This can be seen by the extremely long N_{pyz}-Mn bonds in $[Mn_{12}$(**L3**-$2H)_4$(**L4**)$_4](OTf)_{16}$. **L4** is incapable of forming [4 x 4] grids with Mn(II) and results in a pseudo [2 x 2] grid. Due to synthetic problems large amounts of **L5** could not be prepared, however further studies may indicate that this ligand is attractive for forming complete [4 x (2 x 2)] grid of grids with other first row transition metal ions. **L6** appears to form complete [4 x 4] Pb(II) and Mn(II) grids, however, in solution there is evidence for species with different charges and number of metal ions present.

From examination of all the structures formed with Mn(II) it is observed that the coordination geometries of this metal ion are highly distorted with very long bond distances. These long bonds arguably hinder the formation of [4 x 4] grids with other transition metal ions. Therefore, it is felt that the future of [4 x 4] grids will be restricted, for transition metal ions that display an octahedral coordination preference, to those that display little or no crystal field preference. Consequently, for first row transition metal ions this will be limited to Mn(II) and Zn(II).

The magnetic properties of the heterocyclic bridged assemblies have similar exchange values, *g*-values and paramagnetic impurities to the [2 x 2] homonuclear Mn(II) grid formed in this study (Chapter Three) and by Thompson and Matthews.[4c] Of particular interest are those assemblies where complete [2 x 2] grids are observed, *i.e.*, $[\mathrm{Mn_4}(\mathbf{L1}\text{-H})_4](\mathrm{OTf})_4$ (Chapter Three), $[\mathrm{Mn_{16}}(\mathbf{L2}\text{-2H})_8](\mathrm{OTf})_{16}$ and $[\mathrm{Mn_4}(\mathbf{L4}\text{-H})_4](\mathrm{ClO_4})_4$. These all have very similar magnetic profiles of χ_m versus T that show a steady increase of χ_m with decreasing temperature followed by a brief plateau and a sharp rise until 2 K. This sharp rise can only ever be modelled by the introduction of a large ρ value, however it probably represents either a different exchange mechanism at low temperatures or even zero field splitting which has been observed in $[\mathrm{Mn_9}(\mathrm{L(N)\text{-}2H})_6](\mathrm{ClO_4})_6$.[57]

Chapter Seven

Pyridazine Bridged Helical Assemblies

7.0 Introduction

The majority of self-assembled metallic helicates contain two metal centres, whilst those containing three or more remain quite rare.[117] However, there are reports of double and quadruple stranded helicates containing five[118] and nine metal ions, respectively[119], whilst triple stranded helicates have not been extended beyond three metal centres. This appears to be a consequence of ligand design and synthesis. The design of **L7** was adapted from the previously reported pd2am (*N*-bis(pyridine-2-amidine)pyridazine-3,6-carboxyamido) that forms a trinuclear Ni(II) chain[120a] and a dodecanuclear Cu(II) picture frame[61] that both suffer from incomplete metal ion coordination. Replacement of the amido link with the more innocuous amidrazone link yields **L7** (Fig. 100), which adopts a *trans* conformation in its "free" state along with the likelihood of intramolecular hydrogen bonding. When an octahedral metal ion is introduced in the correct stoichiometry (M:L = 4:3) this should effect a change in conformation of **L7** to a *cis* mode leading to the binding of four metal ions in a linear array.

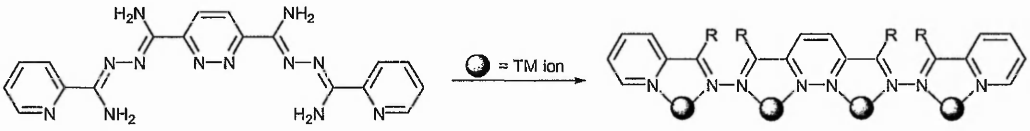

Figure 100 **L7** in its predicted "free" conformation and its change in geometry when introduced to an octahedral metal ion.

Synthesis

The preparation of **L7** requires a synthesis that exploits the symmetrical nature of the ligand. Consequently the ligand is disconnected into three fragments consisting of two pyridine-2-amidrazone molecules (**37**) and one dimethyl pyridazine-3,6-diimidate molecule (**38**) (Fig. 101). Pyridine-2-amidrazone (**37**) was prepared in large quantities by reaction of 2-cyanopyridine with an excess of hydrazine monohydrate according to a standard literature procedure,[64] while the dimethyl imidate (**38**) was prepared in a similar manner to diethyl pyridazine-3,6-diimidate (**18**) and is preferred over the latter due to an easy isolation.

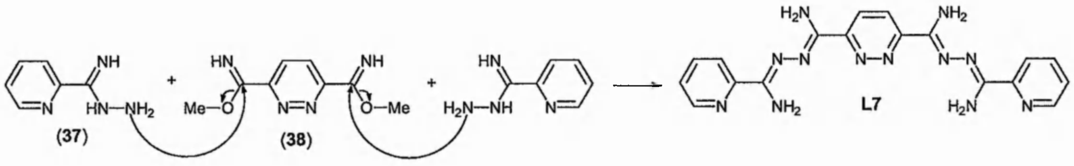

Figure 101 Formation of **L7** *via* the double nucleophilic substitution of pyridine-2-amidrazone (**37**) on dimethyl pyridine-3,6-diimidate (**38**).

Reaction of (**38**) with pyridine-2-amidrazone (**37**) in dry MeOH along with a catalytic amount acetic acid gives **L7** in high yields.

Complexation

Addition of the ligand to a slight excess of a metal salt (perchlorate or triflate) in water followed by the addition of methanol or acetonitrile yielded crystals suitable for further study in the cases of Cu(II), Ni(II) and Zn(II). This methodology did not work for Mn(II) which was overcome by stirring a mixture of $Mn(ClO_4)_2{\cdot}6H_2O$ with **L7** in acetonitrile overnight. Removal of the solvent yielded a red solid that turned dark on exposure to air, but once crystallised *via* vapour diffusion the sample appeared stable under atmospheric conditions.

7.1 Solution Studies

ESI-MS in acetonitrile at 50 °C with cone voltages between 0 and 20 V indicated that the desired product existed in solution. The Mn(II), Cu(II) and Zn(II) assemblies all show a series of peaks corresponding $[M_4(\mathbf{L7})_3(\text{anion})_n]^{8-n}$ (n = 3-6) along with their acetonitrile adducts and some evidence is provided for cluster formation between individual assemblies (Fig. 102). The Ni(II) assembly shows a slight deviation in the expected numbers. This was simply accounted for by the addition of a single molecule of water to the molecule.

Visible spectroscopy for the Cu(II) assembly in acetonitrile shows a single absorbance at 780 (ε = 602 $dm^3\ mol^{-1}\ cm^{-1}$) that is typical of this cation in an octahedral field.[85] The Ni(II) assembly shows a single absorbance at 776 (ε = 921 dm^3 mol^{-1} cm^{-1}) that is tentatively assigned to the $^3A_{2g}\rightarrow{}^3T_{2g}$ transition, however this peak is rather broad and may represent a mixture of transitions.

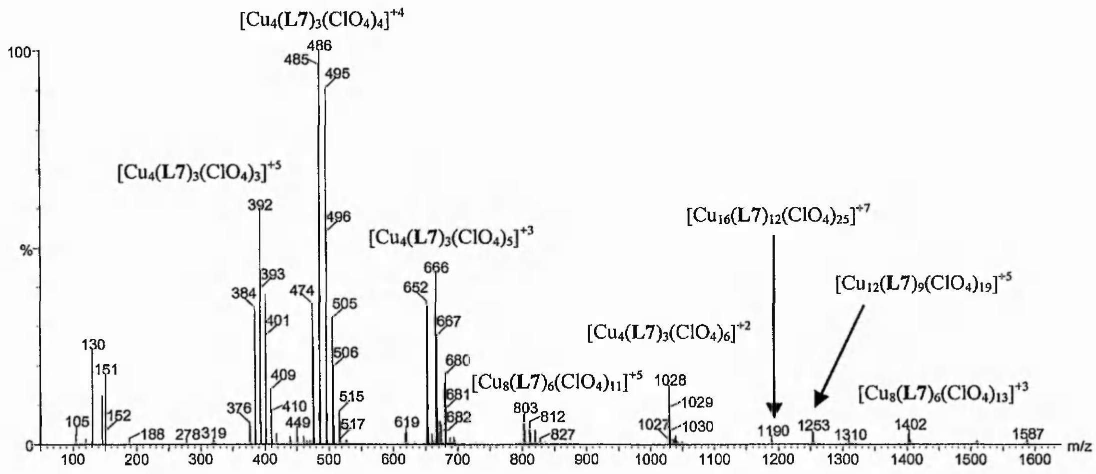

Figure 102 ESI-MS spectra of [Cu$_4$(**L7**)$_3$(ClO$_4$)$_8$] in acetonitrile at 0 V and 50 °C.

^{1}H NMR of [Zn$_4$(**L7**)$_3$](OTf)$_8$ in acetonitrile at 298 K shows five sets of well-resolved aromatic peaks along with four broader peaks situated slightly further upfield (Fig. 103). Each of the pyridyl protons has been assigned by assuming the withdrawal of electron density from the aromatic ring, the application of COSY methodology and by comparison of the NMR of the free ligand in dimethyl

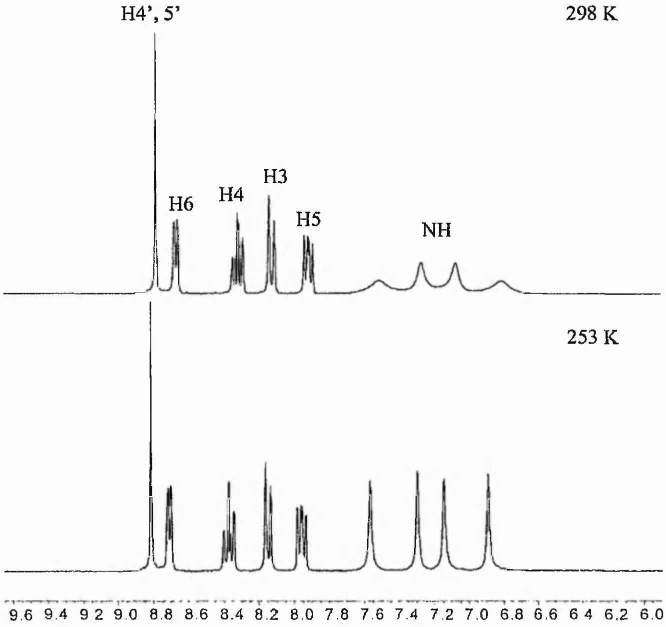

Figure 103 Top: ^{1}H NMR of [Zn$_4$(**L7**)$_3$(OTf)$_8$] at 298 K in CD$_3$CN and bottom ^{1}H NMR of [Zn$_4$(**L7**)$_3$(OTf)$_8$] at 253 K.

sulfoxide. Such a simple spectrum indicates that all three ligands are in such fast exchange that the NMR time scale is unable to resolve them; furthermore each individual ligand is symmetrical about its central axis. Using this symmetry, it is assumed that the four broader peaks are associated with the hydrogens located on the peripheral amine groups with each individual hydrogen atom being in a different chemical environment. On cooling down to 253 K there is no change in the aromatic region of the spectrum. However, the four singlet peaks associated with the peripheral amine groups become resolved and appear as sharp singlets. Such an increase in resolution is due to the reduction of thermal energy that consequently reduces the level of fast exchange of the protons associated with the amine groups.

Electrochemical studies in acetonitrile of each assembly show no reversible peaks within the range of -2 to 2 V with peaks only associated with ligand reduction and oxidation. Similar observations have been noted in a series of dinuclear diazine bridged systems.[120b]

7.2 Solid-State Studies

The first assembly to be structurally characterised was the Cu(II) analogue and consequently this will be discussed first. In all cases, Cu(II), Mn(II), Ni(II) and Zn(II) there is no ligand disorder that is commonly observed with **L1** and the structures are at a reasonable level of refinement. The Ni(II) and Zn(II) assemblies have two individual cations present within the asymmetrical unit that are structurally very similar and the cation with the most varied bond lengths and angles will be discussed in each case.

$[Cu_4(\mathbf{L7})_3](ClO_4)_8 \cdot 14H_2O$ (**A23**)

The structure contains a large cation made up from three ligands and four Cu(II) ions surrounded by eight perchlorate anions and approximately fourteen waters of crystallisation. Removal of the anions and solvent reveal the cation, which from closer inspection can be seen as a chain of four Cu(II) ions that are bridged by $N_{diazine}$ bonds (Fig. 104). The ligands spiral around the chain of Cu(II) ions in such manner that they rotate through an angle greater than 180° which is a consequence of the flexible nature of the diazine link. Therefore the cation is best described as a tetrametallic triple helicate and is the first ever reported.[76] The array of Cu(II) ions are almost linear with angles for Cu1-Cu2-Cu3 of 172° and 171° for Cu2-Cu3-Cu4 and is therefore termed a pseudo linear array that defines the helical axis. The long external dimension of the cation is approximately 18 Å and the internal Cu1 to Cu4 distance is ~ 11 Å with adjacent copper-copper separations of Cu1-Cu2 3.73, Cu2-Cu3 3.74 and Cu3-Cu4 3.74 Å.

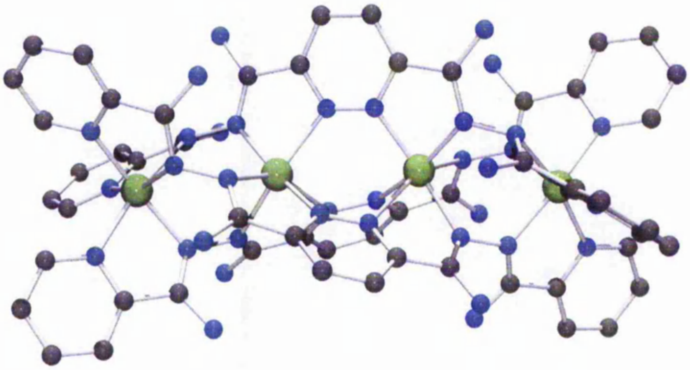

Figure 104 POV-Ray representation of $[Cu_4(\mathbf{L7})_3]^{+8}$ cation.

The flexible nature of the diazine causes a twist between adjacent metal centres that can be estimated by examination of their least square planes. The twist is defined as the angle created between the least-squares plane of N_{py}-C-C-$N_{diazine}$ and $N_{diazine}$-C-C-N_{pdz} for the Cu(II) ions bridged by diazine and the difference between $N_{diazine}$-C-C-N_{pdz} and N_{pdz}-C-C-$N_{diazine}$ for Cu(II) ions bridged by pyridazine. Thus values ranging from 75-89° are observed for Cu(II) ions bridged by diazine and 3-11° for those bridged by pyridazine. The latter, smaller angles reflect the rigid nature of the pyridazine heterocycle.

The four copper ions have distorted octahedral geometries that become more extreme from Cu1 to Cu4 (Table 40 and 41). Cu1 has an extremely long contact of 2.41 Å, along with four reasonably short equatorial contacts (1.99-2.06 Å) and one axial Cu-N bond of 2.20 Å making assignment to a square-based pyramid reasonable. An elongated tetragonal geometry is observed at Cu2 with axial bonds of 2.25 and 2.27 Å, however Cu3 and Cu4 display a variety of bond lengths making assignment to a specific geometry unsuitable. This type of coordination geometry has been observed

Table 40 Bond lengths for Cu(II) ions in $[Cu_4(\mathbf{L7})_3]^{+8}$ cation.

Cu1-N25	1.997(7)	Cu2-N4	1.989(7)	Cu3-N9	1.974(7)	Cu4-N34	2.015(7)
Cu1-N15	2.014(6)	Cu2-N6	2.001(7)	Cu3-N19	1.988(7)	Cu4-N24	2.019(7)
Cu1-N27	2.045(7)	Cu2-N16	2.048(6)	Cu3-N21	2.046(7)	Cu4-N36	2.119(8)
Cu1-N1	2.063(7)	Cu2-N30	2.088(7)	Cu3-N7	2.150(7)	Cu4-N12	2.163(8)
Cu1-N13	2.203(7)	Cu2-N28	2.247(7)	Cu3-N33	2.178(7)	Cu4-N10	2.212(8)
Cu1-N3	2.409(7)	Cu2-N18	2.267(7)	Cu3-N31	2.313(7)	Cu4-N22	2.225(7)

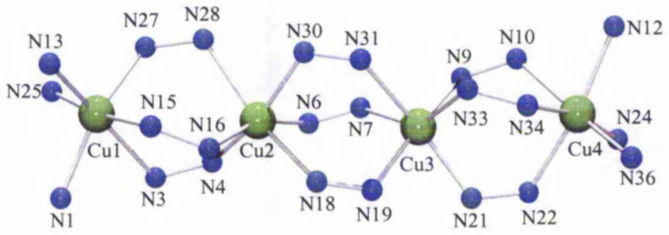

Figure 105 POV-Ray representation of $[Cu_4(\mathbf{L7})_3]^{+8}$ inner core.

Table 41 Bond angles for Cu(II) ions in $[Cu_4(\mathbf{L7})_3]^{+8}$ cation.

N25-Cu1-N15	171.7(3)	N16-Cu2-N30	98.2(3)	N9-Cu3-N31	104.2(3)
N25-Cu1-N27	79.9(3)	N4-Cu2-N28	92.9(3)	N19-Cu3-N31	85.9(2)
N15-Cu1-N27	92.0(3)	N6-Cu2-N28	108.8(3)	N21-Cu3-N31	152.3(2)
N25-Cu1-N1	95.6(3)	N16-Cu2-N28	89.9(2)	N7-Cu3-N31	83.0(2)
N15-Cu1-N1	92.7(3)	N30-Cu2-N28	73.4(2)	N33-Cu3-N31	69.9(2)
N27-Cu1-N1	159.8(3)	N4-Cu2-N18	113.8(3)	N34-Cu4-N24	167.6(3)
N25-Cu1-N13	101.8(3)	N6-Cu2-N18	93.1(3)	N34-Cu4-N36	78.4(3)
N15-Cu1-N13	77.2(3)	N16-Cu2-N18	72.9(2)	N24-Cu4-N36	99.5(3)
N27-Cu1-N13	98.8(3)	N30-Cu2-N18	83.5(2)	N34-Cu4-N12	97.0(3)
N1-Cu1-N13	101.4(3)	N28-Cu2-N18	148.9(2)	N24-Cu4-N12	95.4(3)
N25-Cu1-N3	91.2(3)	N9-Cu3-N19	167.2(3)	N36-Cu4-N12	99.7(3)
N15-Cu1-N3	90.3(2)	N9-Cu3-N21	96.0(3)	N34-Cu4-N10	89.8(3)
N27-Cu1-N3	86.1(3)	N19-Cu3-N21	77.4(3)	N24-Cu4-N10	93.5(3)
N1-Cu1-N3	74.3(3)	N9-Cu3-N7	75.9(3)	N36-Cu4-N10	166.5(3)
N13-Cu1-N3	166.7(2)	N19-Cu3-N7	97.8(3)	N12-Cu4-N10	75.1(3)
N4-Cu2-N6	77.2(3)	N21-Cu3-N7	120.7(3)	N34-Cu4-N22	91.6(3)
N4-Cu2-N16	95.0(3)	N9-Cu3-N33	89.5(3)	N24-Cu4-N22	76.6(3)
N6-Cu2-N16	159.9(3)	N19-Cu3-N33	101.5(2)	N36-Cu4-N22	98.0(3)
N4-Cu2-N30	160.9(3)	N21-Cu3-N33	91.9(3)	N12-Cu4-N22	161.5(3)
N6-Cu2-N30	94.3(3)	N7-Cu3-N33	145.1(3)	N10-Cu4-N22	88.6(3)

for a dicopper(II) double stranded helicate and has been described as a dynamic Jahn-Teller effect.[93] Why such varied geometries form is unclear, but it is felt that this is mainly due to the crystal field preference of the Cu(II) ion rather than ligand restraint.

From examination of the other structures, Mn(II), Ni(II) and Zn(II), a number of comparisons can be made and reduce the necessity for individual structural discussion.

(1). The cations all have a similar external dimension around 18 Å and an internal dimension (M1-M4) ranging from 11.1 to 11.5 Å.

(2). Metal-metal separations show little variation across the series with average values for Cu(II) = 3.74 Å, Mn(II) = 3.83 Å, Ni(II) = 3.74 Å and Zn(II) = 3.79 Å.

(3). The twists of the ligand between adjacent metal centres have generally quite large ranges. Those experienced across diazine are for Cu(II) = 75-89°, Mn(II) = 66-83°, Ni(II) = 72-88° and Zn(II) = 78-89°. Those experienced across the pyridazine rings having ranges Cu(II) = 3-11°, Mn(II) = 3-19°, Ni(II) = 3-16° and Zn(II) = 1-12°.

(4). The bond angles around each metal ion are generally similar due to the arrangement of the donors on the ligand strand.

(5). The bond distances in the cases of Mn(II) and Zn(II) show very little variation because of no CFSE. As previously discussed the Cu(II) motif shows varying bond lengths and a very similar effect is observed in the Ni(II) motif. This displays a terminal Ni(II) ion (Ni4) with an extremely long bond of 2.44 Å suggesting a square based pyramidal type geometry analogous to that observed in the Cu(II) motif, which appears to have a significant effect on the magnetic properties of this assembly.

The solid state structures are generally consistent especially in the cases of Mn(II) and Zn(II) that show very little differences due to their electronic configurations. Both the Cu(II) and Ni(II) structures have varied bond lengths that appear to become

Table 42 Bond lengths/ Å for Mn(II) ions in $[\mathrm{Mn_4}(\mathbf{L7})_3]^{+8}$ cation.

Mn1-N47	2.20	Mn2-N11	2.14	Mn3-N22	2.20	Mn4-N33	2.19
Mn1-N20	2.20	Mn2-N34	2.16	Mn3-N10	2.21	Mn4-N52	2.21
Mn1-N21	2.26	Mn2-N15	2.17	Mn3-N14	2.21	Mn4-N13	2.23
Mn1-N18	2.26	Mn2-N27	2.22	Mn3-N16	2.23	Mn4-N59	2.24
Mn1-N24	2.26	Mn2-N9	2.24	Mn3-N19	2.23	Mn4-N37	2.25
Mn1-N23	2.28	Mn2-N12	2.28	Mn3-N30	2.24	Mn4-N32	2.26

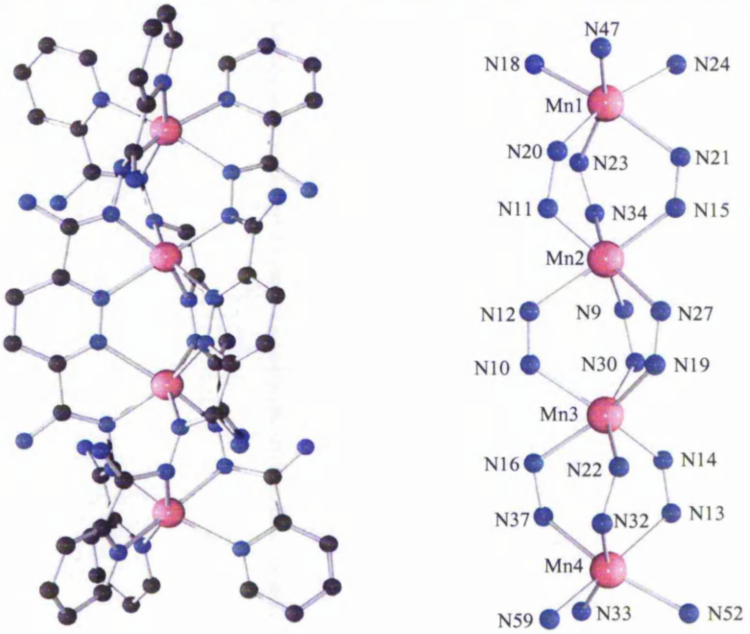

Figure 106 Left: POV-Ray representation of $[\mathrm{Mn_4}(\mathbf{L7})_3]^{+8}$ cation and right: POV-Ray representation of inner core.

Table 43 Bond angles/ ° formed around Mn(II) ions in $[\mathrm{Mn_4}(\mathbf{L7})_3]^{+8}$ cation.

N47-Mn1-N20	75	N11-Mn2-N34	93	N22-Mn3-N10	111	N33-Mn4-N52	97
N47-Mn1-N21	103	N11-Mn2-N15	91	N22-Mn3-N14	94	N33-Mn4-N13	103
N47-Mn1-N18	94	N11-Mn2-N27	113	N22-Mn3-N16	92	N33-Mn4-N59	92
N47-Mn1-N24	100	N11-Mn2-N9	149	N22-Mn3-N19	72	N33-Mn4-N37	76
N47-Mn1-N23	159	N11-Mn2-N12	73	N22-Mn3-N30	152	N33-Mn4-N32	159
N20-Mn1-N21	89	N34-Mn2-N15	91	N10-Mn3-N14	151	N52-Mn4-N13	75
N20-Mn1-N18	97	N34-Mn2-N27	150	N10-Mn3-N16	71	N52-Mn4-N59	103
N20-Mn1-N24	161	N34-Mn2-N9	70	N10-Mn3-N19	94	N52-Mn4-N37	161
N20-Mn1-N23	89	N34-Mn2-N12	111	N10-Mn3-N30	91	N52-Mn4-N32	101
N21-Mn1-N18	163	N15-Mn2-N27	73	N14-Mn3-N16	94	N13-Mn4-N59	165
N21-Mn1-N24	75	N15-Mn2-N9	113	N14-Mn3-N19	108	N13-Mn4-N37	89
N21-Mn1-N23	90	N15-Mn2-N12	153	N14-Mn3-N30	71	N13-Mn4-N32	93
N18-Mn1-N24	101	N27-Mn2-N9	92	N16-Mn3-N19	154	N59-Mn4-N37	95
N18-Mn1-N23	75	N27-Mn2-N12	93	N16-Mn3-N30	112	N59-Mn4-N32	73
N24-Mn1-N23	100	N9-Mn2 -N12	90	N19-Mn3-N30	89	N37-Mn4-N32	90

Table 44 Bond lengths/ Å for Ni(II) ions in $[\mathrm{Ni_4}(\mathbf{L7})_3]^{+8}$ cation.

Ni1-N3	2.00	Ni2-N44	1.99	Ni3-N27	1.99	Ni4-N12	1.99
Ni1-N41	2.02	Ni2-N46	2.01	Ni3-N29	2.02	Ni4-N50	2.04
Ni1-N43	2.03	Ni2-N24	2.04	Ni3-N49	2.11	Ni4-N32	2.07
Ni1-N21	2.09	Ni2-N4	2.17	Ni3-N9	2.15	Ni4-N10	2.08
Ni1-N1	2.23	Ni2-N6	2.19	Ni3-N7	2.20	Ni4-N52	2.21
Ni1-N23	2.29	Ni2-N26	2.31	Ni3-N47	2.24	Ni4-N30	2.44

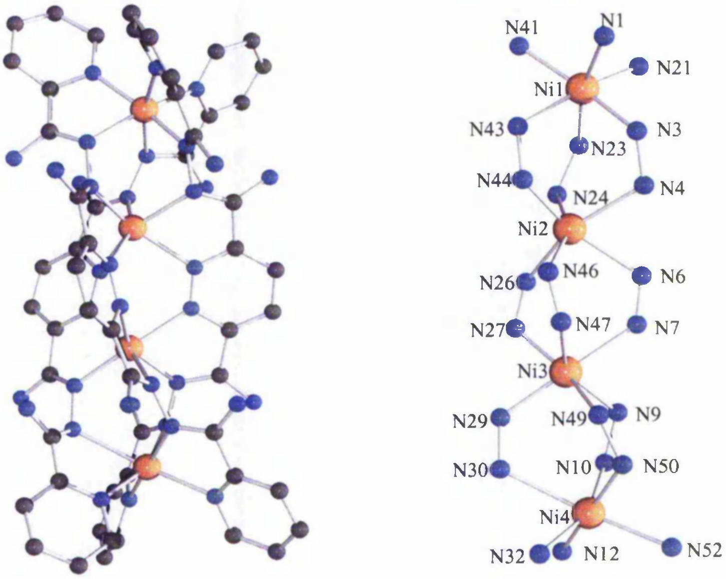

Figure 107 Left: POV-Ray representation of $[\mathrm{Ni_4}(\mathbf{L7})_3]^{+8}$ cation and right: POV-Ray representation of inner core.

Table 45 Bond angles/ ° for Ni(II) ions in $[\mathrm{Ni_4}(\mathbf{L7})_3]^{+8}$ cation.

N3-Ni1-N41	166	N44-Ni2-N46	78	N27-Ni3-N29	78	N12-Ni4-N50	171
N3-Ni1-N43	90	N44-Ni2-N24	95	N27-Ni3-N49	157	N12-Ni4-N32	95
N3-Ni1-N21	95	N44-Ni2-N4	90	N27-Ni3-N9	112	N12-Ni4-N10	80
N3-Ni1-N1	76	N44-Ni2-N6	156	N27-Ni3-N7	93	N12-Ni4-N52	104
N3-Ni1-N23	93	N44-Ni2-N26	118	N27-Ni3-N47	92	N12-Ni4-N30	91
N41-Ni1-N43	80	N46-Ni2-N24	156	N29-Ni3-N49	94	N50-Ni4-N32	94
N41-Ni1-N21	98	N46-Ni2-N4	108	N29-Ni3-N9	96	N50-Ni4-N10	92
N41-Ni1-N1	96	N46-Ni2-N6	93	N29-Ni3-N7	161	N50-Ni4-N52	76
N41-Ni1-N23	96	N46-Ni2-N26	92	N29-Ni3-N47	113	N50-Ni4-N30	90
N43-Ni1-N21	161	N24-Ni2-N4	95	N49-Ni3-N9	90	N32-Ni4-N10	157
N43-Ni1-N1	98	N24-Ni2-N6	102	N49-Ni3-N7	100	N32-Ni4-N52	101
N43-Ni1-N23	88	N24-Ni2-N26	70	N49-Ni3-N47	71	N32-Ni4-N30	72
N21-Ni1-N1	102	N4-Ni2-N6	71	N9-Ni3-N7	72	N10-Ni4-N52	103
N21-Ni1-N23	73	N4-Ni2-N26	149	N9-Ni3-N47	146	N10-Ni4-N30	86
N1-Ni1-N23	168	N6-Ni2-N26	85	N7-Ni3-N47	83	N52-Ni4-N30	164

Table 46 Bond lengths/ Å for Zn(II) ions in $[Zn_4(\mathbf{L7})_3]^{+8}$ cation.

Zn1-N21	2.107(8)	Zn2-N44	2.099(8)	Zn3-N49	2.090(7)	Zn4-N12	2.123(8)
Zn1-N1	2.129(8)	Zn2-N24	2.100(7)	Zn3-N29	2.095(7)	Zn4-N32	2.139(8)
Zn1-N41	2.133(8)	Zn2-N4	2.126(8)	Zn3-N9	2.110(7)	Zn4-N52	2.152(8)
Zn1-N3	2.144(8)	Zn2-N6	2.153(7)	Zn3-N47	2.190(8)	Zn4-N30	2.174(7)
Zn1-N43	2.197(8)	Zn2-N26	2.158(7)	Zn3-N27	2.201(7)	Zn4-N10	2.193(7)
Zn1-N23	2.212(8)	Zn2-N46	2.175(8)	Zn3-N7	2.213(7)	Zn4-N50	2.196(8)

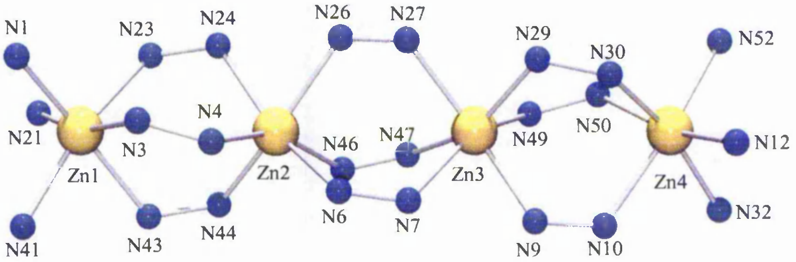

Figure 108 POV-Ray representation of $[Zn_4(\mathbf{L7})_3]^{+8}$ cation inner core.

Table 47 Bond angles/ ° for Zn(II) ions in $[Zn_4(\mathbf{L7})_3]^{+8}$ cation.

N21-Zn1-N1	98.6(3)	N4-Zn2-N6	73.8(3)	N49-Zn3-N7	151.7(3)
N21-Zn1-N41	96.9(3)	N44-Zn2-N26	155.2(3)	N29-Zn3-N7	111.8(3)
N1-Zn1-N41	97.6(3)	N24-Zn2-N26	74.1(3)	N9-Zn3-N7	72.7(3)
N21-Zn1-N3	164.3(3)	N4-Zn2-N26	107.4(3)	N47-Zn3-N7	89.1(3)
N1-Zn1-N3	76.7(3)	N6-Zn2-N26	90.6(3)	N27-Zn3-N7	86.9(3)
N41-Zn1-N3	98.6(3)	N44-Zn2-N46	74.2(3)	N12-Zn4-N32	96.5(3)
N21-Zn1-N43	95.5(3)	N24-Zn2-N46	110.0(3)	N12-Zn4-N52	97.5(3)
N1-Zn1-N43	165.2(3)	N4-Zn2-N46	155.1(3)	N32-Zn4-N52	99.3(3)
N41-Zn1-N43	76.1(3)	N6-Zn2-N46	88.9(3)	N12-Zn4-N30	162.4(3)
N3-Zn1-N43	90.9(3)	N26-Zn2-N46	90.3(3)	N32-Zn4-N30	76.1(3)
N21-Zn1-N23	75.5(3)	N49-Zn3-N29	92.4(3)	N52-Zn4-N30	99.5(3)
N1-Zn1-N23	99.4(3)	N49-Zn3-N9	92.5(3)	N12-Zn4-N10	75.7(3)
N41-Zn1-N23	162.2(3)	N29-Zn3-N9	92.6(3)	N32-Zn4-N10	98.8(3)
N3-Zn1-N23	90.4(3)	N49-Zn3-N47	73.7(3)	N52-Zn4-N10	161.2(3)
N43-Zn1-N23	88.5(3)	N29-Zn3-N47	152.5(3)	N30-Zn4-N10	89.6(3)
N44-Zn2-N24	92.9(3)	N9-Zn3-N47	111.3(3)	N12-Zn4-N50	98.6(3)
N44-Zn2-N4	93.8(3)	N49-Zn3-N27	114.8(3)	N32-Zn4-N50	164.6(3)
N24-Zn2-N4	92.0(3)	N29-Zn3-N27	73.7(3)	N52-Zn4-N50	75.7(3)
N44-Zn2-N6	107.9(3)	N9-Zn3-N27	149.4(3)	N30-Zn4-N50	90.2(3)
N24-Zn2-N6	155.2(3)	N47-Zn3-N27	90.5(3)	N10-Zn4-N50	87.9(3)

more extreme from M1 to M4. This increasing distortion may be accounted for by the self-assembly process that would either promote binding from the middle pockets outwards or in a linear fashion. Consequently, the last ion to be bound would obviously be located at the outer positions and thus probably receives the most strained geometry from the ligand system.

Comparing these structures to similar structurally characterised ones reported in the literature yields a number of similarities. Thompson has produced a series of dinuclear triple helicates that are similarly bridged by the diazine group, with metal-metal separations around 3.7 Å for the Mn(II) and Ni(II) assemblies and smaller twist angles *via* $N_{diazine}$ around 70°.[5] Cu(II) still forms a dinuclear structure but is only bridged by a single ligand strand with nitrate anions and water molecules completing the coordination geometry with a twist between metal centres around 100°.[5] Hannon has been working on a similar ligand system however his work is mainly limited to tetrahedral diamagnetic anions. There are examples of octahedral metal ions (Ni(II) and Fe(II)) however these helical assemblies are bridged by a bis phenylene group that causes large metal-metal separations around 11.6 Å.[37]

Magnetism

Variable temperature magnetic susceptibility measurements were made on powdered samples of the previously discussed tetranuclear chains except the Zn(II) assembly that is purely diamagnetic. The raw data obtained from the SQUID are manipulated to give values of χ_m that have been diamagnetically corrected for both sample holder and organic components of the structure. Fitting of the data requires a suitable model based upon a linear system, which yields the Hamiltonian expression (18).

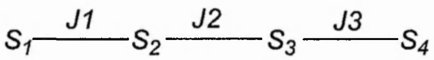

Figure 109 Proposed model for a tetranuclear chain.

$$H_{ex} = -2J1\{S_1 \cdot S_2\} - 2J2\{S_2 \cdot S_3\} - 2J3\{S_3 \cdot S_4\} \qquad (18)$$

From examination of any structure in this chapter it can be seen that there are two distinct types of diamagnetic bridge that separate adjacent metal centres. Using Fig. 109, the pairs of spins S_1-S_2 and S_3-S_4 are separated by a triple diazine link and S_2-S_3 by three pyridazine rings. Consequently it is assumed that $J1 = J3$ allowing the system to be modelled with only two J values. MAGMUN is able to handle this type of system but does require the generation of two energy profiles in ow0L.

Examination of the twist of the diazine link between metals *via* their least square planes has been used previously to predict the type exchange behaviour. It has been reported that twist angles less than ~ 80° propagate weak ferromagnetic behaviour whereas those greater than ~ 80° can propagate significant antiferromagnetic behaviour.[5] Pyridazine rings have been reported to propagate weak to strong antiferromagnetic interactions.[123]

*[Cu_4(**L7**)$_3$](ClO_4)$_8$ (**A24**)*

This sample has a room temperature effective magnetic moment of 4.01 μ_b that decreases upon cooling down to 3.60 μ_b at 5 K that would suggest a very weak antiferromagnetic interaction (Fig. 110). However, structural considerations indicate a more complex scenario with mixtures of both ferro- and antiferromagnetic behaviour because of the varying twist angles observed between adjacent metal centres. Examination of the twist angles across the triple diazine bridge gives an average value of 80° with a range from 75 to 89° implying a very weak ferromagnetic interaction. As previously mentioned pyridazine rings are known to propagate weak to strong antiferromagnetic behaviour. Fitting of the data between 300 and 5 K as a tetranuclear chain with four spins of $S = 1/2$ with two J values to accommodate a weak ferromagnetic interaction and a varying antiferromagnetic interaction does suprisingly yield a good fit of the data leading to $g = 2.12$, $J1$ (diazine) = 0.53 cm^{-1}, $J2$ (PDZ) = -1.65 cm^{-1}, TIP = 800 x 10^{-6} emu mol^{-1} and 10^{2}R = 1.46.

*[Mn_4(**L7**)$_3$](ClO_4)$_8$ (**A25**)*

Upon cooling, the sample shows a steady decrease in effective magnetic moment from a room temperature value of 12.07 μ_b down to 5.06 μ_b at 2 K (Fig. 110). The room temperature effective magnetic moment is in good agreement with a spin only value of 11.83 μ_b. The decrease observed in effective magnetic moment would suggest weak antiferromagnetic behaviour. However, as with the Cu(II) assembly, structural considerations indicate a more complex scenario with mixtures of both ferro- and antiferromagnetic behaviour because of the varying twist angles observed between adjacent metal centres.

The twist angles formed across the diazine links between the Mn(II) centres have an average value of 76° (range 66-83°) implying a very weak ferromagnetic interaction while the twist angles across the central pyridazine rings are considerably smaller with an average value of 10° (range 4-19°) which is known to cause antiferromagnetic exchange. However, a two exchange model for a linear chain (Fig. 109) with four spins of S = 5/2 expecting mixtures of ferro and antiferromagnetic behaviour will not fit the experimental data. An adequate fit between 300 and 5 K can be achieved when both interactions are assumed to be weakly antiferromagnetic. Thus g = 2.10, $J1$ (diazine) = -0.96 cm^{-1}, $J2$ (PDZ) = -0.66 cm^{-1} and 10^{2}R = 2.41 (fig 111), the introduction of other parameters only decreased the quality of the fit.

Interestingly, a more acceptable fit of the data is obtained when the system is modelled as a pair of non-interacting dimers with no exchange across the pyridazine ring, thus $J2$ = 0. This very weak/ no exchange has been reported in a polymeric Ni(II) pyridazine bridged system.[124] Using the dimer model a fit is obtained with g = 2.09. $J1$ = -1.11 cm^{-1} and 10^{2}R = 1.95 (Fig. 110).

$[Ni_4(L7)_3](OTf)_8$ (**A26**)

Upon cooling, the effective magnetic moment decreases from 4.44 down to 3.67 μ_b at 2 K suggesting very weak anitferromagnetic exchange (Fig. 110). However, when compared to the spin-only value for four S = 1 species of 5.65 μ_b there is a large difference, which could be a consequence of very strong antiferromagnetic coupling. This is certainly not the case because of the small change in effective magnetic

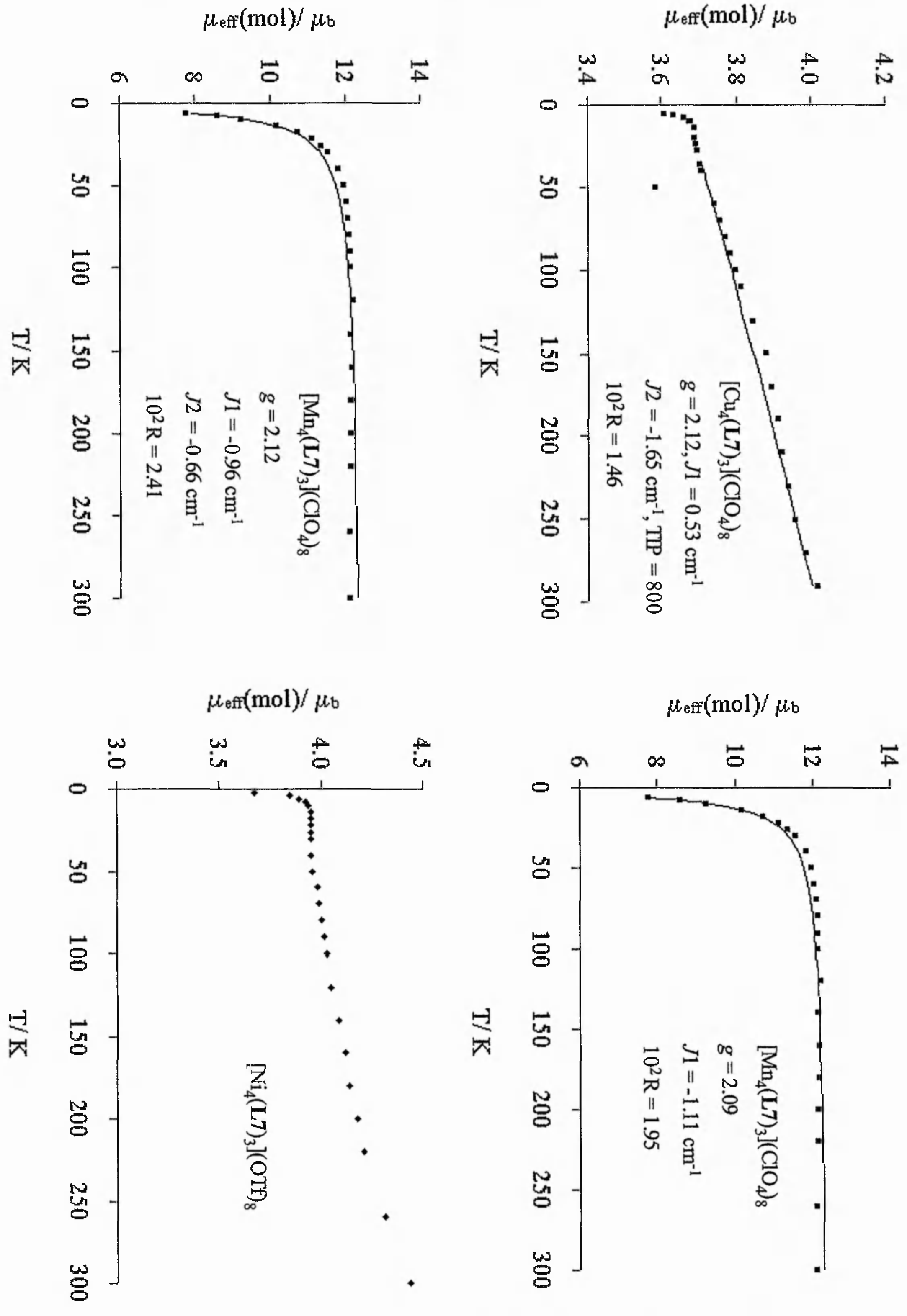

Figure 110 Top right: $[Cu_4(\mathbf{L7})_3](ClO_4)_8$ (**A24**) displaying predominantly antiferromagnetic exchange, top left: $[Mn_4(\mathbf{L7})_3](ClO_4)_8$ (**A25**) displaying antiferroamgnetic exchange ($J1 \neq J2 \neq 0$), bottom right: $[Mn_4(\mathbf{L7})_3](ClO_4)_8$ (**A25**) displaying antiferroamgnetic exchange ($J1 \neq 0$, $J2 = 0$) and bottom left: $[Ni_4(\mathbf{L7})_3](OTf)_8$ (**A26**) displaying antiferroamgnetic exchange.

moment upon cooling. Therefore, it is suggested that either some Ni(II) ion are vacant from the assembly or more likely that some have a diamagnetic spin state. This latter idea is supported by the crystal structure where Ni4 has a square based pyramidal type geometry that can often lead to an $S = 0$ spin state.[85] However, assuming only three $S = 1$ Ni(II) ions per tetranuclear chain still does not yield an adequate fit of the data and it is suggested that upon drying there is probably a mixture of coordination environments leading to random mixtures of spin states associated with the Ni(II) ions.

Other Metal Ions

Attempts to make tetranuclear helical chains with other labile transition metal ions have been unsuccessful. Firstly, the Co(II) derivative was attempted with various anions (ClO_4^-, OTf^-, BF_4^-, PF_6^- and NO_3^-) in a manner of different ways, however no crystalline material was ever obtained. Further characterisation of the powders by ESI-MS did not indicate the motif to be present. Room temperature magnetic moment of the triflate salt gave a value of zero μ_b indicating no paramagnetic component present and it is likely that the Co(II) has been oxidised to Co(III) in presence of air.[38] ^1H NMR of the triflate analogue only displayed broad and resolved peaks over the typical aromatic range, but appear to show some paramagnetic shifting in minor amounts. From these studied it is proposed the solids obtained are probably a mixture a various mixed oxidation Co(II) and Co(III), possibly with different configurations. Further investigations under anaerobic conditions have not been undertaken.

Fe(II) triflate yields a powder which could not be crystallised. ESI-MS indicated very small amounts of the desired chain present along with a lot of other species and the ^1H NMR displayed a mixture of species that are paramagnetically shifted. Addition of the ligand to a hot solution of $Fe(II)(ClO_4)_2$ in methanol yields a precipitate after stirring briefly to avoid oxidation to Fe(III), examination of this low yielding solid by ESI-MS indicated the +4 and +3 states of the chain present along with some other unidentifiable species. Further investigations and attempts to crystallise this product have not been undertaken. Both the $Fe(III)(ClO_4)_3$ and the

Cr(III)(OTf)$_3$ yielded solids that are only water soluble and showed no ESI-MS signal.

7.3 Other Chain-Like Assemblies

Subtle changes in ligand design can often lead to completely different structural motifs. In this case replacement of the terminal amidrazone with the carboxyamido group yields **L7A** (Fig. 111). It was envisaged that this ligand may form a complete [4 x 4] grid when reacted with Cu(II) similar to that previously reported by Matthews.[61] However, reaction of **L7A** with various first row transition metal salts only yielded powders that could not be crystallised. The only set of crystals were obtained by reaction of the ligand with an excess of $Cu(ClO_4)_2 \cdot 6H_2O$ in acetonitrile followed by the addition of two equivalents of triethylamine and water.

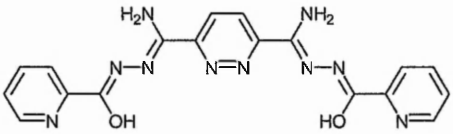

Figure 111 L7A was envished to form a complete [4 x 4] grid with Cu(II).

The structure is made up from a cation surrounded by six perchlorate anions along with a number of water and acetonitrile molecules. The cation is made from two separate ligand strands that spiral around a bowed arrangement of five Cu(II) ions and is best described as a pentametallic double helicate which is the largest chain-like Cu(II) assembly ever reported (Fig. 112). From a simple charge balance each ligand is assigned with a -3 charge indicating three protons have been removed, however it is unclear from the structure, which protons have been retained. The cation has an external length of ~ 21 Å with an internal distance separating the most extreme Cu(II) ions of ~ 15 Å. The structure has a *C2/c* space group with each cationic asymmetric unit made from one individual ligand strand and three Cu(II) ions. The Cu(II) ions have separations Cu1-Cu2 ~ 4.72 Å and Cu2-Cu3 ~ 3.90 Å with a Cu1-Cu2-Cu3 angle of ~ 135° confirming the bow shaped structure.

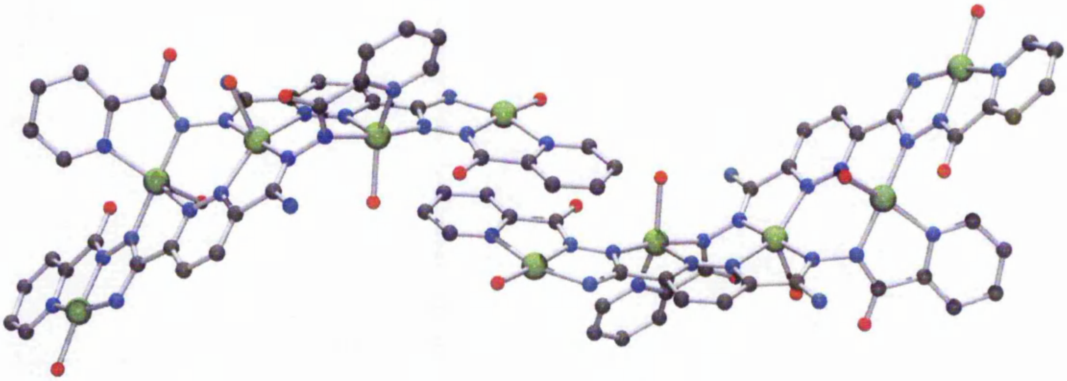

Figure 112 POV-Ray representation of $[Cu_5(\mathbf{L7A}\text{-}3H)_2]^{+6}$ cation showing the close proximity of separate chains.

Table 48 Selected bond angles/ ° and lengths/ Å for $[Cu_5(\mathbf{L7A}\text{-}3H)_2]^{+6}$ cation.

Cu1-N1	2.025(6)	N2-Cu1-O11	174.6(2)	N9i-Cu2-N5	94.77(18)
Cu1-N2	1.904(5)	N2-Cu1-N4	80.6(2)	N3-Cu2-N5	76.34(18)
Cu1-N4	1.967(5)	O11-Cu1-N4	99.6(2)	N10i-Cu2-N5	120.04(19)
Cu1-O11	1.951(5)	N2-Cu1-N1	80.2(2)	O12-Cu2-N5	93.6(2)
Cu2-N3	1.950(5)	O11-Cu1-N1	99.1(3)	N8-Cu3-N8i	177.7(3)
Cu2-N5	2.223(5)	N4-Cu1-N1	160.1(2)	N8-Cu3-N6i	101.69(18)
Cu2-N9	1.935(5)	N9i-Cu2-N3	169.3(2)	N8-Cu3-N6	78.92(18)
Cu2-N10	2.012(5)	N9i-Cu2-N10i	80.9(2)	N8i-Cu3-N6	101.69(18)
Cu2-O12	2.079(5)	N3-Cu2-N10i	98.2(2)	N6i-Cu3-N6	150.8(3)
Cu3-N6	2.074(4)	N9i-Cu2-O12	93.1(2)	N8-Cu3-O13	88.83(14)
Cu3-N8	1.933(5)	N3-Cu2-O12	93.4(2)	N6-Cu3-O13	104.59(13)
Cu3-O13	2.258(7)	N10i-Cu2-O12	146.1(2)		

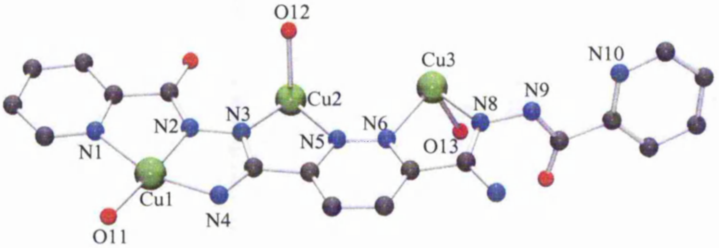

Figure 113 Asymmetric unit of $[Cu_5(\mathbf{L7A}\text{-}3H)_2]^{+6}$ cation.

Each of the three Cu(II) ions have different donors. Cu1 has a distorted square planar geometry that is quite common for Cu(II)[85] with its donors made up from three nitrogen donors consisting of N_{py}, $N_{diazine}$ and N_{amine}, and one oxygen donor associated with a water molecule. The bond lengths and angles are listed in Table 48 and are not particularly out of the ordinary. Cu2 has a distorted N_4O square based pyramidal geometry with four reasonably short bonds less than 2.08 Å and one long equatorial contact to N5 of 2.223(5) Å, which is indicative of the Jahn-Teller distortion often observed in Cu(II) coordination compounds. Cu3 has a similar distorted N_4O square based pyramidal geometry with a long equatorial contact of 2.258(7) Å to O13.

The twist between the metal ions can be estimated as with the tetrametallic chains by examination of the least square plane of the relevant ligand framework. Between Cu1 and Cu2 there is a single *trans* diazine link that is reasonably flat with a twist around 9°. One *cis* diazine link and a pyridazine ring, with twist angles of 75° and 7°, separate Cu2 and Cu3, respectively.

Fig. 113 indicates that the individual pentametallic chains lie in close proximity with separations less than 3.6 Å between adjacent ligand strands. The reasons for this are unclear, the aromatics are ellipsed making π-π stacking unlikely, however, there are numerous disordered acetonitrile molecules around the terminal pyridine rings that appear to be acting as bridging hydrogen bond donors to the hydrogen atoms associated with the terminal pyridine rings. Consequently, it appears that this interaction holds the individual chains together giving the extended structure a wave-like pattern (Fig. 112).

The chain like compound is not evident from ESI-MS with few ions formed at varying cone voltages. Electrochemical studies show no reversible peaks over the range -2 to 2 V with some irreversible peaks at a negative potential associated with reduction of the ligand framework.

No magnetic studies have been carried out; however modelling of any variable temperature data should be relatively straightforward with a two exchange integral model based upon five spins of $S = 1/2$. Exchange between Cu1 and Cu2 across the single diazine bridge would probably be strongly antiferromagnetic,[125] whilst that between Cu2 and Cu3 will have competing anti- and ferromagnetic interactions.

7.4 Conclusion

L7 has shown the ability to from tetranuclear chains with a select number of first row transition metals. The stability of these complexes is confirmed in solution by ESI-MS along with their acetonitrile adducts. Their formation is limited to metal ions that which are formally in the +2 oxidation state and display an octahedral coordination preference. However, the ligand appears to be not too rigid, allowing deviation across the first row of transition metal ions, associated with the ion's specific coordination preference. The magnetic data are consistent with their structures, however in each case there is a fine balance between the different superexchange pathways and even drying of the samples may alter the magnetic properties. **L7A** introduces a novel ligand binding mode by the deprotonation of the peripheral amine group that is observed later on (chapter 8) in the formation of a Cu_{20} assembly. No evidence *via* solution or solid-state studies suggests the formation of any particular structural motif when **L7A** is reacted with other first row transition metal ions, demonstrating the versatility of the Cu(II) ion.

Chapter Eight

Pyrimidine Bridged Helical Assemblies

8.0 Introduction

The formation of more structurally diverse assemblies rather than helical chains and grids is regularly achieved by a combination of both designed and serendipitous approaches.[126] However, most of these structurally diverse assemblies often contain either diamagnetic metal ions or paramagnetic metal ions separated by long diamagnetic bridges that hinder any significant magnetic interaction.[117]

Examination of the ligands successfully utilised to form both helical chain and grid like assemblies indicated that simple structural changes could be programmed into the ligand strand to allow the formation of some more diverse structural assemblies. This approach should produce assemblies with close metal ion proximity and thus, promote intramolecular magnetic exchange.

Design

L8 is structurally comparable to **L7** that forms tetrametallic triple helicates (Chapter Seven). However, substitution of the pyridazine heterocycle for a pyrimidine heterocycle confers a bowed arrangement of bridging bidentate binding sites on the ligand framework (Fig. 114) and hence, it is likely to form a circular type assembly.

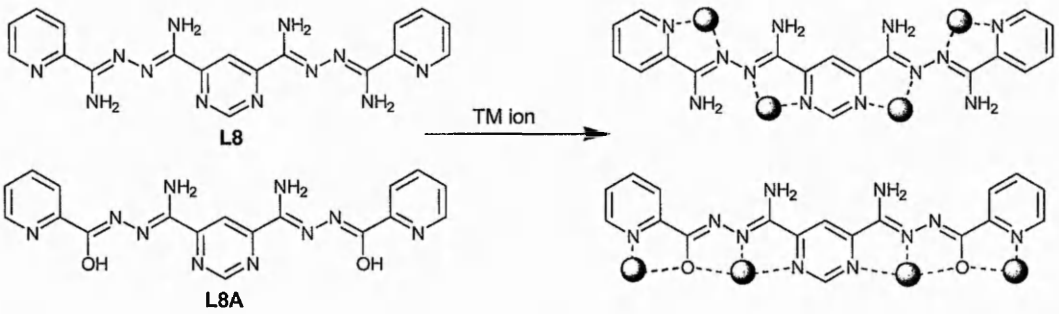

Figure 114 **L8** has a bowed arrangement of bidentate donors, whilst **L8A** has a mixture of both tridentate and bidentate donors.

Further modification of **L8** through replacement of the terminal amidine group by an carboxyamido group furnishes **L8A,** which provides a linear array of two internal tridentate and two external bidentate pockets. The external bidentate pockets programmed into **L8A** could potentially bind in two ways; either as depicted or as seen in **L8**. However, the formation of a non-homoleptic [4 x 4] grid was envisaged when **L8A** was reacted with a transition metal ion, which displays an octahedral coordination preference.

Synthesis

These ligands can be readily prepared by methodology laid out in chapter 7 *via* addition of the desired capping group (pyridine-2-amidrazone **(33)** for **L8** and pyridine-2-hydrazido **(35)** for **L8A**) to crude diethyl pyrimidine-4,6-diimidate **(7)** (Chapter Six) in dry methanol along with a catalytic amount of glacial acetic acid. In both cases this methodology allowed the preparation of large quantities of ligand suitable for further study.

*Structure of **L8***

Crystals of this ligand were accidentally obtained when it was reacted with a large excess of $Mn(ClO_4)_2 \cdot 6H_2O$ in aqueous acetonitrile. The IR spectra of these crystals indicated no anion present with an almost identical fingerprint to the free ligand. This was confirmed by single crystal X-ray studies, which located the desired ligand along with water and acetonitrile molecules. Examination of the structure shows that there are a number of intramolecular hydrogen bonds that hold the ligand in an essentially flat conformation (Fig. 115). The assignment of hydrogen bonds is made from short N-H contacts that have a range from ~ 2.30 to ~ 2.53 Å. Within the unit cell the individual ligand strands stack in layers with large separations between adjacent aromatic rings around 8.0 Å due to sandwiched intermolecular hydrogen bonded water molecules between pairs of ligands.

Examination of this result suggests poor reactivity of **L8** towards transition metal ions due to numerous intramolecular hydrogen bonds and thus, **L8** is more likely to react with very labile metal ions that display a variety of coordination preferences, *i.e.*, Cu(II).

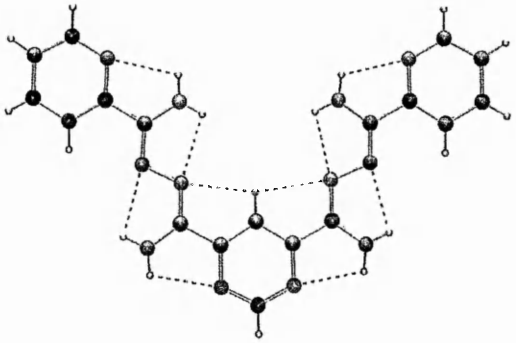

Figure 115 POV-Ray representation of **L8** with intramolecular hydrogen bonds noted as dotted lines.

*Complexation: **L8** + $Cu(ClO_4)_2{\cdot}6H_2O$*

Addition of the ligand to excess $Cu(ClO_4)_2{\cdot}6H_2O$ in aqueous acetonitrile yielded a brown solution which upon standing deposited a green powder. Recrystallisation of the powder from a concentrated solution of nitromethane and acetonitrile yielded crystals suitable for X-ray analysis.

*Solid-State Studies: $[Cu_8(\mathbf{L8})_4(H_2O)_8](ClO_4)_{16}$ (**A28**)*

The structure revealed a highly symmetrical cation with an S_4 axis made up of a pair of Cu(II) ions bridged by diazine strands which has been recently published.[126] The assembly is best described as a circular single stranded side-by-side complex[117a] or as a circular single stranded mesocate.[117b] The structure contains eight Cu(II) ions in a bowl-shape arrangement that is composed of two bowed pairs of parallel ligands and eight coordinated water molecules (Fig. 116). The cation has an external long dimension of approximately 20.1 Å with a reasonably large internal cavity around 4.5 Å wide that contains a number of anions and may be solvent molecules, which are held in position by numerous hydrogen bonds to the peripheral amine groups located on the ligand strand. Each ligand strand provides an array of four bidentate donors that bind to four separate Cu(II) ions in a similar manner to that observed in **L7**, however, the central pyrimidine ring stops the formation of a linear chain, instead preferring a bowl shaped arrangement. This causes a distinct twist across the $N_{diazine}$ bond between adjacent metal centres in such a way that the terminal pyridine rings are almost perpendicular with respect to the central pyrimidine ring. The twist

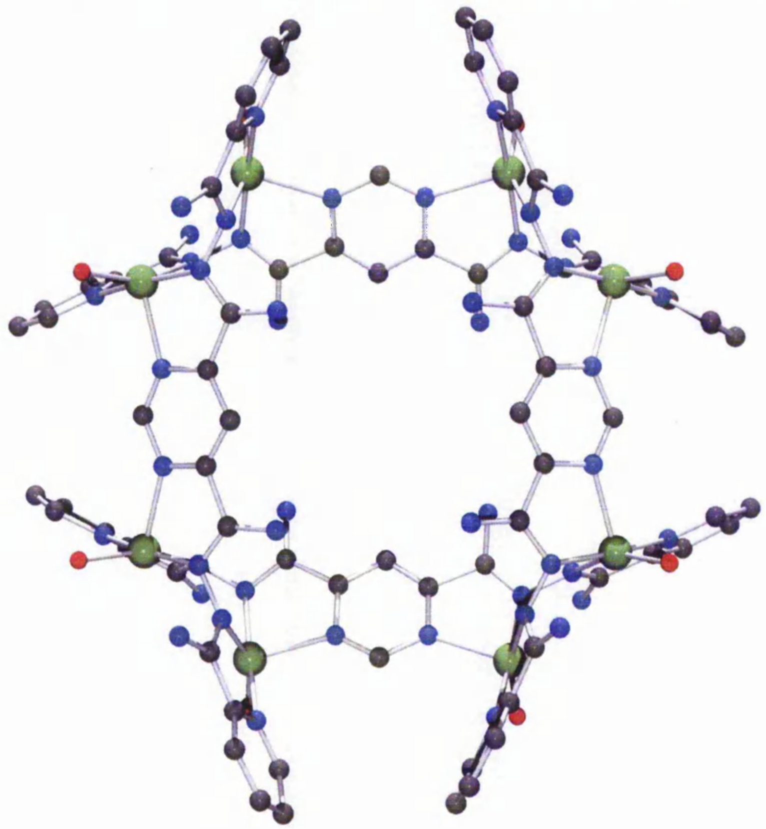

Figure 116 POV-Ray representation of $[Cu_8(\mathbf{L8})_4]^{+16}$ cation.

Table 49 Selected bond lengths/ Å and angles/ ° for $[Cu_8(\mathbf{L8})_4]^{+16}$ cation.

Cu1-N1	1.977(5)	N1-Cu1-N3	79.75(17)	N4-Cu2-N6	76.05(15)
Cu1-N3	1.992(4)	N1-Cu1-N7	101.72(18)	N4-Cu2-N10	90.31(16)
Cu1-N7	2.253(4)	N1-Cu1-N9	169.56(18)	N4-Cu2-N12	170.55(18)
Cu1-N9	1.998(4)	N1-Cu1-O1	95.4(2)	N4-Cu2-O2	94.77(16)
Cu1-O1	1.970(5)	N3-Cu1-N7	102.20(15)	N6-Cu2-N10	105.65(15)
Cu2-N4	1.999(4)	N3-Cu1-N9	90.60(16)	N6-Cu2-N12	103.42(19)
Cu2-N6	2.269(4)	N3-Cu1-O1	165.4(3)	N6-Cu2-O2	91.70(18)
Cu2-N10	1.994(4)	N7-Cu1-N9	76.26(16)	N10-Cu2-N	1280.7(2)
Cu2-N12	1.985(5)	N7-Cu1-O1	92.2(3)	N10-Cu2-O2	162.6(2)
Cu2-O2	1.996(4)	N9-Cu1-O1	95.0(2)	N12-Cu2-O2	94.7(2)

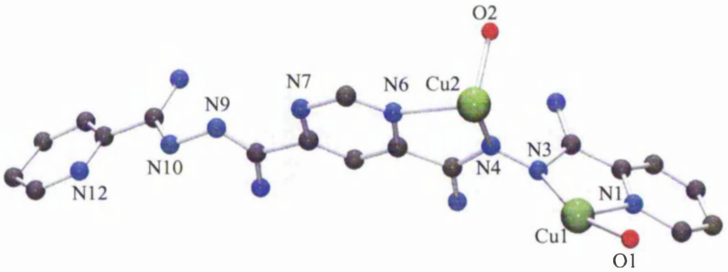

Figure 117 POV-Ray representation of $[Cu_8(\mathbf{L8})_4]^{+16}$ asymmetric unit.

adjacent metal centres as previously set out in chapter 7 to give an average value of 81° which is similar to that reported by other authors.[125] The separation of the Cu(II) ions across the $N_{diazine}$ link is around 3.74 Å and even greater across N_{pym} with a value around 6.59 Å.

The Cu(II) ions have a square based pyramidal coordination geometry that is made up from two sets of bidentate chelating sub-units, one terminal N_{py}-$N_{diazine}$ and one central $N_{diazine}$-N_{pym} that are located on different ligand strands and one water molecule. The bond lengths are typical for Cu(II) in this geometry (Table 49) with four reasonably short bonds to three nitrogen donors (N_{py}, $N_{diazine}$ and $N_{diazine}$) and the water molecule that are less than 1.996(4) Å, and one long contact to N_{pym} around 2.26 Å associated with its low donor power and Jahn-Teller distortion of the Cu(II) ion.

Solution Studies

Along with the perchlorate assembly both the tetrafluoroborate and the triflate analogues have also been prepared in the same manner, the former has been structurally characterised and contains the same central cation surrounded by anions and solvent molecules. These studies demonstrate that the anion does not control the formation of the octanuclear species, in contrast to other circular species.[127] Further evidence is provided by ESI-MS in acetonitrile at a range of cone voltages (0-20 V) for all three assemblies that display peaks that correspond to the successive loss of the appropriate anion. Visible spectroscopy in acetonitrile confirms the presence of the Cu(II) ion with a broad absorbance at 660 nm ($\varepsilon = 1596\ dm^3\ mol^{-1}\ cm^{-1}$) which is in accord with the [2 x 2] homometallic Cu(II) grid observed in chapter 3.

*Magnetism: $[Cu_8(\mathbf{L8})_4(H_2O)_8](ClO_4)_{16}$ (**A28**)*

Upon cooling, the effective magnetic moment shows a steady increase from a room temperature value of 5.23 μ_b up to 6.17 μ_b at 2 K. This increase at low temperatures is indicative of weak ferromagnetic exchange and has been observed in similar Cu(II) motifs with diazine twists between adjacent metal centres less than ~ 80°.[123] The exchange across the pyrimidine ring is assumed to be negligible.[108] Modelling of the data as a dinuclear species with one exchange integral and two spins of $S = 1/2$ yields the Bleaney-Bowers equation (chapter 1). Fitting on this basis, yields an excellent fit of the data with $g = 2.11$, $J = 15.78$ cm^{-1} and 10^2 R = 0.54 (Fig. 118).

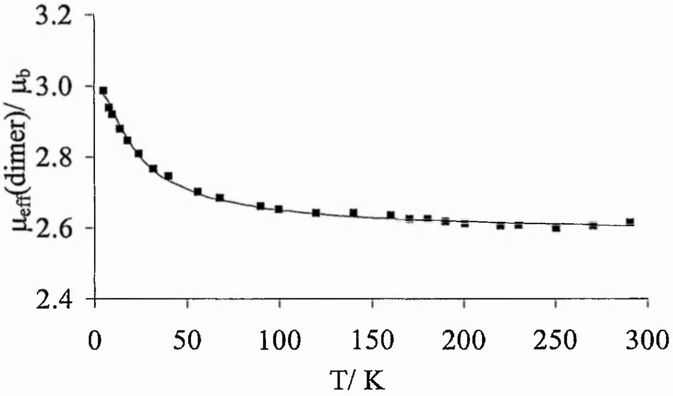

Figure 118 Indicates a ferromagnetic interaction within $[Cu_8(\mathbf{L8})_4(H_2O)_8](ClO_4)_{16}$. Solid line represents modelled data and points represent experimental data.

Other Metal Ions

From this initial lead and the failure of any labile anions to produce assemblies with the first row transition metal ions, for example **L8** will not react with $Mn(ClO_4)_2{\cdot}6H_2O$, more strongly coordinating anions were investigated. The basis of this idea was that strongly bound anions, *i.e.*, chloride, would only allow the addition of four further donors to a single octahedrally coordinated metal ion. Hence, the binding of two bidentate pockets per metal ion was envisaged and the formation of an octanuclear species analogous to $[Cu_8(\mathbf{L8})_4(H_2O)_8](ClO_4)_{16}$ (Fig. 119). However, the strongly bound anions effectively make the assemblies neutral and hence, cannot be detected by ESI-MS.

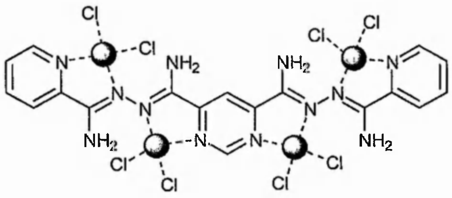

Figure 119 Suggested binding mode of **L8** when reacted with a first row transition metal chloride.

*Complexation: **L8** + $MnCl_2{\cdot}4H_2O$*

Addition of **L8** dissolved in DMF to a solution of excess $MnCl_2{\cdot}4H_2O$ in methanol deposited large red crystals upon standing overnight. X-ray analysis of the crystals only gave a very weak diffraction pattern, but the structure of the assembly is unambiguous (Fig. 120).

Solid-State Studies: $[Mn_6(\mathbf{L8})_4Cl_{12}]$

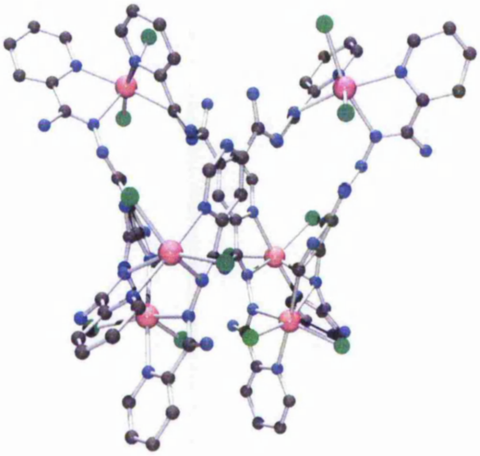

Figure 120 POV-Ray representation of $[Mn_6(\mathbf{L8})_4Cl_{12}]$ (**A29**).

The structure consists of four ligand strands that wrap around six Mn(II) ions in an unsymmetrical manner (Fig. 120). Each ligand strand donates three bidentate donors rather than four as observed in $[Cu_8(\mathbf{L8})_4(H_2O)_8](ClO_4)_{16}$, since the vacant coordination site is blocked by an intramolecular hydrogen bond (Fig. 122). This ligand binding mode forms two dimeric diazine bridged subunits (Mn1-Mn2 and Mn5-Mn6) that connect with two mononuclear units (Mn3 and Mn4). The monomeric units are separated from each other by ~ 9.63 Å with similar separations towards the dimeric subunits, Mn4-Mn6 ~ 9.8 Å and Mn3-Mn2 ~ 10.0 Å. Within the dimeric subunits the metal have separations of Mn1-Mn2 ~ 4.75 Å and Mn5-Mn6 ~ 4.71 Å that are considerably longer than those observed in $[Cu_8(\mathbf{L8})_4(H_2O)_8](ClO_4)_{16}$ (**A28**) and other diazine bridged Mn(II) ions.[5] The twist *via* the diazine link can be estimated by examination of the least square planes as previously set out in chapter 7. In each dimeric subunit there are two diazine bridges, which have a range from 49 to

Table 50 Selected bond angles/ ° of $[\mathrm{Mn_6}(\mathbf{L8})_4\mathrm{Cl_{12}}]$.

N24-Mn1-N3	79.1(6)	N21-Mn2-N4	112.3(7)	N41-Mn3-N43	73.7(7)
N24-Mn1-N1	113.7(6)	N21-Mn2-N23	68.7(5)	N41-Mn3-N12	93.2(8)
N3-Mn1-N1	68.7(5)	N4-Mn2-N23	78.6(6)	N43-Mn3-N12	89.9(7)
N24-Mn1-Cl2	151.6(5)	N21-Mn2-N6	176.9(6)	N41-Mn3-N10	160.7(8)
N3-Mn1-Cl2	97.8(6)	N4-Mn2-N6	69.2(6)	N43-Mn3-N10	92.9(7)
N1-Mn1-Cl2	90.7(5)	N23-Mn2-N6	109.3(5)	N12-Mn3-N10	72.5(6)
N24-Mn1-N26	69.8(6)	N21-Mn2-Cl3	93.2(5)	N41-Mn3-Cl5	94.8(8)
N3-Mn1-N26	110.8(6)	N4-Mn2-Cl3	93.9(5)	N43-Mn3-Cl5	88.5(6)
N1-Mn1-N26	176.1(6)	N23-Mn2-Cl3	155.3(5)	N12-Mn3-Cl5	171.0(5)
Cl2-Mn1-N26	85.5(5)	N6-Mn2-Cl3	89.4(4)	N10-Mn3-Cl5	98.8(5)
N24-Mn1-Cl1	92.3(5)	N21-Mn2-Cl4	90.5(7)	N41-Mn3-Cl6	91.5(6)
N3-Mn1-Cl1	154.5(5)	N4-Mn2-Cl4	148.2(5)	N43-Mn3-Cl6	165.2(5)
N1-Mn1-Cl1	93.6(4)	N23-Mn2-Cl4	90.3(5)	N12-Mn3-Cl6	89.4(5)
Cl2-Mn1-Cl1	100.7(3)	N6-Mn2-Cl4	87.1(5)	N10-Mn3-Cl6	101.0(6)
N26-Mn1-Cl1	88.1(5)	Cl3-Mn2-Cl4	107.2(3)	Cl5-Mn3-Cl6	94.4(4)

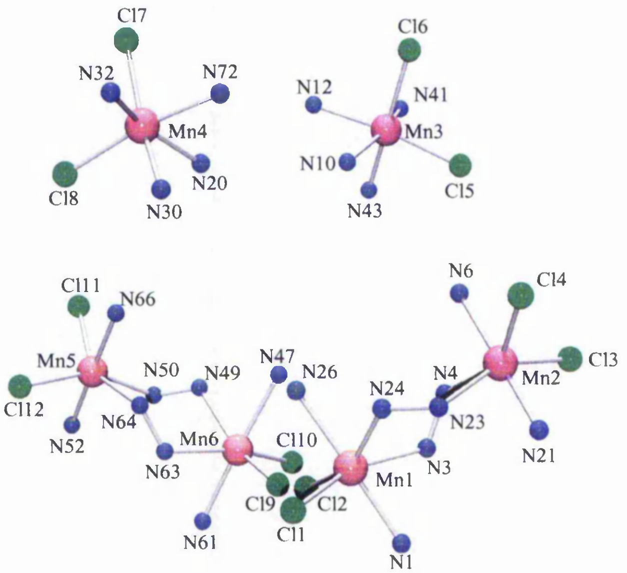

Figure 121 POV-Ray representation of $[\mathrm{Mn_6}(\mathbf{L8})_4\mathrm{Cl_{12}}]$ inner core.

Table 51 Selected bond lengths/ Å of $[\mathrm{Mn_6}(\mathbf{L8})_4\mathrm{Cl_{12}}]$.

Mn1-Cl1	2.457(7)	Mn2-Cl3	2.439(7)	Mn3-Cl5	2.389(9)
Mn1-Cl2	2.377(9)	Mn2-Cl4	2.467(10)	Mn3-Cl6	2.432(10)
Mn1-N24	2.187(18)	Mn2-N21	2.227(17)	Mn3-N41	2.176(19)
Mn1-N3	2.292(16)	Mn2-N4	2.242(19)	Mn3-N43	2.19(2)
Mn1-N1	2.316(16)	Mn2-N23	2.357(17)	Mn3-N12	2.223(17)
Mn1-N26	2.389(16)	Mn2-N6	2.380(17)	Mn3-N10	2.315(18)

71° similar to those reported in Chapter Seven and in the literature.[5] The Mn(II) ions have highly distorted *cis*-Cl_2N_4 octahedral geometries with basal planes consisting of two Cl ions and two N donors. N_{py} and $N_{diazine}$ have relatively short bonds with a range of 2.176(19) to 2.292(16) Å, whilst extremely long bonds are observed towards the chloride ions and N_{pym} with ranges of 2.337(9) to 2.467(10) Å and 2.223(17) to 2.389(16) Å respectively (Table 51).

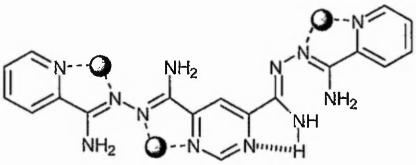

Figure 122 Binding mode of **L8** in [Mn_6(**L8**)$_4Cl_{12}$] with a intramolecular hydrogen represented by the dashed bond.

*Magnetism: [Mn_6(**L8**)$_4Cl_8$] (**A29**)*

No variable temperature magnetisation studies have been done on [Mn_6(**L8**)$_4Cl_8$], however it is predicted from the twist angles across $N_{diazine}$ to be weakly ferromagnetic with six spins of $S = 5/2$. The exchange integral would have one value across Mn1-Mn2 and Mn5-Mn6, with Mn2 and Mn4 providing a spin-only contribution.

*Complexation: **L8A** + $Cu(ClO_4)_2{\cdot}6H_2O$*

Examination of this ligand suggests that it should favour grid formation (Fig. 114) however, after numerous attempts to form assemblies, especially with Mn(II), no suitable crystals could be formed for X-ray analysis and the powders presented no identifiable peaks when examined by ESI-MS. These included a number attempts with triethylamine as a base. However, the addition of two equivalents of triethylamine to a solution of excess $Cu(ClO_4)_2{\cdot}6H_2O$ in acetonitrile followed by the addition of ethanol and a small amount of water yielded, upon standing, small red plates.

Solid-State Studies: $[Cu_{20}(\mathbf{L8A}\text{-}4H)_4(\mathbf{L8A}\text{-}2H)_4(H_2O)_{16}](ClO_4)_{16}$ (**A30**)

Examination of the crystals by a synchrotron source indicated a highly symmetrical structure with a *P4(2)* space group. The structure has not been fully refined and consequently only the central cation is clear. From examination of the coordination modes of the ligand strands and the number of metal ions present it is suggested that the cation has an overall charge of +16, which is supported by chemical analysis.

The large cation has a pseudo octagonal perimeter with a long external dimension around 19.4 Å and is the third largest Cu(II) assembly ever reported (largest using a single ligand), containing twenty metal ions (Fig. 123). Only the four central Cu(II) ions are bound in a grid-like manner with those towards the perimeter being bridged by $N_{diazine}$ giving the cation a mixture of helical and grid-like ligand binding modes (Fig. 124). Consequently, these binding modes give the cation depth with the Cu(II) ions from top to bottom having a separation of ~ 9.5 Å. The ligand strands adopt two different modes with one type of strand adopting a typical grid-like conformation with a formal charge of -2 due to the removal of alkoxide protons and the second has helical type conformation allowing the diazine link to act as a bridge between metal centres with a formal charge of -4 (Fig. 125).

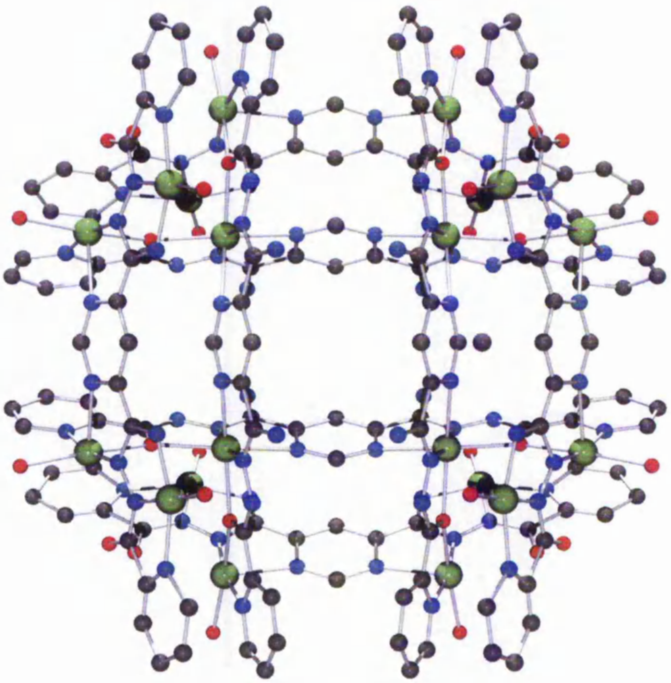

Figure 123 POV-Ray representation of $[Cu_{20}(\mathbf{L8A}\text{-}4H)_4(\mathbf{L8A}\text{-}2H)_4(H_2O)_{16}]^{+16}$ cation.

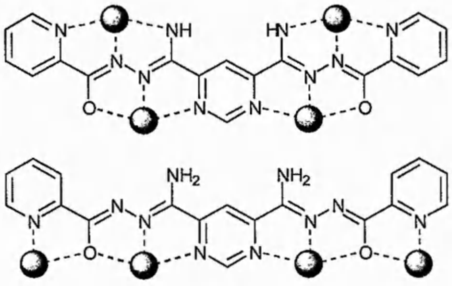

Figure 124 Binding modes of **L8A** in $[Cu_{20}(\mathbf{L8A}\text{-}4H)_4(\mathbf{L8A}\text{-}2H)_4(H_2O)_{16}](ClO_4)_{16}$.

The structure is made from four identical pentanuclear subunits (*P4* symmetry) that are separated by pyrimidine rings with metal-metal separations around ~ 6.5 Å. Within each subunit the five Cu(II) ions are related by a centre of inversion leading to three crystallographically different Cu(II) ions (Fig. 125). Cu3 occupies the corner of one subunit and is held in a typical distorted octahedral arrangement that is found in Cu(II) grid-like assemblies with the basal plane made from two N_{pym} donors and two alkoxide donors. The *cis*-N_4O_2 geometry appears to be analogous to that observed in the homometallic [2 x 2] grid (Chapter Three) and is axially compressed, $N_{diazine}$ ~ 1.94 Å, due to Jahn-Teller distortion. Cu1 has a five coordinate square based pyramidal geometry with the basal array composed of N_{py}, $N_{diazine}$, alkoxide, and a water molecule and the long axial position is occupied by N_{pym} that is typical of Cu(II) in this coordination geometry (Fig. 125).[62] The $N_{diazine}$ bridges Cu1 and Cu2, with the later having a four coordinate square planar structure made up from N_{py}, $N_{diazine}$, water and a deprotonated amine donor, which is analogous to the pentametallic Cu(II) chain observed in Chapter Seven. The twist across of the diazine link between Cu2 and Cu1 is relatively small ~ 6° indicating that the link is essentially flat and this is clearly seen from Fig. 126. The metal ions have separations of Cu1-Cu2 ~ 4.76 Å and Cu2-Cu3 ~ 4.04 Å with the bond angle formed between the latter pair *via* the alkoxy bridge having a value of ~ 140°.

Even at this poor level of crystallographic refinement a single perchlorate anion has been located within the central cavity and appears to be held by hydrogen bonds towards the peripheral amine groups. This suggests that this anion provides a template to allow formation of the assembly and this effect has been observed in numerous other structures.[127] No suitable crystals could be obtained with other non-coordinating anions supporting the template effect.

Table 52 Preliminary bond lengths/ Å for $[Cu_{20}(\mathbf{L8A}\text{-}4H)_4(\mathbf{L8A}\text{-}2H)_4(H_2O)_{16}]^{+16}$ asymmetric unit.

Cu1-N3	1.94	Cu2-N2	1.88	Cu3-N8	1.94
Cu1-N6	1.98	Cu2-N4	1.95	Cu3-O2	2.20
Cu1-O2	2.09	Cu2-O4	1.95	Cu3-N10	2.28
Cu1-O3	2.12	Cu2-N1	2.03		
Cu1-N5	2.29				

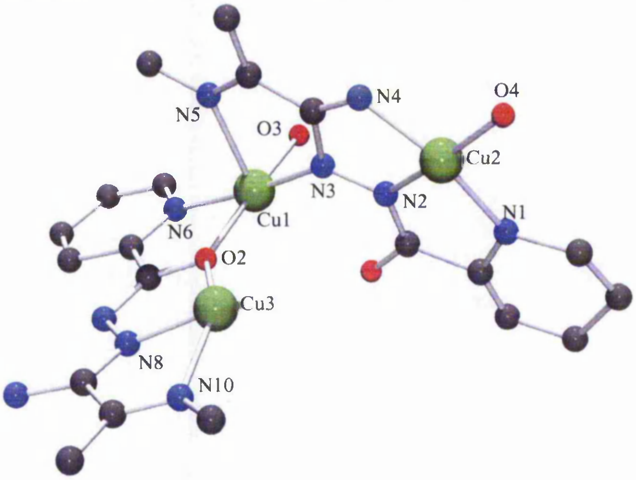

Figure 125 POV-Ray representation of $[Cu_{20}(\mathbf{L8A}\text{-}4H)_4(\mathbf{L8A}\text{-}2H)_4(H_2O)_{16}]^{+16}$ asymmetric unit.

Table 53 Preliminary bond angles/ ° of $[Cu_{20}(\mathbf{L8A}\text{-}4H)_4(\mathbf{L8A}\text{-}2H)_4(H_2O)_{16}]^{+16}$ asymmetric unit.

N3-Cu1-N6	168	N2-Cu2-N4	78	N8-Cu3-N8_7	169
N3-Cu1-O2	93	N2-Cu2-O4	176	N8-Cu3-O2	75
N3-Cu1-O3	93	N2-Cu2-N1	80	N8-Cu3-O2_7	112
N3-Cu1-N5	77	N4-Cu2-O4	99	N8-Cu3-N10_7	97
N6-Cu1-O2	80	N4-Cu2-N1	158	N8-Cu3-N10	76
N6-Cu1-O3	95	O4-Cu2-N1	102	N8_7-Cu3-O2	112
N6-Cu1-N5	94			N8_7-Cu3-O2_7	75
O2-Cu1-O3	172			N8_7-Cu3-N10_7	76
O2-Cu1-N5	92			N8_7-Cu3-N10	97
O3-Cu1-N5	95			O2-Cu3-O2_7	96
				O2-Cu3-N10_7	88
				O2-Cu3-N10	150
				O2_7-Cu3-N10_7	150
				O2_7-Cu3-N10	88
				N10_7-Cu3-N10	103

No evidence is provided for solution stability. ESI-MS in acetonitrile at ranging cone voltages and temperatures only produce very weak spectra that are difficult to differentiate between background noises. No other solution studies were undertaken due to lack of sample.

Magnetism: $[Cu_{20}(\mathbf{L8A}\text{-}4H)_4(\mathbf{L8A}\text{-}2H)_4(H_2O)_{16}](ClO_4)_{16}\cdot 14H_2O$ (**A32**)

This compound is unique because it contains a mixture of grid- and helical-like binding modes that introduce extra complications into the modelling of magnetic data due to different superexchange pathways. Fortunately, the structure has a high level of symmetry allowing simplifications to be made and reducing the size of the calculations. Consequently, the structure is simply modelled as five interacting Cu(II) ions with no exchange expected across the bridging pyrimidine ring (Fig. 126).[108] Examination of the pentanuclear subunit reveals a pseudo chain of five Cu(II) ions with two distinct superexchange pathways. Cu1-Cu2 are linked by a single diazine bridge that is essentially flat and from examination of the geometries around these ions the single unpaired electrons would be non-orthogonal to one another and consequently the exchange interaction would be expected to be strongly antiferromagnetic. On the other hand, Cu1 and Cu3 are bridged by a single alkoxide bridged with Cu3 exhibiting an axially compressed geometry. The single unpaired electron on this metal ion points axially and is orthogonal to Cu1's magnetic orbital and hence a very weak ferromagnetic exchange interaction is expected. Further symmetry within the structure repeats the same bridging functionalities allowing modelling of the data with two exchange integrals.

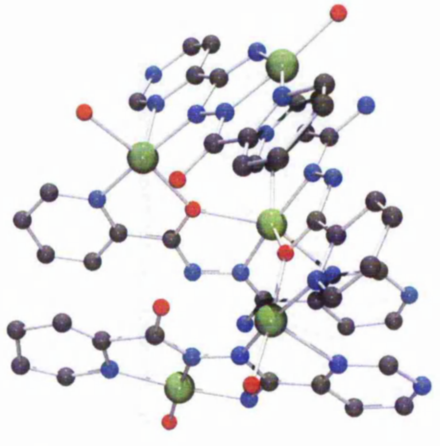

Figure 126 POV-Ray representation of Cu_5 subunit in $[Cu_{20}(\mathbf{L8A}\text{-}4H)_4(\mathbf{L8A}\text{-}2H)_4(H_2O)_{16}]^{+16}$ cation.

Upon cooling, the sample shows a steady decrease in effective magnetic moment from a room temperature value of 8.91 μ_b down to 5.22 μ_b at 2 K, which is in reasonable agreement with the room temperature spin-only value of 7.75 μ_b (Fig. 127). This decrease is indicative of antiferromagnetic exchange and is expected from structural considerations. Attempts to model the data as a pentanuclear chain with two exchange integrals to represent coupling across $N_{diazine}$ and alkoxide with the former integral being strongly antiferromagnetic would not yield adequate fits (10^2 R ~ 20). Strangely, a good fit of the experimental data was obtained when the interactions were swapped in magnitude, hence strong antiferromagnetic coupling across alkoxide and weak interaction across $N_{diazine}$. This model leads to values, g = 2.05, J (alkoxide) = -103.2 cm^{-1}, J (diazine) = -1.6 cm^{-1}, ρ = 0.0007, TIP = 1000 and 10^2 R = 1.18. This may suggest that Cu3 is dynamically Jahn-Teller distorted and consequently interacts strongly with Cu2, however Cu1 should always be strongly interacting with Cu2. Therefore, it is suggested that there are competing exchange pathways that are making modelling of the data in accord with the observed structure difficult.

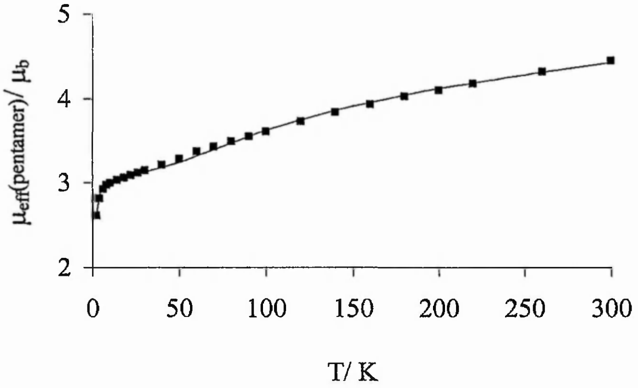

Figure 127 Represents the decrease in effective magnetic moment with temperature that is indicative of antiferromagnetic behaviour in the assembly $[Cu_{20}(\mathbf{L8A}\text{-}4H)_4(\mathbf{L8A}\text{-}2H)_4(H_2O)_{16}](ClO_4)_{16}\cdot 14H_2O$.

8.1 Conclusion

The formation of a novel cyclic octanuclear Cu(II) assembly is reported and is a rare example of a polynuclear circular assembly containing more than six Cu(II) ions.[128] The controlled formation of this assembly occurs because of the bidentate coordination pockets programmed into the ligand strand and the square based pyramidal coordination preference of the Cu(II) ion. These coordination pockets cause an acute twist between adjacent Cu(II) centres *via* $N_{diazine}$ leading to ferromagnetic behaviour. Reaction of **L8** with metal ions that display an octahedral coordination preference yielded a hexanuclear Mn(II) assembly that suffers from incomplete metal ion coordination due to intramolecular hydrogen bonding within the ligand framework. Whilst, **L8A** forms a decaconte Cu(II) assembly upon the addition of base by adopting two types of binding mode, one grid-like and one helical-like. The structure is truly three dimensional, but the magnetic properties are inconsistent with the structure.

Chapter Nine

Other Assemblies and Ligand Systems

9.0 Introduction

During this study a variety of ligands were prepared most of which have been discussed in previous chapters, however, there are some ligands which could not be suitably manipulated to give assemblies containing transition metal ions. Some would only give characterisable solids by reaction with Pb(II), whilst others appeared not to react at all. The following chapter will cover some interesting assemblies formed Pb(II), with suggestions relating to their formation, along with unsuccessful ligand designs.

Pyrazine Bridged Ligands

Following the leads observed with **L8** and **L8A** preparation of their pyrazine analogues was attempted and was expected to give similar motifs in an interwoven manner.[52] However, the ligands could not be obtained in high purity because of contamination of a half product where only one end of the central diimidate heterocycle has reacted (Fig. 128). Even the application of larger volumes of solvent and different solvents, to help solubilise the half product, would not increase the purity. The solids formed were eventually washed with hot DMF to remove most of the half product and used crude for further investigation.

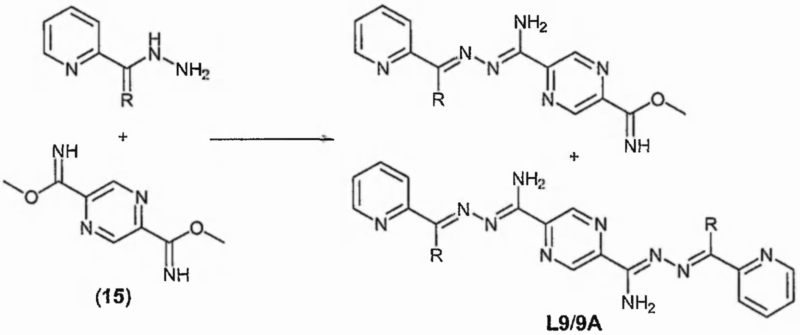

Figure 128 Formation of half product where only one pyridine derivative has attached and the desired ligands, R = NH_2 = **L9** and R = OH = **L9A**.

Attempts at reacting of both these ligands with various first row transition metal ions regularly led to no reaction. This was primarily confirmed by no distinct colour change of the solution of metal salt and the ligand remaining out of solution. Further examination of the suspected free ligand by IR confirmed this with no anions present and an identical fingerprint to the free ligand. **L9** will react with various Cu(II) salts to give brown solids and examination of these by ESI-MS in acetonitrile with ranging temperatures and cone voltages only indicated minor species that could not be identified. Consequently, both **L9** and **L9A** were reacted with $Pb(OTf)_2$ in a variety of ways and crystals were obtained from a mixture of water, methanol and acetonitrile with **L9A** that were suitable for further analysis.

Examination of the crystals by ESI-MS in acetonitrile at ranging cone voltages and temperatures only produce spectra of very weak intensity that could not be assigned. However, ^{1}H NMR at 298 K, in a mixture of acetonitrile and D_2O, does provide solution evidence for a highly symmetrical structure. The spectrum, which is of only weak intensity, displays five peaks of equal intensity within the aromatic region and the signal observed is not derived from the free ligand because it has no solubility in the solvent mix used.

Solid-State Studies: $[Pb_4($**L9A**$-2H)(OTf)_6(H_2O)_2]_n$ (**A31**)

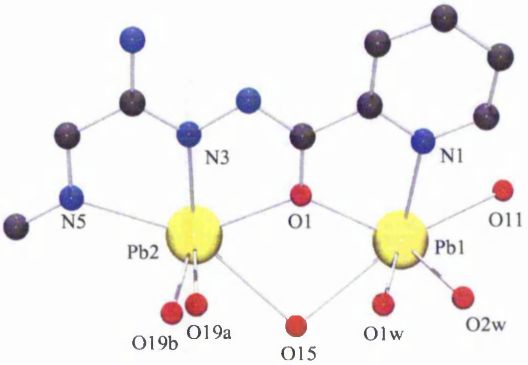

Figure 129 POV-Ray representation of $[Pb_4($**L9A**$-2H)(OTf)_6(H_2O)_2]_n$ asymmetric unit.

X-Ray analysis confirms the highly symmetrical structure with an asymmetric unit comprising two Pb(II) ions, half a ligand strand, three triflate anions and one water molecule. The three anions and the single water molecule are coordinated to the Pb(II) ions with the anions bridging to another Pb(II) ion on a different asymmetric unit making the structure polymeric. The water molecule and one of the triflate anions are disordered over two sites; however removing this disorder shows the three-dimensional nature of the compound (Fig. 130). This gives the structures layers of stacked ligand strands with channels of Pb(II) ions, water molecules and triflate anions.

The Pb(II) ions are typical with a distinct $6s^2$ sterochemically active lone pair as observed in this study and by others.[105b] They have a six coordinate environment consisting of nitrogen, alkoxy, water and triflate donors (Table 54 and Fig. 129) with a variety of bond lengths and angles typical of Pb(II) in this study.

Table 54 Selected bond lengths/ Å and angles/ ° for $[Pb_4(\mathbf{L9A}\text{-}2H)(OTf)_6(H_2O)_2]_n$.

Pb1-O1	2.385(7)	O1-Pb1-N1	68.0(3)	O19B-Pb2-N3	94.2(5)
Pb1-N1	2.447(8)	O1-Pb1-O17Bi	104.0(3)	O19B-Pb2-O1	98.2(5)
Pb1-O15	2.759(7)	O1W-Pb1-O15	69.9(4)	N3-Pb2-O1	65.9(2)
Pb1-O1W	2.562(16)	O1-Pb1-O1W	72.6(4)	O19B-Pb2-O19A	15.4(5)
Pb1-O11	2.704(6)	N1-Pb1-O1W	81.3(4)	N3-Pb2-O19A	85.0(4)
Pb2-N5	2.676(8)	O11-Pb1-O15	146.2(2)	O1-Pb2-O19A	83.2(4)
Pb2-O19B	2.282(13)	O1-Pb1-O11	136.9(3)	O19B-Pb2-N5	76.0(5)
Pb2-N3	2.370(8)	N1-Pb1-O11	81.5(3)	N3-Pb2-N5	63.8(3)
Pb2-O1	2.394(7)	O1W-Pb1-O15	69.9(4)	O1-Pb2-N5	128.7(2)
Pb2-O19A	2.502(14)	O1W-Pb1-O11	133.4(4)	O19A-Pb2-N5	83.0(4)
		O1-Pb1-O15	66.1(2)		
		N1-Pb1-O15	131.2(2)		

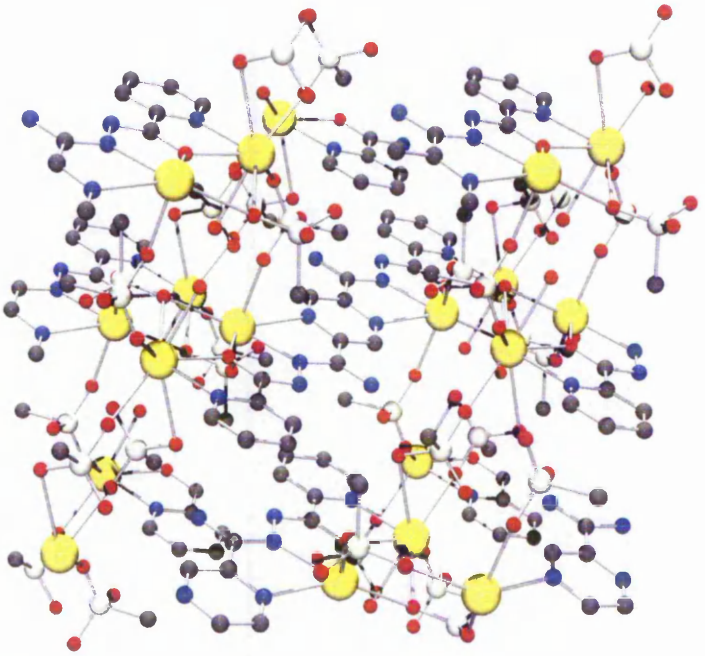

Figure 130 POV-Ray representation of $[Pb_4(\mathbf{L9A}\text{-}2H)(OTf)_6(H_2O)_2]_n$. Note fluoride atoms have been omitted for clarity.

[5 x 5] Ligands

Ligands with the potential of form [5 x 5] grids, which contain heterocyclic rings as bridging groups require an unsymmetrical synthetic strategy, whilst those containing the being purely alkoxide bridged can be synthesised in a symmetrical manner. Consequently, a relatively simple purely alkoxide ligand, **L10** (Fig. 131), was designed and can be seen as a simple extension of **L6,** although, the ligand is potentially very flexible and likely to only form grid-like structures with Mn(II) and Pb(II) as with the purely alkoxide bridged [4 x 4] grids observed in chapter 6.

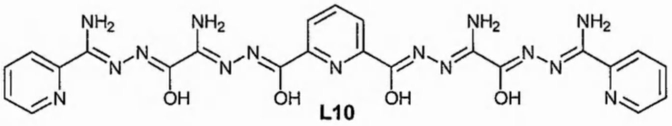

Figure 131 L10 contains a linear array of five tridentate pockets with the potential of forming a [5 x 5] grid.

However, attempts at **L10**'s preparation were unsuccessful (Fig. 132). Following the methodology used to form **L6**; reaction of pyridine-2,6-dihydrazido (**39**) with ethyl carboethoxyformimidate (**34**) in methanol along with a catalytic amount of glacial acetic acid gave the desired extended ethyl ester (**40**) in high yields. Displacement of the ethoxy groups by the addition of an excess of hydrazine furnished the corresponding dihydrazido (**41**) after being maintained at reflux for two days. Normally, this type of hydrazido compound reacts smoothly with methyl pyridine-2-imidate (**2**) to give the corresponding capped ligand in high yields. This is not the case here, because of the high insolubility of the dihydrazido derivative that appears to hinders any reaction. Attempts with longer reaction times, more polar solvents and different stoichiometries only gave very small amounts of **L10** along with mainly starting material as suggested by ESI-MS.

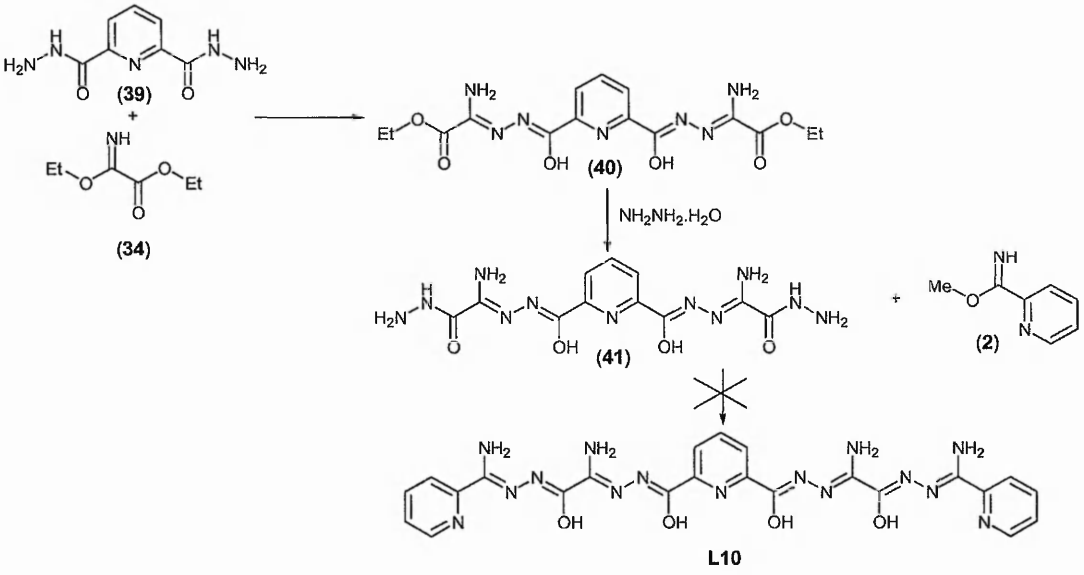

Figure 132 Attempted preparation of **L10**.

[6 x 6] Ligands

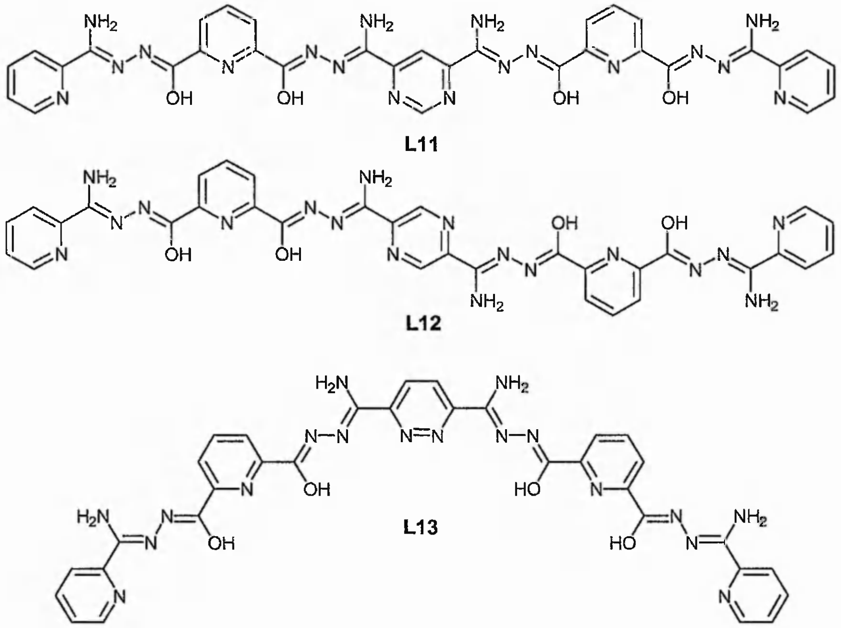

Figure 133 Ligands with the potential of forming [6 x 6] molecular grids.

Following the three heterocyclic bridged [4 x 4] ligands, **L2-4**, three analogous [6 x 6] ligands were designed. As with their [4 x 4] analogues, their designs are rationalised by providing a linear array of six tridentate pockets separated by alkoxide and heterocyclic bridges (Fig. 133).

The synthesis of **L11-13** were achieved by addition of *N*-(6'-hydrazidopyridine-2'-amido)pyridine-2-amidine (**43**) to the corresponding diimidate heterocycle in dry methanol that contained a catalytic amount of glacial acetic acid. Heating the solutions under reflux precipitated the desired ligands that were isolated *via* hot filtration. These were fully characterised by conventional techniques with insignificant/ no half product present by ESI-MS and NMR. *N*-(6'-hydrazidopyridine-2'-amido)pyridine-2-amidine (**43**) was prepared according to Fig. 134 starting from diethyl pyridine-2,6-dicarboxylate (**44**).

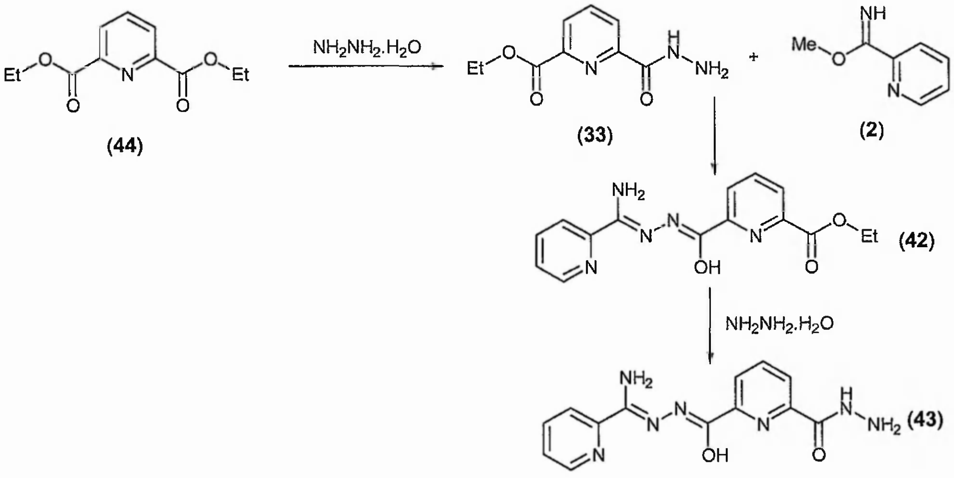

Figure 134 Formation of capping group used to prepare ligands with the potential of forming [6 x 6] molecular grids.

Reaction of these ligands with various first row transition metal ions in a variety of ways only yielded powders and no single crystals. Examination of these powders by ESI-MS in acetonitrile, with ranging cone voltages and temperatures, yielded spectra that displayed very little ion formation. Consequently, the large Pb(II) ion was investigated and single crystals were obtained when **L13** was reacted with a large excess of $Pb(OTf)_2$ in a mixture of water, methanol and acetonitrile in a low yield (10 %).

Examination of the crystals by ESI-MS in acetonitrile at 70 °C at a cone voltage of 10 V produced a spectrum with a large number of peaks that could not be assigned. No NMR was attempted due to a lack of sample.

Solid-State Studies: $\{[Pb_5(\mathbf{L13}\text{-}(4H + H_2O))(OTf)_5(H_2O)_5](OTf)(H_2O)_6\}_n$ (**A32**)

The crystals were characterised by X-ray analysis, which displayed a bent chain of five Pb(II) ions with bridging triflate anions to a second bent chain making the structure polymeric, analogous to that observed for **L9A**. The vacant coordination is caused by cyclisation of the hydrazide link by the elimination of water to give a triazole ring (Fig. 135). This cyclisation probably only occurs in minor amounts and reflects the low yield obtained. By a simple charge balance with the number of metal ions and anions there is a difference of unity that is accounted for by assuming that the newly formed pyrazole ring is deprotonated. Comparable cyclisations have been observed in similar ligand systems along with the triazole ring being deprotonated.[129] The Pb(II) ions have a mixture of six and seven coordination numbers with a distinct $6s^2$ stereochemically active lone pair causing a large void around the ion.[105b]

Table 55 Selected bond lengths/ Å for $\{[Pb_5(\mathbf{L13}\text{-}(4H + H_2O))(OTf)_5(H_2O)_5](OTf)(H_2O)_6\}_n$.

Pb1-N3	2.35	Pb2-N5	2.46	Pb3-O2	2.50	Pb4-O84	2.59
Pb1-O1	2.38	Pb2-O81	2.49	Pb3-N9	2.59	Pb5-N16	2.39
Pb1-O53a	2.51	Pb2-O2	2.51	Pb4-O3	2.40	Pb5-O85	2.47
Pb1-N1	2.56	Pb2-O41	2.60	Pb4-O83	2.57	Pb5-O3	2.48
Pb1-O44a	2.58	Pb3-O82	2.33	Pb4-N14	2.59	Pb5-N18	2.57
Pb2-O1	2.41	Pb3-N7	2.44				

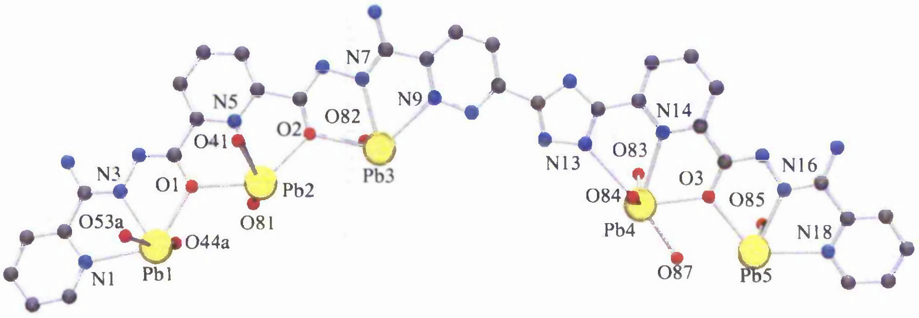

Figure 135 POV-Ray representation of $\{[Pb_5(\mathbf{L13}\text{-}(4H + H_2O))(OTf)_5(H_2O)_5](OTf)(H_2O)_6\}_n$ cation.

Table 56 Selected bond angles/ ° for {[Pb$_5$(**L13**-(4H + H$_2$O))(OTf)$_5$(H$_2$O)$_5$](OTf)(H$_2$O)$_6$}$_n$.

N3-Pb1-O1	67	O1-Pb2-N5	67	O82-Pb3-N7	86	O83-Pb4-N14	78
N3-Pb1-O53a	86	O1-Pb2-O81	74	O82-Pb3-O2	85	O83-Pb4-O84	150
N3-Pb1-N1	65	O1-Pb2-O2	130	O82-Pb3-N9	102	N14-Pb4-O84	76
N3-Pb1-O44a	79	O1-Pb2-O41	82	N7-Pb3-O2	63	N16-Pb5-O85	78
O1-Pb1-O53a	94	N5-Pb2-O81	80	N7-Pb3-N9	62	N16-Pb5-O3	65
O1-Pb1-N1	132	N5-Pb2-O2	64	O2-Pb3-N9	124	N16-Pb5-N18	65
O1-Pb1-O44a	81	N5-Pb2-O41	75	O3-Pb4-O83	93	O85-Pb5-O3	86
O53a-Pb1-N1	79	O81-Pb2-O2	87	O3-Pb4-N14	65	O85-Pb5-N18	79
O53a-Pb1-O44a	165	O81-Pb2-O41	151	O3-Pb4-O84	90	O3-Pb5-N18	130
N1-Pb1-O44a	94	O2-Pb2-O41	96				

Examination of the unit cell contents display an interesting polymeric network with an interlocking type structure that is caused by one bent chain being joined to another bent chain, which is inverted (Fig. 136). This gives the structure a wave-like appearance with separate chains half overlapping *via* bridging triflate anions.

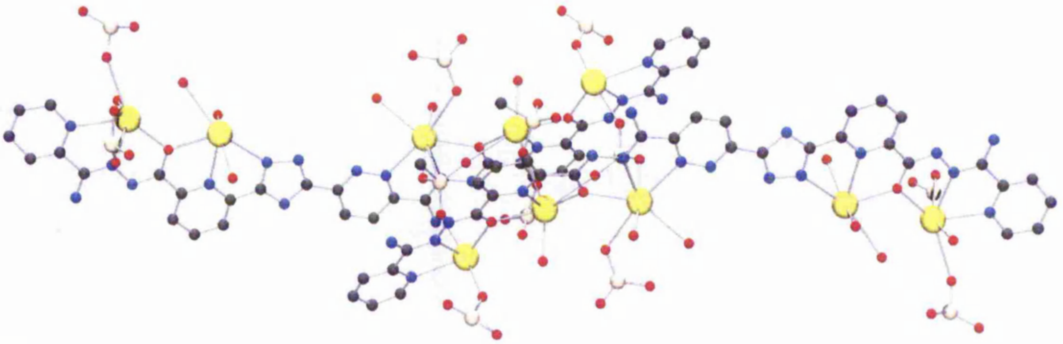

Figure 136 Wave like structure observed in {[Pb$_5$(**L13**-(4H + H$_2$O))(OTf)$_5$(H$_2$O)$_5$](OTf)(H$_2$O)$_6$}$_n$ unit cell. Note: fluoride atoms have been omitted for clarity.

9.1 Conclusion

This brief chapter demonstrates the versatility of the Pb(II) ion to give polymeric species which are not observed with first row transition metal ions. Examination of **L11-13** suggests that heterocyclic bridged grids will be restricted to those with dimensions of [4 x 4], however it is felt that purely alkoxide bridged systems, *i.e.*, **L10**, could lead to a [5 x 5] molecular grid when reacted with a first row transition metal ion that displays no crystal field preference. This would obviously be dependent on a suitable synthesis of **L10**.

References

1). (a) D. A. Thompson and J. S. Best, *IBM J. Res. Develop.*, 2000, **44**, 311. (b) P. Vettiger, M. Despont, U. Drechsler, U. Drig, W. Hberle, M. I. Lutwyche, H. E. Rothuizen, R. Stutz, R. Widmer and G. K. Binning, *IBM J. Res. Develop.*, 2000, **44**, 323.

2). http://www.people.man.ac.uk/%7Embdssrew/winpeny.html.

3). J.-M. Lehn, *Supramolecular Chemistry*, VCH, Weinheim, 1995.

4). For examples see (a) L. Zhao, C. J. Matthews, L. K. Thompson and S. L. Heath, *Chem. Commun.*, 2000, 265. (b) L. Zhao, Z. Xu, L. K. Thomspon, S. L. Heath, D. O. Miller and M. Ohba, *Angew. Chem. Int. Ed. Engl.*, 2000, **39**, 3114. (c) L. K. Thompson, O. Waldmann and Z. Xu, in *Magnetism: Molecules to Materials IV*, Eds. J. S. Miller and M. Drillon, Wiley-VCH, 2002, 173. (d) O. Walmann, J. Hassmann, P. Muller, G. S. Hanan, D. Volkmer, U. S. Schubert and J.-M. Lehn, *Phys. Rev. Lett.*, 1997, **78**, 3390. (e) M. Ruben, E. Breunuing, M. Barboiu, J.-P. Gisselbrecht and J.-M. Lehn, *Chem. Eur. J.*, 2003, **9**, 291. (f) J. Rojo, J.-M. Lehn, G. Baum, D. Fenske, O. Waldmann and P. Muller, *Eur. J. Inorg. Chem.*, 1999, 517.

5). L. K. Thompson, *Coord. Chem. Rev.*, 2002, 193.

6). (a) D. Gatteschi and R. Sessoli, *Angew. Chem. Int. Ed. Engl.*, 2003, **42**, 268. (b) R. Sessoli, D. Gatteschi, A. Caneschi and M. A. Novak, *Nature*, 1993, **365**, 141. (c) European Science Foundation, Molecular Magnets, http://www.esf.org/mm.

7). For diamagnetic corrections (Pascal's' constants) see for example: R. L. Carling, *Magnetochemistry*, Springer-Verlag, Heidelberg, 1986.

8). (a) P. W. Anderson, *Phys Rev.*, 1959, **115**, 2. (b) P. W. Anderson in *Magnetism*, Eds. G. T. Rado and H. Suhl, Academic Press Inc., New York, Vol. 1, 1965.

9). (a) J. B. Goodenough, *Phys. Rev.*, 1955, **100**, 564. (b) J. B. Goodenough and A. L. Loeb, *Phys. Rev.*, 1953, **93**, 391. (c) J. B. Goodenough, *J. Phys. Solids*, 1958, **6**, 287.

10). J. Kanamori, *J. Phys. Chem. Solids*, 1959, **6**, 287.

11). O. Khan, *Angew. Chem. Int. Ed. Engl.*, 1985, **24**, 834.

12). J. H. Van Vleck, *Theory of Electronic and Magnetic Susceptibilities*, Oxford University Press, London and New York, 1932.

13). B. Bleaney and K. D. Bowers, *Proc. R. Soc. London Ser. A.*, 1952, **214**, 451.

14). K. Kambe, *J. Phys. Soc. Japan*, 1950, **5**, 48.

15). K. S. Murray, in *Advances in Inorganic Chemistry*, Ed. A. G. Sykes, Academic Press Inc, 1995, **43**, 261.

16). T. Lis, *Acta Crystallogr. B*, 1980, **36**, 2041.

17). R. Sessoli, H-L. Tsai, A. R. Schake, S. Wang, J. B. Vincent, K. Folting, D. Gatteschi, G. Christou and D. N. Hendrickson., *J. Am. Chem. Soc.*, 1993, **115**, 1804.

18). (a) R. E. P. Winpenny, *J. Chem. Soc., Dalton Trans.*, 2001, **1**, 1. (b) R. E. P. Winpenny, in *Advances in Inorganic Chemistry*, Ed. A. G. Sykes, Academic Press Inc, 2001, **52**, 1.

19). S. L. Castro, Z. Sun, C. M. Grant, J. C. Bollinger, D. N. Hendrickson and G. Christou, *J. Am. Chem. Soc.*, 1995, **120**, 2365.

20). M. Murugesu, M. Habrych, W. Wernsdorfer, K. A. Abboud and G. Christou, *J. Am Chem. Soc.*, 2004, **126**, 4766.

21). K. Wieghardt, K. Pohl, I. Jibril and G. Huttner, *Angew. Chem. Int. Ed. Engl.*, 1984, **23**, 77.

22). C. Delfs, D. Gatteschi, L. Pardi, R. Sessoli, K. Wieghardt and D. Hanke, *Inorg. Chem.*, 1993, **32**, 3099.

23). D. Gatteschi, R. Sessoli and A. Corina, *Chem. Commun.*, 2000, 725.

24). J. C. Goodwin, R. Sessoli, D. Gatteschi, W. Wernsdorfer, A. K. Powell and S. L. Heath, *J. Chem. Soc., Dalton Trans.*, 2000, 1835.

25). A. K. Powell, S. L. Heath, D. Gatteschi, L. Pardi, R. Sessoli, G. Spina, F. Del Giallo and F. Pieralli, *J. Am. Chem. Soc.*, 1995, **117**, 2491.

26). M. Murray, S. J. Teat, H. Stoeckli-Evans and H. U. Gudel, *Angew. Chem. Int. Ed. Engl.*, 2003, **42**, 4653.

27). C. Cadiou, M. Murray, C. Paulsen, V. Villar, W. Wernsdorfer and R. E. P. Winpenny, *Chem. Commun.*, 2001, 2666.

28). H. Andres, R. Basler, A. J. Blake, C. Cadiou, G. Chaboussant, C. M. Grant, H. U. Gudel, M. Murray, S. Parsons, C. Paulsen, F. Semadini, V. Villar, W. Wernsdorfer and R. E. P. Winpenny, *Chem. Eur. J.*, 2002, **8**, 4867.

29). J. Larionova, R. Clerac, B. Boury, J. Le Bideau, L. Lecren and S. Willemin, *J. Mater. Chem.*, 2003, **13**, 795.

30). A. Corina, A. C. Fabretti, M. Pacchioni, L. Zobbi, D. Bonacchi, A. Caneschi, D. Gatteschi, R. Biagi, U. Del Pennino, V. De Renzi, L. Gurevich and S. J. Van der Zant, *Angew. Chem. Int. Ed. Engl.*, 2003, **42**, 1645.

31). S. Willemin, G. Arrachart, L. Lecren, J. Larionova, T. Coradin, R. Clerac, T. Mallah, C. Guerin and C. Sanchez, *New J. Chem.*, 2003, **27**, 1533.

32). (a) U. Knof, A. von Zelewsky, *Angew. Chem. Int. Ed. Engl.*, 1999, **38**, 302. (b) C. Piguet, J.-C. G. Bunzli, *Eur. J. Solid State Inorg. Chem.*, 1996, **33**, 165. (c) F. A. Cotton, L. M. Daniels, C. A. Murillo and X. Wang, *Chem. Commun.*, 1999, 2461.

33). C. Piguet, G. Bernardinalli and G. Hopfgartner, *Chem. Rev.*, 1997, **97**, 2005.

34). J.-M. Lehn, A. Rigault, J. Siegel, J. Harrowfield, B. Chevrier and D. Moras, *Proc. Natl. Acad. Sci. USA*, 1987, **84**, 2565.

35). A. F, Williams, *Chem. Eur. J.*, 1997, **3**, 15.

36). W. J. Stratton, D. H. Busch, *J. Am. Chem. Soc.*, 1958, **80**, 1286. (b) W. J. Stratton, D. H. Busch, *J. Am. Chem. Soc.*, 1960, **82**, 4834.

37). M. J. Hannon, C. L Painting, A. Jackson, J. Hamblin and W. Errington, *Chem. Commun.*, 1997, 1807.

38). Z. Xu, L. K. Thompson, D. O. Miller, H. J. Case, J. A. K. Howard and A. E. Goeta, *Inorg. Chem.*, 1998, **37**, 3620.

39). M.-T. Youinou, N. Rahmouni, J. Fischer and J. A. Osborn, *Angew. Chem. Int. Ed. Engl.*, 1992, **31**, 733.

40). A. M. Garcia, F. J. Romero-Salguero, D. M. Bassani, J.-M. Lehn, G. Baum and D. Fenske, *Chem. Eur. J.*, 1999, **5**, 1803.

41). (a) G. S. Hannon, D. Volkmer, U. S. Schubert, J.-M. Lehn, G. Baum and D. Fenske, *Angew. Chem. Int. Ed. Engl.*, 1997, **36**, 1842. (b) H. Nierengarten, E. Leize, E. Breuning, A. Garcia, F. Romero-Salguero, J. Rojo, J.-M. Lehn and A. Van Dorsselaer, *J. Mass Spectrom.*, 2002, **37**, 56. (c) E. Breuning, M. Ruben, J.-M. Lehn, F. Renz, Y. Garcia, V. Ksenofontov, P. Gutlich, E. Wegelius and K. Rissanen, *Angew. Chem. Int. Ed. Engl.*, 2000, **39**, 2504. (d) M. Ruben, E. Breuning, J.-M. Lehn, V. Ksenofotov, F. Renz, P. Gutlich and G. B. M. Vaughan, *Chem. Eur. J.*, 2003, **9**, 442.

42). (a) D. M. Bassani, J.-M. Lehn, K. Fromm and D. Fenske, *Angew. Chem. Int. Ed. Engl.*, 1998, **37**, 2364. (b) D. M. Bassani, J.-M. Lehn, S. Serroni, F. Puntoriero and S. Campagna, *Chem. Eur. J.*, 2003, **9**, 5936.

43). E. Breuning, U. Ziener, J.-M. Lehn, E. Wegelius and K. Rissanen, *Eur. J. Inorg. Chem.*, 2001, 1515.

44). (a) A. Semenov, J. P. Spatz, M. Moller, J.-M Lehn, B. Sell, D. Schubert, C. H. Weidel and U. S. Schubert, *Angew. Chem. Int. Ed. Engl.*, 1998, **38**, 2547. (b) J. Rojo, J.-M. Lehn, G. Baum, D. Fenske, O. Waldmann and P. Muller, *Eur. J. Inorg. Chem.*, 1999, 517.

45). (a) C. J. Matthews, Z. Xu, S. K. Mandal, L. K. Thompson, K. Biradha, K. Poirier and M. J. Zaworotko, *Chem. Commun.*, 1999, 347. (b) L. Zhao, C. J. Matthews, Z. Xu, L. K. Thompson and D. O. Miller, *Mol. Cryst. Liq. Cryst.*, 2002, **376**, 389.

46). J. Hausmann, G. B. Jameson, S. Brooker, *Chem. Commun.*, 2003, 2992.

47). D. S. Cati, J. Ribas, J. Ribas-Arino and H. Stoeckli-Evans, *Inorg. Chem.*, 2004, **43**, 1021.

48). A. Gelasco, A. Askenas and V. L. Pecoraro, *Inorg. Chem.*, 1996, **35**, 1419.

49). (a) A. J. Amoroso, A. M. W. Cargill Thompson, J. C. Jeffery, P. L. Jones, J. A. McCleverty and M. D. Ward, *Chem. Commun.*, 1994, 2751. (b) H. Brunner and T. Scheck, *Chem. Ber.*, 1992, **125**, 701.

50). J. C. Jeffery, P. L. Jones, K. L. V. Mann, E. Psillakis, J. A. McCleverty, M. D. Ward and C. M. White, *Chem. Commun.*, 1997, 175.

51). K. L. V. Mann, E. Psillakis, J. C. Jeffery, L. H. Rees, N. M. Harden, J. A. McCleverty, D. Gatteschi, F. Totti, F. E. Mabbs, E. J. L. McInnes, P. C. Reidi and G. M. Smith, *J. Chem. Soc., Dalton Trans.*, 1999, 339.

52). T. Bark, M. Duggeli, H. Stoeckli-Evans and A. von Zelewsky, *Angew. Chem. Int. Ed. Engl.*, 2001, **40**, 2848.

53). H. Gang, G. Dong, D. Chun-Ying, M. Hong and M. Qing-Jin, *New J. Chem.*, 2002, **10**, 137.

54). J. P. Plante, P. D. Jones, D. R. Powell and T. E. Glass, *Chem. Commun.*, 2003, 336.

55). (a) P. N. W. Baxter, J.-M. Lehn, J. Fischer and M.-T. Youinou, *Angew. Chem. Int. Ed. Engl.*, 1994, **33**, 2284. (b) A. Marquis, J.-P. Kintzinger, R. Graff, P. N. W. Baxter and J.-M. Lehn, *Angew. Chem. Int. Ed. Engl.*, 2002, **41**, 2760.

56). E. Breuning, G. S. Hanan, F. J. Romero-Salguero, A. M. Garcia, P. N. W. Baxter, J.-M. Lehn, E. Wegelius, K. Rissanen, H. Nierengarten and A. van Dorsselaer, *Chem. Eur. J.*, 2002, **8**, 3458

57). O. Waldman, L. Zhao and L. K. Thompson, *Phys. Rev. Lett.*, 2002, **88**, 066401-1.

58). T. S. M. Abedin, L. K. Thompson, D. O. Miller and E. Krupicka, *Chem. Commun.*, 2003, 708.

59). P. N. W. Baxter, J.-M. Lehn, G. Baum and D. Fenske, *Chem. Eur. J.*, 2000, **6**, 4510.

60). M. Barboiu, G. Vaughan, R. Graff and J.-M Lehn, *J. Am. Chem. Soc.*, 2003, **125**, 10257.

61). C. J. Matthews, S. T. Onions, G. Morata, M. B. Salvina, M. R. J. Elsegood and D. J. Price, *Chem. Commun.*, 2003, 320.

62). F. R. Heirtzler, *Syn. Lett.*, 1999, **8**, 1203.

63). A. Hirsch and D. G. Orphanos, *Can. J. Chem.*, 1966, **44**, 1551.

64). F. Case, *J. Org. Chem.*, 1965, **30**, 931.

65). S. Ohuchida, M. Toda and T. Miyamoto, *Eur. Pat. Appl.*, 1989, **27**, EP 323590 A2 19890712.

66). E. Boucher, M. Simard and J. D. Wuest, *J. Org. Chem.*, 1995, **60**, 1408.

67). P. E. Spoerri and A. Erickson, *J. Am. Chem. Soc.*, 1938, **60**, 400.

68). N. Sato, Y. Shimomura, Y. Ohwaki and R. Takeuchi, *J. Chem. Soc., Perkin Trans. 1*, 1991, **11**, 2877.

69). G. S. Hannan, U. S. Schubert, D. Volkmer, E. Riviere, J.-M. Lehn, N. Kyritsakas and J. Fischer, *Can. J. Chem.*, 1997, **75**, 169.

70). A. McKillop, S. K. Chattopadhyay, A. Henderson and C. Avendano, *Synthesis*, 1997, 301.

71). D. L. Arora, K. Lal, S. P. Gupta and S. K. Sahni, *Polyhedron*, 1986, **10**, 1499.

72). For preparation see: K. S. Hagen, *Inorg. Chem.*, 2000, **39**, 5867 and references cited therein.

73). D. Wenkert and R. B. Woodward, *J. Org. Chem.*, 1983, **48**, 284.

74). I. Antonini, F. Claudi, G. Cristalli, P. Franchetti, M. Grifantini and S. Martelli, *J. Med. Chem.*, 1981, **24**, 1181.

75). Md. A. Masood, B. P. Sullivan and D. J. Hodgson, *Inorg. Chem.*, 1999, **38**, 5425.

76). C. J. Matthews, S. T. Onions, G. Morata, L. J. Davis, S. L. Heath and D. J. Price, *Angew. Chem. Int. Ed. Eng.*, 2003, **43**, 3166.

77). L. Weeks, L. K Thompson, L. G. Shapter, K. J. Pope and Z. Xu, *J. Microsc.*, 2003, **212**, 102.

78). A. J. Bard and L. R. Faulkner, *Electrochemical Methods: Fundamentals and Applications* (2nd edition), Wiley and Sons Inc, 2001.

79). M. A. Weiner and A. Basu, *Inorg. Chem.*, 1980, **19**, 2797.

80). J. G. Gaudiello, P. R. Sharp and A. J. Bard, *J. Am. Chem. Soc.*, 1982, 104, 6373.

81). P. K. S. Tsang, P. Cofre and D. T. Sawyer, *Inorg. Chem.*, 1987, **26**, 3604.

82). D. E. Richardson, H. Taube, *Inorg. Chem.*, 1981, **20**, 1278.

83). H.-R. Chang, S. K. Larsen, P. D. W. Boyd, C. G. Pierpont and D. N. Hendrickson, *J. Am. Chem. Soc.*, 1988, **110**, 4565, and references cited there in.

84). A. K. Brisdon, *Inorganic Spectroscopic Methods*, O. U. P., 1998.

85). F. A. Cotton and G. Wilkinson, *Advanced Inorganic Chemistry: A Comprehensive Text,* 5th Ed., John Wiley & Sons, 1998.

86). Z. Xu, K. He, L. K. Thompson and O. Waldmann, MAGMUN4.0, Memorial University of Newfoundland, St. Johns, NF, Canada, 2002.

87). Z. Xu, L. K. Thompson, V. A. Milway, L. Zhao, T. Kelly and D. O. Miller, *Inorg. Chem.*, 2004, **42**, 2950.

88). S. Brooker, D. J. de Guest, R. J. Kelly, P. G. Plieger, B. Moubaraki, K. S. Murray and G. B. Jameson, *J. Chem. Soc., Dalton Trans.*, 2002, 2080.

89). M. Cantuel, G. Bernardinelli, D. Imbert, J. C. G. Bunzli, G. Hopfgartner and C. Piguet, *J. Chem. Soc., Dalton Trans.*, 2002, 1929.

90). J. B. Vincent, H.-R. Chang, K. Folting, J. C. Huffman, G. Cristou and D. N. Hendrickson, *J. Am. Chem. Soc.*, 1987, **109**, 5703.

91). (a) Z. Xu, L. K. Thompson, C. J. Matthews, D. O. Miller, A. E. Goeta and J. A. K. Howard, *Inorg. Chem.*, 2001, **40**, 2446. (b) W. Clegg, *Private Communication.*

92). L. Zhao, Z. Xu, L. K. Thompson, S. L. Heath, D. O. Miller and M. Ohba, *Angew. Chem. Int. Ed. Eng.*, 2000, **39**, 3114.

93). C. R. Rice, S. Worl, J. C. Jeffery, R. L. Paul, M. D. Ward, *J. Chem. Soc., Dalton Trans.*, 2001, 550.

94). Z. Xu, L. K. Thompson, V. A. Milway, L. Zhao, T. Kelly and D. O. Miller, *Inorg. Chem.*, 2003, **42**, 2950.

95). (a) L. Zhao, Z. Xu, H. Grove, V. A. Milway, L. N. Dawe, T. S. M. Abedin, L. K. Thompson, T. L. Kelly, R. G. Harvey, D. O. Miller, L. Weeks, J. G. Shapter and K. J. Pope, *Inorg. Chem.*, 2004, **43**, 3812. (b) L. K. Thompson, T. L. Kelly, L. N. Dawe, H. Grove, M. T. Lemaire, J. A. K. Howard, E. C. Spencer, C. J. Matthews, S. T. Onions, S. J. Coles, P. N. Horton, M. B. Hursthouse and M. E. Light, *Inorg. Chem.*, 2004, **43**, 7605.

96). K. Dimitrou, A. D. Brown, T. E. Concolino, A. L. Rheingold and G. Christou, *Chem. Commun.*, 2001, 1284.

97). S. Wang, M. S. Wemple, J. Yoo, K. Folting, J. C. Huffman, K. S. Hagen, D. N. Hendrickson and G. Christou, *Inorg. Chem.*, 2000, **39**, 1501.

98). C. D. Schmulbach and T. V. Oommen, *Anal. Chem.*, 1973, **45**, 820.

99). A. M. Garcia, F. J. Romero-Salguero, D. M. Bassani, J.-M. Lehn, G. Baum, D. Fenske, *Chem. Eur. J.*, 1999, **6**, 1803.

100). H. Nierengarten, E. Leize, E. Breuning, A. Garcia, F. Romero-Salguero, J. Rojo, J.-M. Lehn, A. V. Dorsselaer, *J. Mass Spectrom.*, 2002, **37**, 56.

101). S. Yamada, S. Terajima and N. Ito, *Jpn. Tokkyo Koho*, 1973. JP 48029229 19730908.

102). R. R. Hunt, J. F. W. Mcomie and E. R. Sayer, *J. Chem. Soc., Abstracts,* 1959, 525.

103). O. I. Gorbyleva, M. I. Evstratova and L. N. Yakhontov, *Chem. of Heterocyclic Comp.*, 1983, 113.

104). For example see: T. N. Sorrell and M. L. Garrity, *Inorg. Chem.*, 1991, **30**, 211.

105). (a) S. T. Onions, A. M. Franklin, P. N. Horton, M. B. Hursthouse, C. J. Matthews, *Chem. Commun.*, 2003, 2864. (b) L. Shimoni-Livny, J. P. Glusker and C. W. Block, *Inorg. Chem.*, 1998, **37**, 1853.

106). D. Luneau, J. M. Savariault and J. P. Tuchagues, *Inorg. Chem.*, 1998, **22**, 3912.

107). (a). O. Waldmann, *Phys. Rev. B*, 2000, **61**, 6138. (b) O. Waldmann, R. Koch, S. Schromm, J. Schulein, I. Bernt, R. W. Saalfrank, F. Hampel and A. E. Balthes, *Inorg. Chem.*, 2001, **40**, 3277.

108). T. Ishida, K. Takayuki, S. Mitsubori, T. Nogami, K. Yamaguchi and H. Iwamura, *J. Chem. Soc., Dalton Trans.*, 2002, **16**, 3177.

109). For a recent example see: A. Delgadillo, P. Romo, A. M. Leiva and B. Loeb, *Helv. Chemica Acta*, 2003, **86**, 2110.

110). J. J. Lafferty and F. H. Case, *J. Org. Chem.*, 1967, 1591.

111). N. Myaura, T. Yanagi and A. Suzuki, *Synth. Commun.*, 1981, **11**, 513.

112). J. K. Stille, *Angew. Chem. Int. Ed. Engl.* 1986, **25**, 508.

113). H. Matondo, S. Souirti and M. Baboulene, *Synth. Commun.*, 2004, 795.

114). E. Tyrrell and P. Brookes, *Synthesis*, 2004, 469.

115). V. Patroniak, P. N. W. Baxter, J.-M. Lehn, M. Kubicki, M. Nissinen and K. Rissanen, *Eur. J. Inorg. Chem.*, 2003, 4001.

116). K. C. Nicolaou, D. Hepworth, N. P. King, M. R. V. Finlay, R. Scarpelli, M. M. A. Pereira, B. Bollbuck, A. Bigot, B. Werschkun and N. Winssinger, *Chem. Eur. J.*, 2000, **6**, 2783.

117). (a). C. Piguet, G. Bernardinelli and G. Hopfgartner, *Chem. Rev.*, 1997, **97**, 2005. (b). C. Piguet, G. Bernardinelli and G. Hopfgartner, *Chem. Rev.*, 1997, **97**, 2005. M. Albrecht, *Chem. Rev.*, 2001, **101**, 3457.

118). J.-M. Lehn and A. Rigault, *Angew. Chem. Int. Ed, Engl.*, 1988, **27**, 1095.

119). S. M. Peng, C. C. Wang, Y. L. Jang, Y. H. Chen, F. Y. Li, C. Y. Mou and M. K. Leung, *J. Magn. Magn. Mater.*, 2000, **209**, 80.

120). (a). L. K. Thompson, C. J. Matthews, L. Zhao, C. Wilson, M. A. Leech and J. A. K. Howard, *J. Chem. Soc. Dalton Trans.*, 2001, 2258. (b). L. Davis and C. J. Matthews, *unpublished results*.

121). X. Zhou, E. F. Kovalev, J. T. Klug and V. Khodorkovsky, *Org. Lett.*, 2001, **11**, 1725.

122). A. Hirsch and D. G. Orphanos, *Can. J. Chem.*, 1966, **44**, 1551.

123). L. K. Thompson, S. S. Tandon and M. E. Manuel, *Inorg. Chem.*, 1995, **34**, 2356 and references cited therein.

124). J. Cano, G. De Munno, F. Lloret and M. Julve, *Inorg. Chem.*, 2000, **39**, 1611.

125). Z. Xu, L. K. Thompson, C. J. Matthews, D. O. Miller, A. E. Goeta, C. Wilson, J. A. K. Howard, M. Ohba, H. Okawa, *J. Chem. Soc., Dalton Trans.*, 2000, 69.

126). S. T. Onions, S. L. Heath, D. J. Price, R. W. Harrington, W. Clegg and C. J. Matthews, *Angew. Chem. Int. Ed. Engl.*, 2004, **43**, 1814.

127). (a) P. L. Jones, K. Byrom, J. C. Jeffery, J. A. McCleverty and M. D. Ward, *Chem. Commun.*, 1997, 1361. (b). B. Hasenknopf, J.-M. Lehn, B. O. Kneisel, G. Baum and D. Fenske, *Angew. Chem. Int. Ed. Engl.*, 1996, **35**, 1838.

128). C.-H. Chang, K. C. Hwang, C.-S. Liu, Y. Chi, A. J. Carty, L. Scoles and S.-M. Peng, *Angew. Chem. Int. Ed. Engl.*, 2001, **40**, 4651.

129). C. J. Matthews, *unpublished results*.